UNIVERSITY OF OXFORD

Searches for New Physics using Dijet Angular Distributions in proton-proton collisions at $\sqrt{s} = 7$ TeV collected with the ATLAS Detector

by

Ryan Mark Buckingham

of

St Edmund Hall

Oxford

Thesis submitted in partial fulfilment of the requirements
for the degree of Doctor of Philosophy

Hilary Term, 2013

UNIVERSITY OF OXFORD

Abstract

Searches for New Physics using Dijet Angular Distributions in proton-proton collisions at $\sqrt{s} = 7$ TeV collected with the ATLAS Detector

by Ryan Mark Buckingham

Angular distributions of jet pairs (dijets) produced in proton-proton collisions at a centre-of-mass energy $\sqrt{s} = 7$ TeV have been studied with the ATLAS detector at the Large Hadron Collider using the full 2011 data set with an integrated luminosity of 4.8 fb^{-1}, and reaching dijet masses up to 4.5 TeV. All angular distributions are consistent with QCD predictions.

Analysis of the dijet angular distribution, using a novel technique simultaneously employing the dijet mass, is employed. This analysis is sensitive to both resonant new physics and phenomena with a slow-onset in mass. Using this technique, new exclusion limits have been set at 95% credibility level for several hypotheses of physics beyond the standard model including: quantum gravity scales, with 6 extra dimensions, below 4.11 TeV, quark contact interactions below a compositeness scale of 7.6 TeV, and excited quarks with a mass below 2.75 TeV.

In a large and complex scientific experiment, such as ATLAS, the collection, management and usability of coherent data and metadata is a challenging operation. The availability of these data to physicists within the experiment is essential to all analysis efforts. A new web-based interface called "RunBrowser", which makes ATLAS and LHC operations data available to the ATLAS Collaboration, is introduced.

Acknowledgements

The journey from inquisitive young boy, to the completion of this thesis, has been aided by many. Here I would like to offer special thanks to some of these.

I believe I have been extremely lucky throughout my schooling to be blessed with enthusiastic, dedicated and knowledgable teachers. My first thanks must go Mrs. West at Lutterworth Grammar School, who pushed me beyond the regular physics curriculum at an early stage. This trend was matched, and furthered, by my experiences at Leicester Grammar School, where thanks to Mr. Inchley, Mr. Cawston, Mr. Handford and especially Mrs. Price, I was pushed to my maximum and given the confidence to strive to pursue a course in academia to the highest standards.

My time at St Edmund Hall will no doubt be among the happiest of my life. I am indebted to many of the college fellows for their guidance and advice throughout my time as JCR President and other roles. Thank-you for an unforgettable 8 years.

As my tutors at St Edmund Hall, I must thank Philipp Podsiadlowski and Jeff Tseng for, yet again, pushing me to strive to the highest targets and for offering essential advice throughout. Thank you both.

As a first year undergraduate, I was lucky enough to take part in a summer research project with Muge Karagoz Yamaoka, Todd Huffman, Jeff Tseng and Farrukh Azfar. This experience sowed the seeds for an enthusiasm for experimental particle physics that would ultimately lead me to this thesis. Thank-you for this opportunity.

Thank-you to Elizabeth Gallas for a fantastic first year project, and ATLAS authorship task. Not only did this project enable me to present my results at the CHEP 2010 conference in Taiwan, it also helped me develop many skills that will be useful beyond physics.

Upon moving to CERN, I joined the Exotics Dijet Team. Here I must thank Frederik Rüehr, Georgios Choudalakis, Nele Boelaert, Thorsten Dietzsch, Mike Shupe and Caterina Doglioni. I had a fantastic time working in this team of brilliant people, and enjoyed learning lots from everyone.

Within the Oxford ATLAS Group, I must also thank Alan Barr, Claire Gwenlan, Tony Weidberg, Hugo Beauchemin and Chris Hayes for their help over the past 4 years. I am also very thankful to my peers (over multiple years) for productive discussions over daily coffees and Friday night beers: Alex Pinder, Dan Short, Sam Whitehead, Chris Boddy, Caterina

Doglioni, Sarah Livermore, Nick Ryder, Adrian Lewis, Ellie Davies, Chris Young, Robert King, David Hall, Lucy Kogan and Alex Dafinca.

With regards to this thesis, I am, of course, most indebted to my supervisor: Çiğdem İşsever, whose guidance, enthusiasm and management, stirred my curiosity and encouraged me to dive straight into the ATLAS Collaboration: striving to contribute and gain responsibility at an early stage. I believe this approach put me in good stead to publish meaningful results, and to ultimately produce this work.

Finally, I would like to thank the STFC, St Edmund Hall, the Institute of Physics and the University of Oxford Department of Physics for their financial support over the last 4 years.

Thank you all.

Contents

Abstract **i**

Acknowledgements **ii**

List of Figures **vii**

List of Tables **xi**

1 Introduction **1**
1.1 New physics searches 2
1.2 An overview of the Standard Model 3
1.3 Searches for New Physics using Dijet Angular Distributions in proton-proton collisions at $\sqrt{s} = 7$ TeV collected with the ATLAS Detector 6
1.4 Author's contribution 8

2 Collider physics and quantum chromodynamics **11**
2.1 Scattering experiments and the parton model 12
2.2 Quantum chromodynamics 13
2.3 The cross-section for a hard hadronic process 19
2.4 Monte Carlo simulation of QCD processes 21
2.5 QCD Monte Carlo simulation used in this thesis 23

3 Experimental apparatus **25**
3.1 The Large Hadron Collider 25
3.2 Overview of the ATLAS detector 28
3.3 The ATLAS trigger system 36
3.4 Simulation of the ATLAS detector 37
3.5 Data used in this thesis 38

4 Beyond the standard model **40**
4.1 Extra dimensions 40

4.2 Quantum Black Holes . . . 46
4.3 Quark sub-structure . . . 49

5 Jet reconstruction **55**
5.1 Motivations for jet definitions . . . 55
5.2 Jet finding algorithms in ATLAS . . . 56
5.3 Jet reconstruction in ATLAS . . . 58
5.4 Jet energy scale & calibration . . . 59
5.5 Jet uncertainties . . . 62

6 Searches for new physics with dijet angular distributions **66**
6.1 Leading order dijet production . . . 66
6.2 Angular dependence of dijet cross-section . . . 69
6.3 Maximising sensitivity to the partonic cross-section . . . 73
6.4 Experimental observables for NP searches . . . 77
6.5 Definition of control regions . . . 82

7 Event selection, systematic uncertainties and resulting distributions **83**
7.1 Event selection . . . 83
7.2 Histogram binning and trigger strategy . . . 88
7.3 QCD predictions . . . 91
7.4 Theoretical systematic uncertainties . . . 93
7.5 Experimental systematic uncertainties . . . 96
7.6 Summary of systematics . . . 99
7.7 Studies of the effects of pileup . . . 101
7.8 Effects from detector malfunction . . . 103
7.9 Validation of the QCD background . . . 105
7.10 Final distributions . . . 106

8 Statistical interpretation and limits on signals for new physics **112**
8.1 Search phase: is there evidence of new physics? . . . 113
8.2 Limit-setting phase: constraints on new physics . . . 121

9 Summary and conclusions **130**
9.1 Summary of results . . . 130
9.2 Comparison of dijet analysis techniques . . . 133
9.3 Future work and conclusions . . . 135

10 Metadata aided run selection **136**
10.1 Introduction & motivation . . . 136
10.2 ATLAS Conditions Database . . . 137
10.3 Event selection using ATLAS TAGS . . . 138
10.4 runBrowser - Dynamic metadata aided Run selection . . . 139
10.5 Conclusions and future work . . . 143

A Determination of binning in χ and m_{jj} **145**
A.1 Determination of binning in χ 145
A.2 Determination of fine binning in m_{jj} 146

B Comparing ATLFAST II to GEANT full simulation **148**

C Determination of trigger efficiencies **150**

D Debug stream investigation in early data **153**

E BLACKMAX `paramter.txt` **155**

F Pileup reweighting **160**

G Cut flows for signal samples **162**

Bibliography **164**

List of Figures

2.1 Loop corrections to the gluon propagator. 15
2.2 Parton kinematics in the x, Q^2 plane for (a) Tevatron and (b) LHC colliders. 18
2.3 Proton PDF distributions for $\sqrt{s} = 7$ TeV as a function of x according to the MSTW collaboration. 19
2.4 Schematic for a proton-proton collision resulting in a hard-scatter between two partons. Other possible interactions from initial and final state radiation and underlying event are also included. 20
2.5 LO, NLO and NNLO cross-section for inclusive jet cross-section as a function of leading jet p_T 21

3.1 Underground layout of the LHC tunnel. 26
3.2 Cross section for various processes as a function of centre of mass collision energy and the event rate. 27
3.3 The ATLAS detector. 28
3.4 Pseudo-rapidity η and polar angle θ in the ATLAS coordinate system. 30
3.5 Computer-generated image of the ATLAS inner detector and its components. 31
3.6 Layout of the ATLAS calorimetry system. 32
3.7 The LAr calorimeter barrel. 34
3.8 Segmentation in depth and η of the tile-calorimeter modules in the central (left) and extended (right) barrels. 35
3.9 Schematic of the ATLAS trigger system. 37
3.10 (a) Cumulative luminosity versus week delivered to (green), and recorded by ATLAS (yellow) during stable beams. (b) The maximum mean number of events per beam crossing versus day. This version shows the average value for all bunch crossings in a lumi-block. 39

4.1 Functional form of factor $k(D)$, defined in Equation 4.7. 45
4.2 Comparison of the q^* m_{jj} distribtions from Pythia 6 with and without the FSR correction, for a q^* mass of 3 TeV. 51
4.3 Sketch of interaction between quark constituents (left) and the low energy approximation of a regular four-point interaction (right). 53

5.1 Overview of the ATLAS jet calibration scheme use for the 2011 dataset. . . . 60
5.2 JER and JAR as function of p_T and η. 65

6.1 Partons a and b from hadrons A and B undergo a hard scatter $ab \to cd$ with cross-section $\hat{\sigma}$. The parton momentum densities are $f_{a/A}$ and $f_{b/B}$. 67

6.2 Schematic of two final-state massless partons in the lab frame (with 4-momenta p_c and p_d) boosted to the centre-of-mass frame giving them equal but opposite rapidities, $\pm y^*$. 69
6.3 Some of the diagrams of dijet production. 71
6.4 Rapidity range of a generic detector, before (grey square) and after (red rectangle) applying selection cuts in Equation 6.27. 74
6.5 $\mathrm{d}\sigma/\mathrm{d}\chi$ distributions for the (a) QBH and (b) quark contact interaction signals. 74
6.6 Normalised χ distributions to demonstrate effect of including y_B cut. 76
6.7 Surface plot describing the expected distribution of event yields in the observables η_{j_1} and η_{j_2} for dijets with $875 \leq m^{jj} \leq 1020$ GeV. 77
6.8 Normalised $\mathrm{d}\sigma/\mathrm{d}\chi$ distributions for the (a) QBH and (b) quark contact interaction signals. 80
6.9 $F_\chi(m_{jj})$ distributions for the (a) QBH, (b) quark contact interaction and (c) excited quark signals. 81

7.1 Event yield, per run, for the analysis selection criteria. 89
7.2 Bin-wise NLO k-factors for (a) the $F_\chi(m_{jj})$ reconstructed mass spectrum and (b) the un-normalised and reconstructed χ spectrum. 93
7.3 Angular distributions generated with NLOJET++ (truth parton level), for various choices of μ_R and μ_F. 94
7.4 Theoretical uncertainty bands for the χ distribution in each broad mass bin. 95
7.5 $F_\chi(m_{jj})$ distributions for 100 of the 1000 JES pseudo experiments described by Equation 7.6. 97
7.6 The upper and lower jet energy scale uncertainty on the χ distribution for each broad dijet mass bin. 98
7.7 (a) JER, (b) JAR, and their associated uncertainties on the χ distributions, for each dijet invariant mass range. 98
7.8 Envelopes for the dominant sources of systematic uncertainty in $F_\chi(m_{jj})$ distributions: JES, scale, and PDF uncertainties. 99
7.9 For the full data and MC samples, these plots show the variation in coarse binned F_χ distributions due to in-time pileup, which is strongly correlated with the number of primary vertices, N_{PV}. 102
7.10 These plots show (a) the variation in dijet χ distributions and (b) the variation in F_χ in coarse m_{jj} bins; as a function of position in a bunch train, which affects the amount of out-of-time pileup. 103
7.11 Distribution of the bad tile channel correction factor for data events with dijet mass above 700 GeV. 104
7.12 Data (black points) are compared to LO QCD (red line). Statistical uncertainties on the QCD MC are included in yellow. 107
7.13 Data (black points) are compared to LO QCD (red line). Statistical uncertainties on the QCD MC are included in yellow. The bottom half of each figure displays the ratio of data/MC, and their associated statistical uncertainties. 108
7.14 The $F_\chi(m_{jj})$ distribution in m_{jj}. 109
7.15 The χ distributions for all dijet mass bins. 110
7.16 Highest mass event passing full event selection. 111

8.1 $-\ln L$ distribution for $F_\chi(m_{jj})$ PE compared to value from data. The corresponding p-value is found to be 0.380. 117
8.2 (a) Possible resonance-like intervals with the corresponding probabilities in data. Each possible mass window is shown as a red horizontal line. Systematic uncertainties are not included. The interval with the smallest probability is found to be the region 1798 - 2882 GeV. Note that the p-values on the y-axis do not include a look-elsewhere effect. (b) Likelihood distribution determined from pseudo-experiments used to convolve the systematic uncertainties, and include a look-elsewhere effect, are employed to determine the $p-$value that quantifies the agreement between the QCD prediction at data. The resulting $p-$value = 0.2031, which corresponds to 0.83 σ. 118
8.3 (a) Possible threshold-like intervals with the corresponding probabilities in data. Each possible mass window is shown as a red horizontal line. Systematic uncertainties are not included. The interval with the smallest probability is found to be the region $m_{jj} > 1798$ GeV. Note that the p-values on the y-axis do not include a look-elsewhere effect. (b) Likelihood distribution determined from pseudo-experiments used to convolve the systematic uncertainties are employed to determine the $p-$value that quantifies the agreement between the QCD prediction at data. The resulting $p-$value = 0.2111, which corresponds to 0.80 σ. 119
8.4 Acceptance times efficiency for each of the signals considered in this thesis. Values are shown as a function of the main signal parameters. 122
8.5 The 95% CL upper limits of $\sigma \times \mathcal{A}$ as a function of the q^* mass using $F_\chi(m_{jj})$ (black filled circles). The black dashed curve shows the 95% CL upper limit expected from Monte Carlo and the light and dark yellow shaded bands represent the 68% and 95% contours of the expected limit, respectively. Theoretical predictions of $\sigma \times \mathcal{A}$ for the excited quark model as shown as dotted lines. The observed (expected) limit occurs at the crossing of the theory curve with the observed (expected) 95% CL upper limit curve. 125
8.6 Distributions for QBH signal samples with $n = 3, 4, 5, 6$ and 7. QCD background is not included. Distributions suggest that angular distribution and mass profile is independent of n. 126
8.7 The 95% CL upper limits of $\sigma \times \mathcal{A}$ as a function of the reduced Planck Mass M_D of the QBH model using $F_\chi(m_{jj})$ (black filled circles). The black dashed curve shows the 95% CL upper limit expected from Monte Carlo and the light and dark yellow shaded bands represent the 68% and 95% contours of the expected limit, respectively. Theoretical predictions of $\sigma \times \mathcal{A}$ are shown for various numbers of extra dimensions. The observed (expected) limit occurs at the crossing of the theory curve with the observed (expected) 95% CL upper limit curve. 127
8.8 2-dimensional surface of F_χ for quark contact interactions as a function of Λ and m_{jj}. 127
8.9 Limit setting for contact interactions using the $F_\chi(m_{jj})$ distribution: observed posterior probability distribution function including systematic uncertainties due to JES and scale uncertainty. 128

10.1 The three dedicated metadata repositories in the ATLAS Experiment. 138

10.2 Detailed screen shot from runBrowser 140
10.3 Flow diagram of the relational dependencies of the Data Bases (DB), COMA tables and the various interfaces. Solid (red) lines signify transfer of metadata and dashed (blue) lines signify transfer of data. 141
10.4 Screen shot from runBrowser results page 143

A.1 Stability and purity, considering migrations in χ and M_{jj}, for two mass bins. 146
A.2 The reconstructed m_{jj} distributions for various excited quark signal samples. 147

B.1 χ distributions, comparing ATLFAST II to GEANT simulation in the lowest m_{jj} bins 149
B.2 χ distributions, comparing ATLFAST II to GEANT simulation in intermediate m_{jj} bins 149
B.3 χ distributions, comparing ATLFAST II to GEANT simulation for highest mass bin, $2600 < m_{jj} < 7000$ GeV 149

C.1 Trigger efficiencies as a function of m_{jj}. Efficiencies are provided to dijet events with (a) $0.0 < y^* < 0.6$ and (b) $0.6 < y^* < 1.7$. 152

D.1 (a) Event display for a debug stream event. The event contains two high p_T jets, with the upper jet pointing to numerous red hits in the muon detectors. These muon hits are indicative of jet punch through. (b) Distribution of jet momentum for events which enter the physics stream vs. the debug stream. A clear bias can be seen for events with high p_T jets to be passed to the debug stream. 154

F.1 Effects of pile-up reweighing for all χ distributions. 161

List of Tables

1.1 The leptons of the standard model. 4
1.2 The electrical charges and masses for the quarks of the standard model. . . . 5
1.3 The gauge bosons of the standard model. 5

2.1 J-slices of Pythia QCD Monte Carlo with their respective leading jet p_T ranges, cross-sections and the number of events that are simulated. 24
2.2 J7 exists as a single sample, but also as a sample split into two leading jet p_T ranges: each is included in the analysis for an increase in statistics. 24

3.1 General performance goals of the ATLAS detector. 29

4.1 Lower limits on M_D (in the Large Extra Dimension scenario) at the 95% confidence level from other accelerator experiments. 42
4.2 Percentage occurrence (Branching Ratio, BR) for each decay topology. . . . 48
4.3 Cross-sections for QBH samples generated with the BlackMax MC simulator for $n = 2 - 7$ extra dimensions and various values of M_D. 48
4.4 Branching ratios and relative decay widths for q^* ($m_{q^*} = 1, 2, 3$ TeV) to various decay channels. 50
4.5 Cross-section and number of events generated for Pythia 8 excited quark at q^* masses from 2 to 4.5 TeV. 52
4.6 Cross-section and number of generated events for Pythia contact interactions model for various values of composite-scale Λ. Sample are split into J-slices corresponding to p_T ranges in Table 2.1. 54

6.1 The invariant matrix elements squared $\overline{\sum} |\mathcal{M}|^2$ for $2 \to 2$ parton sub-processes with massless partons, and their corresponding values for $\hat{\theta} = \pi/2$. 70
6.2 Comparison of expected limits calculated using different definitions for the numerator of F_χ. 82

7.1 Values of m_{jj} for which single-jet triggers become 99% efficient. 84
7.2 Cut flow for the full 2011 exotics data sample. 86
7.3 Cut flow for the Pythia QCD MC. 87
7.4 Triggers used for $F_\chi(m_{jj})$ and their effective luminosity. 88
7.5 Triggers used for χ and their effective luminosity 90
7.6 Table containing χ bin boundaries. 90
7.7 Summary of systematic uncertainties for $F_\chi(m_{jj})$ due to JES, scale and PDF, along with their total. 100

7.8 Summary of systematic uncertainties for χ distribution in mass bin $m_{jj} >$ 2.6 TeV due to JES, scale and PDF, along with their total. 100

8.1 Comparing χ distributions to QCD predictions. p-values are calculated for each of the broad dijet mass bins using the likelihood defined in Equation 8.8. 116
8.2 Lower limits at the 95% CL on M_D of the QBH model with $n = 2 - 7$ extra dimensions. 125

9.1 The 95% CL lower limits on the masses and energy scales of the models exampled in this thesis. All limit analyses are Bayesian, with statistical and systematic uncertainties included. 131
9.2 ATLAS previous and current expected 95% CL upper limits on new phenomena. 132

A.1 Table containing χ bin boundaries. 146

G.1 Cut flow and efficiency for excited quark sample with $m_{q^*} = 3$ TeV. 162
G.2 Cut flow and efficiency for QBH with $m_{q^*} = 3$ TeV. 162
G.3 Cut flow and efficiency for contact interaction sample with $\Lambda = 10$ TeV. . . . 163

To my family, for their guidance, support and confidence through all of my endeavours.

Chapter 1

Introduction

For hundreds of years, humans have been struggling to come to grips with the complex behaviour of the universe around them. Some physicists have sought to identify the most fundamental ingredients of our existence and the illusive forces that dictate their behaviour. This reductionist approach has given birth to the field of particle physics, which over decades of research, has led to the development of what we now call the **S**tandard **M**odel (**SM**).

After nearly 20 years of design, development, construction and testing: on the 9^{th} of December of 2009 the **L**arge **H**adron **C**ollider (**LHC**) [1] took up the mantle as the world's highest energy particle collider. The experiment is hosted by European Organisation for Nuclear Research (**CERN**).

The Large Hadron Collider will allow us to push our understanding of the fundamental structure of nature to the next level. Through studies of proton collisions at this new energy regime, it hoped that our understanding of nature will be advanced. Be it the Standard Model Higgs, Supersymmetry or even Extra Dimensions, results from the LHC are bound to stimulate our curiosity and prompt yet more flavours of possible theories of nature.

Although the SM has been shown to be a very successful theory, it is believed by most to be incomplete, or a restricted subset of a more general and complete model. In total, the SM has 19 free parameters including the coupling constants of the forces, the lepton and quark masses, the mass of the Z boson and the four parameters of the CKM matrix[1]. One obvious short fall of the standard model is the absence of gravity in its interactions. A consistent renormalisable quantum theory of gravity has long been a goal of modern particle physics, with string theory providing one possible idea.

[1]The **CKM** (**C**abbibo-**K**obayashi-**M**askawa) matrix describes the extent to which quarks from different generations mix through the weak force. For a further description: see [2].

If, in fact the SM is part of some more fundamental theory, then there is a strong case for new physical processes at the TeV energy scale, which either extend or alter our understanding of the SM. This thesis is concerned with the search for such phenomena.

1.1 New physics searches

A search for a previously unobserved physical process must have a clearly defined goal and strategy. Without this structure, biases can creep into the analysis: leading to a false discovery or a missed opportunity to identify a new physics effect.

As a first step, one must have a solid understanding of the dominant processes that are observed in particle collisions. By analysing the phenomenology of such processes, one can identify situations in which an additional *new* physics process would lead to a measurable departure from the expected SM behaviour.

Whether or not one begins with a particular new physics model in mind should not effect the result of the analysis. For example, in a search for the SM Higgs boson: although some final-state signatures are well-motivated, and therefore are popular to study, emphasis must be placed on understanding the *background* processes dominating that final-state, and on calculating an unbiased quantification of the agreement between the data and the background estimation.

Before any data is analysed, new kinematic variables may be constructed, which provide optimised differentiation between the SM background and a new physics process. For example, in this thesis a variable is constructed that allows one to differentiate between the angular behaviour of jets of particles produced in the SM, to the angular behaviour of jets of particles produced by a set of new physics signal hypotheses.

An analysis should identify a *control region*, i.e. a restricted sector of the kinematic phase space, where a new physical signal is not expected and it is therefore believed that the observables in the analysis are well-understood. A *search region* should also be defined, where one will look for any deviation from the expected kinematic behaviour.

Once data has been recorded, the control region can be used as a test for any background simulation, or can even be used to determine an overall process normalisation to be extrapolated to the search region. The data that falls into the search region should not be analysed until the behaviour of data in the control region is well-understood - once this condition is satisfied, then the search phase of the analysis can begin.

The aim of the search phase is to assess the extent to which the recorded data agrees with a background hypothesis: known as the *Null Hypothesis*. A full explanation of the methodology for this process is given in Chapter 8 of this thesis. Briefly, a p-value is calculated: defined as the probability of observing data that is at least as discrepant from the null hypothesis as the data that was observed, taking into consideration all of the uncertainties associated with the data and null hypothesis simulation. No new physics scenarios need to be considered at this stage. If this p-value is found to be very small[2], then one is not able to place much confidence in the original null hypothesis: and it is possible that a new physics process has been observed.

In the event that the p-value indicates no significant deviation from the null hypothesis, then we can proceed to the limit-setting stage of the analysis. For the limit-setting state, the question is posed: *"If I assume that my new physics model is valid: given the null-result in the search phase, what constraints can I place on the free parameters of my model?"* In order to answer this question, a simulation of the new physics signal is required, where it is possible to vary the parameters that we wish to constrain. The method for containing a model parameter is discussed in detail in Chapter 8.

Briefly, the *'observed'* constraint on the model parameter is obtained by considering the probability distribution of the observable about the null hypothesis. The data is then compared to this distribution of possible outcomes. Disregarding the data, for the moment, it is possible to calculate an *'expected'* constraint on a model parameter, where one pretends that the recorded data behaves *exactly* as the background simulation. Comparing the expected and observed results, one is able to gain another indication of the extent to which the data agrees with the null hypothesis of the background.

1.2 An overview of the Standard Model

The **S**tandard **M**odel (**SM**) [2–6] is a relativistic quantum field theory consisting of an array of elementary particles along with a Lagrangian that describes their behaviour and interactions. The elementary particles can be split into two groups: the spin-1/2 fermions from which matter is formed, and the spin-1 gauge bosons which are responsible for mediating three of the fundamental forces.

[2] A common convention is to require a p-value of less than (or equal to) 0.0000003 in order to claim a discovery of a new physics process. For an observable, which follows a normal distribution, this corresponds to measuring a value that is greater than (or equal to) 5 standard deviations from the mean.

The SM describes three of the four known fundamental interactions: the electromagnetic, the weak and the strong; leaving out the gravitational interaction. Although gravity does not fit into the SM[3] it is predicted by some theories that the force may be mediated by the hypothetical electrically neutral and massless spin-2 graviton. The possible inclusion of gravity into a more-complete model for particle physics provides a strong motivation for this thesis and a part of Chapter 4 is dedicated to this subject.

Within the SM, there are twelve fermions (each with a respective anti-fermion), twelve gauge bosons and one neutral Higgs particle. The fundamental fermions are split into groups: quarks and leptons: quarks carry non-integer electric charge and also carry colour charge (meaning that they interact via the strong force), however leptons carry unit electric charge and carry no colour charge (and consequently do not interact via the strong force). Each of these groups can then be grouped into three generations. For the leptons, each generation is composed of an electrically charged lepton and an electrically neutral neutrino: electron (ν_e, e^-), muon (ν_μ, μ^-) and tau (ν_τ, τ^-). The SM leptons and their properties are summarised in Table 1.1.

	Particles		Anti-particles		
Generation	Flavor	Charge (Q)	Flavor	Charge (Q)	Rest Mass
1	electron - e	-1	$\bar{e}$	$+1$	$0.510998910 \pm 13 \times 10^{-9}$ MeV
	ν_e	0	$\bar{\nu}_e$	0	< 1 MeV
2	muon - μ	-1	$\bar{\mu}$	$+1$	$105.658367 \pm 4 \times 10^{-6}$ MeV
	ν_μ	0	$\bar{\nu}_\mu$	0	< 1 MeV
3	tau - τ	-1	$\bar{\tau}$	$+1$	1776.84 ± 0.17 MeV
	ν_τ	0	$\bar{\nu}_\tau$	0	< 1 MeV

TABLE 1.1: The leptons of the standard model [8]. Recent experimental evidence [9] suggests that neutrinos have non-zero masses, however these masses can be assumed negligible in the context of this thesis.

For the quarks, the six flavours are grouped into three generations according to: (u, d), (c, s) and (t, b). The up (u), charm (c) and top (t) quarks have an electric charge of $+2/3$, and the down (d), strange (s) and bottom (b) quarks have an electric charge of $-1/3$. The SM quarks and their properties are summarised in Table 1.2.

The interactions between the SM fermions are mediated by the gauge bosons. A summary of these particles and their properties is given in Table 1.3. The photon is associated with the electromagnetic force, the $W^\pm$ and Z are associated with the weak force, and the gluon is associated with the strong force.

[3]Gravity cannot be included in any current renormalisable quantum field theory [7].

	Particles		Anti-particles		
Generation	Flavor	Charge (Q)	Flavor	Charge (Q)	Rest Mass
1	up - u	$+2/3$	anti-up - $\bar{u}$	$-2/3$	$1.5 - 3.3$ MeV
	down - d	$-1/3$	anti-down - $\bar{d}$	$+1/3$	$3.5 - 6.0$ MeV
2	charm - c	$+2/3$	anti-charm - $\bar{c}$	$-2/3$	1270^{+70}_{-110} MeV
	strange - s	$-1/3$	anti-strange - $\bar{s}$	$+1/3$	104^{+26}_{-34} MeV
3	top - t	$+2/3$	anti-top - $\bar{t}$	$-2/3$	171.2 ± 2.1 GeV
	bottom - b	$-1/3$	anti-bottom - $\bar{b}$	$+1/3$	$4.2^{+0.17}_{-0.07}$ GeV

TABLE 1.2: The electrical charges and masses for the quarks of the standard model [8].

Boson	Charge (Q)	Spin	Rest Mass
Photon - γ	0	1	$< 1 \times 10^{-18}$ eV
Z	0	1	91.1876 ± 0.0021 GeV
W^+	$+1$	1	80.398 ± 0.025 GeV
W^-	-1	1	80.398 ± 0.025 GeV
Gluon - g	0	1	0

TABLE 1.3: The gauge bosons of the standard model [8]. Note that the gluon has a theoretical mass of zero, however a mass as large as a few MeV may not be precluded [8].

The SM is based on the gauge group [3–6] $SU(3)_C \times SU(2) \times U(1)$, where C denotes *colour*. The complete Lagrangian is obtained as the sum of the electro-weak Lagrangian, $\mathcal{L}_{EW}$, and the QCD (quantum chromodynamics) Lagrangian, $\mathcal{L}_{QCD}$. The electro-weak Lagrangian, which is invariant under the $SU(2)_L \times U(1)$ part of the SM, is not discussed here[4]. The QCD Lagrangian, which is invariant under the $SU(3)_C$ part of the SM, describes particle interactions under the strong force and is therefore particularly relevant in the context of jets. QCD and its role in a hadron collider is described in Chapter 2.

1.2.1 The hierarchy problem

One common motivation for new physics is the hierarchy problem. In the context of the Higgs boson, large quantum corrections due to radiation of virtual particles (mostly top quarks) enter into its mass term. Without the presence of new physical processes below the Planck scale[5], these corrections will become quadratically divergent. Divergences are resolved through *fine-tuning*, however this is regarded as *unnatural*, since terms are required

[4]See [10] for a good description of the electro-weak Lagrangian and its properties.

[5]The Planck scale [8] is the energy scale at which the non-renormalisability of gravity becomes problematic for quantum field theory. The Planck scale is further discussed in Section 4.1.1.

to cancel with a precision of $\sim \mathcal{O}(M_D^2/M_{EW}^2) \sim 10^{-32}$, where M_{EW} is the Electro-weak scale[6]. Alternatively, the need for fine-tuning can be avoided if new physics is in the order of the Higgs scale. Contenders for such a theory include Supersymmetry [11], technicolor [12] and extra dimensions (see Section 4.1), however the scope for some of these theories has been limited by the recent observation of a new particle consistent with the SM Higgs Boson [13, 14].

1.2.2 Current status: on the existence of the Higgs boson

On the 4^{th} of July 2012, both the ATLAS and CMS experiments at CERN announced that they had observed a new particle, consistent with a SM Higgs boson [13, 14].

The ATLAS result [13], based on 4.8 fb^{-1} of 7 TeV data and 5.8 fb^{-1} of 8 TeV data, observed a neutral boson with measured mass $126 \pm 0.4(\text{stat}) \pm 0.4(\text{sys})$ GeV with a significance of 5.9 standard deviations[7].

The CMS result [14], based on 5.1 fb^{-1} of 7 TeV data and 5.3 fb^{-1} of 8 TeV data, observed a neutral boson with measured mass $125.3 \pm 0.4(\text{stat}) \pm 0.5(\text{sys})$ GeV with a significance of 5.0 standard deviations.

Further work is currently in progress, which will aim to measure Higgs boson production in all of its possible decay channels, and also to understand its properties.

1.3 Searches for New Physics using Dijet Angular Distributions in proton-proton collisions at $\sqrt{s} = 7$ TeV collected with the ATLAS Detector

In this thesis, I will describe the most recent experimental results from searches for new physical processes in the never-before explored territory of hadron collisions with a centre of mass energy of 7 TeV. This thesis will concentrate on the analysis of collisions that result in the production of two high energy jets. The production of particle jets is a dominant process at the LHC and will thus provide the signal or define the measurement environment

[6]The Electro-weak scale is the typical energy associated with electro-weak interactions. A commonly quoted value for the electro-weak scale is the vacuum expectation value of the Higgs field $v = (G_F\sqrt{s})^{-1/2} = 246$ GeV [8].

[7]A significance of 5.9 standard deviations corresponds to a background fluctuation probability of 1.7×10^{-9}.

for many analyses. A search for new physics signals within dijets is therefore also well-suited for searches employing early LHC data.

As by far the most dominant process for producing such final states, the motivation, evidence and simulation of **Q**uantum **C**hromo**d**ynamics (**QCD**) will be introduced in Chapter 2.

As the experimental apparatus of this thesis, the LHC and, in particular, the ATLAS detector are introduced in Chapter 3. The detector design and layout is discussed, however the description is mostly limited to those components that contribute to the reconstruction of jets.

In Chapter 4, the possibility of physics **B**eyond the **S**tandard **M**odel (**BSM**) will be explored. Three models are chosen that are predicted to have significant deviations from the standard model dijet behaviour. These models, which are fundamentally different in their phenomenology, are used as benchmark scenarios: allowing comparison between similar analyses at other experiments. In the event of finding good agreement between data and the SM, simulation of these BSM models allow one to constrain the possible values of certain model parameters. This, in turn, guides theorists to explore the most likely models, given our experimental observations.

Two models for quark sub-structure are described: these have been traditionally used as *benchmark models*, such that exclusion limits from various collider experiments can be easily compared. In addition, models including the extra spacial dimensions, aiming to explain gravity's relation to the SM, are discussed. As a relatively unexplored model, with a large rate of decay to dijets, Quantum Black Holes are described in Section 4.2.

The methodology and performance of jet reconstruction in ATLAS is discussed in Chapter 5. The journey from voltage measurements in the ATLAS calorimetry system to a full-calibrated jet object, which is compared to a detailed Monte Carlo situation, is described.

Chapter 6 will then describe the phenomenology of the dominant signature of QCD: two-jet final states, or more commonly, dijets. By combining angular, momentum and energy information of the jets, an analysis objective is to explore as much of the dijet kinematic phase space as possible. Variables are defined which enable one to explore this phase space, with the aim testing agreement between data and simulation in the tails of the kinematic reach, whilst reducing exposure to systematic uncertainties. Techniques detailed in this section include a new method, developed with Dr. Frederik Rüehr (University of Arizona), for probing mass-dependent changes in the angular behaviour of the dijet system. This method, which is sensitive to both resonant new physics and threshold effects that operate

above a given energy scale, was first used in [15] and is the main analysis method for this thesis.

In Chapter 7, the analysis procedure is described in detail. The selection of an unbiased sample of dijet events from LHC collisions is described. Systematic uncertainties arising from theoretical simulation of background process and experimental effects are considered in full and their effects on the physics analysis are quantified. Environmental effects such as detector malfunction and the high rate of proton-proton collisions are also discussed. Finally, control distributions are produced in order to validate the simulated background processes.

Chapter 8, will discuss statistical interpretation of results from the analysis of 4.8 fb^{-1} of proton-proton collisions at $\sqrt{s} = 7$ TeV. Emphasis is placed on a new and novel technique, known as $F_{\chi}(m_{jj})$, which is sensitive to both a resonant excess of central dijet events, and the slow onset of angular behaviour producing an excess of dijet events. In the event of good agreement between data and the SM Monte Carlo prediction, limits are placed on selected model parameters. The process for this limit setting is described in detail.

Chapter 9 will summarise and draw conclusions based on the previous chapters. Implications of results are discussed in both the immediate context of the LHC, and further: to implications for physics, in general. Future work and areas for potential improvements in the analysis are also discussed.

Finally, Chapter 10 outlines work performed as part of the ATLAS Tag Coordination group. This work is independent of the physics analysis described in this thesis, and summarises contributions made to the area of data management and coordination: foremost the development of the RunBrowser interface for accessing ATLAS data based on the selection of various LHC and detector conditions.

1.4 Author's contribution

The work described in this thesis includes a combination of contributions from multiple members of the ATLAS Collaboration. Most of the analysis, results and conclusions have been performed by the Exotics Dijet Analysis team, of which I am a member, with the support of the ATLAS Jet Performance Group. Throughout this thesis I endeavour to reference particular individual contributions from my colleagues.

In this section I will attempt to outline, in chronological order, my contributions to the work contained in this thesis, and related publications.

Although not the topic as this thesis, during the 2009 summer preceding the official beginning of my DPhil, I worked on an ATLAS internal note [16] investigating the use of the charge asymmetry in $W+jets$ production as a new probe of parton distribution functions in different kinematic regions at the LHC. This method is now being further developed for use within ATLAS.

Each new member of the ATLAS collaboration must carry out 'service work' in order to become a qualified author. I began this work at the beginning of my first year: working with Dr. Elizabeth Gallas and the ATLAS Tag Coordination Group. The details of this work are outlined in Chapter 10. This work involved developing a new web-interface - allowing ATLAS users to locate portions of data which satisfy a variety of selection criteria. A portion of the results from this work were presented in a poster session at the Computing in High Energy Physics (CHEP) conference in Taipei, Taiwan in October 2010 [17–19]. The proceedings of this contribution were published in [20].

Towards the end of my first year, I began to look at the first data coming from the LHC at $\sqrt{s} = 7$ TeV. In particular, I concentrated on trying to understand the rate and physics of events that were being diverted into a separate 'debug stream' independent from the main 'physics stream' which contains events primarily designated for analysis. As the first person to analyse this debug stream data, I was able to identify a bias for high-p_T, high multiplicity events to cause time-outs in the High-Level-Trigger (HLT) system. After further investigation, along with my supervisor Dr. Çiğdem İşsever, it was decided that these events should be included in all physics analyses. This work contributed to many jet-based measurements resulting in a number of publications for the International Conference in High-Energy Physics (ICHEP)[21–24] and also the first ATLAS publications at $\sqrt{s} = 7$ TeV [25–27]. This investigation also led to an improvement in the on-line muon trigger algorithms [28], which in-turn eliminated the bias for jet events to enter the debug stream.

At the beginning of my second year, I relocated to CERN for a long-term attachment. I joined the Exotics dijet team, responsible for searching for evidence of new physics resulting in two-jet final states. The search strategy for this team can be divided into two categories: resonance searches and analysis of dijet angular distributions. I decided to concentrate on the latter: since this method lends itself to searches for threshold effects such as extra-dimensions and strong gravity described in Chapter 4.

I became a key analyst for analysis of the full 2010 data-set of 36.4 pb^{-1} resulting in a publication at the beginning of 2011 [15]. Working with Dr. Frederik Rüehr (University of Arizona) and Dr. Nele Boelaert (Neils Bohr Institute, Copenhagen), I was made responsible for limits based on distributions with fine binning in angular distributions, and coarse binning

in mass. This publication also resulted in first limits on the Quantum Black Hole models [29] described in Section 4.2 of this thesis. This paper was published in the New Journal of Physics [15] and was subsequently selected by the journal editors for inclusion in the exclusive *'Highlights of 2011'*[8] collection [30].

In 2011, I enjoyed further responsibility within the research group. Working again with Dr. Frederik Rüehr (University of Arizona), I was responsible for limits based on a new angular analysis strategy using the variable $F_\chi(m_{jj})$ (see Chapter 7). These results formed a publication with 4.8 fb^{-1} of data, the analysis and results of which form the bulk of this thesis. The results of this analysis were published in [31].

[8]Papers are chosen on the basis of referee endorsement, novelty, scientific impact and broadness of appeal.

Chapter 2

Collider physics and quantum chromodynamics

Over the last century, much headway has been made in understanding the behaviour of particles that interact through nature's dominant force - *the strong force*. Beginning with the first attempts to explain the observed spectra of hadrons (baryons and mesons) by G. Zweig and M. Gell-Mann, the idea of the quark as a fundamental constituent of the hadrons, was born. The postulation of only 3 flavours of quark: up, down and strange, was sufficient to explain some of the observed phenomena - and even led to the prediction of the later observed Ω^-. We now know that there are six flavours of quark, with the discovery of the charm, bottom and top - where the top quark was discovered as recently as 2005. The main interest at the LHC lies in the interactions of the proton constituents: the quarks and gluons. The theory concerning the interactions of these constituents is **Q**uantum **C**hromo**d**ynamics (**QCD**).

This chapter will introduce the motivation, theory and application of QCD - the theory that describes the strong force. As the dominant orchestrator of the physical interactions considered in this thesis, the evolution of the development of QCD and its experimental confirmation over the years, will be briefly discussed. To start, the experimental motivations for QCD will be discussed in Section 2.1, followed by an introduction to the theoretical framework in Section 2.2. As a hadron-hadron collider at a new energy frontier, the LHC presents a unique opportunity to test the accuracy of QCD in a never-before encountered regime. The phenomenology of proton-proton collisions at the LHC will be introduced in Section 2.3 and their simulation using Monte Carlo techniques is discussed in Section 2.4.

2.1 Scattering experiments and the parton model

The idea that quarks carry a three-fold 'colour' charge was introduced in order to explain the observation of particles such as the Δ^{++}. This extra degree of freedom was required in order to allow the Δ^{++} to have simultaneously the correct permutational symmetry and satisfy Fermi-Dirac statistics.

Further progress was made through deep inelastic scattering experiments (discussed below), where a high energy lepton is scattered from a hadron. A key factor to consider is the wavelength, λ, of the probing particle, which is related to the transferred momentum Q^2 by

$$\lambda \sim \frac{1}{\sqrt{Q^2}}. \tag{2.1}$$

Therefore, a large momentum transfer is equivalent to a high resolution. J. D. Bjorken [32] predicted that, in the limit of infinite Q^2 (know as the *deep inelastic limit*), the hadronic factor in the cross section would depend only only on the Lorentz-invariant ratio

$$x = \frac{Q^2}{2p \cdot q} \tag{2.2}$$

where $Q^2 = -q^2 = -(p - p')^2$ is the difference between the initial (p) and final (p') lepton 4-momentum. R. P. Feynman [33] interpreted this effect, known as *'scaling'*, as elastic scatterings with constituents of the hadron that he called *'partons'*: the parton model. Bjorken's x variable can be identified as the fraction of the longitudinal hadron momentum carried by a given parton. This prediction was initially verified by a joint experiment of the SLAC and MIT groups [34].

Subsequent data on deep inelastic scattering showed that the scattering cross-section also varies with Q^2 and that the carriers of electric charge within hadrons have spin 1/2 [35–38]. The experimental evidence suggests that the proton is made up from 3 valence quarks - two up quarks and one down quark, along with a 'sea' of lower energy quark-anti-quark pairs that continuously pair-produce and annihilate.

The contribution of each quark flavour is described by its momentum distribution function $q(x, Q^2)$, where $q(x, Q^2)\mathrm{d}x$ represents the probability of carrying a momentum fraction of the parent hadron between x and $x+\mathrm{d}x$, when the hadron is probed at scale Q^2. The combination $xf_i(x, Q^2)$ is known as the **P**arton **D**istribution **F**unction (**PDF**) for the parton of flavour i, where parton can refer to a quark, anti-quark or gluon. PDFs are further discussed in Section 2.2.3.

In terms of these momentum distributions functions, for the proton we have the following sum rules:

$$\int_0^1 u_v(x, Q^2)\ \mathrm{d}x = 2, \qquad \int_0^1 d_v(x, Q^2)\ \mathrm{d}x = 1, \tag{2.3}$$

where u_v and d_v are the valence contributions to the patron momentum distribution functions. It was also found that if one sums over the momenta of all quarks and anti-quarks in the nucleon, expressed as $\Sigma(x, Q^2)$, then one observes that

$$\int_0^1 x\Sigma(x, Q^2)\ \mathrm{d}x \sim 0.5. \tag{2.4}$$

This, at first, unexpected result is now explained fully within the framework of QCD due to the momentum carried by gluons: the gauge boson responsible for the strong force, which is described by the theory of quantum chromodynamics.

2.2 Quantum chromodynamics

The strong force is described by **Q**uantum **C**hromo**d**ynamics (**QCD**), which is a **Q**uantum **F**ield **T**heory (**QFT**) based on the non-Abelian $SU(3)_C$ group, where C denotes the colour charge, which is conserved under the strong force. The 8 generators of the $SU(3)_C$ group, A^μ_a, $a = 1, \ldots, 8$, result in the 8 types of gluon that are responsible for mediating the force. The quantity g_s is the QCD coupling constant.

The QCD Lagrangian density is given by

$$\mathscr{L}_{QCD} = \sum_f \bar{\psi}^i_f (i\gamma^\mu (D_\mu)_{ij} - m_f \delta_{ij})\psi^j_f - \frac{1}{4} G^a_{\mu\nu} G^{\mu\nu}_a, \tag{2.5}$$

where ψ_f are the Dirac spinors of the different quark fields, which come in a colour triplet representation with red (r), green (g) and blue (b), γ^μ are the Dirac spin matrices[1], D_μ is the covariant derivative (described below), and m_f are the quark masses. The gluon field strength tensor $G^{\mu\nu}_a$ is given by

$$G^{\mu\nu}_a = \partial^\mu A^\nu_a - \partial^\nu A^\mu_a - i g_s [A^\mu_a, A^\nu_a] = \partial^\mu A^\nu_a - \partial^\nu A^\mu_a + g_s f^{bc}_a A^\mu_b A^\nu_c, \tag{2.6}$$

where A_a ($a = 1, \ldots, 8$) are the eight gluon fields and f_{ijk} are the structure constants of the $SU(3)_C$ group. The covariant derivative D^μ describes the interaction between the fields and

[1] For a good explanation of the Dirac spin matrices, and their role in the Dirac equation describing the behaviour of particles with spin, see [2].

is given by

$$D^{\mu}_{ij} = \delta_{ij}\partial^{\mu} + ig_s(t^a)_{ij}A^{\mu}_a, \tag{2.7}$$

where $(t^a)_{ij}$ are the 3×3 hermitian matrices which, for the fundamental triplet representation of $SU(3)$, are $(\lambda^a)_{ij}/2$, where λ^a are the Gell-Mann matrices[2]. The strength of the strong interaction is determined by the coupling strength g_s, which defines the strong coupling constant $\alpha_s = g_s^2/4\pi$. The non-Abelian nature of the $SU(3)_C$ group leads to self-interaction between the gluons - this can be seen in the Lagrangian as through the presence of the final term in Equation 2.6.

2.2.1 Calculation of a cross-section from a Lagrangian

The Lagrangian in Equation 2.5, describing the theory of the strong force, is constructed such that it is invariant under the symmetries of the $SU(3)$ group. By respecting the symmetries of the group, the theory is able to benefit from the mathematical representations of the group, and their properties.

A prescription for calculating the rates for processes in any QFT was developed by Feynman. Each term in the Lagrangian represents the interaction between various fields, and the strength with which they interact. Feynman rules can be derived for each of the terms[3]. Feynman diagrams are then used as a short hand to describe a calculation for one process of a fixed order of perturbation theory. Perturbation theory is a method for calculating the solution to an equation for which there is no analytical solution. Perturbation theory is applicable if the problem at hand can be formulated by adding progressively "smaller" terms to the mathematical description of the exactly solvable problem. This leads to an expression for the desired solution in terms of a formal power series in some "small" parameter, α, that quantifies the deviation from the exactly solvable problem. The precision of the perturbative solution will then depend up on the number of terms that are included and the sizes of additional terms. The highest power of α included in the expansion is know as the *order*[4] of the expansion. Figure 2.1 shows a few terms in the perturbative expansion of gluon propagation (depicted by the curly lines) between two fermions (depicted by the straight lines). Vertical displacement represents particle motion and time proceeds horizontally from left to right. Each diagram carries a definite quantum mechanical *amplitude* for the process that it represents. These amplitudes (commonly known as *matrix elements*) are constructed

[2]The Gell-Mann matrices are one representation of the $SU(3)$ group. For further details, see [2].

[3]These rules are derived using QFT. For a good introduction, see [39].

[4]It is a common convention to refer to processes as *'leading order'* (LO) or *'next-to-leading order'* (NLO), depending upon the order of α included in the perturbative expansion.

from the Feynman rules, where each factor in the matrix element is formed from a term associated with a feature of the diagram. Lines, of all sorts, represent the propagation of particles, and vertices (points where two or more lines meet) represent the interaction between particles. A full description of the Feynman rules associated with the SM is given in [39].

Once a matrix element has been formed for a process, QFT provides a proscription for arriving at a final cross-section: see [39] for a description of these calculations.

2.2.2 Singularities, renormalisation and asymptotic freedom

Ultra-violet divergences can arise from divergent integrals, when one tries to include all possible quantum fluctuations into the perturbative expansion: in the case of the gluon propagator, loop insertions can be due to both fermions (quarks) and gluons. The first three terms in the perturbative expansion for the gluon propagator are shown in Figure 2.1. Both contributions diverge logarithmically but with coefficients of opposite sign.

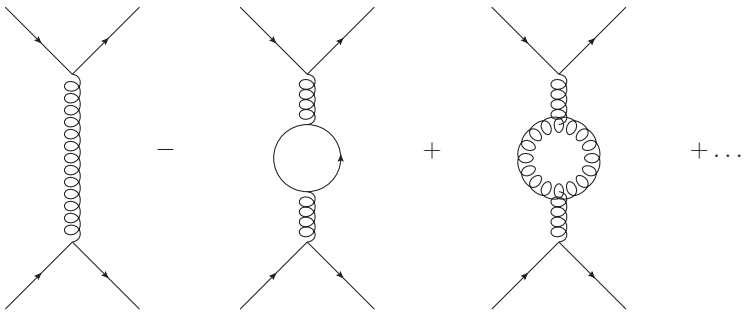

FIGURE 2.1: Loop corrections to the gluon propagator.

These non-physical infinities can be removed via *renormalisation*, resulting in a finite solution. Renormalisation works by subtracting infinities through counter-terms embedded in so-called *bare* parameters, which are not measurable. The procedure introduces a correction to the 'renormalised parameter' depending on the renormalisation scale μ_R - which can be interpreted as the scale at which the subtraction is made. As an arbitrary parameter, solely introduced to allow one to approximate calculations, μ_R cannot ultimately influence the relationship between physical observables. When calculating QCD effects, one is forced to choose a value of μ_R. As a result, the physical observables of the calculation will develop an additional dependence upon the relation between μ_R and the physical scale of the interaction Q^2.

In the case of the QCD coupling constant, α_s, the scale-dependence is described by the β function:

$$Q\frac{\partial\alpha_s}{\partial Q} \equiv 2\beta_{QCD} = -\frac{\beta_0}{2\pi}\alpha_s^2 - \frac{\beta_1}{4\pi^2}\alpha_s^3 - \mathcal{O}(\alpha_s^4) \tag{2.8}$$

where $\beta_0 = 11 - \frac{2}{3}n_f$ and $\beta_1 = 51 - \frac{19}{3}n_f$ and n_f is the number of 'active' quark flavours at the scale Q. Using Equation 2.8, one can calculate the value of α_s at any scale Q, starting from an experimental measurement of α_s at a known scale μ_R, via

$$\ln\left(\frac{Q^2}{\mu_R^2}\right) = \int_{\alpha_s(\mu_R)}^{\alpha_s(Q)} \frac{d\alpha}{\beta(\alpha)}. \tag{2.9}$$

It is conventional to quote a value of the strong coupling constant at a mass of the Z-boson, which is determined for a combination of various measurements. The current preferred value, based on next-to-next-to leading order perturbative calculations is given by $\alpha_s(M_Z) = 0.1182 \pm 0.0027$ [40].

Calculating Equation 2.8 to LO in $\beta(\alpha_s)$:

$$\alpha_s(Q^2) = \frac{\alpha(\mu_R^2)}{1 - \alpha(\mu_R^2)\beta_0 \ln(Q^2/\mu_R^2)}, \tag{2.10}$$

and making the substitution $\ln(\Lambda_{QCD}^2) = \ln(\mu_R^2) - \frac{1}{\beta_0\alpha_s(\mu_R^2)}$ gives

$$\alpha_s(Q^2) = \frac{1}{\beta_0 \ln(Q^2/\Lambda_{QCD}^2)}. \tag{2.11}$$

From this expression, we can interpret Λ_{QCD} as the scale at which α_s becomes infinite. The remarkable result that $\alpha_s(Q^2) \to 0$ as $Q^2 \to \infty$ is known as *asymptotic freedom*: when a hadron is probed at low scales (corresponding to a low spatial resolution - see Equation 2.1) we observe confined quarks, however for a high Q^2 interaction (corresponding to a high spatial resolution), such as deep inelastic scattering, we observe almost free quarks. The fact that the strong force increases at larger length scales, results in the confinement of coloured particles, i.e. it is not possible to produce a particle with colour charge in isolation and only colour singlets composed of quarks and gluons can be observed. The increasing strength of the strong force with distance, causes perturbative methods to break down as colour charges move apart.

2.2.3 Parton distribution functions

With an understanding of how QCD predicts the interactions between coloured partons, it is possible to further-develop the parton model described in Section 2.1. In particular, one can model the hadron as a dynamic object containing three valence quarks along a sea of quarks and gluons which are continuously radiated and absorbed by each other. As described above, through scattering experiments, it has been possible to measure the contribution of each parton flavour to the parent hadron. By combining these experimental measurements with theoretical tools provided by the QCD framework, we can deduce the phenomenology of hadron interactions.

Within the proton, gluon emission gives a quark a large momentum k_T with probability proportional to $\alpha_S dk_T^2/k_T^2$ at large k_T. In the collinear region (as $k_T \to 0$), this leads to a non-physical divergence, since the perturbative QCD approximation is not valid in this region. This divergence is removed by introducing a *factorisation scale*, μ_F: which can be interpreted as an energy limit for describing the parton behaviour within the proton. In a similar fashion to the renormalisation scale, the factorisation scale absorbs the collinear divergences, resulting in a scale-dependent PDF.

Although perturbative QCD provides no absolute prediction for the PDF, it does dictate how the PDF will evolve with Q^2. This scale-evolution is described by the DGLAP[5] equations, which are coupled equations for the change of the quark, anti-quark and gluon densities

$$\frac{\partial}{\partial \ln Q^2}\begin{pmatrix} q_i(x,Q^2) \\ g(x,Q^2)\end{pmatrix} = \frac{\alpha_s(Q^2)}{2\pi}\sum_j \int_x^1 \frac{d\xi}{\xi}\begin{pmatrix} P_{q_iq_j}(\frac{x}{\xi},\alpha_s(Q^2)) & P_{q_ig}(\frac{x}{\xi},\alpha_s(Q^2)) \\ P_{gq_j}(\frac{x}{\xi},\alpha_s(Q^2)) & P_{gg}(\frac{x}{\xi},\alpha_s(Q^2))\end{pmatrix}\begin{pmatrix} q_j(\xi,Q^2) \\ g(\xi,Q^2)\end{pmatrix}, \tag{2.12}$$

where the q_i, q_j are momentum distribution functions and are taken to include both quarks and anti-quark distributions. The splitting function $P_{ba}(z,Q^2)$ represents the probability for parton a to radiate parton b, where b takes a fraction z of a's momentum. In analogy with the running coupling constant described in Section 2.2.2, the PDF must be measured at some known scale μ_R before it can be evolved across the kinematic range. A combination of complementary measurements is employed from many scattering experiments[6], has allowed constraint of each of the individual parton PDFs over a range of values of x and Q^2. The extent to which this phase space have probed to date is shown in Figure 2.2. From the diagram, it is clear that the LHC will present the opportunity to probe the proton at

[5] Dokshitzer-Gribov-Lipatov-Altarelli-Parisi

[6] Example scattering experiments include the ZEUS and H1 experiments at HERA, which was an electron-proton collider at the DESY laboratory, as well as CDF and DØ experiments at the Tevatron, which was a proton-anti-proton collider at Fermilab.

previously un-explored regions of low-x and high-Q^2. In addition, the overlap with previous experiments allows the opportunity to test the validity of previous PDF fits that have been derived from the collisions of different types of particle.

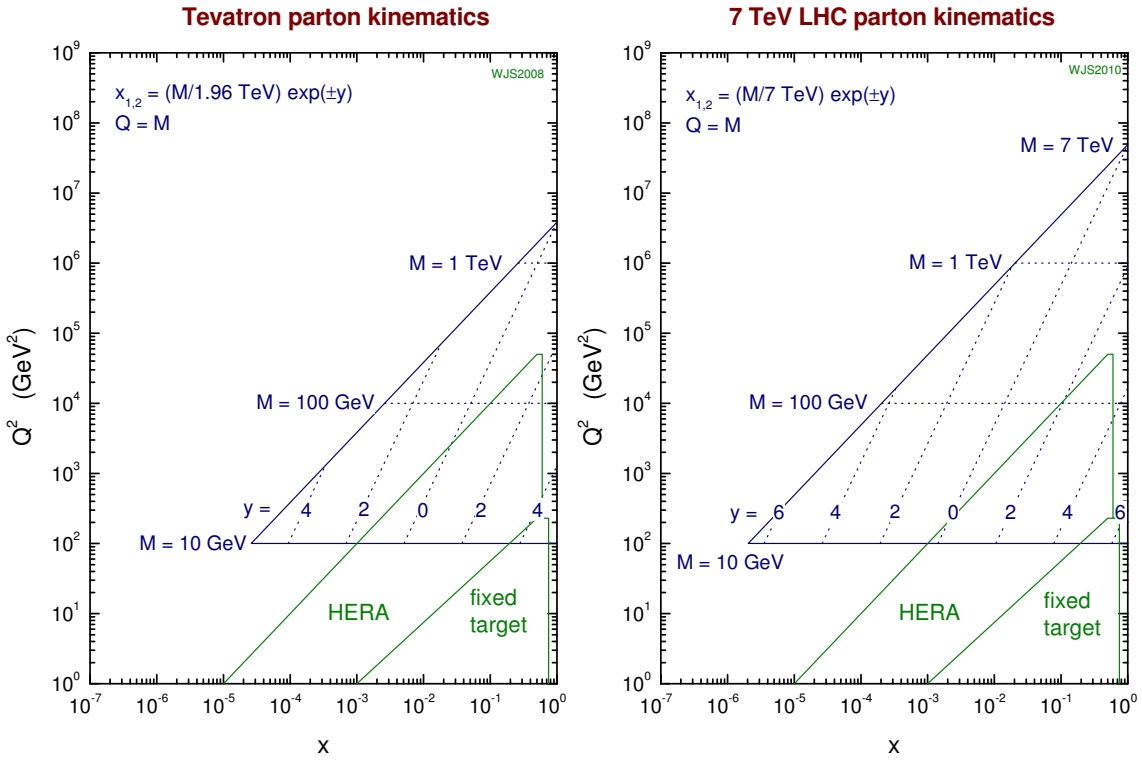

(a) Tevatron parton kinematics

(b) LHC parton kinematics at $\sqrt{s} = 7$ TeV

FIGURE 2.2: Parton kinematics in the x, Q^2 plane for (a) Tevatron and (b) LHC colliders [41]. Kinematic ranges reached by the HERA collider and fixed target experiments are included for comparison. In the Figure, M indicates the mass of a given heavy particle produced at rapidity y.

There are various competing PDF parameterisations, with each providing varying degrees of agreement across the currently explored kinematic range. Examples are MSTW [42] (see for example Figure 2.3), CTEQ [43] and combined fits to the HERA[7] data [44]. There are some overall constraints, such as sum rules to guarantee the correct quantum numbers of the mother hadrons, that are used to motivate parametrised functions at some starting scale. These parametrisations can then be evolved to the Q^2 of the data using next-to-leading order perturbative QCD. The parameters are then determined by a χ^2 fit to the data. For the PDF parametrisations mentioned above, most supply systematic errors, which are larger than their statistical errors. A correct treatment of systematic errors is therefore very important, especially for extrapolation to higher Q^2. The effect of the uncertainty associated with PDF

[7]HERA is an electron-proton collision experiment at the DESY laboratory in Hamburg, Germany.

parametrisations on the production of two-jet event considered in this analysis is discussed in Section 7.4.

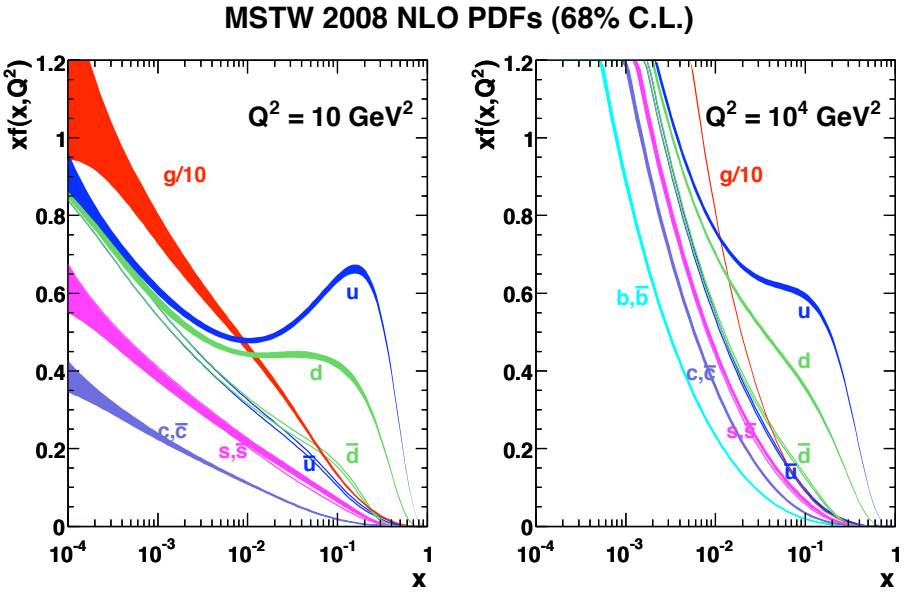

FIGURE 2.3: Proton PDF distributions for $\sqrt{s} = 7$ TeV as a function of x according to the MSTW collaboration [42] for up (u), down (d), charmed (c) and strange (s) quarks and their corresponding anti-quarks are shown. The left plot is for $Q^2 = 10\,\text{GeV}^2$ and the right plot shows function for $Q^2 = 10^4\,\text{GeV}^2$. Both plots also show distributions for $g/10$ which is the gluon distribution scaled down by a factor of 10 in order to fit the same scale as the other partons.

2.3 The cross-section for a hard hadronic process

The entire process of a general hadron-hadron event involving a hard scatter, shown in Figure 2.4, can be factorised into several scale-dependent processes. For a collision between two protons, the resulting scatter can be characterised as either *hard*, involving a large momentum transfer, or *soft*, involving a lower momentum transfer. Although QCD is responsible for describing each of these interaction types, there are vital differences in the understanding. For a hard interaction with a large momentum transfer, the methods of perturbative QCD, discussed above, can be used: since α_s is small when Q^2 is large. Conversely, for scales closer to Λ_{QCD} the coupling α_s becomes large and perturbative techniques are no-longer valid. It is common for a hard-scatter to be accompanied by the possibility of quark and gluon **I**nitial-**S**tate **R**adiation (**ISR**) and **F**inal-**S**tate **R**adiation (**FSR**) as depicted in Figure 2.4. The remnants of the original protons, with one parton removed, are no longer colour singlets

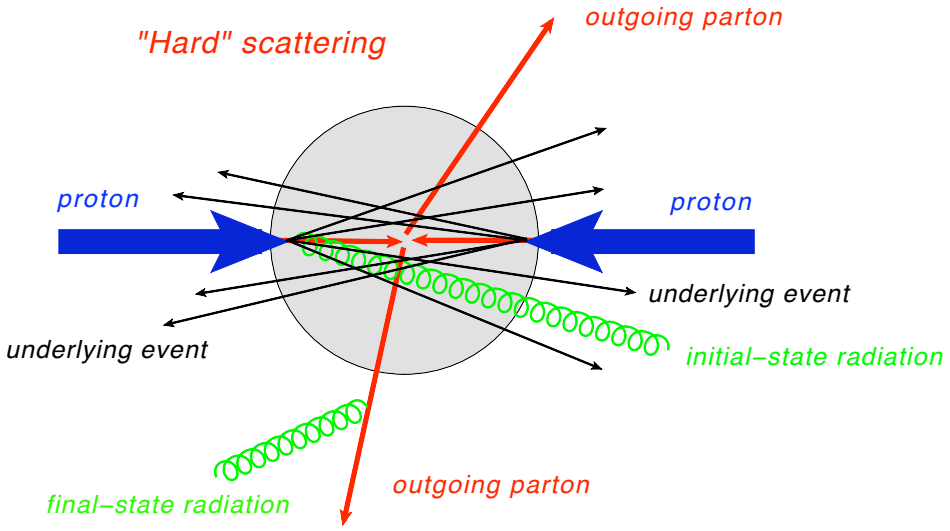

FIGURE 2.4: Schematic for a proton-proton collision resulting in a hard-scatter between two partons. Other possible interactions from initial and final state radiation and underlying event are also included.

and will react to produce an underlying distribution of soft partons. This distribution is known as the **U**nderlying **E**vent (**UE**).

The *factorisation theorem* [45] states that the hadron-hadron cross-section can be constructed from a convolution of the calculable parton-level cross-section, with the parton momentum distribution functions of the incident hadrons. This theorem is based on the differing time-scale, energy-scale and distances involved in each of the terms. One may think of μ_F as the scale that separates these two regimes and so separates what we refer to as the hard interaction itself, and what could be referred to as the inner-workings of the proton, described by the PDF. We therefore have a cross-section that is dependent upon two scales: the renormalisation scale μ_R is associated with the limited precision of hard scatter calculations in α_s; and the factorisation scale μ_F is the scale associated with the partons within the proton. We summarise this in the expression for the cross-section:

$$\mathrm{d}\sigma_{\mathrm{hard}}(p_A, p_B, Q^2) = \sum_{ab} \int \mathrm{d}x_a \mathrm{d}x_b \; f_{a/A}(x_a, \mu_F^2) f_{b/B}(x_b, \mu_F^2) \; \mathrm{d}\hat{\sigma}_{ab\to cd}(\alpha_s(\mu_R^2), Q^2/\mu_R^2) \quad (2.13)$$

where $\mathrm{d}\hat{\sigma}_{ab\to cd}$ is the parton-parton cross-section at a hard scale Q^2 and $f_{a/A}$ is the parton momentum density of a parton a in hadron A at a factorisation scale μ_F. The initial parton momenta are given by $p_a = x_a p_A$ and $p_b = x_b p_B$.

Given that it is not possible to perform calculations to all orders, the final cross-section will retain some dependence on the renormalisation scale (μ_R) and the factorisation scale (μ_F). The variation of these parameters will therefore present a systematic uncertainty on

behaviour of a large number QCD simulations. Figure 2.5 shows the inclusive jet cross-section as a function of leading jet momentum, where $\mu_R = \mu_F = \mu$ and is compared to the leading jet p_T - note that this plot is for $\sqrt{s} = 8$ TeV and is the *only* distribution for this energy included in this thesis (unfortunately, the plot was not available for $\sqrt{s} = 7$ TeV). It can be seen that whilst the LO cross-section falls with the scale of the interaction, the NLO cross-section reaches a maxima for $\mu/p_{T,1}$ equal to 1. This fact alone is a strong motivation for using an NLO cross-section: whilst one can '*handpick*' a cross-section for LO by choosing the scale, the NLO contains a maxima. A convention within ATLAS is to set the nominal scale values to this maximum: $\mu/p_{T,1} = 1$. The uncertainty on this choice is then calculated by varying μ_R and μ_F by a factor of 2, up and down.

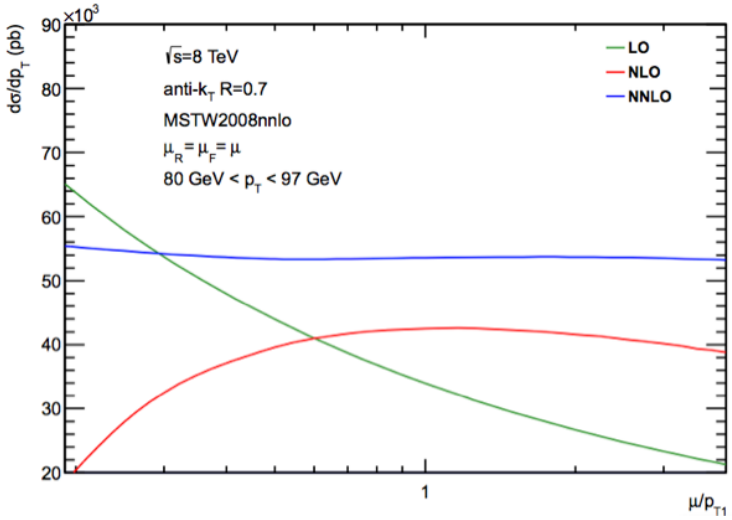

FIGURE 2.5: LO, NLO and NNLO cross-section for inclusive jet cross-section as a function of leading jet p_T [46].

It is noted that a change from LO to NLO cross-section calculation will not only increase the accuracy of the prediction, but also decreases the uncertainty on the choice of scales. This serves as additional motivation for using an NLO calculation, where possible. Determination of theoretical systematics and NLO calculations will be discussed in Sections 7.3 and 7.4.

2.4 Monte Carlo simulation of QCD processes

In this analysis, Monte Carlo simulation of QCD processes from proton-proton collisions is used as a null hypothesis, in order to search for beyond the standard model physics signals. As by far the dominant background to any process involving a jet in the final state, a good understanding of the simulation of QCD interactions is paramount to identifying all potential sources of systematic uncertainty. When two protons collide there is a vast array of possible

outcomes, with the probability of each outcome described by Equation 2.13. Therefore, in order to deduce any significant conclusions, a very large number of proton-proton collisions needs to be considered. The LHC will provide billions of proton-proton collisions that will be recorded for analysis. In order to quantify the agreement between the data and theory, one must therefore simulate a large number of Monte Carlo processes for comparison. The generation of these Monte Carlo events can be split into multiple steps outlined below.

The nature of the incoming partons taking part in the hard subprocess, i.e. their flavour and momentum distributions (described in Section 2.2.3), determine the main characteristics of the event. One parton from each beam particle initiates a shower of partons: the remainder of which contribute to the beam remnants, or may take part in multiple parton interactions.

2.4.1 Simulation of the hard scattering process

The leading order cross-sections for a given physics process can be calculated using Equation 2.13. Calculations for NLO effects (and beyond) for the hard scattering are notoriously difficult - and due to the large scale of the interaction, it is usually sufficient to restrict the calculation to leading order. However, in some areas of phase-space, next-to-leading order effects (and beyond) can be non-negligible Although some NLO MC event generators are available for some subprocesses (e.g. POWHEG-BOX [47–49]), these have taken many years to develop and are still not completely trusted.

2.4.2 Parton showering

When two coloured particles exist in either the initial or final state, there is a finite probability of either of the particles radiating another parton. As seen in Section 2.2.2, this can lead to either infra-red or collinear divergences. An alternative to summing higher order terms from the DGLAP formalism is provided by some Monte Carlo generators. In the parton shower approach, e.g. used by PYTHIA [50], the few partons produced in the hard interactions are related to partons close to the QCD scale Λ_{QCD}. At this scale a phenomenological model can then be used to perform the hadronisation of final state partons. The evolution can be expressed in Sudakov form factors, which give the probability that a parton evolves to a higher scale than a given value[8]. For a further discussion of Sudakov form factors and their behaviour at different scales, see [51]. Parton showers provide a very good description of

[8]In PYTHIA 6.4, which is used in this thesis, the relative transverse momentum of the two partons is used as the scale of choice.

collinear and infra-red emission, while the fixed order calculations can be used for the widely separated partons. Care must be taken to avoid double-counting in kinematics regions where both techniques overlap.

2.4.3 Hadronisation of coloured particles in the final state

Hadronisation is the process by which colour neutral hadrons are created from outgoing quark and gluons from the final state. As coloured particles move apart, the strong interaction between them increases. The potential between the two partons increases linearly with their separation, until there is sufficient energy to produce a new parton pair. This new parton pair is then able to neutralise the colour charge of each of the initial partons producing a hadronic state. Within a collision experiment, all outgoing partons will therefore undergo parton showering and transform into hadrons. These hadrons will in-turn form jets - sprays of particles, which to a good approximation point in the direction of the original high energy parton. This process is called *hadronisation* and results in the experimentally measurable jets. As the hadronisation process evolves, the scale of the parton radiation will decrease leading to a larger strong coupling - perturbative methods cannot therefore be used to describe the hadronisation process and phenomenological models must be relied upon instead. Models describing hadronisation include the Lund string model [52] (used in e.g. Pythia) and the cluster model [53] (used in e.g. Herwig [54]). In each of these models, colour singlet structures are formed from colour connected partons and are decayed into hadrons, whilst ensuring that energy and momentum are conserved.

2.5 QCD Monte Carlo simulation used in this thesis

The background process considered in this thesis will consist of events generated at leading-order for the hard scattering process by the Pythia generator. Pythia [50] is a complete, multi-purpose event generator with leading-order matrix elements. This program has become the standard across multiple experiments due to its wide range of simulated processes from both within and beyond the standard model. The QCD hard scattering interactions are simulated using the Pythia 6.4 [50] event generator with the ATLAS AUET2B LO** tune [55] which uses the MRSTMCal [56] modified leading-order (LO**) parton distribution functions (PDF).

As shown Figures 7.12(c) and 7.12(d), the inclusive jet cross-section features a steep drop with jet p_T: the simulation of the QCD process is therefore split between certain regions

in leading jet p_T. This allows the generation of a large number of events across the whole spectrum, ensuring sufficient statistics for a quantitative conclusion. The samples are split into the 'J' samples (where 'J' stands for jet) in Table 2.1 and Table 2.2.

Slice name	p_T range [GeV]	cross-section [nb]	N_{events} simulated
J0	8-17	1.2030E+07	1400000
J1	17-35	8.0726E+05	1399500
J2	35-70	4.8048E+04	1399999
J3	70-140	2.5369E+03	1393998
J4	140-280	9.9608E+01	2799997
J5	280-560	2.5950E+00	2799497
J6	560-1120	3.5489E-02	2798499
J7	1220-2240	1.3391E-04	399999
J8	2240+	5.6799E-09	2798997

TABLE 2.1: J-slices of Pythia QCD Monte Carlo with their respective leading jet p_T ranges, cross-sections and the number of events that are simulated.

Slice name	p_T range [GeV]	cross-section [nb]	N_{events} simulated
J7a	1120-1680	1.3282E-04	1400000
J7b	1680-2240	1.1057E-06	1389999

TABLE 2.2: J7 exists as a single sample, but also as a sample split into two leading jet p_T ranges: each is included in the analysis for an increase in statistics.

In order to obtain a next-to-leading order (NLO) prediction for jet production in this thesis, NLO k-factors are used and are described in Section 7.3. Next-to-leading order effects will be included using the NLOJET++ [57] generator. Although a new Monte Carlo generator POWHEG-BOX now includes NLO inclusive jet production complete with parton showers, this generator is not considered in this thesis[9].

[9]This generator is not considered, since at the time of the analysis, the generator had not been validated within the ATLAS software framework.

Chapter 3

Experimental apparatus

This chapter will describe the motivation, design and layout of the experimental apparatus used in this thesis. After a brief overview of the Large Hadron Collider itself (Section 3.1), the ATLAS detector will be described (Section 3.2) with particular attention being paid to tracking, calorimetry and triggering. As the main sub-detector for this thesis, the ATLAS calorimeter systems are described in Section 3.2.3. Other crucial aspects of the ATLAS detector such as the trigger and data acquisition systems are described in Section 3.3.

3.1 The Large Hadron Collider

The **L**arge **H**adron **C**ollider (**LHC**) is a proton-proton (pp) collider situated about 100 m underground, crossing the French-Swiss border. Its mandate is to push our current understanding of the fundamental structure of our universe to new limits, whilst offering the first opportunity to test theories: predicting the existence of new particles and forces that manifest themselves at $\mathcal{O}$(TeV) energies.

Large superconducting magnets focus two counter-rotating beams of protons in separate beam tubes (or for some experiments heavy Pb ions are used instead). The collider is situated in the former **L**arge **E**lectron **P**ositron (**LEP**) collider tunnel, which has a circumference of about 27 km.

The layout of the LHC main ring is a series of eight arcs and straight regions. In four of these straight regions, proton beams are forced to cross and collide at the centre of large detectors. The other four regions are mainly used for beam cleaning, beam dump systems

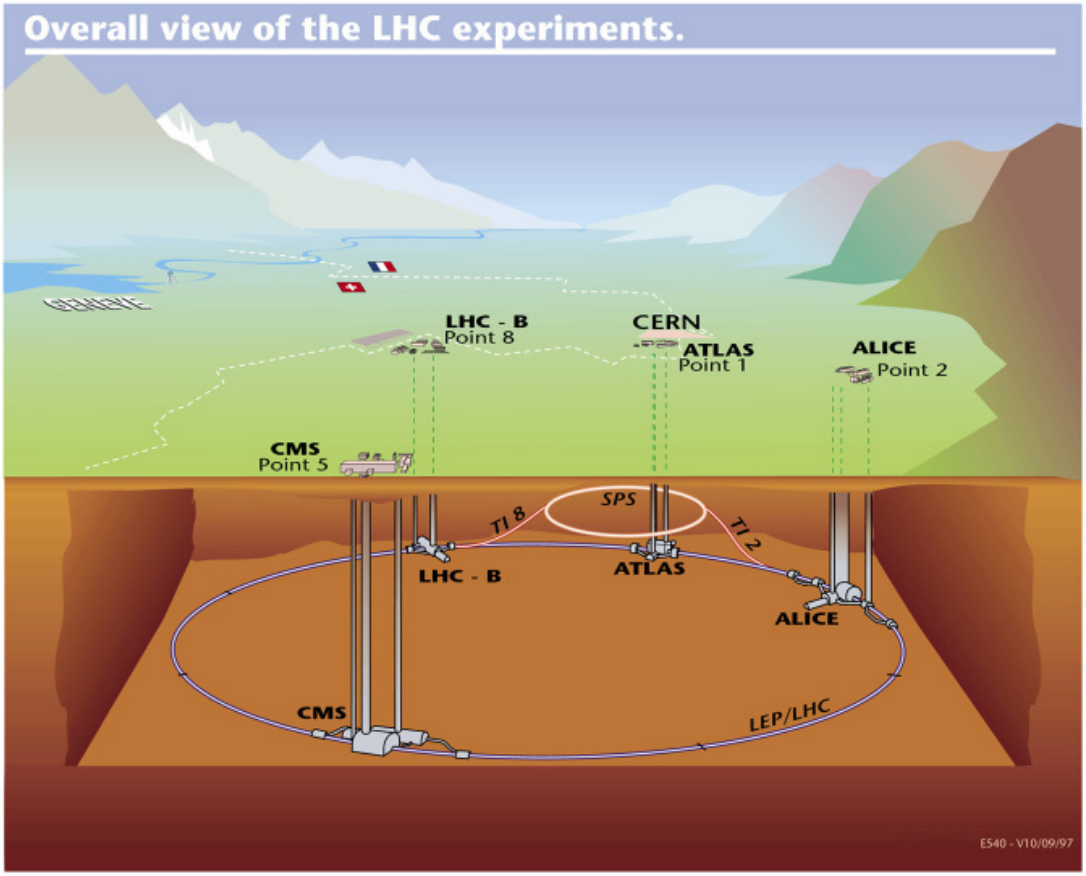

FIGURE 3.1: Underground layout of the LHC tunnel. The Super Proton Synchrotron (SPS) and its connection to the LHC is also shown. Also shown, are the locations of ATLAS, CMS, LHCb and ALICE. This Figure is taken from [58].

and **R**adio **F**requency (RF) and beam instrumentation. A view of the LHC experiments is shown in Figure 3.1.

The LHC is designed to have up to 2808 circulating proton *'bunches'*, where each bunch is made up of about 1011 protons. The bunches are organised into *'trains'*, with a spatial distance of about 7.5 cm between bunches. Proton bunches are directed by 8.3 T magnetic fields generated locally by more than 1200 superconductive magnets.

With a nominal luminosity of $\mathcal{L} = 10^{33}$ cm^{-2}s^{-1}, the number of events per second produced in the centre of the detector is

$$\frac{\mathrm{d}N_{event}}{\mathrm{d}t} = \mathcal{L}\sigma \tag{3.1}$$

where σ is the cross section for a given physical process. The cross section for various processes as a function of centre of mass collision energy and the event rate are shown in Figure 3.2. Over an interval of time, one can expect $N_{events} = \int \mathcal{L}\sigma \, \mathrm{d}t$. Due to the small cross-sections of some physical processes, it is imperative that the LHC is able to maximise

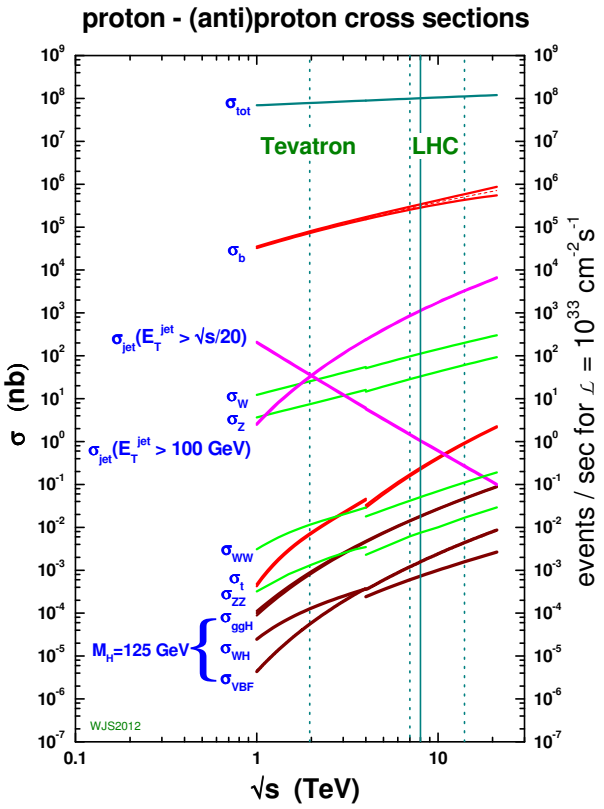

FIGURE 3.2: Cross section for various processes as a function of centre of mass collision energy and the event rate [41].

its delivered luminosity. The calculation of the instantaneous luminosity delivered by the LHC is discussed in [59].

The detectors at the four separated interaction points are named **ATLAS** (**A** **T**oroidal **L**HC **A**pparatu**S**), **CMS** (**C**ompact **M**uon **S**olenoid), **ALICE** (**A** **L**arge **I**on **C**ollider **E**xperiment) and **LHCb** (**LHC** **b**eauty). ATLAS and CMS are general purpose detectors designed to cover a multitude of physics: ranging from the confirmation of Standard Model physics to the search for new particles and forces. ALICE is a heavy ion collision detector and LHCb is specially designed for b-physics study[1].

Two further experiments operating at the LHC are **TOTEM** (**TOT**al cross section, **E**lastic scattering and diffraction dissociation **M**easurement at the LHC), designed for precise measurement of the proton-proton interaction cross-section, and **LHCf** (**LHC** **f**orward), designed to study of neutral particles, produced from proton-proton collisions at very small angles to the beam line.

[1]This involves studies of particles which contain b quarks which allow us to study the phenomenon of **C**harge-**P**arity (**CP**) symmetry violation.

3.2 Overview of the ATLAS detector

The ATLAS detector [60], which is located at interaction point 1 of the LHC tunnel, is a general purpose detector designed to detect electrons, photons, muons, hadrons and missing transverse momentum. The overall layout of the detector is shown in Figure 3.3.

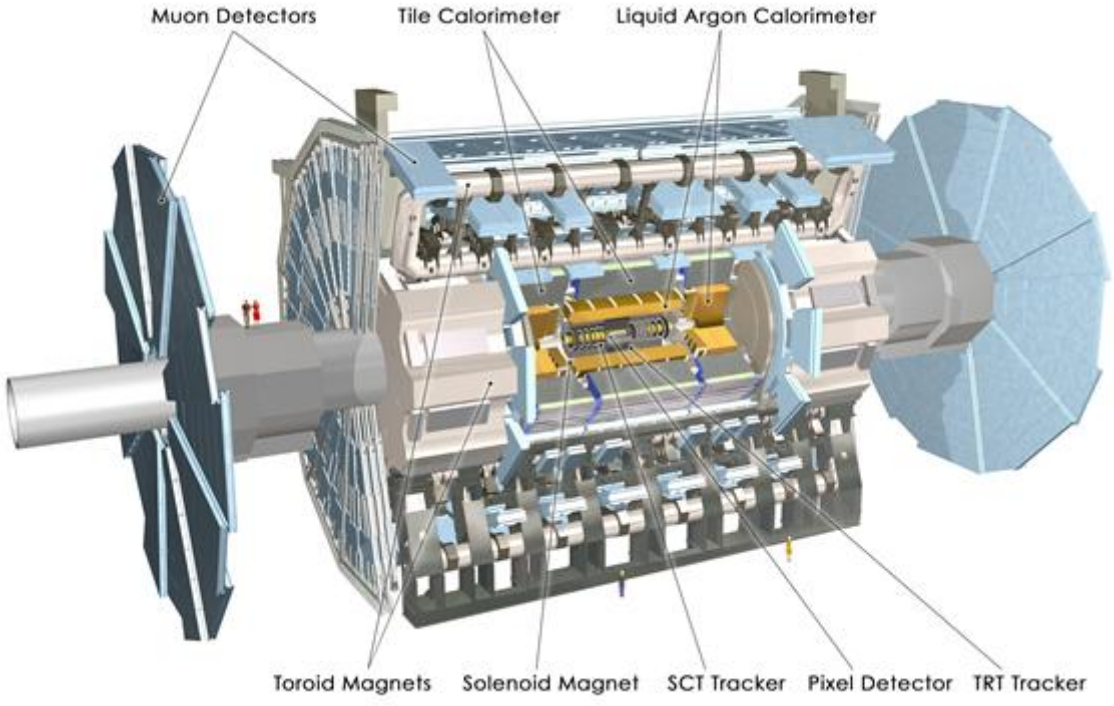

FIGURE 3.3: The ATLAS detector [58].

The detector consists of layered concentric sub-detector, which encompass the collision point in the centre, with four major components: the Inner Detector (comprising of the SCT Tracker, Pixel Detector and TRT Tracker) is used to measure the tracks of charged particles, the liquid argon and tile calorimetry is designed to contain and measure the energy of electromagnetic and hadronic showers of particles, and the muon spectrometer is used to detect muons.

By combining the data collected from these layers, we are able to track, identify and measure the momentum and energy of certain particles produced after a collision. The main performance goals of the sub-detectors are described in [60] and are summarised in Table 3.1.

ATLAS includes two magnet systems: used to bend the trajectories of charged particles so that their momenta can be measured. A 5 Tesla solenoid surrounds the inner detector and a large $2-8$ Tesla superconducting barrel toroidal magnet lies outside the calorimeter. The

Detector component	**Required resolution**	**η coverage**	
		Measurement	Trigger
Tracking	$\sigma_{p_T}/p_T = 0.05\% p_T \oplus 1\%$	± 2.5	
EM calorimetry	$\sigma_E/E = 10\%/\sqrt{E} \oplus 0.7\%$	± 3.2	± 2.5
Hadronic calorimetry (jets)			
barrel and end-cap	$\sigma_E/E = 50\%/\sqrt{E} \oplus 3\%$	± 3.2	± 3.2
forward	$\sigma_E/E = 100\%/\sqrt{E} \oplus 10\%$	$3.1 < \lvert\eta\rvert < 4.9$	$3.1 < \lvert\eta\rvert < 4.9$
Muon spectrometer	$\sigma_{p_T}/p_T = 10\%$ at $p_T = 1$ TeV	± 2.7	± 2.4

TABLE 3.1: General performance goals of the ATLAS detector [60]. Note that, for high-p_T muons, the muon-spectrometer performance is independent of the inner-detector system. The units for p_T and E and GeV.

toroidal magnet is specifically designed to bend the track of muons that are able to penetrate the rest of the detector.

3.2.1 The ATLAS coordinate system

The ATLAS coordinate system has the nominal interaction point at its origin with the $+z$ axis defined by the clockwise beam direction. The $x-y$ plane is transverse to the beam direction with the $+x$ axis pointing towards the centre of the LHC ring and the $+y$ axis pointing upwards. The azimuthal angle ϕ is measured in the $x-y$ plane, whilst the polar angle θ is measured from the beam axis. In most of the analysis which follows, it shall be convenient to use the pseudo-rapidity η defined as

$$\eta = -\ln\tan\left(\theta/2\right), \tag{3.2}$$

which is the ultra-relativistic approximation to the Lorentz-invariant rapidity given by $y = \frac{1}{2}\ln\left(\frac{E+p_L}{E-p_L}\right)$, where E is the particle energy and p_L is the component of the particle momentum which is parallel to the beam axis. The relation between η and θ is depicted in Figure 3.4. For particles with zero mass: $\eta = y$. Angular distances within the detector are measured in ΔR, which is defined in the pseudo-rapidity-azimuthal angle space as:

$$\Delta R = \sqrt{\Delta\phi^2 + \Delta\eta^2}. \tag{3.3}$$

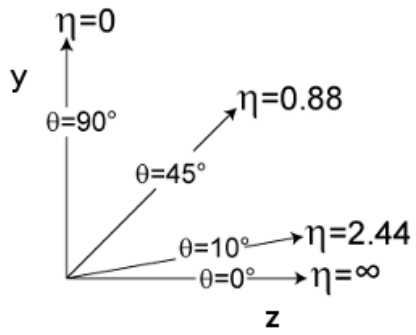

FIGURE 3.4: Pseudo-rapidity η and polar angle θ in the ATLAS coordinate system.

3.2.2 The ATLAS inner detector

At the heart of ATLAS, the inner detector is designed to make the most precise measurements possible. The system consists of high-resolution silicon detectors with full coverage in ϕ space and a pseudo-rapidity range of $|\eta| < 2.5$. Arranged in concentric cylinders around the beam axis, these detectors allow location of the interaction vertex, as well as measurement of displaced vertices from long-lived particles. The presence of the 2 T magnetic field, generated by the superconducting solenoidal magnet, allows measurement of track momenta. The primary vertex is defined as the vertex with the highest sum of transverse momentum (p_T) pointing to it, normalised by the number of tracks.

A computer-generated image of the inner detector, with its components, is shown in Figure 3.5. The system consists of a silicon **Pixel** detector (**Pixel**), a silicon strip **S**emi**C**onductor **T**racker (**SCT**) and a **T**ransition **R**adiation **T**racker (**TRT**). The Pixel detector consists of semiconducting pixels, assembled in silicon wafers called sensors. The SCT is build from modules formed from semiconductor micro-strips arranged parallel to the beam pipe in the barrel region, and radially in the end caps. By gluing sensors together in pairs at a 40 mrad stereo angle, the z-coordinate of the track can also be determined. Finally, the TRT is comprised of straw tubes filed with a Xenon-based gas mixture. The TRT is designed to provide particle identification: in particular it is designed to distinguish between electrons and pions. Further details of all Inner Detector components are given in [60].

3.2.3 The ATLAS calorimeters

Calorimetry, or energy measurement, is an integral part of modern particle physics experiments. A complete discussion of the ATLAS calorimeters is included in [60]. Combined with accurate momentum measurement, calorimetry can also provide particle identification over

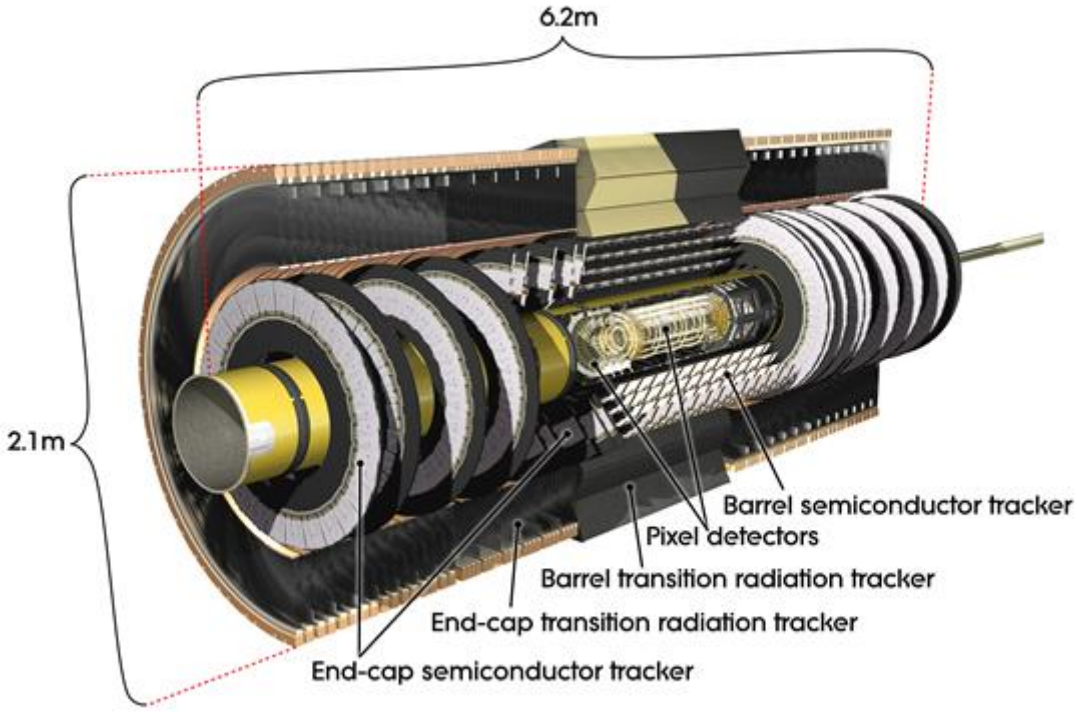

FIGURE 3.5: Computer-generated image of the ATLAS inner detector and its components [61].

a range of energies. All calorimetry measurements are destructive processes: and for this reason calorimeters are located spatially outside of other sub-detector systems. The ATLAS calorimetry system employs a sampling technique. Layers of active and passive material, allow the calorimeter to both absorb and measure energy: resulting in a compact design with almost complete containment of the showers.

Calorimetry can be split into two broad classes: electromagnetic (EM) and hadronic. Whilst EM calorimeters employ fine granularity for precise measurement of electrons, positrons and photons, hadronic calorimeters employ a coarser granularity which is sufficient to contain and measure the energy of incident hadrons[2]. In the case of hadronic showers, during the interactions of particles, there will be a component of energy that is absorbed in nuclear breakups and excitations that is fundamentally undetectable in the calorimeter - this is known as *invisible energy*. As well, there may be muons and neutrinos produced that will often escape the detector without being detected - this leads to *escaped energy*. In order to account for these energy losses, calorimeters can be designed to be compensating. *However*, the ATLAS calorimeters are non-compensating: the hadron response is lower than the response for electromagnetically interacting particles, for the same incident particle energy.

[2]EM calorimeter data is also used in the energy measurement of hadrons, since a hadron may begin showing before it has reached the hadronic Tile calorimeter.

The correct energy scale for hadronic interactions is restored 'offline' - at the data analysis level. The techniques employed to calculate this **J**et **E**nergy **S**cale, (**JES**) are discussed in Section 5.4.

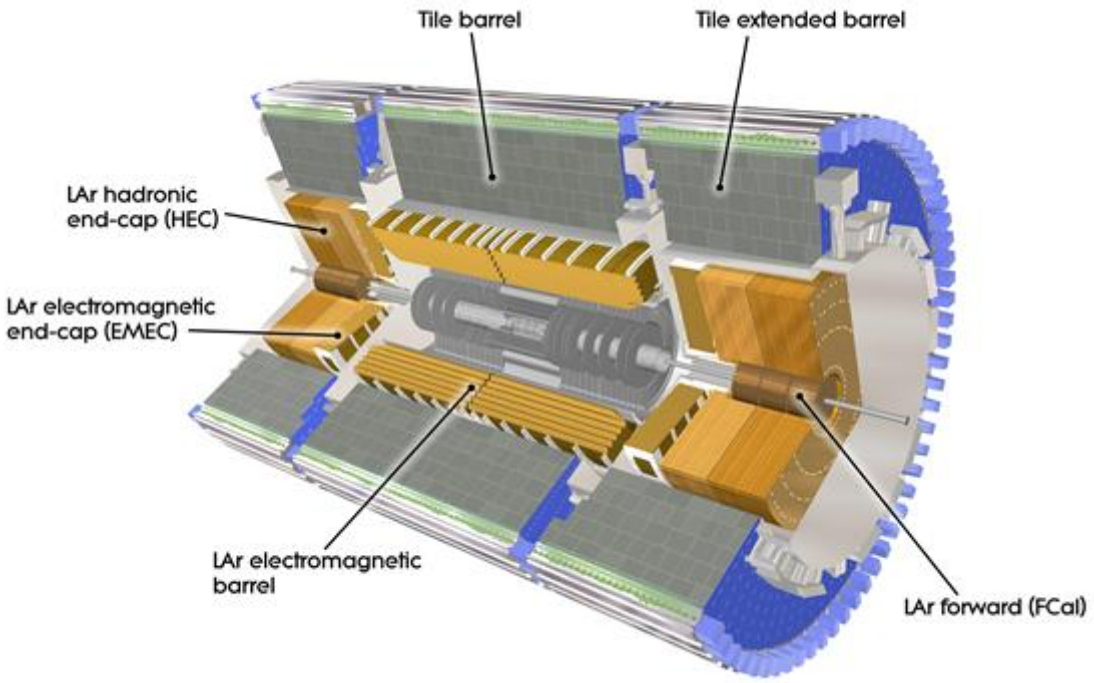

FIGURE 3.6: Layout of the ATLAS calorimetry system [58].

The ATLAS calorimetry is comprised of six subsystems divided into barrel, extended barrel and end-cap regions (See Figure 3.6). The barrel region consists of a **L**iquid **Ar**gon (**LAr**) electromagnetic calorimeter and presampler, and a scintillating plastic **TILE** hadronic calorimeter (**TILE**). The end-cap calorimeters are all based on LAr sampling technology: an electromagnetic presampler and **E**lectro**M**agnatic **E**nd-**C**ap (**EMEC**), the **H**adronic **E**nd-**C**ap (**HEC**) and the **F**orward **CAL**orimeter (**FCAL**). An extended barrel region of hadronic calorimeter surrounds the end cap calorimeters, as seen in Figure 3.6.

The calorimeters are designed to provide a good containment of electromagnetic and hadronic showers: otherwise a shower may punch-through into the muon system. The calorimeter depth is tailored to limit this punch-through. The total thickness of the EM calorimeter is ≈ 22 radiation lengths (X_0) in the barrel and ≈ 24 X_0 in the end caps: where 9.7 interaction lengths (λ) of active calorimeter material in the barrel (and 11 λ in the end-cap) is adequate to provide good resolution for high-energy jets - see Table 3.1.

3.2.3.1 Electromagnetic LAr calorimetry

The ATLAS Electromagnetic calorimeters (commonly known as the LAr calorimeters and a section of which is shown in Figure 3.7) are sampling calorimeters consisting of layers of liquid argon, steel and lead. Sheets of 1.5 mm thick lead plates sandwiched between 0.2 mm of stainless steel are structured with an accordion geometry in order to provide complete coverage in the ϕ coordinate. Lead is used as an absorber in order to induce showering within the calorimeter. Liquid argon has been chosen as the active material for its intrinsic linear behaviour, its stability of response over time and its intrinsic radiation hardness.

As charged particles penetrate the calorimeter, they ionise the liquid argon with the resulting electrons drifting towards copper electrodes. At $\eta = 0$, a 2 kV electric field results in an electron drift time of approximately 450 ns. This drift time is dependent upon environmental factors such as electric field and temperature - these factors must therefore be monitored (and kept as constant as possible) when in operation. The width of the gap is 2.1 mm in the barrel, but varies with η. Therefore, the high voltage must vary in order to ensure a uniform calorimeter response over the full η range.

The two LAr calorimeter barrels span up to $|\eta| = 1.475$. In the forward region, two coaxial wheels give coverage over $1.375 \leq |\eta| < 2.5$ and $2.5 \leq |\eta| < 3.2$. A '*crack*' region exists between the barrel and forward detectors in order to accommodate instrumentation and cooling infrastructure to the inner detector. The crack region corresponds to $1.375 \leq |\eta| < 1.52$.

The structure of the LAr calorimeter barrel is depicted in Figure 3.7. The calorimeter consists of three main layers: the first has a fine granularity of $\Delta\eta \times \Delta\phi = 0.0031 \times 0.098$, which is used to reconstruct the η position of the shower and provide particle identification information; and the other two, with a granularity of $\Delta\eta \times \Delta\phi = 0.0245 \times 0.0245$ and 0.0245×0.05, collect the bulk and tail of the electromagnetic shower. A particle can travel between 22 and 33 radiation lengths when traversing the LAr detector.

A significant amount of inactive material lies in front of the EM calorimeter, which can lead to energy loss. In order to correct for this, a **P**re**S**ampler (**PS**) is placed in front of the EM calorimeter and is read out independently. The energy within the presampler is weighted to recover the correct energy for particle which begin to shower before reaching the calorimeters.

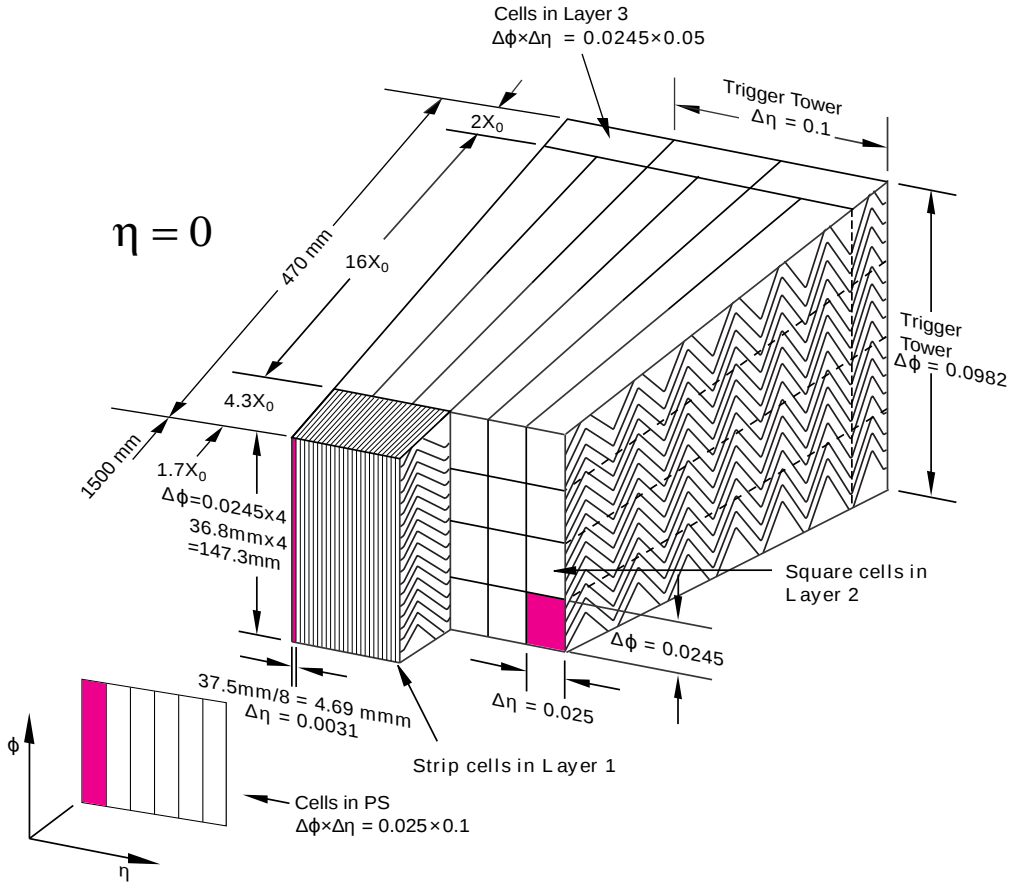

FIGURE 3.7: The LAr calorimeter barrel [61].

3.2.3.2 Hadronic Tile calorimetery

The hadronic tile calorimeter (commonly known as the *Tile*) is a sampling calorimeter consisting of alternate layers of steel and scintillating plastic. The plastic tiles are staggered in depth and are connected at both sides to photomultiplier tubes via optical fibres. The Tile is a non-compensating calorimeter with longitudinal segmentation allowing jet energies to be weighted based on depth of energy deposition. Particles interact with the scintillator producing an amount of light proportional to the energy deposited. This light is then collected using wavelength-shifting fibres.

The Tile is shielded by the EM barrel calorimeter (with approx. 1.2 λ) and the coil of the solenoid used to generate the magnetic field for the inner detector. It is split into three sections: a central barrel region with $|\eta| < 0.8$ and two extended barrel sections at $0.8 < |\eta| < 1.7$. A vertical gap between the two regions contains cabling and service pipes for the EM calorimeters. Each section of the barrel and extended barrel is split into three layers (See Figure 3.8).

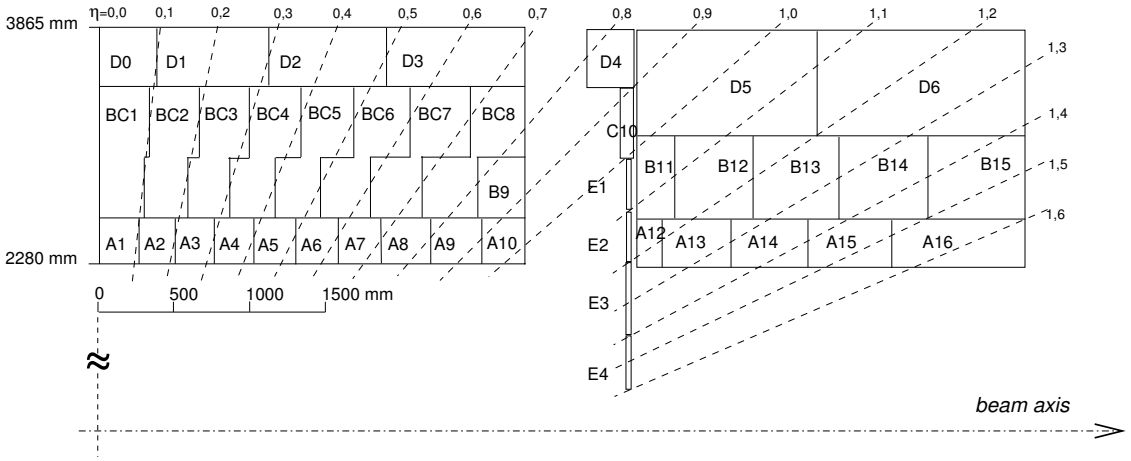

FIGURE 3.8: Segmentation in depth and η of the tile-calorimeter modules in the central (left) and extended (right) barrels. The bottom of the picture corresponds to the inner radius of the tile calorimeter [60].

3.2.3.3 Forward Calorimetry

In the forward region, calorimetry is provided by the hadronic end-caps, at $1.5 < |\eta| < 3.2$. Due to the larger and higher energy particle flux in the forward direction, liquid argon is again employed as the active material[3]. The hadronic end-caps are situated 2.03 m from the interaction point, with 8.5 mm active gaps between the copper plates. Each hadronic end-cap consists of two wheels: each with different widths for the copper plates. There is also a forward calorimeter (commonly known as the **FCal**) extending up to $|\eta| < 4.9$, however this detector is not employed in this analysis.

3.2.4 The ATLAS muon system

The muon spectrometer measures the momentum of muons by measuring their curvature in the ATLAS toroidal magnetic field. The spectrometer consists of four subsystems: the **M**onitored **D**rift **C**hambers (**MDT**), the **C**athode **S**trip **C**hambers (**CSC**), the **R**esistive **P**late **C**hambers (**RPC**) and the **T**hin **G**ap **C**hambers (**TGC**). The latter two subsystems are used for triggering. Further details of the ATLAS muon sub-detector are included in [60].

[3]The large radiation environment in the forward regions makes plastic scintillation a poor detector material, since the high radiation levels will lead to accelerated ageing of the scintillator causing it to turn black. however, liquid argon can be readily replaced without dismantling the detector.

3.3 The ATLAS trigger system

With up to 1 GHz of data being delivered by the LHC during nominal running conditions, it is impractical to store all of the detector information for every collision event. The multilevel trigger system of ATLAS is designed to allow efficient identification and recording of 'events of interest'. For a full description of the ATLAS trigger system and its performance, see [62]. The identification of interesting events is based on the presence of one or more high transverse momentum objects - for example a muon, electron, photon, jet, tau lepton or **M**issing **T**ransverse **E**nergy (**MET**)[4]. These interesting events are characterised by sets of criteria known as a *trigger configuration* (or *trigger menu*) which are composed of *trigger chains*. Each one of these chains can be thought of as a logically independent set of criteria which is either passed or failed by each event. For processes with high cross-sections, a trigger prescale may be defined such that, for example, only 1 in 200 of events which satisfy that trigger are recorded for further analysis. These prescales may be adjusted during data taking in order to synchronise with the software model for offline processing and analysis.

ATLAS employs a three-level trigger system, with the rate of data recording being reduced at each stage as a more stringent triggering criteria is applied. The **L**evel **1** (**L1**) trigger is hardware-based, using coarse detector information from the calorimeter, muon and forward subsystems. The next two trigger levels are collectively known as the **H**igh **L**evel **T**rigger (**HLT**), and individually known as the **L**evel 2 (**L2**) and **E**vent **F**ilter (**EF**). The HLT is software-based with the EF running a physics reconstruction that is close to the offline software. A schematic of the ATLAS trigger system, along with the nominal data-rates and latencies[5], is shown in Figure 3.9.

3.3.1 Triggering on jets

In this thesis, jet triggers are used to select events that contain a jet with high transverse momentum. The inputs to the L1 jet trigger are the $\Delta\eta \times \Delta\phi = 0.1 \times 0.1$ calorimeter towers. A sliding window algorithm selects local maxima in transverse energy, E_T. For a

[4] Assuming that the total linear momentum in the transverse plane of the detector is zero, the *missing* momentum (or energy) is calculated from the vector sum of the momenta of all of the object coming from the primary vertex.

[5] *Latency* is how long the trigger hardware takes to reach a decision. In the case of the L1, the latency is a strict limit of 2.5 μs, since this is the length of the data pipelines. In addition to latency, *dead-time* is a trigger veto that exists to stop the readout hardware being overwhelmed. Simple dead-time occurs when the L1 trigger accepts an event: the system will subsequently not accept any event from the next 5 bunch crossings. The dead-time gives the readout system a breathing space of 125 ns to deal with the accepted event.

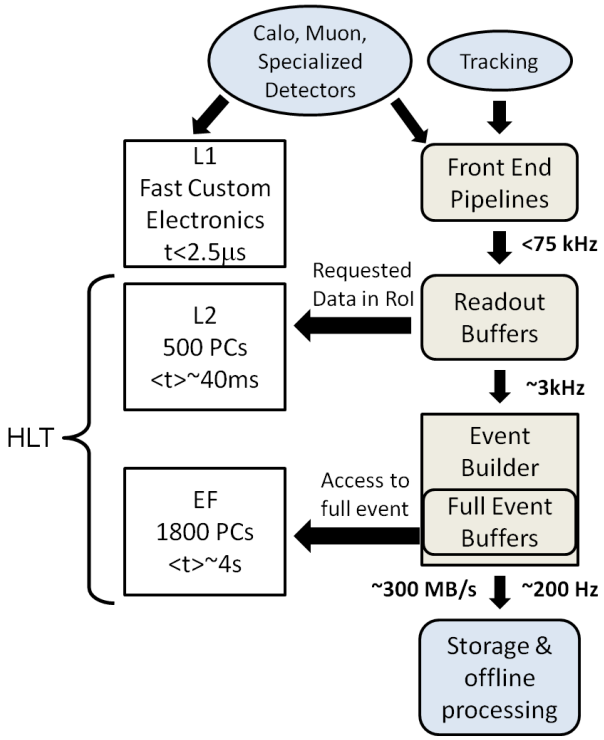

FIGURE 3.9: Schematic of the ATLAS trigger system. The latency of each trigger level and the desired output rates are shown [62].

given event, if the measured E_T is above the trigger threshold, then the event is retained and the raw data within the ***R**egion **O**f **I**nterest* (**ROI**)[6] is passed to the L2 trigger. The L2 trigger is based on a simplified version of a cone clustering algorithm[7]. The EF uses the same reconstruction algorithms as the offline reconstruction, the only difference being the calorimeter calibration, and the fact that the clusters used to make the jets are only those inside a ROI surrounding the direction of the L1 jet. Further details of the L2 and EF jet triggers can be found in [61].

3.4 Simulation of the ATLAS detector

In order to compare recorded data to our SM theory predictions, one must have an accurate simulation of the ATLAS detector and its performance. The GEANT4 software package [63], along with the ATLAS simulation framework [64] has been designed for this purpose. The energy deposited by particles in the active detector material is converted into detector signals

[6]The ROI has a typical size of 0.1×0.1 in $\eta - \phi$.
[7]See Section 5.1 for an introduction to Jet algorithms.

and reconstructed with the same format as the ATLAS detector read-out and online software. The simulation is tuned by using data from test-beam and in-situ measurements.

The analysis presented in this thesis uses the ATLFAST II [65] package in order to provide a faster and less CPU-intensive simulation of the ATLAS detector. ATLFAST II employs FastCaloSim [66] for the simulation of electromagnetic and hadronic showers in the calorimeter. Careful comparisons with detailed simulations of the ATLAS detector [63, 64] using the Geant4 package [63] show differences of the order of $1 - 2\%$. A study performed in the context of the dijet angular analysis is included in Appendix B.

3.5 Data used in this thesis

After a brief period of running at $\sqrt{s} = 900$ GeV, the LHC energy was increased to $\sqrt{s} = 2.36$ TeV in late 2009. The machine energy was then ramped up to $\sqrt{s} = 7$ TeV - delivering 48.1 pb^{-1} of data in 2010 and 5.61 fb^{-1} of data in 2011.

The dataset analysed in this thesis corresponds to approximately 4.8 fb^{-1} recorded between March and October of 2011. Although the LHC delivered 5.61 fb^{-1} of data in 2011, analysis can only be performed on a subset of this data. This is mainly due to ATLAS being unavailable for short periods of time and also the time taken for ATLAS to begin recording data once the LHC has achieved *stable beams*. The systematic error on the integrated luminosity for the dataset considered in this thesis (this corresponds to data collected between March and November of 2011) is 3.9% [59].

Figure 3.10 (a) shows the luminosity delivered and recorded by the LHC and ATLAS during 2011 proton-proton collisions. One can see the exponential increase in the instantaneous luminosity, which occurs as a consequence of the continuous beam development.

A side effect of an increase in instantaneous luminosity is an increase in the number of proton-proton interactions within the same bunch - know as *in-time pile-up*. It is also possible to have multiple interactions from different bunches during the time taken for the detector to process a single event - known as *out-of-time pile-up*. Out-of-time pile-up has a further contribution from the circulation of multiple subsequent bunches in neighbouring bunch-trains. The effects of pile-up are discussed further in Chapters 5 and 7.

The peak average number of proton interactions per bunch crossing is shown in Figure 3.10 (b). As expected, the increase in the peak average is noticeably correlated to the instantaneous luminosity (i.e. the gradient of the distribution in Figure 3.10 (a)).

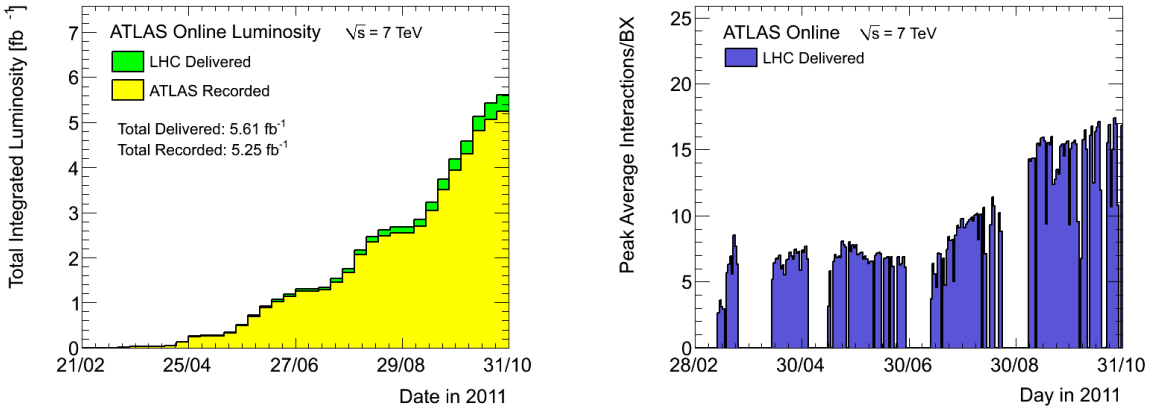

(a) (b)

FIGURE 3.10: (a) Cumulative luminosity versus week delivered to (green), and recorded by ATLAS (yellow) during stable beams. (b) The maximum mean number of events per beam crossing versus day. This version shows the average value for all bunch crossings in a lumi-block. The online luminosity measurement is used for this calculation as for the luminosity plots. Only the maximum value during stable beam periods is shown [67].

Chapter 4

Beyond the standard model

Although the SM allows precise predictions for many processes: there is still room for many alternative (and/or extended) theories to be correct. This chapter will introduce two scenarios of beyond the standard model physics for which the analysis of this thesis is sensitive. The scenarios are presented as effective theories with measurable deviation from the dominant QCD cross-section and are considered as benchmark models: used to quantify the search reach of a new physics analysis.

As well as being interesting examples of new physics scenarios, the three models are chosen due to their fundamentally different final state phenomenology. Whilst the excited quark model (Section 4.3.1) produces a resonance state, the quark contact interaction model (Section 4.3.2) and Quantum Black Hole (Section 4.2) models are threshold processes with a slow turn-on above a certain energy scale. In addition, whilst quantum black hole production is independent of any other SM processes, the quark contact interaction model interferes with the dominant QCD background.

4.1 Extra dimensions

Our every day experience is that of four dimensions - three of space and one of time. But is it necessary that these are the only dimensions in our universe? Extra dimensions are often postulated by theories which attempt to solve some of the biggest problems in theoretical physics, for example: the hierarchy problem, quantum gravity and unification of the fundamental forces of nature.

Whilst **G**eneral **R**elativity (**GR**) is one of the most successful and elegant theories in terms of cosmological and astrophysical observations, its down fall occurs in the form of singularities which occur at the high energies for which quantum effects become important. At the other extreme, **Q**uantum **M**echanics (**QM**) impressively accounts for all known small scale physics - however conceptual problems occur when it is applied to macroscopic systems. A convolution of the two - a *quantum theory of gravity* is a holy grail of modern physics.

One belief is that the forces of the standard model, and perhaps also gravity, are in fact manifestations of the *same* underlying force. This is known as *unification*. Some work towards this goal has been achieved. Extra dimensions were first considered in connection to these issues by the pioneering works of Kaluza [68] and Klein [69] in the 1920s. These works used higher dimensional representations of the metric tensor in order to unify electromagnetism with gravity.

The existence of > 3 spatial dimensions would have many interesting phenomenological consequences, many of which, depending on the size and number of the 'extra' dimensions, could be observable at the LHC.

If extra dimensions do exist, there must be some reason that we do not experience them in our every day lives. Traditionally, this phenomenon is explained by supposing that any extra dimensions are compactified on a small scale. Perhaps the two most popular configurations of extra dimensions are the **ADD** (**A**rkani Hamed-**D**imopoulos-**D**vali) [70] and **RS** (**R**andall-**S**undrum) [71].

4.1.1 The Planck mass, M_D

In the ADD [70] scenario of extra dimensions, space-time can be factorised into a 4-dimensional part and a n-dimensional part (for n extra spatial dimensions). Following the PDG convention [8], the space is constructed as $R^4 \times M_n$, where R^4 is our usual 4-dimensional space-time and M_n is a $n-$dimensional compact space with finite volume V_n. The factorisation of the 4-dimensional and $n-$dimensional parts of the space-time allow one to express the 4-dimensional reduced Planck mass as

$$\bar{M}_{Pl}^2 = \bar{M}_D^{2+n} V_n, \tag{4.1}$$

where $\bar{M}_{Pl} = M_{Pl}/\sqrt{8\pi} = 2.4 \times 10^{18}$ GeV and $\bar{M}_D$ is the reduced Planck mass for the D-dimensional theory. Following [72], the fundamental $D-$dimensional Planck mass is given

by

$$M_D = (2\pi)^{n/(2+n)} \bar{M}_D. \tag{4.2}$$

In the ADD scenario, the hierarchy problem is solved by hypothesising that M_D is $\mathcal{O}$(TeV) with the apparent $\bar{M}_{Pl}$ being obtained with a large value of V_n.

4.1.2 Experimental limits from other experiments

Limits have been set on the parameter M_D by other experiments. A summary table of the latest such limits, from collider experiments, in the large extra dimension scenario are shown in Table 4.1.

n	LEP ($\sqrt{s} = 209$ GeV)	CDF ($\sqrt{s} = 1.96$ TeV)	DØ ($\sqrt{s} = 1.96$ TeV)
2	1.60	1.18	0.884
3	1.20	0.99	0.864
4	0.94	0.91	0.836
5	0.77	0.86	0.820
6	0.66	0.83	0.797
7	-	-	0.797
8	-	-	0.797

TABLE 4.1: Lower limits on M_D (in the Large Extra Dimension scenario) at the 95% confidence level from other accelerator experiments [73].

The most stringent limits to date (for the ADD model) derive from astrophysical observations:

- the supernova SN 1987A did not emit more Kaluza Klein gravitons than compatible with neutrino signal distributions observed by Kamiokande and IMB, leading to limits of $M_D > 22$ TeV for $n = 2$ [74];
- the Energetic Gamma Ray Experiment Telescope (EGRET) lead to limits [75, 76]: from cosmic γ-ray background analysis of $M_D > 70(5)$ TeV for $n = 2(3)$; from neutron star halo analysis of 100 MeV γ-rays of $M_D > 97, 8, 1.5$ TeV for $n = 2, 3, 4$; and analysis of neutron starts in the galactic bulge leading to limits of $M_D > 1130, 57, 7, 1.8$ TeV for $n = 2, 3, 4, 5$.

Table top experiments such as [77], have also tested the $1/r^2$-law of gravitation excluding extra dimensions with $R > 44\mu m$

Discussion of limits from this analysis, as well as other analyses from the LHC, are discussed in Chapter 9.

4.1.3 Warped extra dimensions

In the RS [71] model for extra-dimensions, the apparent weakness of gravity in our everyday 4-dimensional space-time is caused by a gravitational red-shift in a warped extra dimension. The theoretical set-up consists of two 4-dimensional branes separated by a 5^{th} y-coordinate. The SM fields are located on the **I**nfra**R**ed (**IR**) brane and the other brane is known as the **U**ltra**V**iolet (**UV**) brane. Solving Einstein's equation given the element

$$ds^2 = \exp(-2k|y|)\eta_{\mu\nu}dx^\mu dx^\nu - dy^2, \tag{4.3}$$

with the UV and IR branes located at $y = 0$ and $y = \pi R$, respectively; R is the compactification radius and k is the curvature of the extra dimension. In contrast to the ADD case, the RS space is not factorised and so the 4-dimensional metric (and so the strength of gravity) is dependent upon the extra-dimensional coordinate y.

4.1.4 Higgsless extra dimensional models

Although not of relevance to the particular models considered in this thesis, it is noted that extra spatial dimensions also offer new possibilities for breaking gauge symmetries. Light Kaluza-Klein modes on compactified spaces, corresponding to broken generators of the group, acquire masses and allow the SM to respect unitarity up to $E \sim 12\pi^2 M_W/g \sim 10$ TeV (for a single extra dimension) [8].

4.1.5 Classical Black holes

The idea of a body so massive that even light could not escape was first put forward by geologist John Michell in a letter written to Henry Cavendish in 1783.

Classically, in order for a particle of mass m to escape from the surface of a planet or star of mass M:

$$\frac{1}{2}mv^2 > \frac{GMm}{r}, \tag{4.4}$$

where G is the gravitational constant and r is the radius of the planet or star. Therefore, in the limit that the escape velocity is equal to the speed of light, c, then

$$r = r_S = \frac{2GM}{c^2}, \tag{4.5}$$

where r_S is known as the Schwarzschild radius: a particle that is at a distance $d < r_S$ from the centre of mass will require a speed $> c$ in order to escape the gravitational attraction of the body. The sphere about the centre-of-mass of M with radius r_S is known as the *event horizon*: due to the universal speed limit of any object being c [78], any event within the event horizon can have no causal effect beyond the event horizon.

For ordinary stars and planets $r > r_S$. For example, our sun has $r = 700,000$ km with $r_S = 3$ km. However, as explained above, for $r < r_S$, we have a situation where an object would require a speed $> c$ in order to escape the star: a black hole is formed.

Later, solutions to Einstein's equations were found for rotating, charged and charged rotating **B**lack **H**oles (**BH**s) eventually leading to the *no-hair theorem* stating that a stationary black hole solution is completely described by the three parameters of the Kerr-Newman metric: mass, angular momentum and electric charge.

4.1.6 Higher dimensional Black Holes

In the absence of extra dimensions, the creation of a BH requires extremely large CM energies: reducing the CM energy down to energy scales accessible at the LHC leads to a Schwarzschild radius, which is so small that a BH can not be formed.

For a universe with extra dimensions, if the Compton wavelength of a given mass is much larger than the size of the extra dimensions, then the mass will behave as a 4-dimensional object: this is the situation for regular objects such as people, planets and classical black holes. If, however, the Compton wavelength of an object is smaller than the size of the extra dimensions, then the object exists as a higher-dimensional object that is completely submerged in a higher dimensional space-time. The presence of the extra dimensions facilitates the creation of BH, since, for a higher dimensional object, the scale of gravity is increased: increasing the corresponding Schwarzschild radius for a given mass.

By lowering Plank scale M_D closer to the EW scale, the possibility of BH production in high-energy scattering processes becomes a possibility for reactions with trans-Plankian centre-of-mass energies, $\sqrt{s} > M_D$. For a centre-of-mass energy $\sqrt{\hat{s}}$ with $D = 4 + n$ space-time dimensions, the Schwarzschild radius is given by [79]

$$r_S = k(D)\frac{1}{M_D}\left(\frac{M}{M_D}\right)^{\frac{1}{D-3}}, \tag{4.6}$$

where $k(D)$ is a numerical coefficient depending only on the number of dimensions[1]:

$$k(D) = \left(2^{D-4} \sqrt{\pi}^{D-7} \frac{\Gamma\left(\frac{D-1}{2}\right)}{D-2} \right)^{\frac{1}{D-3}}. \tag{4.7}$$

The functional form of the $k(D)$ factor is shown in Figure 4.1.

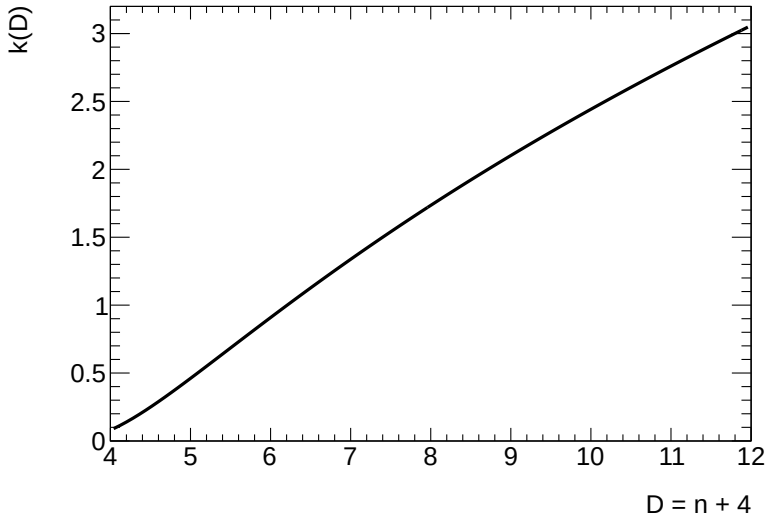

FIGURE 4.1: Functional form of factor $k(D)$, defined in Equation 4.7.

There are a variety of predictions as to the behaviour and properties of these 'micro-BHs'. One class of theories, describes *semi-classical* BHs which, like their larger cousins, have a *Hawking temperature* [80] and therefore decay thermally via *Hawking radiation* [81]. It is possible to calculate this emission spectrum if one assumes that the energy of the emitted particle is small compared to the BH mass, $M_{BH} \gg \omega$. This is necessary so that the presence of the emitted particle does not effect the metric in the vicinity of the BH. In turn, this requires that the Hawking temperature, T_H be small compared to M_{BH}, and therefore $M_{BH} \gg M_D$. Of course, this condition must break down at some point: what happens after this point is a source of much debate.

If the impact parameter, b, between the two particles is less than the Schwarzschild radius, r_S, then according to GR and the *Hoop-conjecture* [82], strong gravitational effects will lead to the production of a BH with production cross-section given by

$$\sigma \sim \pi b^2 \sim \pi r_S^2. \tag{4.8}$$

[1]This equation uses the Gamma function $\Gamma(n) = \int_0^\infty t^{n-1} e^{-t} \mathrm{d}t = (n-1)!$.

During this process, not all of the incident energy of the two particles is bound to the BH. A fraction of the energy will be lost through gravitational radiation.

In a scenario with extra dimensions, the trans-Plankian regime may lie slightly above the TeV scale. In this case, it is entirely possible trans-Plankian reactions already take place in the atmosphere [83–86]. In this thesis, the possibility of these reactions taking place under the controlled conditions of the LHC is considered.

4.2 Quantum Black Holes

In [87–90] it is argued that the semi-classical black holes (described above) are highly suppressed and will in-fact occur in only a very limited parameter range of the models, if at all. In addition, the expected number of particles to be emitted from the BH is only above 2 for $M_{BH} \geq 1.5M_D$. The steeply falling parton distributions functions of the proton lead to a cross-section for BH production that is strongly peaked at their production threshold, which is assumed to be M_D. As alluded to above, the behaviour of particle interactions around the Planck scale is shrouded by a lack of knowledge of quantum gravity. It is therefore perhaps more appropriate to refer to such an interaction of a 'quantum gravitational effect' or 'resonance', however we follow the common convention of referring to such states as **Q**uantum **B**lack **H**oles (**QBH**).

Despite the absence of a complete quantum theory of gravity, by making a few assumptions and relying on fundamental principals [91], it is possible to construct a model for production and decay of QBHs in proton proton collisions at the LHC [79].

4.2.1 Quantum black hole production at the LHC

For a proton-proton (pp) collision, following the arguments outlined above, it is required that any two partons (i, j) have an impact parameter $b < b_c \simeq r_S$, where b_c is the critical value and r_S is given in Equation 4.6. The parton-level production cross-section is simply $\sigma_{ij} \simeq \pi r_S^2(\hat{s})$, where $\sqrt{\hat{s}}$ is the centre-of-mass energy of the colliding partons. In order to construct the complete cross-section, we must sum over all possible parton combinations, and weight them according to the parton distribution functions $f_i(x)$, which give the probability of finding a parton of flavour i, with momentum fraction x of the colliding proton. The total pp cross-section for the production of a BH from the collision of two partons, a and b, may

be written as

$$\sigma(QBH^{q}_{p_1p_2}) = \sum_{a,b} \int_{M^2/s}^{1} dx_{min} \int_{x_{min}}^{1} \frac{dx}{x} f_a \left(\frac{x_{min}}{x}\right) f_b(x) \pi r_S^2, \tag{4.9}$$

where $sx_ax_b = sx_{min} = \hat{s}$ (x_a and x_b are the fractional energies of the two partons relative to the proton energies), and f_a and f_b are the PDFs for the proton. The naming convention for QBH states used in [79] has been adopted in this thesis such that the state $QBH^{q}_{p_1p_2}$ is formed from parton types p_1 and p_2 and has electric charge q. Since it is natural for local gauge symmetries of QCD colour and electric charge to be conserved during the black hole formation [90], the possible decay states of the QBH are determined by q and the colour state composed from p_1 and p_2. It should be remembered that this production cross-section is, most likely, an over-estimation, since we have assumed $b_c \simeq r_S$ and that all of the energy goes into the creation of the BH. As discussed above, it more likely that $b_c < r_S$ and that a significant fraction of the CM energy is lost through gravitational radiation effects.

4.2.2 Simulation with the BlackMax generator

QBH simulations are produced using the BlackMax V2.0 Monte Carlo generator [92, 93]. BlackMax is a versatile semi-classical and quantum black-hole generator that simulates a number of different extra dimension models and black-hole evolution scenarios. In this thesis, a QBH model resulting in two final-state particles is simulated. A basic model is chosen for QBH states to be produced for $M_D \leq \sqrt{\hat{s}} \leq \sqrt{s}$, where 100% of the combined partonic energy is included in the QBH production[2]. The production and decay of the QBH is simulated as an s-channel process with an isotropic decay distribution in the final state. In the decay of the QBH states, it is required that baryon number be conserved. The resulting branching ratios to SM particles for the case of $M_D = 4$ TeV and $n = 6$ are shown in Table 4.2 - the total branching ratio for dijet final states is 96.32%.

The production cross-section for $n = 6$ extra dimensions and values of M_D ranging from 2 TeV to 5 TeV are given in Table 4.3. For limit setting purposes, 10,000 events of each mass-point for the $n = 6$ scenario were simulated and passed through the ATLAS simulation chain described in Section 2.4.

As the value of M_D increases, so does the energy threshold for the production of QBH states: resulting in a lower production cross-section. The variation of the production cross-section with n can be understood through Equation 4.7 and Figure 4.1.

[2]The parameter file for the particular model is included in Appendix E of this thesis.

Topology	Branching ratio (%)
qq	91.11
qg	5.07
gg	0.14
ll	0.03
$\nu\nu$	0.01
$l\nu$	0.03
$\gamma\gamma$	0.00
VV	0.02
HH	0.00
other	3.58

TABLE 4.2: Percentage occurrence (Branching Ratio, BR) for each decay topology. Values are for BLACKMAX parameters described in Appendix E, with $M_D = 4000$ TeV and $n = 6$.

M_D	Cross-section σ [pb]					
[TeV]	$n = 2$	$n = 3$	$n = 4$	$n = 5$	$n = 6$	$n = 7$
2	2.0892E+01	4.1668E+01	6.5877E+01	9.4451E+01	1.2425E+02	1.5844E+02
2.25	7.7299E+00	1.5526E+01	2.4428E+01	3.5195E+01	4.6859E+01	5.8936E+01
2.5	2.9191E+00	5.8983E+00	9.4895E+01	1.3440E+01	1.7818E+01	2.2345E+01
2.75	1.1186E+00	2.2533E+00	3.5908E+00	5.1773E+00	6.8306E+00	8.6651E+00
3	4.2543E-01	8.5510E-01	1.3637E+00	1.9626E+00	2.5969E+00	3.2996E+00
3.5	5.7247E-02	1.1637E-01	1.8583E-01	2.6797E-01	3.5423E-01	4.5084E-01
4	6.7466E-03	1.3708E-02	2.1921E-02	3.1515E-02	4.2397E-02	5.3352E-02
4.5	6.5117E-04	1.3148E-03	2.1365E-03	3.0650E-03	4.1171E-03	5.1739E-03
5	4.5274E-05	9.2105E-05	1.4964E-04	1.9574E-04	2.9195E-04	3.6673E-04
5.5	1.9733E-06	4.0274E-06	6.5051E-06	9.3774E-06	1.2541E-05	1.6037E-05
6	3.8140E-08	7.7826E-08	1.2722E-07	1.8384E-07	2.4380E-07	3.1513E-07

TABLE 4.3: Cross-sections for QBH samples generated with the BLACKMAX MC simulator for $n = 2 - 7$ extra dimensions and various values of M_D.

4.3 Quark sub-structure

The SM does not predict the masses of fermions or their family structure described in Section 1.2. In addition, the SM does not motivate the relationship between the charges of elementary particles. This situation allows a hint for the possibility of fermions being composite objects.

It is hypothesised that if quarks and leptons consist of bound constituents (often named preons) then new interactions will be measurable at some energy scale Λ, known as the composite scale. In the following sections, two effective models of quark sub-structure are described. These models provide a popular benchmark scenario for NP searches among high-energy collider experiments: allowing simplified comparison between the performance and methods of different collaborations.

4.3.1 Excited quarks

The excited quark model [94–96] is one implementation of a theory with quark sub-structure and is a commonly used benchmark signal in high-energy experiment searches: used to quantify the search reach of an analysis. Quarks consisting of tightly bound elementary constituents are energised to excited states and then subsequently decay in an s-channel process. If the energy scale at which compositeness effects are relevant, Λ, is smaller than the centre-of-mass energy of the LHC then it is expected that such quark resonances will be visible.

Taking the first generation of excited quarks, denoted as q^* (u^*, d^*), are assumed to have spin and isospin equal to 1/2 with their couplings to SM quarks and gauge bosons dictated by the Lagrangian [96]:

$$\mathcal{L}_{q^*} = \frac{1}{2\Lambda}\bar{q}^*_R\sigma^{\mu\nu}\left[g_s f_s\frac{\lambda^a}{2}G^a_{\mu\nu} + gf\frac{\tau}{2}W_{\mu\nu} + g'f'\frac{Y}{2}B_{\mu\nu}\right]q_L + h.c. \tag{4.10}$$

where $G^a_{\mu\nu}$, $W_{\mu\nu}$ and $B_{\mu\nu}$ are the field-strength tensors of the $SU(3)$, $SU(2)$ and $U(1)$ gauge fields, respectively. The quantities λ^a, τ and Y (g_s, g and g') and the corresponding gauge structure constants (gauge coupling constants). The parameters f_s, f and f' control the composite dynamics and are expected to be of order one. For $m_{q^*} > m_V$ ($V = W^{\pm}, Z^0$) and

	1 TeV	2 TeV	3 TeV		1 TeV	2 TeV	3 TeV
$BR(u^* \to ug)$	82.7%	81.4%	80.7%	$BR(d^* \to dg)$	82.7%	81.4%	80.7%
$BR(u^* \to u\gamma)$	2.4%	2.5%	2.6%	$BR(d^* \to d\gamma)$	0.6%	0.6%	0.7%
$BR(u^* \to uZ^0)$	3.5%	3.8%	4.0%	$BR(d^* \to dZ^0)$	5.3%	5.7%	5.9%
$BR(u^* \to uW^-)$	11.4%	12.3%	12.8%	$BR(d^* \to dW^+)$	11.4%	12.3%	12.8%
$\Gamma(u^*)/m_{u^*}$	0.0374	0.0352	0.0341	$\Gamma(d^*)/m_{d^*}$	0.0374	0.0352	0.0341

TABLE 4.4: Branching ratios and relative decay widths for q^* ($m_{q^*} = 1, 2, 3$ TeV) to various decay channels. Using ATLAS MC09 tuning [99] and taken from [100].

massless ground-state quarks, the partial widths [96–98] for the q^* decays are

$$\begin{aligned} \Gamma(q^* \to qg) &= \frac{1}{3}\alpha_S f_S^2 \frac{m_{q^*}^3}{\Lambda^2}, \\ \Gamma(q^* \to q\gamma) &= \frac{1}{4}\alpha f_\gamma^2 \frac{m_{q^*}^3}{\Lambda^2}, \\ \Gamma(q^* \to qV) &= \frac{1}{8}\frac{g_V^2}{4\pi} f_V^2 \frac{m_{q^*}^3}{\Lambda^2}\left(1 - \frac{m_V^2}{m_{q^*}^2}\right)^2\left(2 + \frac{m_V^2}{m_{q^*}^2}\right), \end{aligned} \tag{4.11}$$

with

$$\begin{aligned} f_\gamma &= fT_3 + f'\frac{Y}{2}, \\ f_Z &= fT_3 \cos^2\theta_W - f'\frac{Y}{2}\sin^2\theta_W, \\ f_W &= \frac{f}{\sqrt{2}}, \end{aligned} \tag{4.12}$$

where T_3 is the third component of weak isospin and Y is the hypercharge of q^*.

A compositeness scale $\Lambda = m_{q^*}$ and SM couplings ($f_S = f = f' = 1$) results in the branching ratios given in Table 4.4. With a coupling strength of $m_{jj}^2/\Lambda^2 \sim \mathcal{O}(1)$, the excited quark production has a coupling greater than 2 orders of magnitude above α_S. Consequently, any interference terms between the excited quark Lagrangian (Equation 4.10) and SM QCD processes can be neglected. Distributions of the excited quark signal for the observables used in this thesis are shown in Sections 8.2.2 and 8.2.3.

This excited quark model is available in the PYTHIA 6 [50] event generator, and has been used as a benchmark to set limits on q^* in ATLAS, in CMS, and in TeVatron experiments. An example of the kinematic distributions for an excited quark with a mass of 1 TeV is shown in Figure 6.7. Unfortunately, in the course of preparing for analysis of ATLAS 2012 collision data it has been found that there is a problem with this benchmark. In 2012, ATLAS is using the C++ based PYTHIA 8 [101] event generator for processes previously simulated with PYTHIA 6 since the older generator will no longer be supported by its authors.

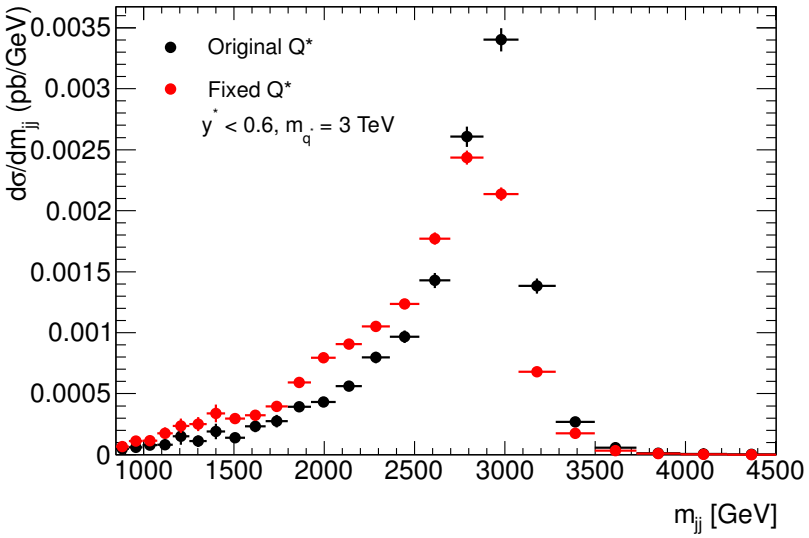

FIGURE 4.2: Comparison of the q^* m_{jj} distribtions from PYTHIA 6 with and without the FSR correction, for a q^* mass of 3 TeV.

In anticipation of this change, a number of studies have been done in ATLAS comparing standard model and NP processes with these two generators. The q^* comparison studies show that there are noticeable differences in the dijet mass distributions predicted by the two generators. In particular, the PYTHIA 8 dijet mass peak for q^* is substantially wider than that for PYTHIA 6.

The PYTHIA authors confirm that there is a problem with the showers in PYTHIA 6 for the excited quark model: the generator gives too little final state radiation (FSR). The problem lies with the matrix-element (ME) correction machinery, which is intended to ensure that the showers are correct to NLO. PYTHIA 6 handles the FSR correctly for SM and MSSM processes but in the case of q^*, and some other processes, it rejects most radiation associated with one of the jets. In PYTHIA 8, the list of matrix elements is the same, but the process identification is more sophisticated, and the colour flow is handled correctly.

The q^* m_{jj} distributions from PYTHIA 6 can be brought into close correspondence with PYTHIA 8 by setting the PYTHIA 6 MSTJ(47) parameter to zero, approximating the correct process identification and restoring the FSR.

Since PYTHIA 6 with the default setting has been used by a number of experiments to set q^* limits, it has been decided to create two sets of MC samples, with and without the FSR modification, and to calculate the q^* exclusion limits for both cases. A comparison of the signal shapes for an excited quark of mass 3 TeV is shown in Figure 4.2.

The corresponding cross-sections and number of events for the excited quark samples generated with PYTHIA 8 are shown in Table 4.5.

m_{q^*} [GeV]	cross-section *sigma* [pb]	N_{events} generated
2000	1.5721	20000
2250	0.54626	20000
2500	0.19819	20000
2750	0.071970	20000
3000	0.026747	20000
3250	0.010041	20000
3500	0.0039463	20000
3750	0.0015547	20000
4000	0.000639	20000
4250	0.00028174	20000
4500	0.00013449	20000

TABLE 4.5: Cross-section and number of events generated for PYTHIA 8 excited quark at q^* masses from 2 to 4.5 TeV.

The best non-LHC exclusion limits, to-date, on the mass of the q^* were set by CDF Run 2 at the Tevatron and excluded the mass region $260 < m_{q^*} < 870$ GeV [102].

4.3.2 Quark contact interactions

In contrast to the tightly bound constituents of the excited quark model in Section 4.3.1, it is often postulated that partons may simply be unstructured collections of preons [103–105]. Of particular interest, is the possibility of a four point '**C**ontact **I**nteraction' (**CI**). For a $2 \to 2$ process, we have the possibility of two energy regimes depicted in Figure 4.3. For $M \ll \Lambda$ the interaction is dominated by classical QCD. However, for energies at and beyond Λ, the interaction can be described by the effective Lagrangian:

$$\mathcal{L}_\Lambda = \frac{g^2}{2\Lambda^2}\left[\eta_{LL}(\bar{q}_L\gamma^\mu q_L)(\bar{q}_L\gamma_\mu q_L) + \eta_{RR}(\bar{q}_R\gamma^\mu q_R)(\bar{q}_R\gamma_\mu q_R) + 2\eta_{RL}(\bar{q}_R\gamma^\mu q_R)(\bar{q}_L\gamma_\mu q_L)\right], \quad (4.13)$$

where the coefficients η_{ab} can be set to 0, $+1$ or -1 in order to turn terms on/off or select constructive/destructive interference.

In this thesis, the common convention of left-left isoscalar destructive interference is employed as a specific example as an alternative to the QCD null hypothesis. The resulting Lagrangian is

$$\mathcal{L}_{\Lambda_{LL}} = \frac{4\pi}{2\Lambda^2}(\bar{q}_L\gamma^\mu q_L)(\bar{q}_L\gamma_\mu q_L). \quad (4.14)$$

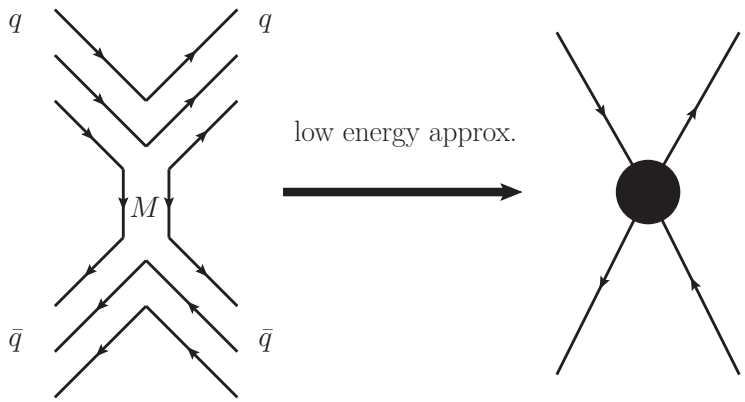

FIGURE 4.3: Sketch of interaction between quark constituents (left) and the low energy approximation of a regular four-point interaction (right).

Adding $\mathcal{L}_{\Lambda_{LL}}$ to the SM QCD Lagrangian leads to an additional interference terms in the differential cross-section[3] $d\sigma/dp_T$ proportional to $1/\Lambda^2$, as well as a pure CI term of $1/\Lambda^4$.

There are also additional contributions to the angular behaviour of the form

$$\frac{\mathrm{d}\sigma_{q_i\bar{q}_i\to q_j\bar{q}_j}}{\mathrm{d}\cos\hat{\theta}} \sim \frac{1}{\Lambda^4}(1+\cos\hat{\theta})^2, \quad i \neq j. \tag{4.15}$$

The cross-section for the destructive interference case can be shown to always be lower than the constructive interference case. Limits placed on the the parameter Λ for destructive interference therefore represent conservative limits on any CI phenomena.

In contrast to the excited quark case, the contact interaction model will probe compositeness scales larger than the dijet invariant mass being recorded: e.g. at $m_{jj} \sim 2.5$ TeV, it is possible to probe $\Lambda \sim 10$ TeV. This leads to a coupling term of $m_{jj}^2/\Lambda^2 \sim 1/16$, which is much closer to α_S, making interference terms with SM QCD non-negligible.

CI signal samples are generated using PYTHIA with the configuration described above. Since the contact interaction signal interferes with the QCD background, it is necessary to simulate the QCD and CI signal at the same time. The samples used in this thesis, together with their cross-sections and number of events generated are contained in Table 4.6. As with the pure QCD background described in Section 2.5, the samples must be split into J-samples in order to ensure sufficient statistics across the whole jet p_T spectrum.

Again, distributions for contact interaction signals are shown for the variables used in this thesis in Sections 8.2.2 and 8.2.3.

[3]The presence of these terms in the differential cross-section can be seen by remembering that the cross-section is obtained from the square of the matrix element (as described in Section 2.2.1) and the matrix element is obtained from the Lagrangian via the Feynman rules.

	cross-section σ [nb]	N_{events} generated
$\Lambda = 4$ TeV		
J3	2.5381E+03	200000
J4	9.9535E+01	299999
J5	2.5913E+00	300000
J6	3.8594E-02	300000
J7	7.7826E-04	300000
J8	7.0357E-07	300000
$\Lambda = 6$ TeV		
J3	2.5386E+03	299998
J4	9.9465E+01	600000
J5	2.5859E+00	600000
J6	3.5180E-02	600000
J7	2.2246E-04	599998
J8	1.3176E-06	600000
$\Lambda = 8$ TeV		
J3	2.5376E+03	300000
J4	9.9482E+01	599500
J5	2.5908E+00	600000
J6	3.4959E-02	599500
J7	1.4484E-04	600000
J8	4.0349E-08	600000
$\Lambda = 10$ TeV		
J3	2.5361E+03	300000
J4	9.9554E+01	600000
J5	2.5901E+00	599999
J6	3.5033E-02	599000
J7	1.2958E-04	599999
J8	1.7067E-08	599999

TABLE 4.6: Cross-section and number of generated events for PYTHIA contact interactions model for various values of composite-scale Λ. Sample are split into J-slices corresponding to p_T ranges in Table 2.1.

Previous restrictions on the scale Λ of such contact interactions have been placed using data from the Tevatron excluding $\Lambda_{qq} < 2.7$ TeV at the 95% confidence level [106].

Chapter 5

Jet reconstruction

A jet is a narrow cone of hadrons and other particles produced by the hadronisation of a quark or gluon. Within the ATLAS detector, many, if not most, interesting final states will include at least one jet in the final state.

The expected behaviour of final state partons was discussed in Chapter 2. This discussion described proton collisions resulting in final state hadrons, together with a cross-section for that process. This chapter will look at these processes from the other direction: starting with energy depositions in the ATLAS calorimetry from highly energetic hadrons, we shall describe the procedure required to extract a measurement of the process at the particle level. The ultimate goal is to be able to compare theoretical predictions, introduced in Section 2.3, with experimental measurements.

5.1 Motivations for jet definitions

Since we are unable to observe the final-state partons of a hard scatter in a proton-proton collision, a common prescription must be defined for accurate comparison of jets from theory and experimentally measured jets. This prescription must describe how to uniquely map a set of four-momenta (whether particles, partons or calorimeter objects) into a jet object. Following the convention of 2007 Les Houches accord [107], a complete jet definition must include:

- a **jet algorithm** that defines how to group four-momenta of particles, partons or calorimeter objects into jets;

- the full specification of the **jet algorithm parameters**;
- the **recombination scheme**: a set of rules for obtaining the four-momentum of the final jet object from its constituents.

The development of a jet definition must take into account both theoretical and experimental considerations. Some of these factors will be discussed below, however a more complete description is given in [108].

As described in Chapter 2, the scaling of the strong coupling constant leads to distinct energy regimes where perturbative QCD methods may or may not be employed. These issues can lead to apparent singularities in the cross-sections associated with infra-red and collinear emissions of quarks and gluons. The jet definition must be resilient to the presence (or absence) of these low-energy emissions. Theoretically, well-behaved jets give finite perturbative results at all orders and allow meaningful comparisons of data with the most recent theoretical predictions. A jet definition that is insensitive to the presence of additional very soft particle radiation[1] is known as *infra-red-safe*. A jet definition that is insensitive to the presence of additional particles radiated at a very small angle, with respect the original parton, is known as *collinear safe*.

It is also required that the jet definition is able to reproduce the same physics results: whether the input objects are particles, partons or calorimeter objects - in other words, the jet definition should be detector-independent. Furthermore, it is desirable that the jet algorithm is invariant under longitudinal boosts along the beam axis: therefore aiding comparison between the lab and the CM frame.

Experimental considerations include the implementation and speed of the jet algorithm, as well as its resilience toward calorimeter noise, pile-up conditions and the calibration scheme. For the ATLAS experiment, the jet reconstruction software is implemented through the ATHENA software framework, which employs the FastJet [109, 110] classes for jet finding. Detector and calibration effects for some jet algorithms are discussed below.

5.2 Jet finding algorithms in ATLAS

There are two broad collections of jet algorithms: those based on geometrical cones in (η, ϕ); and those that involve repeated recombination of constituent particles, based on some

[1] i.e. In the limit of increasingly low momentum particle radiation

predefined distance parameter. Each approach has relative theoretical and experimental strengths and so are employed in different areas of an ATLAS analysis.

5.2.1 The cone algorithm

The seeded fixed cone algorithm starts with ordering the inputs according to decreasing transverse momentum, p_T. The highest p_T object is selected if it satisfies a seed threshold of 1 GeV. Subsequently, all objects within a cone of fixed-radius R_{cone} in (η, ϕ) are combined with the seed. The four-momenta of the grouped objects are added to form the four-momentum of a secondary seed around which a new cone is formed. Objects are then (re-)collected in this new cone. The process continues until the direction of the collected cone is stable, i.e. does not change significantly during successive iterations - resulting in a final jet object. This process then begins again taking the next-highest p_T seed.

The final collection of jets may share constituents, therefore a split and merge step is included: jets that share more than a fraction f_{sm} ($f_{sm} = 0.5$ in ATLAS) of the p_T of the jets are merged, otherwise they are split.

The seeded cone algorithm is collinear but not infra-red safe: i.e. soft particles can easily modify its behaviour. However, due to its speed, the seeded cone algorithm is used in order to quickly form jet objects within the ATLAS jet trigger software: see Section 3.3.1.

5.2.2 The anti-k_T algorithm

The anti-k_T jet algorithm is an example of a sequential recombination algorithm and is the default ATLAS jet algorithm. For this algorithm, all pairs (i, j) of input objects are analysed with respect to their relative distance measures:

$$d_{ij} = \min\left(\frac{1}{p_{T,i}^2}, \frac{1}{p_{T,j}^2}\right)\frac{\Delta R_{ij}^2}{R^2} = \min\left(\frac{1}{p_{T,i}^2}, \frac{1}{p_{T,j}^2}\right)\frac{\Delta\eta_{ij}^2 + \Delta\phi_{ij}^2}{R^2} \tag{5.1}$$

and $d_{iB} = 1/p_{T,i}^2$, where the index B stands for *Beam* and R is a pre-defined cone size parameter (for which we use $R = 0.6$). The algorithm then progresses as:

- The minimum distance d_{min} among d_{ij} and d_{iB} is found.
- If d_{min} corresponds to value from the list of d_{ij}: the objects i and j are combined into a new object k.

- Elements i and j are removed from the list of input objects and k is added to the list.
- If d_{min} corresponds to a value from the list of d_{iB}: object i is considered a jet and is removed from the list.
- The procedure is repeated until all objects are removed from the list.

The anti-k_T algorithm is both infra-red and collinear safe and requires no split and merge stage.

After a detailed study of jet algorithms within ATLAS [111] (considering cone sizes of 0.4 and 0.7) it was decided that the anti-k_T algorithm demonstrated the best overall performance - and so was adopted as the default algorithm for offline reconstruction. It was found that the anti-k_T algorithm is stable against pile-up, due to the fact that it is infra-red and collinear safe. However, since the algorithm does not use a seed, it is more sensitive to electronic noise in the calorimeter. As a result of this, the algorithm is used with input objects that are noise suppressed - see Section 5.3.

It was also found that the ATLAS trigger efficiency would improve through the use of anti-k_T, however for the measurement described in this thesis, this has not-yet been implemented and the trigger uses the cone algorithm.

5.3 Jet reconstruction in ATLAS

For the ATLAS experiment, jets can be reconstructed from different physics objects. In this thesis, topological clusters, or *topoclusters* [112] are used as an input to the anti-k_T jet algorithm with $R = 0.6$. Alternative input objects are: groups of geometrically delimited groups of calorimeter cells, known as *towers*; and reconstructed tracks, resulting in *track jets*. *Truth jets* are also used in some studies, which are reconstructed from stable[2] particles generated by the Monte Carlo event generator. For a more complete description of the behaviour of jets in ATLAS, see [113].

Topological clusters are groups of calorimeter cells that are designed to follow the shower development, whilst taking advantage of the fine segmentation of the ATLAS calorimeters. Starting with a *seed cell*, whose signal-to-noise ratio[3] is above a threshold of 4, neighbouring cells are included iteratively if their signal-to-noise ratio is ≥ 2, and then all neighbouring

[2] A stable particle is defined to have a lifetime > 10 ps.

[3] The signal-to-noise ratio is estimated as the energy deposited in the calorimeter cell divided by the RMS of the energy distributions measured in randomly triggered events.

cells are also also included. Once all prospective cells have been added together, all cells in a topocluster are scanned for local maxima in terms of energy content. Any local maxima are then used as seeds for a new iteration for topological clustering, which will split the original cluster into more topoclusters.

Four-vectors for the final topoclusters are constructed with energy equal to the sum of the energy of the included cells, zero mass and a reconstructed direction as that of a unit vector originating from the centre of the ATLAS coordinate system and pointing to the energy-weighted topocluster barycentre. The process for calibrating the energy of each of the topoclusters, as well as moving the direction of each topocluster to the primary vertex, is described in Section 5.4.

5.4 Jet energy scale & calibration

As described in Section 3.2.3, the ATLAS calorimeters are non-compensating. Starting with energy deposits that have been calibrated at the electromagnetic scale, it is therefore necessary to re-scale the energy of topoclusters to account for the lower hadronic response. This Section will provide a basic description of the method used to calculate this **J**et **E**nergy **S**cale (**JES**). The uncertainty on this knowledge is the major contributor to the systematic uncertainty of the final observables of this thesis: details associated with the derivation, application and uncertainty associated with the JES are discussed.

As a starting point, the energy deposits within individual readout cells are recorded at the **E**lectro**M**agnetic (**EM**) scale. The EM scale calibration and its uncertainty are derived from a combination of techniques, including: comparison of electronic pulse signal shapes[4], and measurement of $Z \to ee$ events[5]. The associated systematic uncertainty on this calibration amounts to 1.5% for the electromagnetic energy deposited in the LAr calorimeters, 5% for the energy deposited in the presampler and 3% for the energy deposited in the Tile calorimeters [119].

Currently, the default ATLAS calibration scheme applies corrections as a function of the jet energy and pseudo-rapidity to jets reconstructed at the EM-scale. By comparing reconstructed jet kinematics to that of the corresponding truth-level jets in Monte Carlo simulation, calibration factors are derived that are applied to the EM-scale jets to transform them

[4]Electronic pulse signal shapes from incident particles are compared to measurements taken using test beams of electrons and muon [114–118], and from MC simulation.

[5]For a $Z \to ee$ decay, the invariant mass of the electron pair can be reconstructed to produce a resonant peak at $M_Z = 91.1876 \pm 0.0021$ GeV, with a natural width of $\Gamma_Z(e^+e^-) = 83.984 \pm 0.086$ MeV [8].

to the hadronic scale. The additional energy contributions due to pile-up are corrected-for before the hadronic energy scale is restored. This is achieved using data-derived factors. As a result, the jet energy scale calibration constants are factorised and do not depend on the number of additional interactions in an event. This calibration scheme is known as the EM+JES calibration scheme [120] and currently restores the hadronic jet response in Monte Carlo to within 2%.

The steps for progressing from EM-scale jets to fully calibrated EM+JES jets are shown in Figure 5.1. These steps are then expanded-upon in the following paragraphs.

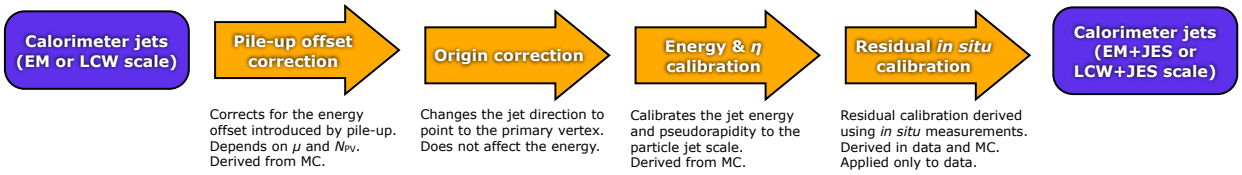

FIGURE 5.1: Overview of the ATLAS jet calibration scheme use for the 2011 dataset. The pile-up, absolute JES and the residual *in situ* corrections calibrate the scale of the jet, while the origin and the η corrections affect the direction of the jet [121].

Offset correction (Pile-up correction) Multiple proton-proton interactions in the same bunch crossing can lead to a situation where a jet can contain energy from more than one interaction. This can lead to a mis-measurement of energy and direction. A correction, derived from minimum bias data, is applied to the transverse energy E_T of jets at the EM-scale,

$$E_T^{\text{corrected}} = E_T^{\text{uncorrected}} - \mathcal{O}(\eta, N_{\text{PV}}, \tau_{\text{bunch}}), \tag{5.2}$$

and is a function of the number of reconstructed primary vertexes N_{PV}, jet pseudo-rapidity η and the spacing between consecutive colliding proton bunches τ_{bunch}. The correction is assumed to be independent of the jet energy, since contributions due to pile-up are uncorrelated with the proton-proton collision producing the jet of interest - this assumption is tested for anti-k_T jets (with $R = 0.6$) in [122]. Further details of the pile-up offsets correction can be found in [122].

Origin correction As explained in Section 5.3, topocluster four-vectors are constructed to point to the geometrical centre of the ATLAS detector. The origin correction moves the direction of each topocluster to point back to the primary vertex[6]. The jet object is redefined as the vector sum of the corrected constituents resulting in a new value of pseudorapidity for

[6]The primary vertex is defined as the vertex with the largest value of the sum of associated track transverse momenta squared ($\sum p_{T,\text{track}}^2$),

the jet, η_{origin}. Note that the origin correction improves the angular resolution whilst leaving the jet energy unaffected.

JES correction The final calibration step uses MC to correct jets to the hadronic scale. Calibration constants are calculated by comparing the kinematics of MC truth jets to the kinematics of the same jets after the full simulation of the ATLAS detector, as outlined in Section 2.4.

Residual in-situ calibration The agreement between data and Monte Carlo is further improved by the application of steps based on in-situ studies [122]. First, the relative response in $|\eta|$ is equalised using an inter-calibration method obtained from balancing the transverse momenta of dijets [123]. Then, the absolute response is brought into closer agreement with Monte Carlo by a combination of various techniques based on momentum balancing method between photons and jets, and between high-momentum jets and a recoil system of low-momentum jets [121]. This completes all stages of the jet calibration.

5.4.1 Jet Cleaning

Jets are classified into three categories [124]: The bad, the ugly and the good.

- Bad: Jets due to either background events or caused by detector effects
- Ugly: Jets in problematic calorimeter regions that are not well measured
- Good: Jets to be used in a physics analysis.

Three sources of bad jets are considered [124]:

- **Electromagnetic coherent noise:** A noise burst in occurring in the electromagnetic (EM) liquid argon (LAr) calorimeter might lead to a "fake" jet. A large fraction of the energy of the resulting jets comes from EM LAr calorimeter input, i.e. f_{LAr}, or bad-quality[7] calorimeter cells., denoted by Q_{LAr} These bad jets in the EM calorimeters are identified by requiring: $f_{LAr} > 0.95$ and $|Q_{LAr}| > 0.8$ and $Q_{LAr}^{mean} > 0.8$ for jets with $|\eta_{\text{em-scale}}| < 2.8$.

[7]The calorimeter quality is a measure of the difference between the measured pulse shape (a_i^{meas}) and the predicted pulse shape (a_i^{pred}) that is used to reconstruct the cell energy. The quality is computed as $\sum_{samples}(a_i^{meas} - a_i^{pred})^2$.

- **Hadronic end-cap spikes:** Most "fake" jets come from sporadic noise bursts in single calorimeter cells in the hadronic end-cap (HEC). The jets typically have a large jet-energy fraction in the HEC, denoted by f_{HEC}. The problematic jets in the HEC are identified by requiring: $f_{HEC} > 0.5$ and $|Q_{HEC}| > 0.5$ and $|Q_{LAr}| > 0.8$; or $|E_{negative}| > 60$ GeV.

- **Non-collision backgrounds and cosmics :** Large amounts of energy can be deposited in the calorimeter outside the nominal timing window for collisions. This is mainly caused by cosmic ray showers or beam backgrounds. To help distinguish these events, we identify f_{max} as the maximum energy fraction in one calorimeter layer, and f_{charge} as the jet charge fraction: the ratio of the sum of the p_T of tracks associated to the jets divided by the calibrated jet p_T. These events are identified by requiring: $f_{LAr} < 0.05$ and $f_{charge} < 0.05$ and $|\eta_{\text{em-scale}}| < 2$; or $f_{EM} < 0.05$ and $|\eta_{\text{em-scale}}| \geq 2$; or $f_{max} > 0.99$ and $|\eta_{\text{em-scale}}| < 2$.

Two sources of ugly jets are considered:

- **Jets extrapolated from masked cells:** Permanently problematic cells and cells affected by high voltage trips are masked during jet reconstruction and their energy is estimated from the surrounding cells. Jets that are built from a large fraction of these masked cells, characterised by an EM energy contribution greater than 50%, are flagged as ugly.

- **Large energy fraction in the tile-gap layers:** The calibration of the scintillator response in the gap between the hadronic tile calorimeter and the end cap is not currently fully understood [124]. Therefore, jets with an energy fraction from this region greater than 50% are labelled as ugly.

The effect of including these cuts on the final analysis can be seen in Table 7.2.

5.5 Jet uncertainties

Uncertainties associated with the energy scale, energy resolution and angular resolution must be considered.

5.5.1 JES uncertainties

The uncertainty on the JES for a given jet is provided by the JESUncertaintyProvider (Version 00-05-10) [121]. The jet energy scale uncertainty is determined for jets with momenta above 15 GeV and $|\eta| < 4.5$, based on the uncertainties of the in-situ techniques and on systematic variations in Monte Carlo simulations. For the most general case, covering all jet measurements made in ATLAS, the correlations among JES uncertainties are described by a set of 59 nuisance parameters. The sources of uncertainty associated with these 59 nuisance parameters, can be assigned to one of four categories: Detector description; Physics modelling; statistics and methodology; and a mix between detector and modelling effects. From the relative η-intercalibration, the dominant uncertainty source is due to MC modelling of jets at forward rapidities, where properties differ for the MC generators considered (Pythia and Herwig) [121].

The fractional JES uncertainties for jets with various p_T and η values is summarised in [121]: a jet of $p_T = 1.5$ TeV carries a fractional JES uncertainty of 3.3% across the η range. This number can be compared to the CDF JES systematic uncertainty, which reaches values of $\sim 3.4\%$ for jet transverse momenta of 500 GeV [125]. The fact that ATLAS has been above to achieve comparable JES uncertainties within two years of operation is an impressive achievement. The DØ collaboration reported a JES uncertainty of $\sim 1.3\%$ for central jets with a transverse momentum of 400 GeV [126]. The impressive DØ JES uncertainty is due to a data-driven absolute calibration - not depending upon a data-to-Monte Carlo comparison of reconstructed physics objects. This allows avoidance of imperfect detector simulation. An absolute calibration has not been employed by LHC experiments mainly because of the difficulties related to the theoretical modelling at a new energy scale, however this situation may change in the future.

Uncertainties due to pile-up, jet flavour, and jet topology are described by five additional nuisance parameters (the uncertainty for jets originating from b quarks excluded). None of these additional effects have an associated uncertainty in excess of 1% in the kinematic range considered [121].

For the high p_T dijet measurements made in the current analysis, the full correlation matrix for the 59 nuisance parameters from the systematic and statistical uncertainties of in-situ techniques is replaced by an equivalent combination of nine nuisance parameters, obtained using a diagonalisation procedure [121]. Together with the pile-up and jet flavour uncertainties, this leads to a total of 14 nuisance parameters to be propagated through the dijet

analysis. Details of the methodology for treatment of these 14 nuisance parameters, and the resulting magnitudes for the effects, is given in Section 7.5.1 of this thesis.

5.5.2 Jet resolution uncertainties

The **J**et **E**nergy **R**esolution (**JER**) is defined as the width of the distribution of the relative difference between the reconstructed energy of a given jet and its truth-level energy. The **J**et **A**ngular **R**esolution (**JAR**) is defined as the width of the corresponding distribution for the difference between reconstructed and truth-level η for a jet. The JER and JAR in 2011 data has been studied thoroughly but so far no result has been available outside of the collaboration. The JER measured with the di-jet balance and the bi-sector techniques [127, 128] in data and Monte Carlo is used to smear jets in the Monte Carlo simulation according to the JER found in data [129]. For a given jet p_T and η, if S is the corresponding JER in MC and U is the corresponding JER uncertainty, the width of a Gaussian from where p_T and energy smearing factors are drawn randomly is:

$$\sigma_{smear} = \sqrt{(S+U)^2 - S^2}. \tag{5.3}$$

The jet energy smearing factors, as a function of jet p_T and the jet angular resolution as a function of η are shown in Figure 5.2. After a steady reduction in the JER smearing factor as a function of p_T, the minima in Figure 5.2(a) corresponds to the range in p_T where the resolution in data and MC have the closest agreement, and therefore the JER uncertainty is at a minimum. Figure 5.2(b) demonstrates an improvement in JAR for jets with larger momentum, and also an improvement in JAR for larger values η.

The isolated single red cell in Figure 5.2(b) (just above 2 TeV) is caused by a single anomalous event, with a low number of events entering that bin.

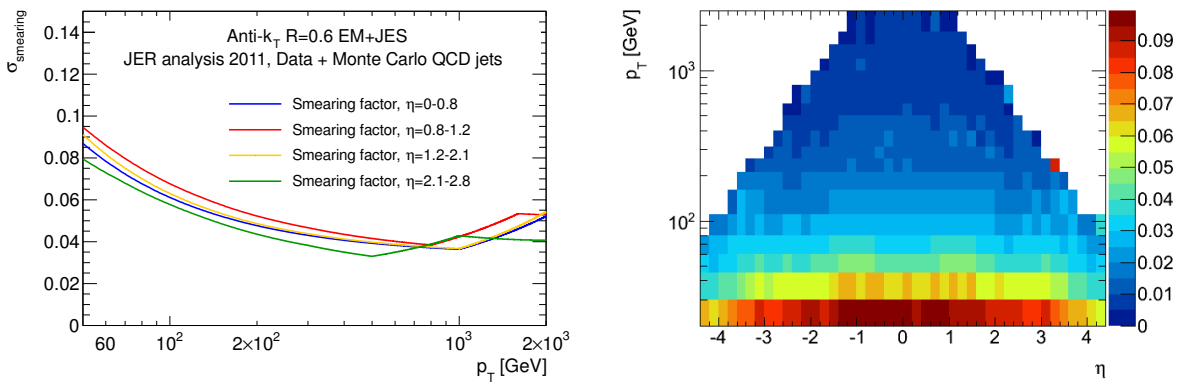

(a) JER (b) JAR

FIGURE 5.2: JER and JAR as function of p_T and η [130].

Chapter 6

Searches for new physics with dijet angular distributions

When two protons collide, the majority of events with large momentum transfer occur when a parton from one hadron scatters from a parton in the other through the exchange of a gluon or a quark. **Q**uantum **C**hromo**d**ynamics (QCD) provides a good description of these $2 \to 2$ processes at high energies. In this chapter, the analysis of proton collisions producing two jets, commonly known as *dijet* events, is discussed.

Beginning with the partonic cross-section for such dijet events in Sections 6.1, methods are then described for disentangling the angular dependence of the partonic-cross-section from the parton distributions functions of the colliding protons (Section 6.2). Thus, it is found that the angular behaviour of dijet events allows the possibility to detect the presence of **N**ew **P**hysics (NP) signals (Section 6.4).

6.1 Leading order dijet production

6.1.1 Parton level kinematics

As a typical parton-parton hard interaction, we consider the sub-process $ab \to cd$, where the initial state partons a and b are contained within the colliding protons A and B - see Figure 6.1.

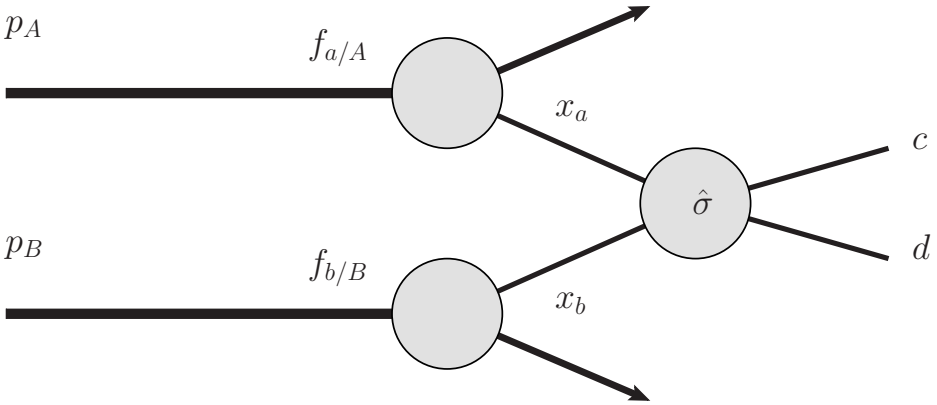

FIGURE 6.1: Partons a and b from hadrons A and B undergo a hard scatter $ab \to cd$ with cross-section $\hat{\sigma}$. The parton momentum densities are $f_{a/A}$ and $f_{b/B}$.

The Lorentz-invariant Mandelstam variables are defined as

$$\hat{s} = (p_a + p_b)^2, \quad \hat{t} = (p_a - p_c)^2, \quad \hat{u} = (p_a - p_d)^2, \tag{6.1}$$

where p_i are the four-momenta of the partons. In the high energy limit, where parton masses can be neglected, the Mandelstam variables can be approximated as

$$\hat{s} \approx 2p_a \cdot p_b, \quad \hat{t} \approx -2p_a \cdot p_c, \quad \hat{u} \approx -2p_a \cdot p_d, \tag{6.2}$$

resulting in the relation $\hat{s} + \hat{u} + \hat{t} = 0$. We can also obtain expressions for $\hat{s}$, $\hat{u}$ and $\hat{t}$ in terms of Centre-of-Mass (CM) frame quantities: letting the initial parton energies $E^* = \sqrt{\hat{s}}/2$ we have that

$$\hat{t} = -\frac{\hat{s}}{2}(1 - \cos\hat{\theta}), \quad \hat{u} = -\frac{\hat{s}}{2}(1 + \cos\hat{\theta}), \tag{6.3}$$

where $\hat{\theta}$ is the CM scattering angle, as defined in Figure 6.2.

If the initial proton four-momenta are P_A and P_A then letting

$$\hat{s} = (p_a + p_b)^2 \approx 2\, p_a \cdot p_b = 2\, x_a x_b\, P_A \cdot P_A, \tag{6.4}$$

where x_a and x_b are the momentum fraction of the initial state protons carried by the interacting partons. In the high energy regime, where we extend the massless approximation to protons (such that $2\, P_A \cdot P_B \approx (P_A + P_B)^2 = s$), we therefore have that

$$\hat{s} = x_a x_b\, s. \tag{6.5}$$

In order to relate theory and experiment, measurable quantities need to be related to kinematic variables in the CM frame. Since we are unable to directly measure quantities such as $\hat{s}$ and the momenta of the initial state partons, we must relate these to the kinematics of the final-state jets. The four-momenta of the initial state patrons can be constructed in terms of the hadron-hadron CM energy $\sqrt{s}$ to give:

$$p_a = \frac{\sqrt{s}}{2}(x_a, 0, 0, x_a) \quad \text{and} \quad p_b = \frac{\sqrt{s}}{2}(x_b, 0, 0, -x_b). \tag{6.6}$$

The four-momenta of the final state partons can be constructed as:

$$p_c = p_T(\cosh y_c, \cos\phi, \sin\phi, \sinh y_c) \quad \text{and} \quad p_d = p_T(\cosh y_d, -\cos\phi, -\sin\phi, \sinh y_d) \tag{6.7}$$

where y_c and y_d are the rapidities[1] of the final state partons, which we assume to be inferable from the rapidities of the final state jets; p_T is the momentum of each of the final-state jets in the transverse $x-y$ plane[2]; and ϕ_c, ϕ_d are the azimuthal angles of the final state partons (as introduced in Section 3.2.1). In these expressions, it is assumed that the initial-state partons carry negligible transverse momentum and parton masses are also still neglected. Employing energy and longitudinal momentum conservation we can combine Equations 6.6 and 6.7 to give:

$$x_a = \frac{p_T}{\sqrt{s}}(e^{y_c} + e^{y_d}) \quad \text{and} \quad x_b = \frac{p_T}{\sqrt{s}}(e^{-y_c} + e^{-y_d}). \tag{6.8}$$

Using the fact that differences in rapidities are invariant under Lorentz transformations, we define

$$y_B(= y_{\text{boost}}) = (y_c + y_d)/2 \quad \text{and} \quad y^* = (y_c - y_d)/2, \tag{6.9}$$

where $\pm y^*$ are the rapidities of the final-state jets in the CM frame, and y_B is the required boost to move between the CM frame and the lab frame. This situation is depicted in Figure 6.2. Combining Equations 6.8 and 6.9, and noting that $\cos\theta^* = \tanh y^*$, one is able to show that

$$x_a = \frac{p_T}{\sqrt{s}} e^{y_B} \cosh y^* \quad \text{and} \quad x_b = \frac{p_T}{\sqrt{s}} e^{-y_B} \cosh y^* \tag{6.10}$$

and therefore

$$\hat{s} = m_{jj}^2 = x_a x_b s = 4p_T^2 \cosh^2 y^*, \tag{6.11}$$

where m_{jj} is the final-state dijet invariant mass.

[1] Rapidity is defined in Section 3.2.1.

[2] Assuming that the initial state patrons carry zero transverse momentum, conservation of momentum leads to the final-state jets having equal and opposite transverse momentum.

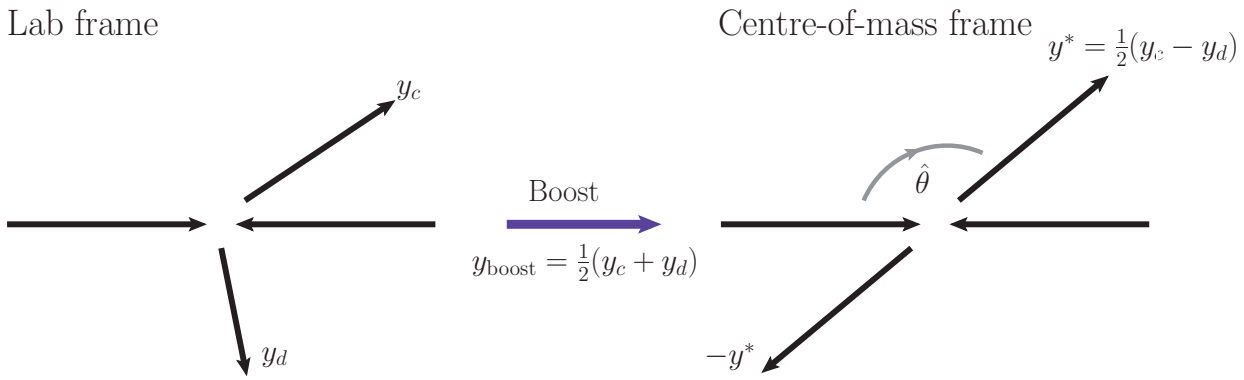

FIGURE 6.2: Schematic of two final-state massless partons in the lab frame (with 4-momenta p_c and p_d) boosted to the centre-of-mass frame giving them equal but opposite rapidities, $\pm y^*$.

6.2 Angular dependence of dijet cross-section

The differential form of the hadron-hadron Master Equation 2.13 for inclusive dijet production can be written as

$$\frac{\mathrm{d}\sigma(AB \to jjX)}{\mathrm{d}\hat{t}} = \sum_{ab} f_{a/A}(x_a, \mu_F^2) f_{b/B}(x_b, \mu_F^2) \frac{\mathrm{d}\hat{\sigma}_{ab\to cd}}{\mathrm{d}\hat{t}}. \tag{6.12}$$

Following the prescription described in Section 2.2.1) of this thesis, the hard scattering cross-section is given by

$$\frac{\mathrm{d}\hat{\sigma}}{\mathrm{d}\hat{t}} = \frac{1}{16\pi\hat{s}^2} \overline{\sum} |\mathcal{M}|^2 \; \delta^4(p_a + p_b - p_c - p_d), \tag{6.13}$$

where $\overline{\sum}$ denotes the average and sum over the initial and final spin states and colour states and $\delta^4(p_a + p_b - p_c - p_d)$ is a Dirac delta function[3] signifying that four-momentum is conserved at the interaction vertex. This calculation has contributions from multiple process: leading-order expressions for $\overline{\sum} |\mathcal{M}|^2 / (4\pi\alpha_s)^2$, together with their value at a centre-of-mass scattering angle $\theta^* = \pi/2$ ($\hat{t} = \hat{u} = -\hat{s}/2$) are shown in Table 6.1. Figure 6.3 shows some of the leading-order diagrams contributing to the dijet production cross-section (the other diagrams are obtained by crossing).

Taking the process $qq' \to qq'$ as an example, the matrix element squared (from Table 6.1) is of the form $\alpha_s^2 \frac{\hat{s}^2 + \hat{u}^2}{\hat{t}^2}$. Using the fact that $|\hat{t}| < \hat{s}$ and $|\hat{u}| < \hat{s}$, it follows that:

$$\frac{\hat{s}^2}{\hat{t}^2} < \frac{\hat{s}^2 + \hat{u}^2}{\hat{t}^2} < \frac{2\hat{s}^2}{\hat{t}^2}, \tag{6.14}$$

[3]For a Dirac delta function $\delta(x)$, $\int_{-\infty}^{+\infty} \delta(x)\, \mathrm{d}x = 1$ and $\int_{-\infty}^{+\infty} f(x)\delta(x-a)\, \mathrm{d}x = f(a)$.

Process	$\overline{\sum}\lvert\mathcal{M}\rvert^2/(4\pi\alpha_s)^2 = \frac{\hat{s}}{\pi\alpha_s^2}\frac{\mathrm{d}\hat{\sigma}}{\mathrm{d}\hat{t}}$	$\hat{\theta}=\pi/2$
$qq' \to qq'$	$\frac{2C_F^2}{N_g}\frac{\hat{s}^2+\hat{u}^2}{\hat{t}^2}$	2.22
$q\bar{q}' \to q\bar{q}'$	$\frac{2C_F^2}{N_g}\frac{\hat{s}^2+\hat{u}^2}{\hat{t}^2}$	2.22
$qq \to qq$	$\frac{2C_F^2}{N_g}\left(\frac{\hat{s}^2+\hat{u}^2}{\hat{t}^2}+\frac{\hat{s}^2+\hat{t}^2}{\hat{u}^2}\right)-\frac{8}{27}\frac{\hat{s}^2}{\hat{u}\hat{t}}$	3.26
$q\bar{q} \to q'\bar{q}'$	$\frac{2C_F^2}{N_g}\frac{\hat{t}^2+\hat{u}^2}{\hat{s}^2}$	0.22
$q\bar{q} \to q\bar{q}$	$\frac{2C_F^2}{N_g}\left(\frac{\hat{s}^2+\hat{u}^2}{\hat{t}^2}+\frac{\hat{t}^2+\hat{u}^2}{\hat{s}^2}\right)-\frac{8}{27}\frac{\hat{u}^2}{\hat{s}\hat{t}}$	2.59
$q\bar{q} \to gg$	$\frac{2C_FC_A}{3}\left(\frac{4}{9}\frac{\hat{t}^2+\hat{u}^2}{\hat{t}\hat{u}}-\frac{\hat{t}^2+\hat{u}^2}{\hat{s}^2}\right)$	1.04
$gg \to q\bar{q}$	$\frac{6C_FC_A}{N_g^2}\left(\frac{4}{9}\frac{\hat{t}^2+\hat{u}^2}{\hat{t}\hat{u}}-\frac{\hat{t}^2+\hat{u}^2}{\hat{s}^2}\right)$	0.15
$gq \to gq$	$\frac{2C_FC_A}{N_g}\left(-\frac{4}{9}\frac{\hat{s}^2+\hat{u}^2}{\hat{s}\hat{u}}+\frac{\hat{u}^2+\hat{s}^2}{\hat{t}^2}\right)$	6.11
$gg \to gg$	$\frac{4C_A^2}{N_g}\left(3-\frac{\hat{t}\hat{u}}{\hat{s}^2}-\frac{\hat{s}\hat{u}}{\hat{t}^2}-\frac{\hat{s}\hat{t}}{\hat{u}^2}\right)$	30.4

TABLE 6.1: The invariant matrix elements squared $\overline{\sum}\lvert\mathcal{M}\rvert^2$ for $2 \to 2$ parton sub-processes with massless partons, and their corresponding values for $\hat{\theta} = \pi/2$. The colour and spin indices are averaged (summed) over initial (final) states. The factors C_F, C_A and N_g are the QCD colour factors (see [131, 132] for further descriptions) and carry values of 4/3, 3 and 8, respectively.

and thus, in a good approximation, $\frac{\hat{s}^2+\hat{u}^2}{\hat{t}^2} \approx \frac{\hat{s}^2}{\hat{t}^2}$. For the other t-channel processes[4], where $\hat{t} \to 0$ (i.e. for small scattering angles when the t-channel gluon exchanges are dominating) it can be shown that there is a similar behaviour for the matrix elements squared. In conclusion, we find that the partonic cross-section is approximately inversely proportional to $\hat{t}^2$:

$$\frac{\mathrm{d}\hat{\sigma}}{\mathrm{d}\hat{t}} \propto \frac{\alpha_s^2}{\hat{t}^2}. \tag{6.15}$$

It is noted that re-writing Equation 6.15 in terms of $\hat{\theta}$ reveals the usual Rutherford scattering behaviour, typical of all t-channel exchange of massless vector bosons (gluons and photons):

$$\frac{\mathrm{d}\hat{\sigma}}{\mathrm{d}(\cos\hat{\theta})} \propto \sin^{-4}(\hat{\theta}/2). \tag{6.16}$$

We define

$$\chi = \exp(y_c - y_d) = \exp(2y^*), \tag{6.17}$$

[4]Note that interactions of the form $q\bar{q} \to q'\bar{q}'$, $q\bar{q} \to gg$ and $gg \to q\bar{q}$ can only take place via an s-channel process. The angular behaviour of these processes, which have the smallest contribution of all processes (see Table 6.1), will therefore not display the same angular characteristics.

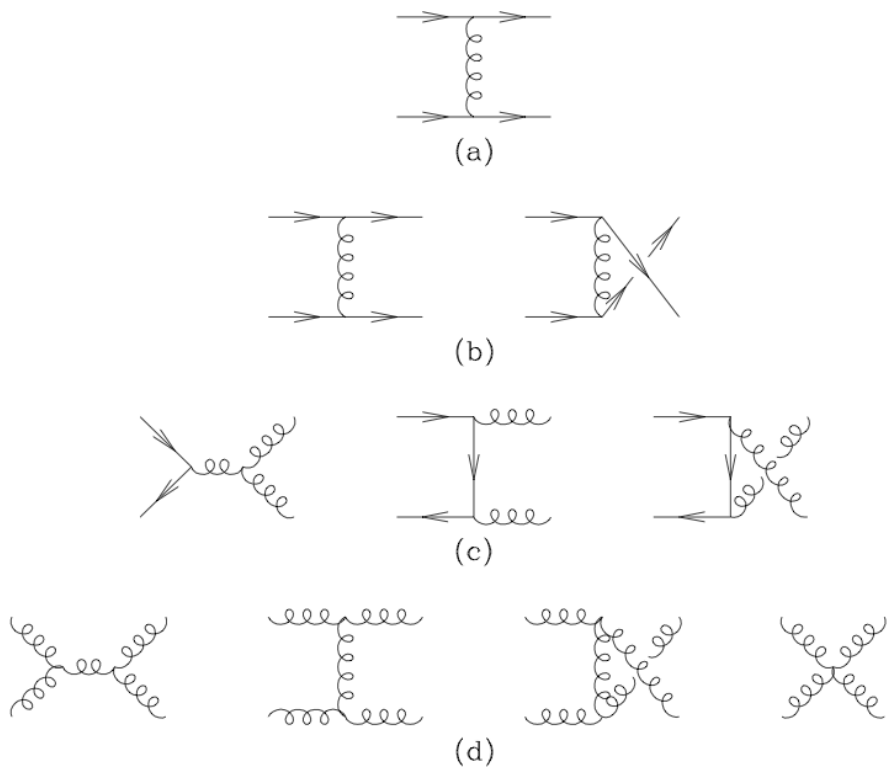

FIGURE 6.3: Some of the diagrams of dijet production [132] (the other diagrams can be obtained by crossing). The distinction is made between identical (rows (b), (c) and (d)) and non-identical final-state patrons.

from which, using $\tanh y^* = \cos\hat{\theta}$, it can be shown:

$$\chi = \frac{1+\cos\hat{\theta}}{1-\cos\hat{\theta}}. \tag{6.18}$$

Since we do not experimentally distinguish between partons in the final state, it is appropriate to symmetrise over $\hat{t}$ and $\hat{u}$ in each of the partonic cross-sections in Table 6.1: this is achieved by adding terms of the form $\hat{t} \leftrightarrow \hat{u}$,[5] and therefore now write[6]:

$$\chi = \frac{1+|\cos\hat{\theta}|}{1-|\cos\hat{\theta}|}. \tag{6.19}$$

It is noted that one may use the definition of χ to write:

$$\sqrt{s} = m_{jj} = 2p_T\cosh(\ln(\chi)/2) = p_T\left(\sqrt{\chi}+\frac{1}{\sqrt{\chi}}\right) \tag{6.20}$$

[5]For a function of two variables $f(x,y)$, adding a term of the form $x \leftrightarrow y$ denotes adding a term of the form of $f(y,x)$, where the y and x variable have swapped places.

[6]Alternatively, the symmetrisation over final states can be motivated by the fact that we collide protons, and the experiment in therefore symmetric along the beam line, at the proton level.

From this expression one can see that for a fixed $\sqrt{s}$, low values of χ correspond to high values of p_T, and vice versa.

To a good approximation,

$$\chi = \frac{1 + |\cos\hat{\theta}|}{1 - |\cos\hat{\theta}|} \sim \frac{1}{1 - |\cos\hat{\theta}|} \propto \frac{\hat{s}}{\hat{t}}. \tag{6.21}$$

Therefore, if one holds $\hat{s}$ fixed, we can re-write Equation 6.15 as:

$$\frac{\mathrm{d}\hat{\sigma}}{\mathrm{d}\chi} \propto \frac{\alpha_s^2}{\hat{s}} \quad \text{(for } \hat{s} \text{ fixed)}. \tag{6.22}$$

It is therefore predicted that $d\sigma/d\chi$ should be approximately flat, as a function of χ, for a restricted range in $\hat{s} = m_{jj}$.

Alternatively, one can note that Equation 6.16 can be rewritten as

$$\frac{\mathrm{d}\hat{\sigma}}{\mathrm{d}(\cos\hat{\theta})} \propto \frac{1}{(1 - \cos\hat{\theta})^2}. \tag{6.23}$$

Therefore, noticing that

$$\frac{\mathrm{d}\hat{\sigma}}{\mathrm{d}\chi} \propto (1 - \cos\hat{\theta})^2 \frac{\mathrm{d}\hat{\sigma}}{\mathrm{d}(\cos\hat{\theta})}, \tag{6.24}$$

it can be seen that $\mathrm{d}\hat{\sigma}/\mathrm{d}\chi$ is expected to be constant. This has been observed experimentally in previous hadron collider experiments [133].

An isotropic angular distribution would be described by a constant value for $\mathrm{d}\hat{\sigma}/\mathrm{d}(\cos\hat{\theta})$. Using Equation 6.19, we see that this would result in a a distribution of the form:

$$\frac{\mathrm{d}\hat{\sigma}}{\mathrm{d}\chi} \propto \frac{1}{(\chi + 1)^2}, \tag{6.25}$$

and a cross-section in χ that is peaked at low χ values.

The difference in the χ behaviour for t-channel gluon exchange processes (such as dominant SM QCD processes), and an s-channel process with isotropic angular distribution makes χ an attractive variable for NP searches. This idea is further-developed in Section 6.4.

6.3 Maximising sensitivity to the partonic cross-section

Re-writing the total cross-section as a function of χ (and summing over all partonic contributions):

$$\frac{\mathrm{d}\sigma}{\mathrm{d}\chi} = \sum_{i,j} \int \mathrm{d}x_a \mathrm{d}x_b f_i(x_a, \mu_F^2) f_j(x_b, \mu_F^2) \frac{\mathrm{d}\hat{\sigma}_{ij}(\mu_R^2, \mu_F^2)}{\mathrm{d}\chi}, \tag{6.26}$$

and noting that (at LO) $y_B = \frac{1}{2} \ln\left(\frac{x_a}{x_b}\right)$, we see that by looking at dijet events with a particular value of y_B, and also a particular value of $m_{jj} = \hat{s} = x_a x_b s$, the values of x_a and x_b are constrained and dependency of the PDF convolution is removed.

In order to study the partonic cross-section, it is therefore desirable to make measurements at constant values of y_B, however this is not realistic, since there are generally an insufficient number of events at individual values of y_B. Therefore, a compromise must be held between opening up a range in y_B, and therefore increasing the statistics of the sample, and opening up sensitivity to the PDF. A kinematic cut on y_B, when coupled with the experimental limitation of only being able to measurable up to a finite value of y_{max}, also leads to a restriction on the largest value of χ that can be measured:

$$\begin{aligned} |y_1 + y_2| &< c, \\ |y_1 - y_2| &< 2y_{max} - c, \end{aligned} \tag{6.27}$$

where $\chi_{max} = \exp(2y_{max} - c)$ and the parameter c is chosen as a compromise between statistics, PDF sensitivity and the measurable range in χ. Figure 6.4 depicts the region of the angular phase space that is selected using these cuts.

We proceed by first choosing a value of χ_{max} and a value of y_{max}. The effect including a cut on y_B is then demonstrated and its value is determined by choosing a value of c in Equation 6.27 which implies the required values of χ_{max} and y_{max}.

At very large y^*, every NP model under consideration is expected to approach QCD. It is therefore required to choose χ (and therefore y^*) only so large as to contain all of the signal of the NP models under study. However, it is also desired to limit the range in χ in order to ensure sufficient statistics across the full χ range. Furthermore, by limiting the minimum jet p_T (through a upper restriction on χ), for a given dijet mass range, it is possible to take advantage of the higher luminosity recorded by triggers with a higher jet momentum threshold. Figure 6.5 shows χ distributions[7] for two of the NP hypotheses considered in this

[7]NOTE: these distributions are not normalised. The binning for these distributions is motivated in Appendix A.

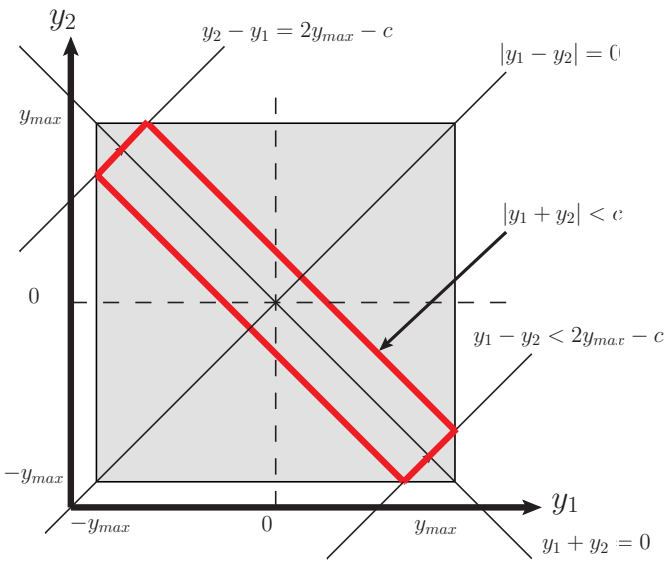

FIGURE 6.4: Rapidity range of a generic detector, before (grey square) and after (red rectangle) applying selection cuts in Equation 6.27.

thesis, including PYTHIA NLO QCD as the dominant background[8]. The dijet mass range contained in this figure represents the search region for this thesis: the motivation for which is described in Section 7.2.2.

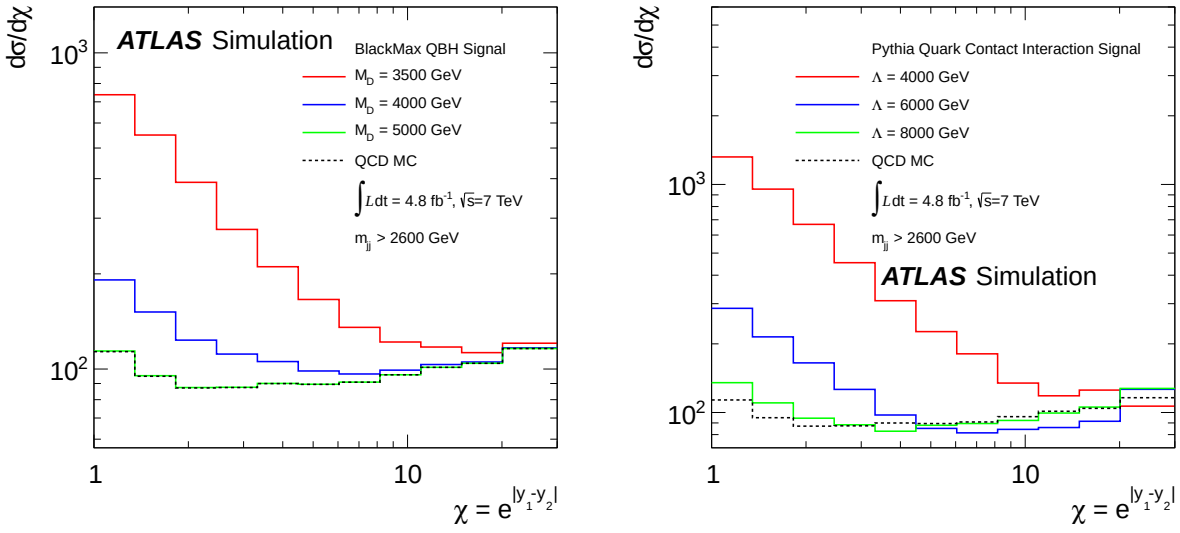

(a) QBH signal

(b) Quark Contact Interaction Signal

FIGURE 6.5: $d\sigma/d\chi$ distributions for the (a) QBH and (b) quark contact interaction signals. For the QBH signal, distributions are shown for $M_D = 3.5, 4, 5$ TeV, whilst for the quark contact interactions, distributions for $\Lambda = 4, 6, 8$ TeV are shown. Each figure also includes NLO Pythia QCD as the dominant SM background process. Dijet events are chosen with $m_{jj} > 2600$ GeV, $y_B < 1.1$ and $\chi < 30$.

[8]A more complete description of the NLO Pythia QCD background is given in Sections 2.4 and 7.3.

Previous ATLAS dijet analysis limits[9] [15] on M_D and Λ, with 36 pb^{-1} of integrated luminosity, are 3.67 TeV and 5.2 TeV. From Figure 6.5 it can be seen that the signal samples corresponding to $M_D = 3.5$ TeV and $\Lambda = 4$ TeV are predominantly contained within the plotted χ range, and therefore the signal strength for which this higher-luminosity analysis is most sensitive will also be contained within $\chi < 30$. A value of $\chi_{max} = 30$ (and a corresponding value of $|y^*| < 1.7$) is therefore used in this analysis.

Motivated by detector and trigger performance in previous analyses, it was decided by the analysis team to only consider jets with $y < 2.8$. This decision is motivated by two main factors: confidence in the JES and its uncertainty across the extended rapidity range, and the desire to not consider triggers that operate in the forward region. In future studies, it should be possible to take further advantage of the full ATLAS geometry.

The above restrictions on χ_{max} and y_{max} are consistent with a value of $c = 2.2$.

As discussed above, there is a theoretical motivation for also including a restriction on the value of y_B. The effect of including this cut is shown in Figure 6.6. For selections including a cut on y_B, the distributions are more flat than without - with the effect being significantly more pronounced at lower dijet masses. This is expected, since even without applying an explicit cut on y_B, there is an implied constraint coming from the dijet mass. From $m^2_{jj,\min} < m^2_{jj} = x_1 x_2\, s < m^2_{jj,\max}$, we find that

$$\frac{1}{x_1}\frac{m^2_{jj,\min}}{s} < x_2. \tag{6.28}$$

In the extreme case of $x_1 = 1$, we have

$$y_B < \frac{1}{2}\ln\left(\frac{s}{m^2_{jj,\min}}\right) = \ln\left(\frac{\sqrt{s}}{m_{jj,\min}}\right). \tag{6.29}$$

This shows that a minimum dijet mass causes an upper value for y_B, which decreases with $m_{jj,\min}$, e.g. for $m_{jj,\min} = 1$ TeV: $y_B < 1.95$.

Moving forward, a value of $c = 2.2$ is chosen such that, when combined with an $y_{max} = 2.8$, Equation 6.27 leads to restrictions of $y_B < 1.1$, $y^* < 1.7$ and $\chi_{max} = 29.9641$.

[9] Here the most conservative expected limits from [15] is quoted.

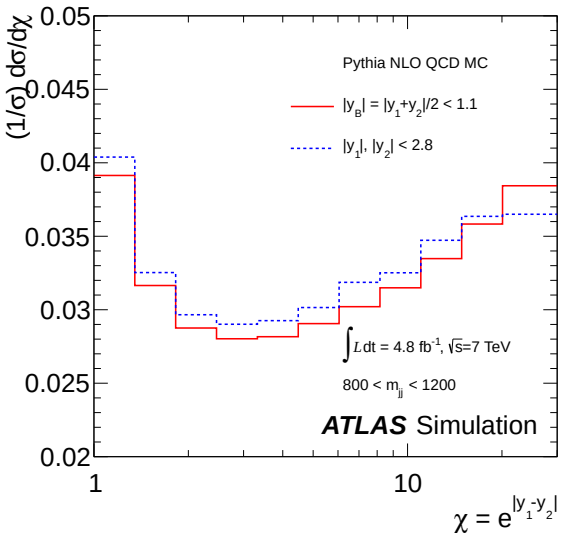

(a)

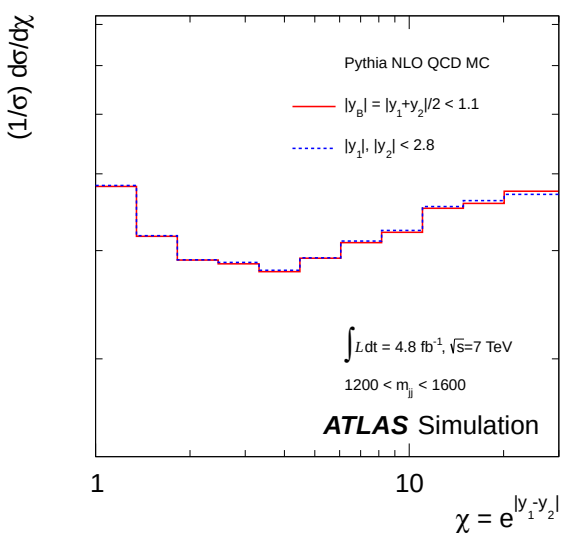

(b)

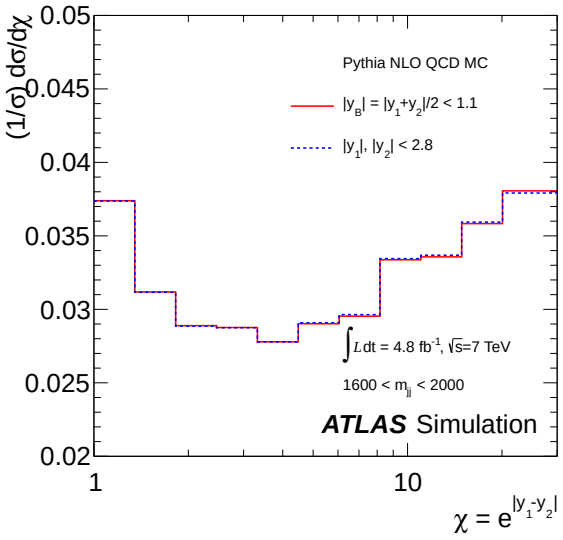

(c)

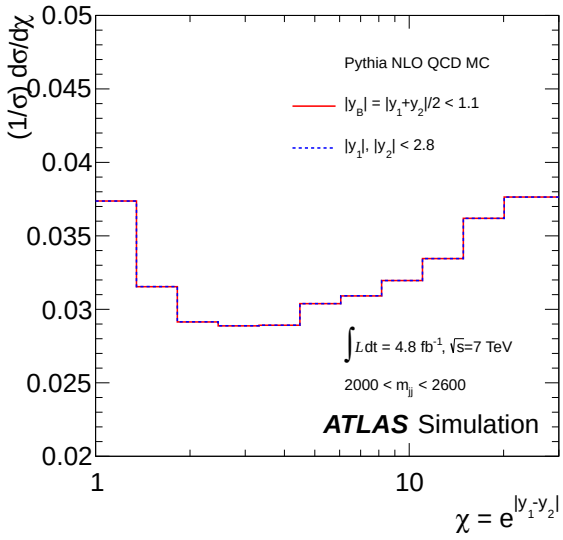

(d)

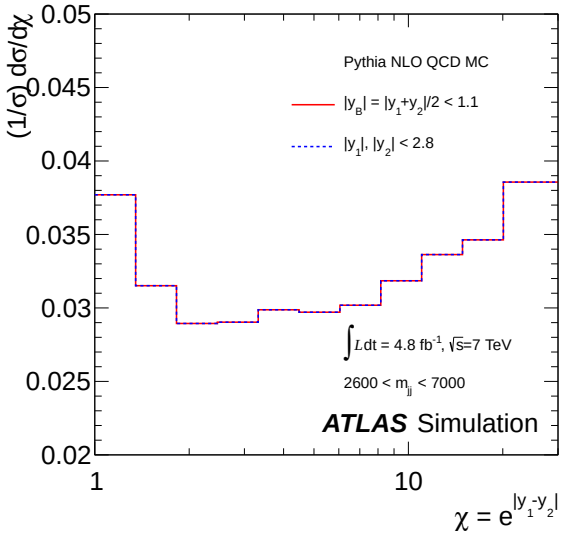

(e)

FIGURE 6.6: Normalised χ distributions to demonstrate effect of including y_B cut.

6.4 Experimental observables for NP searches

The most obvious way to search for evidence of a new particle or resonance is to look for a feature in the invariant mass of the dijet system. However, this thesis has demonstrated that there is also a lot of angular information available to further distinguish between QCD and a new physical process. Figure 6.7 demonstrates the clear difference in angular distributions predicted by QCD and a resonant NP signal due to an excited quark[10] with mass of 1 TeV. Figure 6.7 (a) shows the distribution of QCD dijet events in the angular phase space, parametrised by η_1 and η_2[11], generated by the PYTHIA MC generator. There is a clear trend for events to contain jets with large (and opposite) values of η. In contrast, the distribution shown in Figure 6.7 (b), corresponding to an isotropic NP process, has a large number of central ($\eta_{1,2} \approx 0$) events.

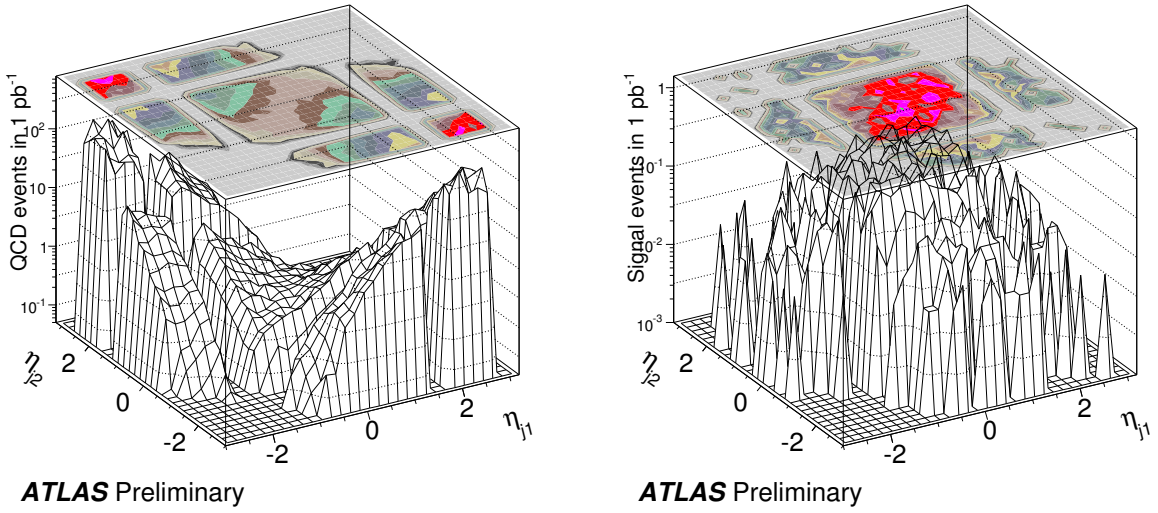

(a) (b)

FIGURE 6.7: Surface plot describing the expected distribution of event yields in the observables η_{j_1} and η_{j_2} for dijets with $875 \leq m^{jj} \leq 1020$ GeV. (a) Shows the distribution predicted by Pythia QCD MC and (b) shows the distribution predicted by a 1 TeV q^* Excited Quark, also generated using Pythia. Figures are taken from [134].

As described in Section 6.2, the angular phase-space of the system is constrained by placing cuts on $y_B = (y_1 + y_2)/2$ and $y^* = (y_1 - y_2)/2$. To compliment this angular information, the most appropriate observable for investigating the energy and momentum of the system is the dijet invariant mass $m_{jj} = \sqrt{(p_1 + p_2)^2}$, where p_i is the four-momentum of the i^{th}-leading jet. A critical step in the formation of dijet mass and angular distributions is to limit the

[10] The excited quark model is an example of a NP process for which the main analysis of this thesis is sensitive. It is introduced in Section 4.3.1.

[11] η_1 is the pseudo rapidity of the leading jet and η_2 is the pseudo rapidity of the sub-leading jet.

phase space to regions where signals associated with NP are most likely to appear. The phase space covered in the current studies is determined by rapidity selection applied to the leading jets and their combined dijet mass.

6.4.1 Slicing the dijet phase space

For a given value of y_B, the kinematic phase space of the dijet system can be parametrised by χ and m_{jj}. The aim of this analysis is therefore to compare the observed $\chi - m_{jj}$ distribution with the predicted distribution from QCD MC. In principle, one could consider one 2-dimensional distribution finely binned in χ and in m_{jj}, but the collision event statistics are insufficient for this to be practical, particularly at the highest dijet masses where new phenomena would be expect to appear. The two-dimensional phase-space is therefore sliced in two ways:

- Large slices in m_{jj} and small slices in χ,
- Small slices in m_{jj} and large slices in χ.

Whilst the first method provides greater sensitivity to the angular behaviour, the second method is more sensitive to the case of a NP signal with the form of a narrow resonance.

For the first method, distributions of $\mathrm{d}\sigma/\mathrm{d}\chi$ are plotted for large ranges of dijet mass. For example, in a recent ATLAS dijet publication [15], mass ranges of $520 < m_{jj} < 800$ GeV, $800 < m_{jj} < 1200$ GeV, $1200 < m_{jj} < 1600$ GeV, $1600 < m_{jj} < 2000$ GeV and $m_{jj} > 2000$ GeV were used. These mass ranges, and the mass ranges used in this thesis, are motivated by the performance of the single jet triggers available (see Section 7.2.2 for a further description). The resulting χ distributions are normalised in order to reduce sensitivity to systematic uncertainties[12].

For the second method, a new[13] variable is introduced: F_χ is the fraction of dijets produced centrally versus the total number of observed dijets for a specified dijet mass range. This

[12]Normalisation of the distribution eliminates sensitivity to the luminosity uncertainty of the data, and also reduces sensitivity to other systematic uncertainties. A full discussion is included in Section 7.4 and Section 7.5.1.

[13]This variable was used for the first time in [15].

definition is extended to a measure that is finely binned in dijet mass intervals:

$$F_\chi([m_{jj}^{min} + m_{jj}^{max}]/2) = \frac{N_{events}(\chi < \chi_{inner}, m_{jj}^{min}, m_{jj}^{max})}{N_{events}(\chi < 30, m_{jj}^{min}, m_{jj}^{max})} \quad (6.30)$$

$$= \frac{N_{events}(|y^*| < |y^*_{inner}|, m_{jj}^{min}, m_{jj}^{max})}{N_{events}(|y^*| < 1.7, m_{jj}^{min}, m_{jj}^{max})}, \quad (6.31)$$

where N_{events} is the number of candidate events with in the χ (or y^*) interval and in the specified m_{jj} range. From this point forward, the variable will be referred to as $F_\chi(m_{jj})$. The interval $\chi < \chi_{inner}$ ($|y^*| < |y^*_{inner}|$) defines the *central region*, where we expect to be most sensitive to new physics, while $\chi < 30$ ($|y^*| < 1.7$) extends the angular range to where QCD processes dominate. Determination of a value for χ_{inner} and y^*_{inner} is explained in Section 6.4.2.

As explained in Section 6.2, Equation 6.22 demonstrates that for a fixed value of $\hat{s}$, and therefore a fixed value of m_{jj}, the χ distribution for QCD is expected to be flat. It is therefore expected that the fraction of QCD events with low χ (and therefore $F_\chi(m_{jj})$) will remain constant, when finely binned in m_{jj}. This result is demonstrated in Figure 6.9.

New phenomena that are localised near a given dijet mass would typically show up as bumps ("resonances") above background in the $F_\chi(m_{jj})$ distributions, with the latter being due to signal events being more isotropic than the QCD background. The same excess of central scatters could conceivably be detected above background in one χ distribution as an excess at low χ, providing that the signal is large enough. The $F_\chi(m_{jj})$ distribution can also map the mass dependence of slow-onset phenomena, such as quark contact interactions from sensitivity to the appearance of greater centrality in the angular distributions. The χ distributions give up some resolution in m_{jj} in order to achieve a high precision measurement of the changing shape of the angular distribution as m_{jj} rises.

Normalised χ and $F_\chi(m_{jj})$ distributions are shown in Figures 6.8 and Figures 6.9, for the NP signals introduced in Chapter 4. For the $F_\chi(m_{jj})$ distributions in Figure 6.9, a value of $\chi_{inner} = 3.32$ ($|y^*| < 0.6$) has been chosen. In the figures, a clear difference can be seen between the QCD background and the NP signals - where the difference reduces at the value of the each of the model parameters increases. This effect is in-line with the discussions of Chapter 4, where we reasoned that, due to the limited partonic collision energy, the production cross-section for each of the NP processes would reduce as the resonance mass or threshold mass increased.

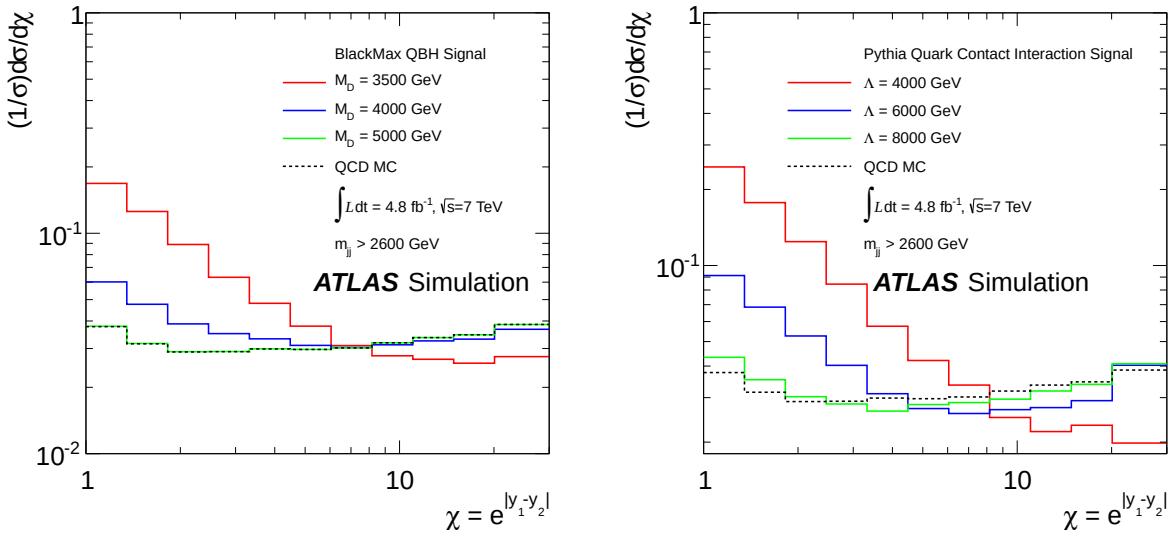

(a) QBH signal

(b) Quark Contact Interaction Signal

FIGURE 6.8: Normalised $\mathrm{d}\sigma/\mathrm{d}\chi$ distributions for the (a) QBH and (b) quark contact interaction signals. For the QBH signal, distributions are shown for $M_D = 3.5, 4, 5$ TeV, whilst for the quark contact interactions, distributions for $\Lambda = 4, 6, 8$ TeV are shown. Each figure also includes NLO Pythia QCD as the dominant SM background process.

6.4.2 Defining the inner and outer regions for $F_\chi(m_{jj})$

The optimal value of χ_{inner} (y^*_{inner}), which corresponds to the numerator of $F_\chi(m_{jj})$, is determined as the value that results in the largest expected limit[14] for the excited quark and quantum black hole models, as introduced in Chapter 4. This choice is therefore not dependent upon the observed data, as required for a totally unbiased result.

The expected limits for various values of y^*, corresponding to the first 3, 4, 5 and 6 bins in the χ distribution are shown in Table 6.2. The precision of these limits has been estimated by calculating 20 independent limits, using a different random seed. The limits for each model are vary by as much as 40 GeV. Whilst the results for $y^* < 0.75$ show a small increase in sensitivity, the values for all choices of y^* are consistent within the estimated precision. Based upon these results, we retain the definition of F_χ used in the previous publication using $F_\chi(m_{jj})$ [15]: $y^* < 0.6$.

[14]The concept of an expected limit was first introduced in Section 1.1 and is discussed in detail in Section 8.2.

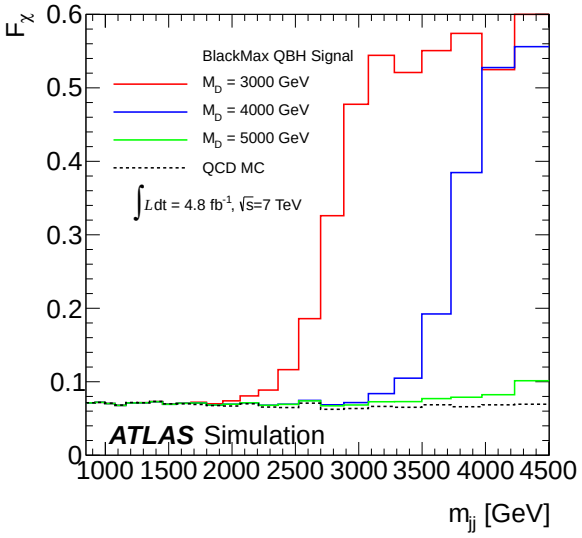

(a) QBH signal

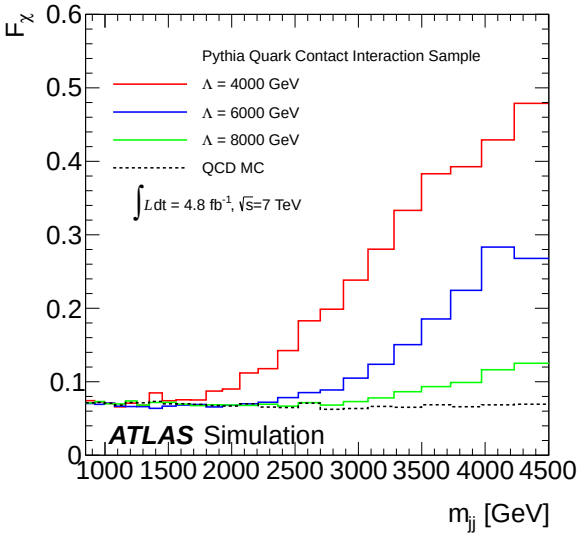

(b) Quark Contact Interaction Signal

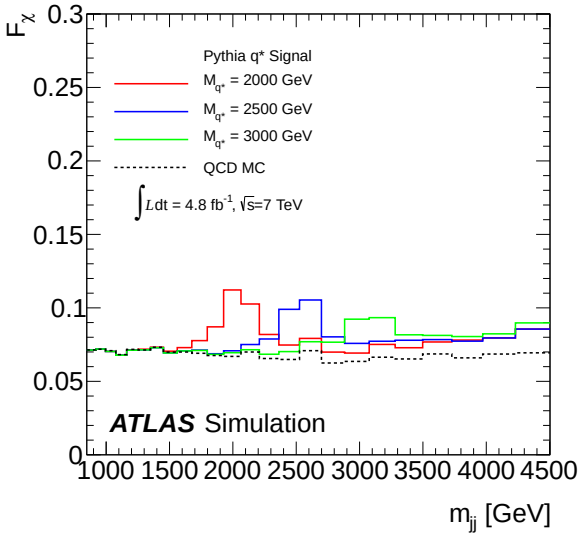

(c) Excited Quark Signal

FIGURE 6.9: $F_\chi(m_{jj})$ distributions for the (a) QBH, (b) quark contact interaction and (c) excited quark signals. For the QBH signal, distributions are shown for $M_D = 3, 4, 5$ TeV; for the quark contact interactions, distributions for $\Lambda = 4, 6, 8$ TeV are shown; and for excited quarks, distributions for $m_{q^*} = 2, 2.5, 3$ TeV are shown.

Model	$y^* < 0.45$	$y^* < 0.6$	$y^* < 0.75$	$y^* < 0.9$
QBH ($n = 6$)	4.15 TeV	4.16 TeV	4.19 TeV	4.17 TeV
Q^*	2.92 TeV	2.95 TeV	2.96 TeV	2.94 TeV

TABLE 6.2: Comparison of expected limits calculated using different definitions for the numerator of F_χ.

6.5 Definition of control regions

As discussed in Section 1.1 of this thesis, in a search for new physics it is important to define a control region and a search region.

The search region for the χ and $F_\chi(m_{jj})$ analyses will aim to increase sensitivity to the highest invariant masses possible, whilst ensuring sufficient events to draw a significant quantitative conclusion. The control region will be used in order to validate the MC background simulation provided by PYTHIA: no normalisation or extrapolation into the search region is required. In the control region, distributions of m_{jj}, $p_T^{1,2}$, $y_{1,2}$, $\phi_{1,2}$, y^*, y^B, and N_{jet} will be compared for data and LO PYTHIA QCD. The results of these comparisons are presented in Section 7.9.

The motivation and definition of these regions is determined by the limitations of the experiment (most notably the trigger) and will be discussed in Section 7.2.3.

Furthermore, for the χ distributions, the lower broad dijet mass bins can also be used as a control region. Given that these distributions will be produced with NLO QCD MC and will include all relevant systematic uncertainties, they allow a more quantitative assessment of the agreement with data. The method for quantifying agreement between data and MC in the χ distributions will be discussed in detail in Chapter 8.

Chapter 7

Event selection, systematic uncertainties and resulting distributions

Building upon the theoretical and experimental foundations of previous chapters, this chapter will discuss the analysis strategy and its results, with full consideration for the associated experimental and theoretical uncertainties. The motivation for event selection criteria is formed from a combination of sensitivity to New Physics, fiducial experimental constraints and limitations of detector performance.

Details of the systematic uncertainties arising from Jet Energy Scale and Resolution are described in Section 7.5.1. The corresponding theoretical systematic uncertainties for the QCD background description are described in Section 7.4. Additional possible uncertainty considerations due to the experimental conditions of Pile-up (Section 7.7) and detector malfunction (Section 7.8) are given at the end of the chapter.

Final distributions for this analysis are shown in Figure 7.10 and their statistical interpretation is described in Chapter 8.

7.1 Event selection

In this section, the motivation and details for the analysis event selection is given. Each of the selection criteria is outlined below, with a summary of the resulting number of events after each cut summarised in Table 7.2. The initial number of events under consideration

corresponds to the number of events passing *any* calorimeter related trigger (after prescale), with a reconstructed dijet mass of > 700 GeV.

B: Trigger Selection - This analysis employs single jet triggers in order to select events containing a pair of jets with a high dijet invariant mass. It is therefore essential to find the dijet mass above which a given single jet trigger is able to efficiently select the majority of such events. Details of jet efficiency measurement are given in Appendix C. To avoid bias from varying on-line trigger efficiency, events are required to pass a trigger in a region where that trigger is $> 99\%$ efficient. If an event passes a given trigger below the trigger's plateau region, that particular trigger is ignored. The event may be accepted if it passes a looser trigger that is 99% efficient.

The point at which the efficiency of each trigger reaches 99% is included in Table 7.1, as well as the threshold including an additional 5% buffer[1].

TABLE 7.1: Values of m_{jj} for which single-jet triggers become 99% efficient. After including a 5% buffer, the bin boundaries are determined that for the lower edge of the plateau region for this analysis.

Trigger	m_{jj} for 99% eff. [GeV]	+5% buffer [GeV]
EF-j75-a4tc-EFFS	600	630
EF-j100-a4tc-EFFS	780	819
EF-j135-a4tc-EFFS	1000	1050
EF-j180-a4tc-EFFS	1330	1396
EF-j240-a4tc-EFFS	1680	1764

The trigger names in Table 7.1 can be broken down into 3 parts: EF and $EFFS$ (Event Filter Full Scan) signify that the trigger uses all three of the trigger levels (L1, L2 and EF); jXXX, where XXX is the threshold in GeV where the trigger starts triggering (at the EM scale); $a4tc$ signifies that a full calorimeter scan of the L1 trigger towers is done using Anti-k_T $R = 0.4$ for jet finding.

If a trigger is unable to make a decision about an event in the allocated amount of time, then this event is placed in a separate *debug stream*. These debug stream events are then reprocessed offline. Events may also be placed in the debug stream if they cause an error or crash in the on-line trigger system. Details of a debug stream analysis performed in early 2010 data are discussed in Appendix D. For the dataset analysed in this thesis (corresponding to data recorded in 2011), no events passing the event selection used in this analysis were placed into the debug stream.

[1] A 5% buffer is included as a precaution to ensure that the analysis is using a trigger when it is maximally efficient. 5% was deemed to be a suitable compromise between retaining the maximum number of events and being cautious of the trigger efficiency.

C: GoodRunsList selection - Events are only considered if they fall into a luminosity block contained within a centrally produced GoodRunsList. Luminosity blocks and GoodRunsLists are both discussed in Section 10.2. Briefly, a luminosity block is a period in time, usually lasting a few minutes, for which the instantaneous luminosity is approximately constant, and a GoodRunsList [135] is a list of luminosity blocks, which have been deemed suitable for a physics analysis. Criteria include stable proton beams from the LHC, detector component temperatures, magnetic field strengths and detector status.

D: Vertex selection - Events are required to have a primary collision vertex defined by two or more charged particle tracks. In the presence of pile-up, the primary collision vertex is the one with the largest scalar sum of p_T^2 for associated tracks, which insures that the highest p_T jets, used to reconstruct the dijet, have been associated with the correct collision vertex.

E: LAr error cut - Events are rejected if the data from the liquid argon calorimeter have an unusual topology[2] or there is evidence of data corruption [136].

F: Check for number of jets - There must be at least two jets within $|y| < 4.4$ in the event, and all jets with $|y| \geq 4.4$ are discarded. The highest p_{T} jet is referred to as the "leading" jet (j_1), and the second highest, as the "next-to-leading" jet (j_2). The two jets are collectively referred to as the '*leading jets*'.

G: Ugly jet cleaning - According to the criteria described in Section 5.4.1, for events to be retained, there must be no poorly measured jets with p_{T} greater than 30% of the p_{T} of the next-to-leading jet. Poorly measured jets correspond to energy depositions in regions where the energy measurement is known to be inaccurate.

H: LAr hole cut - A selection has been implemented to avoid an electromagnetic calorimeter defect in the region from -0.1 to 1.5 in η, and from -0.9 to -0.5 in ϕ that occurred during part of the running period. The average energy loss for jets in this region is 20% to 30%. Jets within $\Delta R = 0.1$ of this region have been rejected if such jets have a p_{T} greater than 30% of the next-to-leading jet p_{T}. In order to retain the shape of dijet angular distributions

[2]Examples of an unusual jet topology include: a jet formed by a single cell in the hadronic end cap (most likely a noisy cell), or an out-of-time energy deposition (most likely due to a cosmic ray).

in χ, the complete η slice from -0.9 to -0.5 in ϕ has been excluded removing 4.3% of the events from the dataset.

I: Bad jet cleaning - Completing the criteria described in Section 5.4.1, if either of the leading jets is not attributed to in-time energy depositions in the calorimeters, the event is to be rejected.

J: Jet p_T cuts - Events are retained if $p_T^{j1} > 100$ GeV and $p_T^{j2} > 50$ GeV. This selection criterion, and those that follow, are applied to jets that have been corrected for the pileup offset, and calibrated to the hadronic scale, as described in Section 5.4

K & L: y^* and y_B cuts - As described in Section 6.4, additional kinematic selection criteria are used to enrich the sample with events in the hard-scattering region of phase space. It is required that events must satisfy $|y^*| < 1.7$ and $|y_B| < 1.1$. The combined y^*, y_B criteria limit the rapidity range of the two leading jets to $|y_{1,2}| < 2.8$. The kinematic selection also restricts the minimum p_T of jets entering the analysis to 80 GeV, with the maximum jet p_T observed at 2000 GeV.

M: m_{jj} cut - Finally, the leading jets in the event are required to result in a reconstructed dijet invariant mass $m_{jj} > 800$ GeV.

Table 7.2: Cut flow for the full 2011 exotics data sample.

Selection criteria	N_{ev}	Efficiency (%)
A (before cuts)	27988283	
B (Events passing any trigger in Table 7.1)	7782504	27.8
C (after GoodRunsList selection)	7240635	93.0
D (vertex check)	7240050	100.0
E (after LAr error cut)	7211390	99.6
F (njet check)	7211390	100.0
G (after ugly jet cleaning)	7210907	100.0
H (LAr hole cut)	6904928	95.8
I (after bad jet cleaning)	6903098	100.0
J (after jet pT cuts)	6899065	100.0
K (after y^* cut)	6378289	92.5
L (after y_B cut)	5600889	87.8
M (after m_{jj} cut)	3827771	68.3
Total Efficiency		13.7

TABLE 7.3: Cut flow for the Pythia QCD MC.

Selection criteria	N_{ev}	Efficiency (%)
A (before cuts)	11534067	
F (njet check)	11534067	100.0
G (after ugly jet cleaning)	11533698	100.0
H (LAr hole cut)	11282606	97.8
I (after bad jet cleaning)	11280222	100.0
J (after jet pT cuts)	11261723	99.8
K (after y^* cut)	11141272	98.9
L (after y_B cut)	10879535	97.7
M (after m_{jj} cut)	10393080	95.5
Total Efficiency		90.1

The selection criteria applied to MC samples are as follows: A, F, G, H, I, J, K, L and M, and the cut flow for QCD MC is shown in Table 7.3. The cut flow and efficiency for a selection of signal samples is shown in Appendix G. The overall signal acceptance (including efficiency) for each signal sample discussed (and shown) in Section 8.2.1.

Cross-checks were employed to ensure that no events were duplicated within the analysis: a situation that could arise due to reconstruction errors, or due to human error. As an additional cross-check, the *yield* of events passing the final event-selection was calculated for each LHC run. It is expected that, assuming the detector performance and beam conditions are approximately stable over time, the yield of events will remain constant, within statistical errors. From the distributions in Figure 7.1, it is possible to identify any anomalies, which could be due to missing data files, or a hardware effect. The distributions have been split into bins of dijet mass, where each individual distribution contains contributions from a single trigger.

From the distributions, we observe that:

- In all mass bins, the yield is approximately flat over time.
- The onset of high-prescaling for the j180 trigger ($1600 < m_{jj} < 2000$ GeV) is visible in the larger error bars.
- The mass bin $2000 < m_{jj} < 2600$ has one entry with large uncertainty. This is from the low-luminosity run 182013 (≈ 100 nb^{-1}), in which one event survived the cuts.
- Similarly in the mass bin $2600 < m_{jj} < 7000$: run 180212 has low-luminosity (≈ 100 nb^{-1}), and has one event recorded.
- Another outlier in the mass bin $2000 < m_{jj} < 2600$ GeV (run 190297), comes from 10 events in a low-luminosity ≈ 1 pb^{-1} run.

- In all mass bins, the yield is lower in the run range including 180614 and ending before 185353, where the LAr hole cut has been applied. During analysis, individual fits show that the event yield is about 12% lower in this run range: consistent with the reduced geometrical acceptance[3].

7.2 Histogram binning and trigger strategy

7.2.1 Binning and trigger strategy for $F_\chi(m_{jj})$

Whilst using an unbinned method to analyse the reconstructed dijet mass spectrum would maximise the amount of useful information that can be extracted [137], due to fluctuations in the detector's jet energy response, the reconstructed invariant mass has a finite resolution below which no useful information can be extracted.

The $F_\chi(m_{jj})$ analysis uses a m_{jj} binning that is motivated by the absolute mass resolution of the reconstructed signal. An explanation of the this method is given in Chapter 4 of [100] and is summarised in Appendix A. The study results in dijet mass bin boundaries of: 500, 548, 601, 657, 717, 780, 847, 919, 995, 1076, 1162, 1253, 1350, 1452, 1561, 1676, 1798, 1927, 2064, 2209, 2363, 2526, 2699, 2882, 3076, 3281, 3498, 3728, 3972, 4230, 4503, 4792, 5098, 5422, 5765, 6128, 6513, 7000 GeV.

The mass boundaries for the use of each trigger are determined from the results in Table 7.1, where the aim is to maximise the total amount of integrated luminosity in each mass bin. By choosing the mass bin boundary immediately above the +5% buffer value, we are led to the trigger strategy described in Table 7.4. The table also includes the *effective luminosity* contained within each mass range. This corresponds to the total integrated luminosity in the mass range, after the effect of the pre-scale has been included. The uncertainty on the integrated luminosity was introduced in Section 3.5 and has a value of 3.9%.

TABLE 7.4: Triggers used for $F_\chi(m_{jj})$ and their effective luminosity.

m_{jj} range [GeV]	Trigger	L_{EFF}/pb
847. - 919.	EF-j100-a4tc-EFFS	19.17
1076. - 1452.	EF-j135-a4tc-EFFS	164.2
1452. - 1798.	EF-j180-a4tc-EFFS	1248.
1798. and above	EF-j240-a4tc-EFFS	4767.

[3]The ϕ_{jet} range from -0.50 to -0.88, which is $\approx 6\%$ of 2π, for either leading jet, corresponds to a yield reduction of 12%.

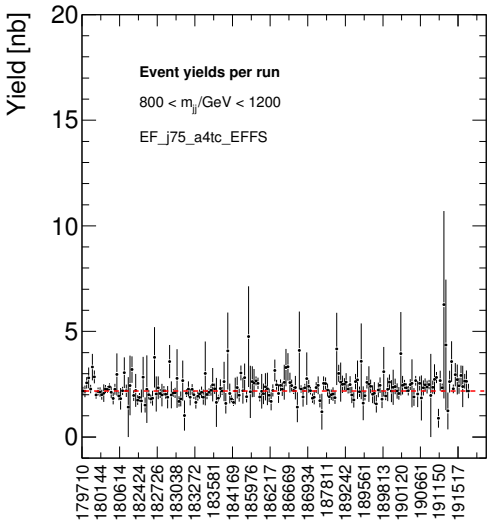

(a) 800 GeV $< m_{jj} <$ 1200 GeV.

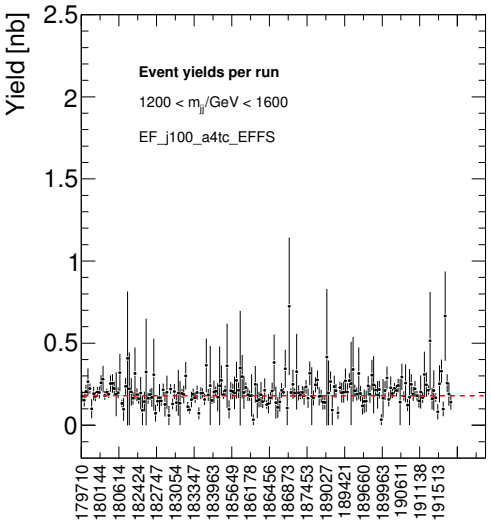

(b) 1200 GeV $< m_{jj} <$ 1600 GeV.

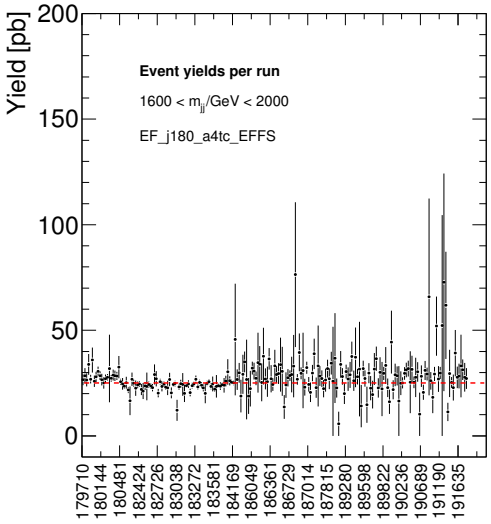

(c) 1600 GeV $< m_{jj} <$ 2000 GeV.

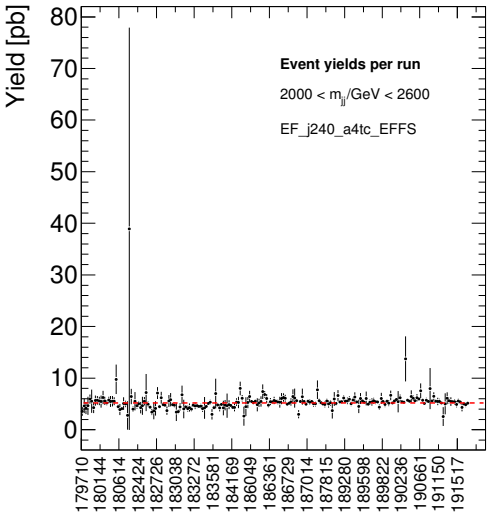

(d) 2000 GeV $< m_{jj} <$ 2600 GeV.

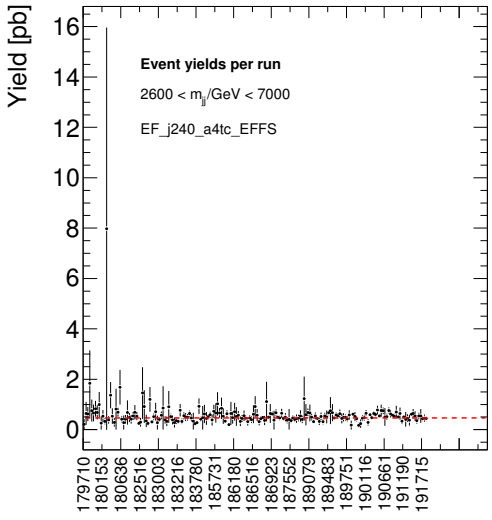

(e) 2600 GeV $< m_{jj} <$ 7000 GeV.

FIGURE 7.1: Event yield, per run, for the analysis selection criteria. The $x-$axis is labelled by run numbers, which are sequential labels for periods of ATLAS data-taking.

7.2.2 Binning and trigger strategy for benchmark χ distributions

The m_{jj} bin boundaries for the benchmark χ distributions are motivated by the efficiency plateaus of the single-jet triggers. Since it is undesirable to mix triggers within a given mass bin, we are led to use the bin boundaries as defined in Table 7.5. Note that the effective integrated luminosity for a the lower threshold triggers is dramatically reduced due to the large prescale that is applied. With 4.767 fb^{-1} of integrated luminosity, there is sufficient statistics to split the EF-j240-a4tc-EFFS trigger over two mass bins. By splitting this mass window, we are able to increase sensitivity to NP processes which occur at higher energy scales. As with Table 7.4, the uncertainty on the integrated luminosity was introduced in Section 3.5 and has a value of 3.9%.

TABLE 7.5: Triggers used for χ and their effective luminosity

m_{jj} range [GeV]	Trigger	L_{EFF}/pb
800. - 1200.	EF-j75-a4tc-EFFS	5.556
1200. - 1600.	EF-j100-a4tc-EFFS	19.17
1600. - 2000.	EF-j180-a4tc-EFFS	1248.
2000. - 2600.	EF-j240-a4tc-EFFS	4767.
2600. and above	EF-j240-a4tc-EFFS	4767.

The binning in χ is determined using QCD MC simulation and aims to minimise the bin migrations between truth level and fully-reconstructed events, whilst also considering the migrations due to the granularity of the ATLAS calorimetry. A further discussion of the methodology is detailed in Appendix A. The resulting bin boundaries are presented in Table 7.6.

7.2.3 Definition of search regions for χ and $F_\chi(m_{jj})$

Based on the trigger and binning discussion above, the search regions for the χ and $F_\chi(m_{jj})$ analyses are defined such that they contain the maximal integrated luminosity. Although it is, in principle, possible to perform a statistical analysis using a search region containing multiple triggers, the situation is complicated by the effect of varying pre-scales between triggers. In this thesis, we therefore consider search regions using a single trigger, generating the highest possible integrated luminosity.

1	1.350	1.822	2.460	3.320	4.482	6.050	8.166	11.023	14.880	20.086	30

TABLE 7.6: Table containing χ bin boundaries. Taken from [138] and discussed further in Appendix A.

Using Tables 7.4 and 7.5, the search regions for χ and $F_\chi(m_{jj})$ are defined as $m_{jj} > 2600$ GeV and $m_{jj} > 1798$ GeV, respectively. The lower regions of these search boundaries are also well below the current best limits on NP models, calculated with these analyses [15]: thus reducing the possibility of missing a NP effect at lower dijet masses.

7.3 QCD predictions

In the analyses described in this thesis, the QCD prediction is based on MC generation of Pythia $2 \to 2$ event samples which cover the kinematic range in χ and m_{jj} spanned by the selected dijet events (See Section 2.5).

In-time pileup is simulated by generating samples of minimum bias events using Pythia 6, which are also passed through detector simulation. To simulate QCD events in the presence of pileup, hard scattering events are overlaid with a number, μ, of minimum bias events, where μ is Poisson distributed and $\langle\mu\rangle$ is chosen to match its expected value in data. The superposition of MC events is performed by summing simulated signals of hard scattering and minimum bias events in each detector electronic channel.

The combined MC events, containing one hard interaction and several soft interactions, are then reconstructed in the same way as collision data, including the jet correction and calibration steps described in Section 5.4.

Since the MC samples have been generated based on an estimate of the average luminosity during the 2011 data-taking, *pileup reweighting* is employed to adjust each MC event such that the μ distribution for the MC sample matches the μ distribution observed in data. A study of the effects of pile-up reweighting is included in Appendix F.

The corrected MC samples are subjected to the same event selection criteria as applied to collision data.

7.3.1 NLO QCD calculations

Within Section 2.4, the issues surrounding simulation of QCD Monte Carlo were explained. The main steps of simulation of the hard scattering process, the initial and final state radiation, multiple interactions and the non-perturbative hadronisation results in a **L**eading **O**rder (**LO**) description. Whilst a LO description may provide a good description of the

main features of the cross-section, it is desirable to take advantage of **N**ext-to-**L**eading **O**rder (**NLO**) calculations in order draw a more precise conclusion.

In this analysis, NLO corrections are applied through the use of bin-wise NLO k-factors, where the k-factors are derived using NLOJET++ [57] and PYTHIA [50]. The prescription developed in [139] is used in order to calculate k-factors for the benchmark-χ distributions, and is then extended to also produce k-factors for the 'inner' and 'outer' distributions of the $F_\chi(m_{jj})$ analysis. This will result in a data-NLO QCD comparison for each of the two analyses.

Four MC samples are generated as a function of x:

1. $\mathbf{run_{COMLETE}}(x)$: A complete LO MC sample (including hard scattering, showers and non-perturbative effects) generated with PYTHIA,
2. $\mathbf{run_{LO}}(x)$: LO matrix elements: generated with both PYTHIA ($\mathbf{run_{LO}}^{\text{Pythia}}(x)$) and NLOJET++ ($\mathbf{run_{LO}}^{\text{NLOJET++}}$),
3. $\mathbf{run_{NLO}}(x)$: NLO matrix elements generated with NLOJET++,
4. $\mathbf{run_{SHOWER}}(x)$: PYTHIA LO hard scattering with parton showers only (non-perturbative processes are switched off),

where each of the runs is produced with the same parameter setting and selection cuts. Note that a LO PDF is needed for the LO calculations, whilst a NLO PDF is needed for the NLO calculations. Using these runs, we are able to improve on our LO $\mathbf{run_{COMPLETE}}(x)$, through the combination

$$\mathbf{run_{COMPLETE}}(x) \times \frac{\mathbf{run_{NLO}}(x)/\mathbf{run_{LO}}^{\text{NLOJET++}}}{\mathbf{run_{SHOWER}}(x)/\mathbf{run_{LO}}^{\text{Pythia}}}, \tag{7.1}$$

where the numerator on the right isolates the NLO part of the calculation from the LO part (leaving only the NLO residual) and the denominator is included to remove the showering contribution from the NLO residual. If one assumes that the $\mathbf{run_{LO}}^{\text{NLOJET++}} \equiv \mathbf{run_{LO}}^{\text{Pythia4}}$[4], then one can conclude that Equation 7.1 is equal to

$$\mathbf{run_{COMPLETE}}(x) \times \overbrace{\frac{\mathbf{run_{NLO}}(x)}{\mathbf{run_{SHOWER}}(x)}}^{k(x)} \tag{7.2}$$

[4]This is a non-trivial assumption, due to the possible differences in parametrisation of the strong coupling constant.

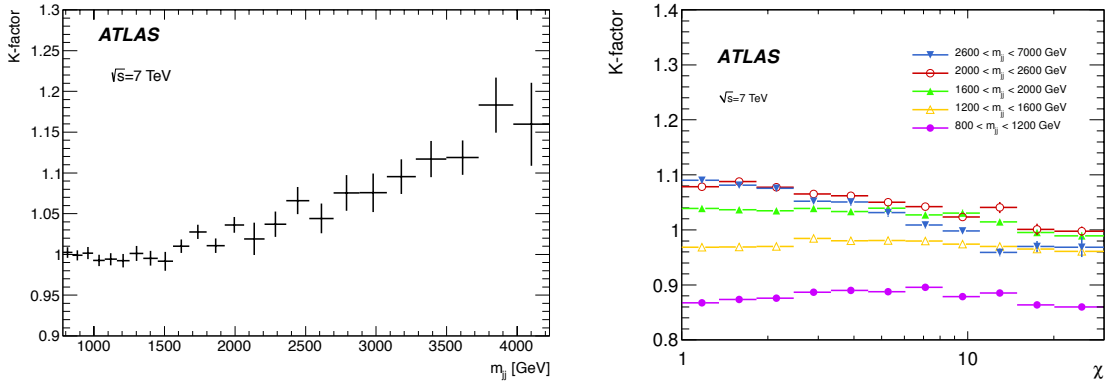

(a) $F_\chi(m_{jj})$ NLO k-factors

(b) χ NLO k-factors

FIGURE 7.2: Bin-wise NLO k-factors for (a) the $F_\chi(m_{jj})$ reconstructed mass spectrum and (b) the un-normalised and reconstructed χ spectrum, split by the broad dijet mass bins defined in Section 7.2.2.

where we can identify the NLO k-factor, $k(x)$.

For this analysis, LO calculations are performed using the CT10 PDF [140], whilst the NLO calculations are performed using the CTEQ66 PDF [141]. All samples use the AUET2B LO** tune [55]. The resulting k-factors for χ and $F_\chi(m_{jj})$ are shown in Figure 7.2. Note that since the k-factors are NLO corrections to the cross-section of the process, they must be applied to the χ distributions before normalising distributions to unit area. From the figures, it can be seen that the k-factors are of order 1 for the lower end of the dijet range, but grow to ~ 1.11 and ~ 1.18 at high dijet masses for χ and $F_\chi(m_{jj})$, respectively.

7.4 Theoretical systematic uncertainties

7.4.1 Uncertainties due to factorisation and renormalisation scale

As discussed in Section 2.3, the uncertainty in the choice of a value of renormalisation (μ_R) and factorisation (μ_F) scale will contribute to the systematic uncertainty on the QCD background prediction. The size and behaviour of this systematic is investigated by measuring the effect of independently setting μ_R and μ_F to 0.5, 1 and 2 times the average transverse momentum μ_0 of the dijet pair, resulting in nine combinations. Distributions for χ and $F_\chi(m_{jj})$ are generated at NLO using NLOJET++ together with APPLgrid [142][5] (using the CT10 NLO PDF), and are shown in Figure 7.3.

[5] APPLgrid [142] provides a fast and flexible way to reproduce the results of full NLO calculations with any input parton distribution set in only a few milliseconds rather than the weeks normally required to gain adequate statistics.

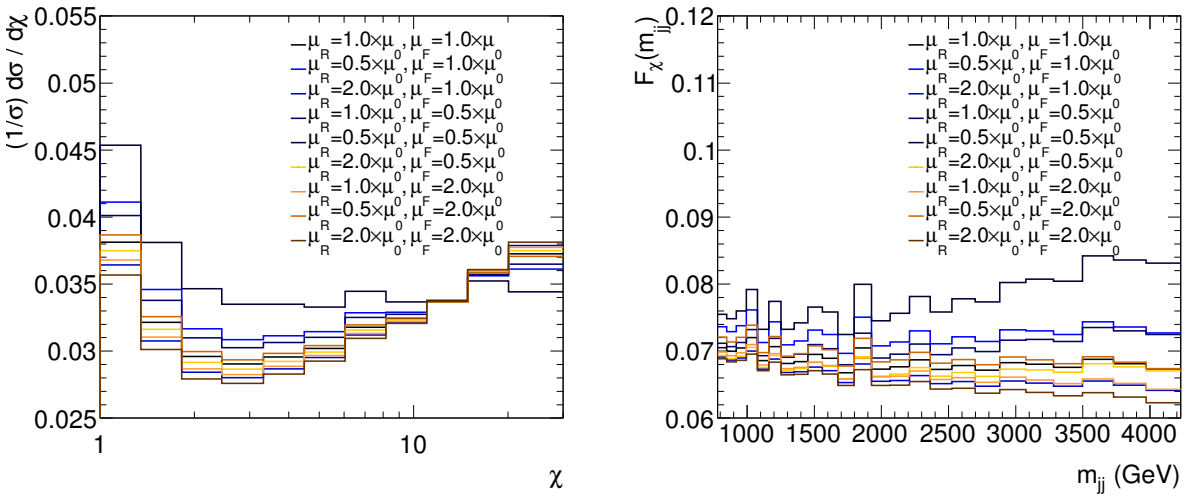

(a) Variations in χ cross-section for $2000 < m_{jj} < 2600$.

(b) Variations in $F_\chi(m_{jj})$ due to scale variation.

FIGURE 7.3: Angular distributions generated with NLOJET++ (truth parton level), for various choices of μ_R and μ_F [130].

The corresponding systematic uncertainties on χ and $F_\chi(m_{jj})$, are calculated as the Root Mean Squared (RMS) deviation of each the μ_R and μ_F variations from the central member. The quantity

$$\Delta = \frac{d\sigma/d\chi(\mu_R = r\mu_0; \mu_F = f\mu_0) - d\sigma/d\chi(\mu_R = \mu_0; \mu_F = \mu_0)}{d\sigma/d\chi(\mu_R = \mu_0; \mu_F = \mu_0)}, \tag{7.3}$$

is calculated for each variation, where r and f are the variation factors for μ_R and μ_F, respectively. The positive (upward) and negative (downward) error bars are then calculated as

$$\text{+ve scale uncertainty} = \sqrt{\frac{2}{8}\sum_{\Delta>0}\Delta^2}\,; \quad \text{-ve scale uncertainty} = \sqrt{\frac{2}{8}\sum_{\Delta<0}\Delta^2}, \tag{7.4}$$

where $\Delta > 0$ implies a sum over all scale variations resulting in a positive value of Δ, and $\Delta < 0$ implies a sum over all scale variations resulting in a negative value of Δ. The factor of $2/8$ in the above expression comes from the fact that we are considering eight variations about the central value (hence a factor of $1/8$); and each sum is only one side of the possible distribution, hence we must multiply the sum by 2 in order to make the error band correspond to the width of the mean-squared distribution.

For $F_\chi(m_{jj})$, the same method is used, where the errors are calculated for $d\sigma/dm_{jj}$ of each mass bin, instead of $d\sigma/d\chi$ of each χ bin. The resulting scale uncertainty bands for the $F_\chi(m_{jj})$ and χ analysis are shown in Figure 7.8 and Figure 7.4(a), respectively. The scale

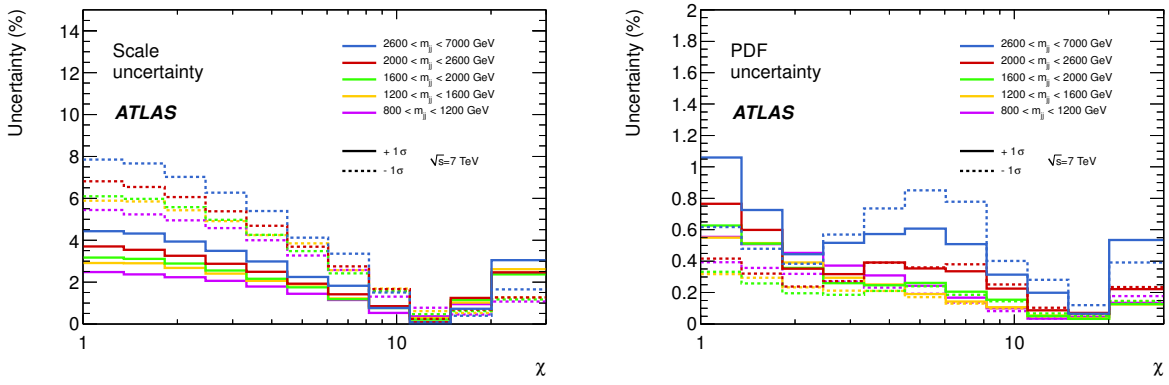

(a) Scale uncertainty for χ distributions

(b) PDF uncertainty for χ distributions

FIGURE 7.4: Theoretical uncertainty bands for the χ distribution in each broad mass bin [130].

uncertainty is largest at low χ and high m_{jj} - reaching uncertainties with a magnitude of 8% for the normalised χ distributions and 18% for $F_\chi(m_{jj})$. Equation 6.20 showed that for constant m_{jj}, low values of χ correspond to high value of p_T: the variation of the scale uncertainty is therefore consistent with a larger uncertainty for jets with higher transverse momentum.

7.4.2 PDF uncertainties

Section 2.2.3 of this thesis included a brief discussion of the evolution of our understanding of the nucleon PDF. It is important to understand the allowed variation in the PDF as this will present a systematic uncertainty on any hadronic collision result. It is regarded as insufficient [51] to simply compare the results from different published parton distributions, since most published sets of PDFs (for example CTEQ and MRST) adopt similar assumptions and the differences between the sets do not fully explore the uncertainties that may exist.

With PDFs having been predominantly determined from Deep Inelastic Scattering and Drell-Yan processes, the gluon distribution has been left relatively unconstrained[6], and thus presents the largest uncertainty of any PDF.

We make use of the Hessian method for calculation of PDF errors, which results in N orthonormal error eigenvectors for N free parameters in the PDF fit. For a given variable X, its value using the central PDF for an error set is given by X_0. X_i^+ is the value of

[6]The gluon distribution has been determined indirectly at low x by measuring the scaling violations mentioned in Section 2.1 of this thesis. Data from the Tevatron has also allowed direct measurement at high-x.

that variable using the PDF corresponding to the "+" direction for eigenvector i and X_i^- is the value for the variable using the PDF corresponding to the "-" direction. The Master Equation is then used to calculate the total PDF error [51]:

$$\begin{aligned} \Delta X_{max}^{+} &= \sqrt{\sum_{i=1}^{N} [\max(X_i^+ - X_0, X_i^- - X_0, 0)]^2} \\ \Delta X_{max}^{-} &= \sqrt{\sum_{i=1}^{N} [\max(X_0 - X_i^+, X_0 - X_i^-, 0)]^2}. \end{aligned} \tag{7.5}$$

The +ve and -ve components may be added in quadrature, since the PDF eigenvectors form an orthonormal basis. We use NLOJET++ connected to APPLgrid with the CT10 error members.

The resulting +ve and -ve PDF errors for $F_\chi(m_{jj})$ are shown in Figure 7.8 and are included in Table 7.7. The PDF uncertainty on F_χ is seen to increase with m_{jj}, ranging from 0.33% to 3.25%. PDF uncertainties are expected to increase with the invariant mass of the dijet system, since these events will tend to be produced in collisions involving partons with higher values of Bjorken-x, where the PDF uncertainty increases.

The resulting PDF uncertainties for χ are shown in Figure 7.4(b) and are included in Table 7.8. The size of the systematic uncertainty is found to range from being negligible to a maximum of 1.06%, with the largest uncertainty occuring at low χ, corrsponding to high jet momentum. This is consistent with the discussion of the PDF uncertainties for $F_\chi(m_{jj})$, where the uncertainty increases with the Bjorken-x of the interacting partons.

7.5 Experimental systematic uncertainties

7.5.1 Jet energy scale uncertainties

JES **P**seudo-**E**xperiments (**PE**s) obtained from MC have been used for the derivation of the JES uncertainty. This is typically done by running over the MC samples 1000 times, each time varying the JES of all jets in all events according to the uncertainty given by the JESUncertaintyProvider. The JESUncertaintyProvider [121] is introduced in Section 5.5.1. The 14 nuisance parameter configuration is used and it is assumed that the uncertainties on jet energies have a Gaussian distribution. This means that each PE has a set of 14 random numbers drawn from a Gaussian with zero mean and $\sigma = 1$. For PE i each jet $ijet$ is then

scaled with a factor:

$$(1 + r_1[i]\,\sigma_1[ijet]) \times (1 + r_2[i]\,\sigma_2[ijet]) \times \cdots \times (1 + r_{14}[i]\,\sigma_{14}[ijet]), \tag{7.6}$$

where $r_{1,2,\ldots,14}$ are 14 rows with random numbers with the dimension equal to the total number of PEs. For each of these PEs the $F_\chi(m_{jj})$ distribution have been constructed, giving rise to an ensemble of PE distributions located around the nominal one. The 1-σ uncertainty is then obtained from the envelope determined by the area that contains 68% of the PEs around the nominal distribution. Figure 7.5 shows the results of 100 JES pseudo-experiments for the $F_\chi(m_{jj})$ distribution. The spread of the pseudo-experiments is observed to increase with dijet mass - reflecting the greater variation in JES for higher energy jets. It is

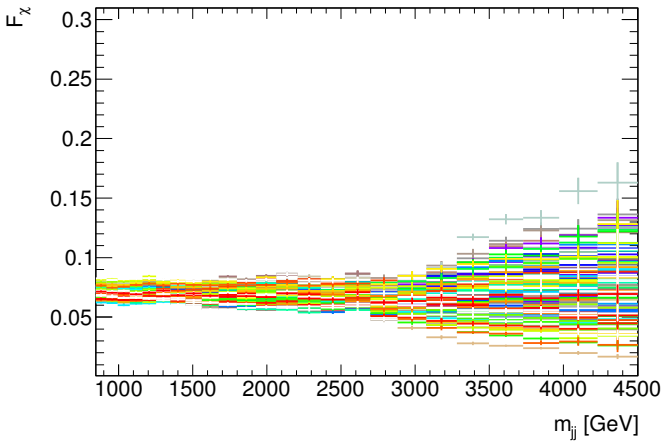

FIGURE 7.5: $F_\chi(m_{jj})$ distributions for 100 of the 1000 JES pseudo experiments described by Equation 7.6. As described in the text, the variance of uncertainty in each mass bin is used to calculate the upper and lower JES uncertainty. It is clear that the final JES 1-σ uncertainty band will increase with m_{jj}.

perfectly possible that the situation is not symmetric, e.g. when there are more distributions above the the nominal distribution than below. Therefore the 68% border of the number of PEs above the nominal distribution (68% from those PE that lie above the nominal, not from the total number of PEs) is used to determine the +1-σ uncertainty, and the 68% border of the number of PEs below the nominal distribution (not the total number) is taken as the -1-σ uncertainty.

The JES uncertainty is currently the largest component of the total systematic uncertainty: as can be seen in Figure 7.8, where it is compared to all other sources of systematic uncertainty. The resulting JES uncertainty for the χ distributions is shown in Figure 7.6. As with the systematic uncertainty due to scale variations, the larger uncertainties at low χ (maximally 17.2% in Figure 7.6) and high m_{jj} (reaching 52.0% from Figure 7.8) are consistent with a higher systematic uncertainty for events with high energy jets.

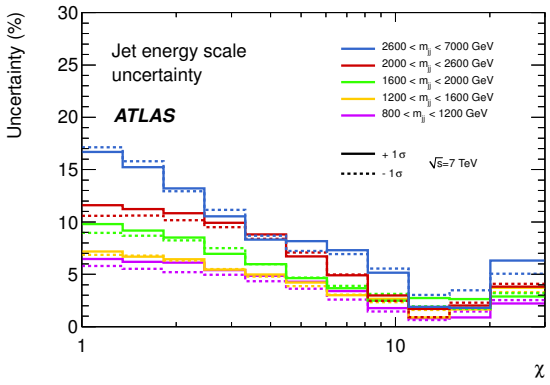

FIGURE 7.6: The upper and lower jet energy scale uncertainty on the χ distribution for each broad dijet mass bin [130].

7.5.2 Uncertainties due to jet energy and angular resolution

The **J**et **E**nergy **R**esolution (**JER**) in 2011 has been discussed in Section 5.5.2. Studies of the effect of a limited jet resolution on this analysis were performed in [130]. Figure 5.2(a) showed the resolution for jets as function of p_T and in various bins of η. The effect of this finite resolution on the χ distributions has been investigated by smearing MC events: for each jet in each event, the resolution is obtained using the 2011 JER Provider package (Version 01-00-00) [121]. This number is then multiplied with a random number pulled from a Gaussian with zero mean and unit width. Next, the χ distributions are reconstructed from this smeared MC sample, and the ratio with respect to the unsmeared distributions is taken. This is shown in Fig. 7.7(a). The distortion caused by the jet energy resolution is uniform in χ and does not exceed 3% and is considered small compared to the other uncertainties included in the analysis.

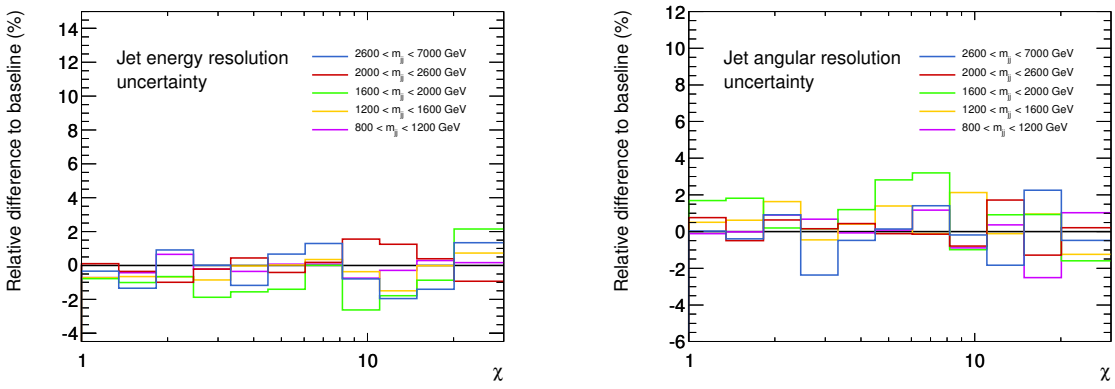

(a) (b)

FIGURE 7.7: (a) JER, (b) JAR, and their associated uncertainties on the χ distributions, for each dijet invariant mass range [130].

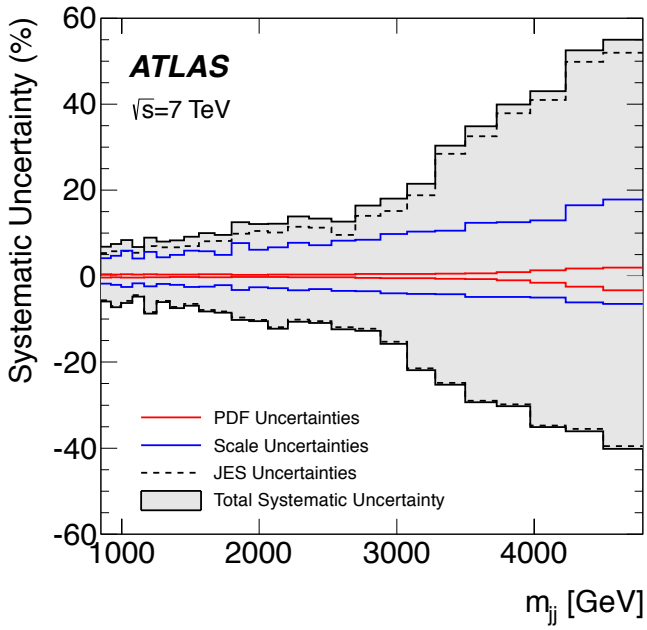

FIGURE 7.8: Envelopes for the dominant sources of systematic uncertainty in $F_\chi(m_{jj})$ distributions: JES, scale, and PDF uncertainties.

The effect of a finite **J**et **A**ngular **R**esolution (**JAR**) has been studied in a similar way. Figure 5.2(b) showed the angular uncertainty in η obtained from MC. The angular resolution has been estimated by matching reconstructed calorimeter jets to truth jets within a cone of $\Delta R = 0.3$, in bins of η and p_T. The RMS of the distribution of the absolute difference between true η and reconstructed η has been taken as a first-order estimate of the angular resolution. From this figure it can be observed that for jets with a p_T above 100 GeV, the resolution in the central region ($\eta < 3.0$) is uniform in χ and does not exceed 3%.

To study the effect on the χ distributions, jets in MC events are smeared in η with 4%, while keeping the mass and energy of the jet unchanged. The ratios of these smeared χ distributions with respect to the nominal distributions are shown in Fig. 7.7(b) and do not exceed 4%: a small number compared to the other uncertainties included in the analysis.

In summary, the effects of JER and JAR are small, when compared to other sources of systematic uncertainty, and result in a variation that is flat in χ. There uncertainties are therefore not further-considered in this thesis.

7.6 Summary of systematics

Due to the construction of both the normalised χ distributions and the $F_\chi(m_{jj})$ distributions, many systematics are significantly reduced. The effects of luminosity uncertainty cancel at

m_{jj} range		JES (%)		Scale (%)		PDF (%)		Total (%)	
(GeV)		up	down	up	down	up	down	up	down
847	919	5.38	-5.62	4.20	-1.72	0.46	-0.33	6.84	-5.88
919	995	5.76	-6.92	4.74	-1.99	0.39	-0.27	7.47	-7.20
995	1076	5.86	-5.73	5.95	-2.52	0.44	-0.30	8.36	-6.27
1076	1162	5.43	-4.44	4.07	-1.68	0.37	-0.29	6.80	-4.76
1162	1253	6.98	-8.37	5.64	-2.38	0.45	-0.28	8.99	-8.70
1253	1350	6.68	-5.75	4.40	-1.81	0.40	-0.24	8.01	-6.03
1350	1452	6.74	-7.14	4.91	-2.04	0.38	-0.21	8.35	-7.43
1452	1561	7.01	-6.42	5.90	-2.48	0.37	-0.18	9.17	-6.88
1561	1676	8.11	-7.84	5.80	-2.45	0.43	-0.26	9.98	-8.21
1676	1798	8.18	-8.24	4.94	-2.05	0.41	-0.23	9.56	-8.49
1798	1927	9.90	-9.63	7.68	-3.21	0.27	-0.16	12.53	-10.16
1927	2064	10.49	-10.15	6.12	-2.56	0.29	-0.19	12.15	-10.47
2064	2209	10.13	-11.87	6.72	-2.81	0.36	-0.21	12.16	-12.20
2209	2363	11.49	-10.08	7.78	-3.26	0.34	-0.25	13.88	-10.60
2363	2526	11.29	-10.45	7.20	-3.01	0.37	-0.26	13.40	-10.88
2526	2699	9.62	-11.87	8.25	-3.40	0.36	-0.26	12.68	-12.35
2699	2882	14.01	-12.19	8.48	-3.47	0.50	-0.39	16.38	-12.68
2882	3076	15.14	-15.21	9.78	-3.97	0.49	-0.48	18.03	-15.73
3076	3281	18.79	-21.43	10.39	-4.16	0.48	-0.44	21.48	-21.83
3281	3498	28.47	-24.85	10.57	-4.22	0.58	-0.59	30.37	-25.21
3498	3728	32.54	-28.94	12.44	-4.82	0.65	-0.68	34.85	-29.35
3728	3972	37.89	-29.83	12.57	-4.85	0.92	-0.95	39.93	-30.24
3972	4230	41.01	-34.72	12.95	-4.95	1.35	-1.54	43.03	-35.11
4230	4503	49.83	-35.49	16.50	-6.07	1.75	-2.45	52.53	-36.09
4503	4792	51.98	-39.53	17.86	-6.43	2.02	-3.25	55.00	-40.19

TABLE 7.7: Summary of systematic uncertainties for $F_\chi(m_{jj})$ due to JES, scale and PDF, along with their total.

χ range		JES (%)		Scale (%)		PDF (%)		Total (%)	
		up	down	up	down	up	down	up	down
1	1.34	9.27	-10.00	4.42	-7.85	1.06	-0.61	10.37	10.70
1.34	1.82	8.01	-11.20	4.31	-7.66	0.72	-0.47	8.78	11.76
1.82	2.45	7.46	-9.87	3.93	-7.02	0.44	-0.38	7.95	10.32
2.45	3.32	6.80	-8.10	3.49	-6.27	0.51	-0.56	7.35	8.74
3.32	4.48	3.83	-7.44	2.98	-5.40	0.57	-0.73	4.43	8.23
4.48	6.04	3.17	-5.56	2.24	-4.12	0.60	-0.85	3.80	6.46
6.04	8.16	2.58	-3.46	1.83	-3.35	0.50	-0.77	3.11	4.27
8.16	11.02	2.06	-1.59	0.76	-1.50	0.31	-0.40	2.38	2.00
11.02	14.87	0.94	-1.26	0.0061	-0.086	0.19	-0.28	1.14	1.54
14.87	20.08	2.17	-2.31	0.72	-0.39	0.066	-0.11	2.24	2.43
20.08	30	3.06	-2.19	3.05	-1.65	0.53	-0.39	3.62	2.60

TABLE 7.8: Summary of systematic uncertainties for χ distribution in mass bin $m_{jj} >$ 2.6 TeV due to JES, scale and PDF, along with their total.

first order and are ignored completely.

For both the normalised χ and the $F_\chi(m_{jj})$ distributions, the dominant systematic uncertainties are found to arise from the JES and the choice of renormalisation and factorisation scale. Numerical values for the systematic uncertainties due to JES, scale and PDF, for $F_\chi(m_{jj})$ and for the χ distribution in the highest dijet mass bin are included in Tables 7.7 and 7.8.

For χ, these uncertainties are maximal for the highest dijet mass bin and at low values of χ, with the JES uncertainty reaching $\sim 16.5\%$ of cross-section and the scale uncertainty reaching $\sim 8\%$ of the cross-section. Conversely, the PDF, JER and JAR are all found to have an uncertainty not exceeding 3% (with the PDF uncertainty $\sim 1\%$).

For $F_\chi(m_{jj})$, each of the derived systematic uncertainties, and their combination in quadrature is shown in Figure 7.8. The total systematic uncertainty is seen to increase across the dijet mass range, ranging from 6.8% at the lowest dijet mass to 55% at the height of the displayed mass range (composed from 52% JES and 18% scale uncertainty). PDF uncertainties are also most significant at the highest mass ranges, but do not exceed $\sim 3\%$. Although not included in Figure 7.8, it is clear from the studies in the previous section that both JER and JAR present a negligible contribution to the total systematic uncertainty - most notably due to their uniform effect over the χ range for all broad mass windows.

Given their relatively negligible contribution to the total systematic uncertainty across both the normalised χ and $F_\chi(m_{jj})$ distributions, the PDF, JER and JAR uncertainties will not be considered further in this thesis.

7.7 Studies of the effects of pileup

The effects of both in and out-of-time pile-up on the final dijet angular distributions have been investigated in [130]. In the following sub-sections, the results of these studies are discussed.

7.7.1 In-time pileup

Between the beginning and end of the ATLAS 2011 data taking period the LHC instantaneous luminosity rose substantially, with the average $\langle\mu\rangle$ of inelastic interactions per bunch

crossing[7] rising above 20 for the run periods with highest instantaneous luminosity.

One way to investigate the effectiveness of the offset correction is to study the variation of F_χ in coarse m_{jj} bins[8] as function of N_{PV}, which correlates with the number of inelastic interactions in each crossing, μ. Fig. 7.9(a) shows the variation of F_χ from data with N_{PV}, and Fig. 7.9(b) shows the same quantity from MC. Note that the MC has been reweighted to represent the current pileup conditions in data: details of this procedure are described in Appendix F. The data in the highest mass bin show a tendency for F_χ to decrease with N_{PV}, though the statistics in this highest mass range are marginal.

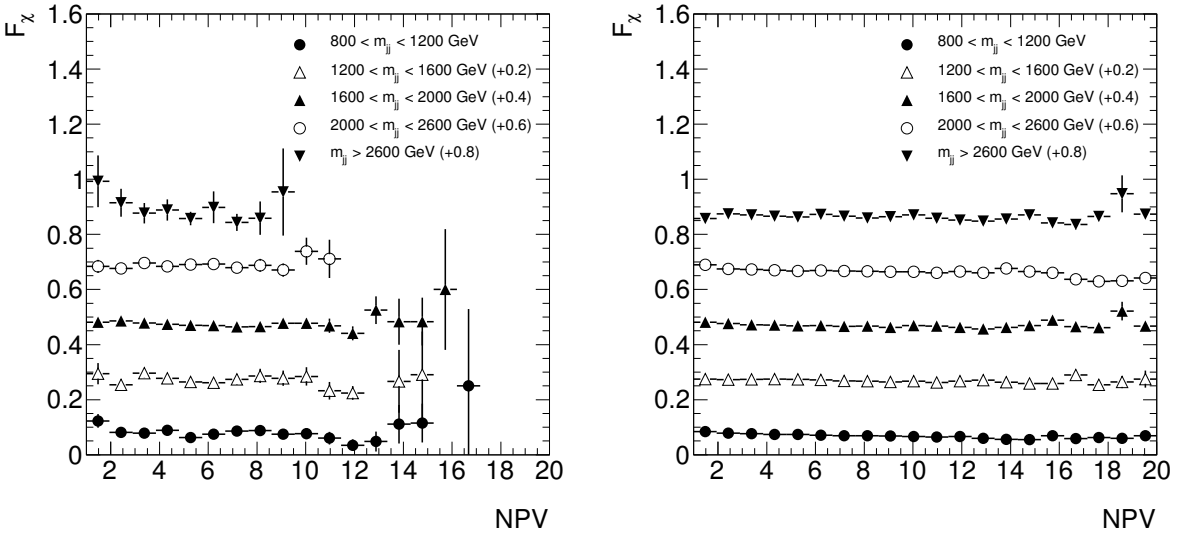

(a) F_χ distributions from data

(b) F_χ distributions from MC

FIGURE 7.9: For the full data and MC samples, these plots show the variation in coarse binned F_χ distributions due to in-time pileup, which is strongly correlated with the number of primary vertices, N_{PV} [130].

7.7.2 Out-of-time pileup

In addition to in-time-pileup caused by minimum bias events in the same bunch crossing, there are "out-of-time" pileup effects due to preceding and successive bunch crossings and bunch train spacings. This effect arises because the LAr calorimeter has an electronic shaping time of 450 ns, which is considerably longer than the bunch spacings in the 2011 data set - ranging from 25 ns to 75 ns during the full run period. The out-of-time pileup is primarily due to the tails of pulses from preceding bunch crossings, but also includes some overlap

[7] $\langle\mu\rangle$ is measured by the ATLAS luminosity detectors [143, 144] and sampled in intervals of approximately two minutes.

[8] Here, F_χ carries the same definition as in Equation 6.31, however the usual '(m_{jj})' dependancy notation has been removed to signify that broad bins in m_{jj} are being considered.

with a few successive crossings because the leading edges of later pulses can be included in the later time samples of the signal pulse being digitised.

When the signal crossing is well-contained within a train of evenly spaced pulses, the out-of-time pileup will be fluctuating around some equilibrium value related to the instantaneous luminosity. But at the beginnings and ends of bunch trains there will be a transition period as the system is reaching the next equilibrium value.

To assure that there are no remaining effects, due to out-of-time pileup and bunch train spacing, that might modify the distributions of dijet observables, χ and coarse-binned F_χ distributions from collision data are studied as a function of event position in the bunch trains. The results of these studies are shown in Fig. 7.10. Although there is a hint of some possible structure within these distributions, when taking the statistical uncertainties into account, these plots are interpreted as being consistent with there being no variation in χ or F_χ as a function of position in a bunch train.

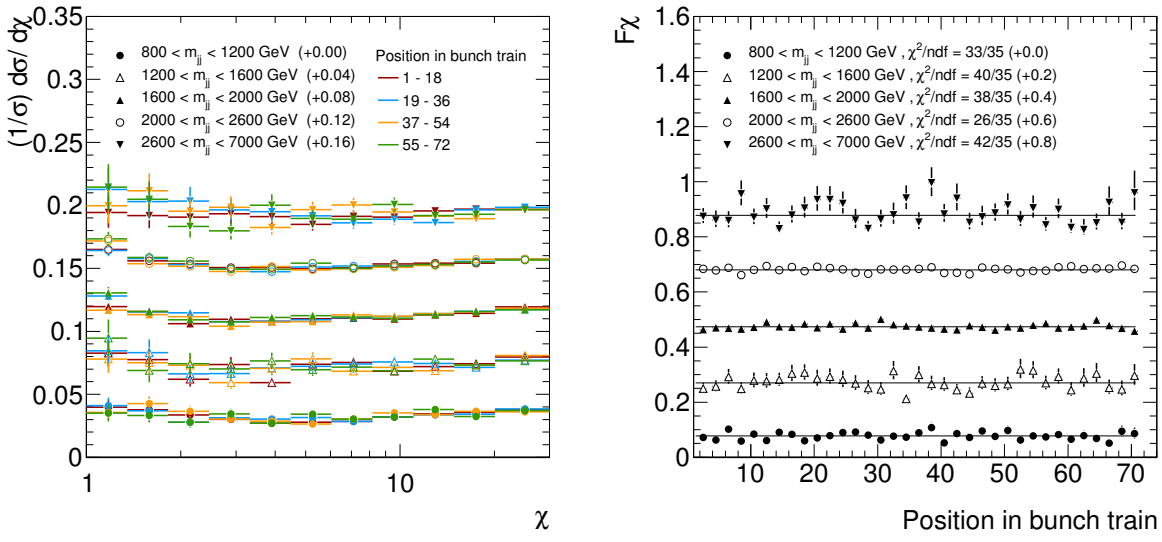

(a) χ distributions

(b) F_χ in coarse m_{jj} bins

FIGURE 7.10: These plots show (a) the variation in dijet χ distributions and (b) the variation in F_χ in coarse m_{jj} bins; as a function of position in a bunch train, which affects the amount of out-of-time pileup [130].

7.8 Effects from detector malfunction

Hardware defects of the calorimeters (e.g. non-working modules, temporary high voltage problems) can lead to specific regions where jets are mis-measured or not measured at all. If these regions are not simulated well within the Monte Carlo simulation, the results of the

angular analyses can be affected because the defects will lead to different jet rates in different pseudorapidity regions.

Permanently dead regions in the calorimeter could affect the measured distributions. In the case of a dead tile calorimeter cell, a correction is applied to its raw energy scale. The correction factor 1.0 − BCH_CORR_CELL is equal to the sum of the energies in the corrected cells neighbouring this cell divided by their total energy, and is applied such that

$$E_{\text{raw, corrected}} = \frac{E_{\text{raw, uncorrected}}}{(1.0 - \text{BCH\_CORR\_CELL})}. \tag{7.7}$$

This correction is done by default in the reconstruction.

An improved correction can be applied at the jet level: BCH_CORR_JET equals the sum of the estimation for bad cells in the jet cone divided by the total energy. The total correction is then given by

$$E_{\text{jet-level corrected}} = E_{\text{raw, corrected}} \frac{(1.0 - \text{BCH\_CORR\_CELL})}{(1.0 - \text{BCH\_CORR\_JET})}. \tag{7.8}$$

The above formula cancels the default cell-based correction step and applies the new correction at the jet level. It is applied to the jet energy at the EM-scale before applying a hadronic calibration. Performance studies have shown that the "jet-level" correction performs better in jet closure tests [121] and therefore we have used it through the entire dijet analysis. Figure 7.11 shows the distribution of correction factors for data events that have a fully reconstructed dijet mass above 700 GeV.

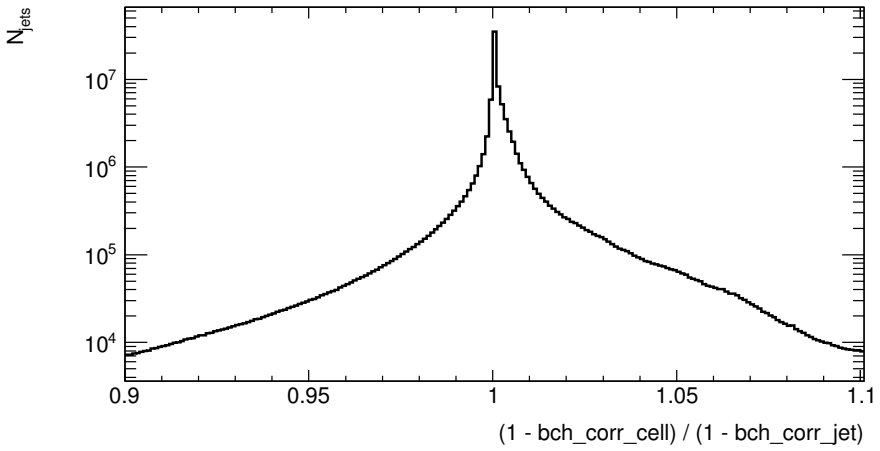

FIGURE 7.11: Distribution of the bad tile channel correction factor for data events with dijet mass above 700 GeV [130].

In extremely rare situations —15 jets in nearly 30 million data events— the correction becomes negative or is such that the corrected energy becomes smaller than the jet mass itself. In those cases the bad channel correction is not applied to the jet. When looking at the jet cleaning it was found that nearly all those jets are labelled as ugly because of a too large value of BCH_CORR_CELL.

7.9 Validation of the QCD background

As discussed in Sections 1.1 and 6.5, a control region is used in order to validate the MC QCD prediction in a region of the kinematic phase space where new physics is not expected. With motivation from the $F_\chi(m_{jj})$ analysis, the dijet mass region $1452 < m_{jj} < 1798$ is considered, since it is the highest luminosity and highest dijet mass region, which is not included in search region. These events also represent a subset of the events considered outside of the search region of the normalised χ spectra analysis. The selection of the subset is motivated only by the trigger, which is shown to be unbiased in the dijet mass ranges considered. Further validation for the normalised χ spectra is provided by analysing the agreement for the normalised χ spectra at lower dijet mass ranges: this is done quantitatively in Section 8.1.3.

As discussed in Section 6.5, below, data is compared to LO Pythia QCD for key kinematic variables: m_{jj}, $p_T^{1,2}$, $y_{1,2}$, $\phi_{1,2}$, y^*, y^B and N_{jet}. Although it would be better to compare data to an NLO QCD prediction, it is not feasible to produce a set of NLO k-factors for every kinematic observable. Data and LO Pythia QCD show excellent agreement in most distributions, however there are some possible discrepancies.

Each of the figures compared data (black dots) to QCD MC simulation (red line). Statistical uncertainties on the QCD MC is also included in yellow. The bottom half of each figure includes the ratio of data/MC, and their associated statistical uncertainties. Distributions of m_{jj} (Figure 7.12(a)), N_{jets} (Figure 7.12(b)), p_T^2 (Figure 7.12(d)), $y_{1,2}$ (Figures 7.12(e) and 7.12(f)), $\phi_{1,2}$ (Figures 7.13(a) and 7.13(b)) and $|y^*|$ (Figure 7.13(c)) all show good agreement between data and the QCD prediction. Figure 7.12(c), showing the leading jet p_T, shows an excess in data at high transverse momentum, however the discrepancy is not significant when taking statistical uncertainties into consideration. Figure 7.13(d), showing the distribution of y_B, also shows an excess at low values of y_B. This excess at low values of y_B suggests an excess of back-to-back events within the kinematic region considered in the plot. One must also remember that these distributions do not include the uncertainty due to the jet energy scale.

7.10 Final distributions

The final distribution for $F_\chi(m_{jj})$ is shown in Figure 7.14. Data (black points), corresponding to 4.8 fb^{-1} of $\sqrt{s} = 7$ TeV proton proton collisions, are compared to an NLO QCD prediction, with systematic uncertainties included. The event selection for the figure, as well as the calculation of associated systematic uncertainties and bin-wise NLO k-factors, have been described throughout this chapter. The systematic uncertainties have been split into two groups: the theoretical uncertainty, due to scale and PDF uncertainties, and the total systematic uncertainty, which also includes the JES uncertainty. Three NP scenarios are also included: a QBH model with 6 extra dimensions and a Plank mass of $M_D = 4$ TeV; an excited quark model with $m_{q^*} = 2.5$ TeV; and a contact interaction model with compositeness scale $\Lambda = 7.5$ TeV. A blue vertical line denotes the lower boundary of the search region. To the left of the blue line (in the control region), it is noticeable that the data points lie consistently above the QCD background. However, all data points do lie within the systematic uncertainties. In the search region, data points continue to lie within the displayed systematic uncertainties. The data appears to be consistent with the QCD prediction, and does not appear to behave as any of the example NP signals depicted in the figure.

The corresponding final distributions for normalised χ distributions are shown in Figure 7.15. As in Figure 7.14, NLO QCD background and each of the systematic uncertainties considered in this chapter as displayed. As an example of a NP scenario, the highest mass bin also includes a QBH signal with 6 extra dimensions and a Plank mass of $M_D = 4.0$ TeV. This highest mass bin, containing events with $m_{jj} > 2.6$ TeV, is the search bin for this analysis, as discussed in previous chapters, with each of the lower mass bins providing a control region for MC validation. The majority of data points are found to lie within the 1-σ systematic uncertainty bands, with a few exceptions in the lower mass bins. By-eye, there appears to be no evidence for an excess of events at low χ. The data does therefore not be behave as predicted by the NP models considered in this thesis, and as exemplified by the QBH model in the figure.

A quantified analysis of each of the distributions in Figures 7.14 and 7.15 is considered in Chapter 8.

An high-energy dijet event candidate, measured with the ATLAS detector from a proton-proton collision at $\sqrt{s} = 7$ TeV, is shown in Figure 7.16. Within the event, two dense sprays of particle tracks are visible in the inner detector, each pointing to areas of energy deposition within the electromagnetic (free) and hadronic (red) calorimeters. These two high-p_T jets are back-to-back in the transverse plane, and are approximately back-to-back in the $r - z$-plane.

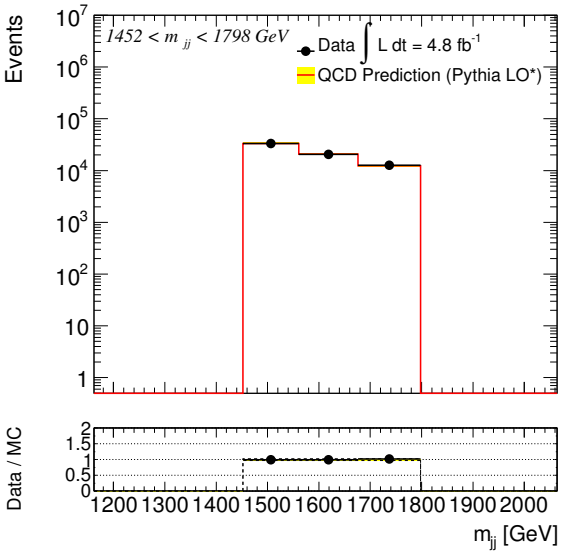

(a) m_{jj}

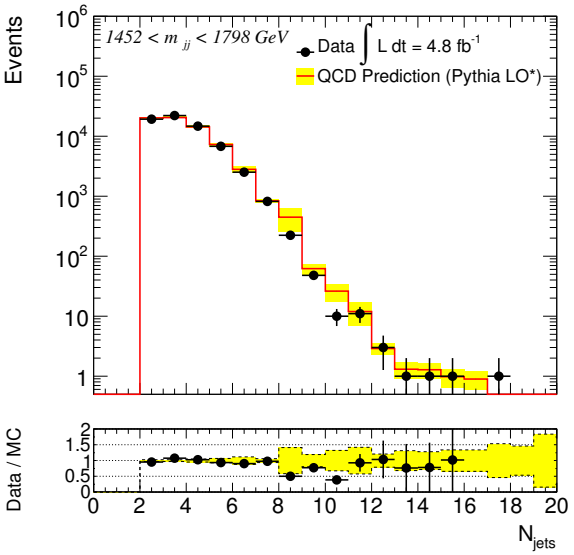

(b) N_{jets}

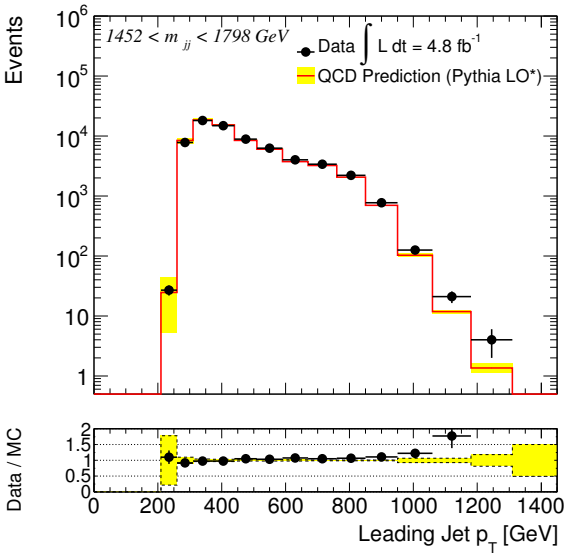

(c) p_T^{j1}

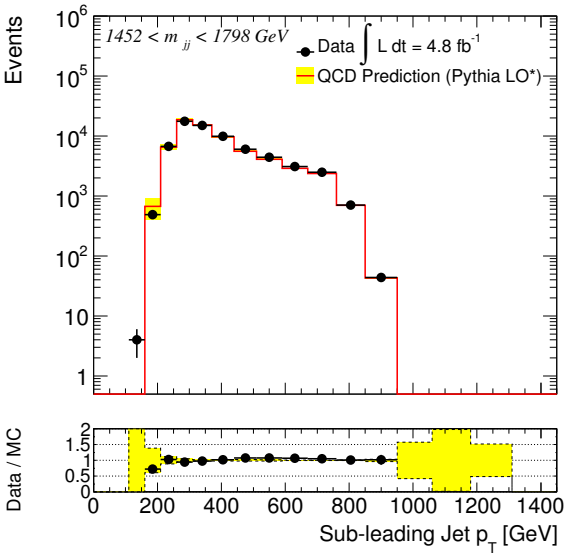

(d) p_T^{j2}

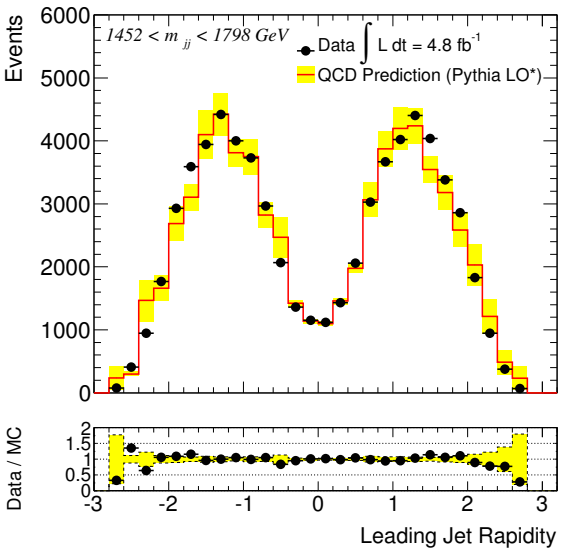

(e) y_1

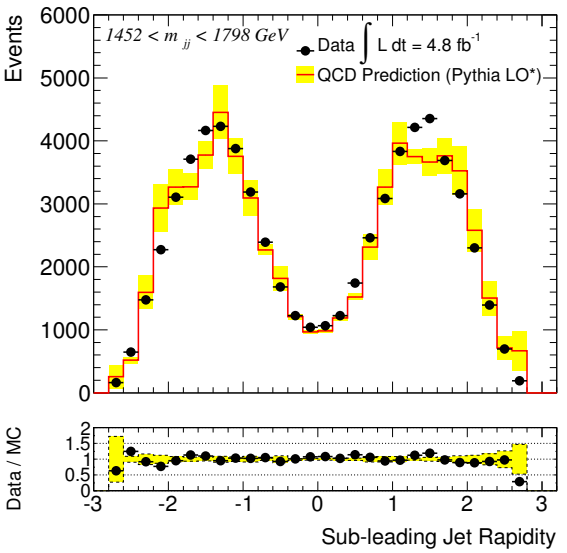

(f) y_2

FIGURE 7.12: Data (black points) are compared to LO QCD (red line). Statistical uncertainties on the QCD MC are included in yellow.

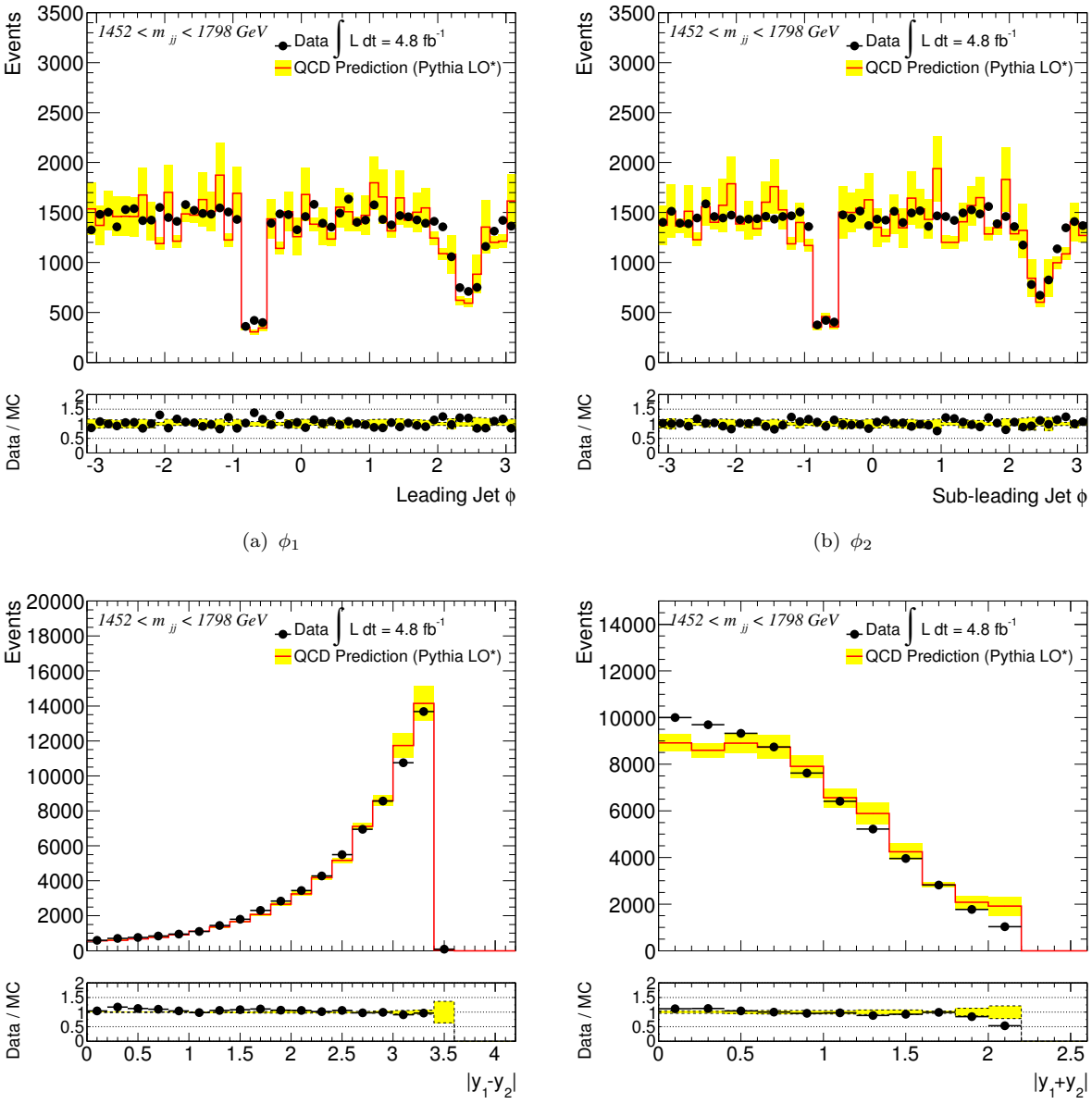

(a) ϕ_1

(b) ϕ_2

(c) $|y^*| = |y_1 - y_2|$

(d) $|y_B| = |y_1 + y_2|$

FIGURE 7.13: Data (black points) are compared to LO QCD (red line). Statistical uncertainties on the QCD MC are included in yellow. The bottom half of each figure displays the ratio of data/MC, and their associated statistical uncertainties.

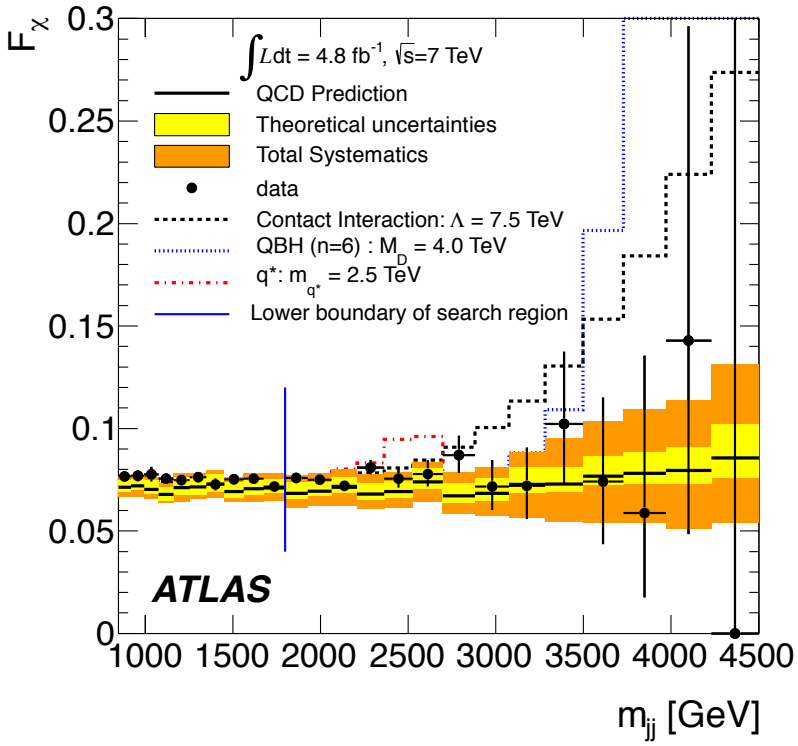

FIGURE 7.14: The $F_\chi(m_{jj})$ distribution in m_{jj}. The QCD prediction is shown with theoretical and total systematic uncertainties (bands), and data (black points) with statistical uncertainties. The blue vertical line indicates the search region for new physics. Various expected new physics signals are shown: a contact interaction with $\Lambda = 7.5$ TeV, an excited quark with mass 2.5 TeV and a QBH signal with $M_D = 4.5$ TeV and $n = 6$.

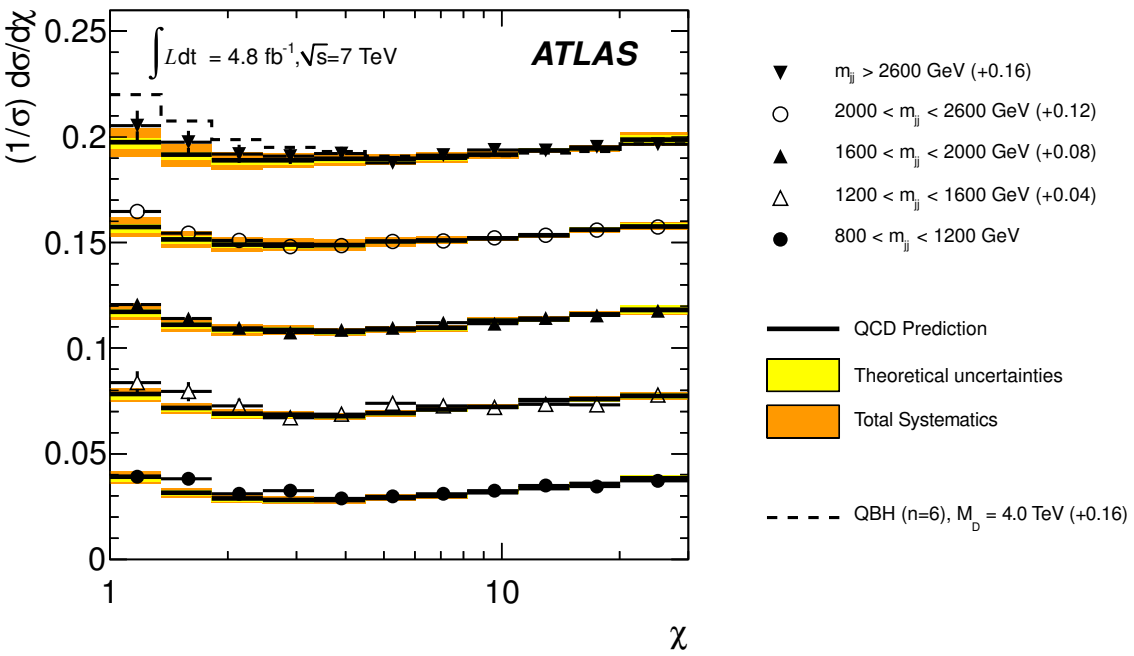

FIGURE 7.15: The χ distributions for all dijet mass bins [31]. The QCD predictions are shown with theoretical and total systematic uncertainties (bands), as well as the data with statistical uncertainties. The dashed line is the prediction for a QBH signal for $M_D = 4.0$ TeV and $n = 6$ in the highest mass bin. The distributions have been offset by the amount shown in the legend to aid in visually comparing the shapes in each mass bin.

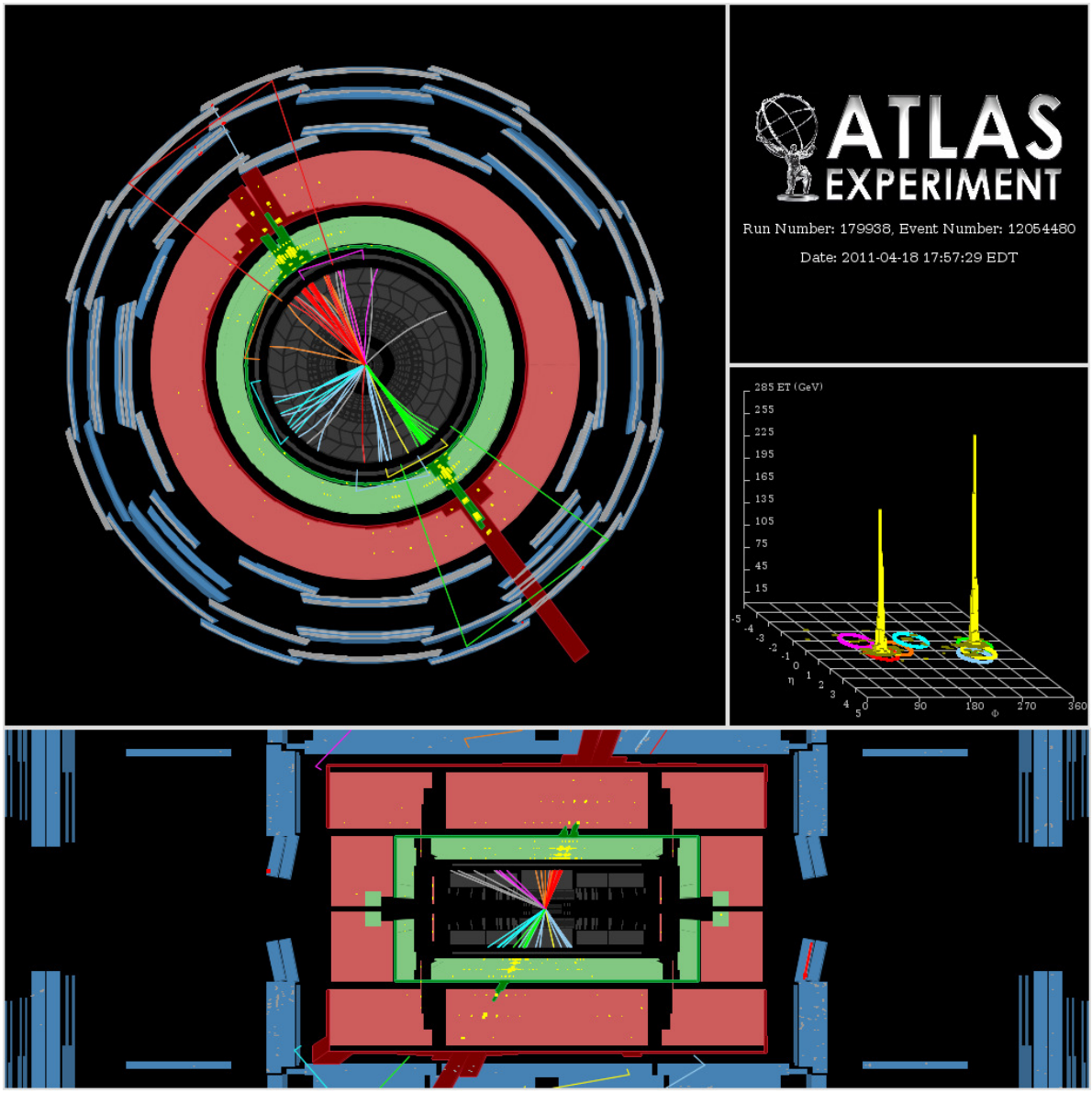

FIGURE 7.16: Highest mass event passing full event selection. The dijet mass is 4040 GeV while the leading jets have (p_T, η, ϕ, colour) of (1850 GeV, 0.32, 2.2, red) and (1840 GeV, -0.53, -0.92, green). This event was observed during run 179938 and has event number 12054480.

Chapter 8

Statistical interpretation and limits on signals for new physics

When it comes to interpreting the results of the analysis, the strategy is clearly split between a 'search phase' and a 'limit-setting phase'.

The search phase is concerned with assessing to what extent the measured data agrees with the simulated background prediction. Quantitatively, the most significant deviation of data from the **M**onte **C**arlo (**MC**) is identified and a corresponding $p-$value that describes the likelihood of such a deviation is calculated. In the event of reasonable agreement between data and the MC prediction, we then proceed to the limit setting stage.

The purpose of the limit-setting phase is to assess the impact of the null-result from the search phase on the phase space of **N**ew **P**hysics (**NP**) scenarios. Multiple 'benchmark' models of NP processes are considered in this thesis, including: excited quarks, quark contact interactions and Quantum Black Holes (see Chapter 4 for more details). One then asks the question: *if I assume that my NP model is valid, given the null-result in the search phase, what constraints can I place on the free parameters of my model?* Since the measurement of data is subject to statistical and systematic uncertainties, it is only possible to constrain model parameters at a certain **C**redibility **L**evel (**CL**). Through constraint of NP model parameters, these experimental results are able to guide theorists to reassess the plausibility of many NP models and, where possible, provide direction for future work.

8.1 Search phase: is there evidence of new physics?

8.1.1 Hypothesis tests and calculation of p-values

In order to infer the presence of a new physical process, which is not currently included in the SM, one must introduce a quantitative hypothesis test. A Null Hypothesis, H_0, is specified as that from which we search for a 'significant' deviation in data. The significance required for the rejection of the null hypothesis must be specified as part of the procedure.

When testing the consistency of some data D with a null hypothesis H_0, 'pseudo-data', using **P**seudo **E**xperiments (**PE**), are produced that assumes H_0. The p-value is calculated in order to assess how the observed data compares to the N possible outcomes that H_0 *could* have produced:

$$p-\text{value} \equiv \mathrm{P}(t \geq t_0 | H_0) \tag{8.1}$$

where the test statistic[1], t, is some function of the observable[2]. The test statistic is a random variable, since it depends on how the pseudo-data fluctuate around H_0. The *observed* test statistic, t_0, is the value of t corresponding to the value of the observable in data.

8.1.2 Bayes' theorem

Bayes' theorem gives the relationship between the probabilities of A and B, $\mathrm{P}(A)$ and $\mathrm{P}(B)$, and the conditional probabilities of A given B and B given A, $\mathrm{P}(A|B)$ and $\mathrm{P}(B|A)$. For proposition A and evidence B:

$$\mathrm{P}(A|B) \propto \mathrm{P}(B|A)\,\mathrm{P}(A), \tag{8.2}$$

where $\mathrm{P}(A)$, the *prior*, is the initial degree of belief in A; $\mathrm{P}(B|A)$, the *likelihood function*, is the probability of observing the evidence B assuming that the proposition A is true; and $\mathrm{P}(A|B)$, the *posterior*, is the updated degree of belief in A having accounted for B. The proportionality can be promoted to an equality by introducing a normalisation factor, which will be denoted by $\mathcal{N}$ in the rest of this thesis.

[1] In this definition of p-value, it is assumed that a larger value of t corresponds to a larger difference between the data/pseud-data and H_0.

[2] Considering an event A and an event B, the notation $\mathrm{P}(A|B)$ denotes *the probability of event A occurring, given that event B occurred.*

Consider N PE, of which S have $t \geq t_0$. The probability of observing S events with $t \geq t_0$ is given by the Binomial probability distribution[3]:

$$\mathrm{P}(S|p\text{−value}) = \binom{N}{S} p\text{−value}^S (1 - p\text{−value})^{N-S}. \tag{8.3}$$

Using Bayes' Theorem, the probability of obtaining a given p-value, given S out of N PE having $t \geq t_0$, is:

$$\mathrm{P}(p\text{−value}|S) = \binom{N}{S} p\text{−value}^S (1 - p\text{−value})^{N-S} \times \frac{\pi(p\text{−value})}{\mathcal{N}} \tag{8.4}$$

where $\mathcal{N}$ is a normalisation constant and $\pi(p\text{−value})$ is the prior probability distribution. For a uniform prior of $\pi(p\text{−value}) = 1$, the most likely result for the p-value[4] is S/N. This result allows us to determine a p-value using a finite number of pseudo-experiments.

The significance required for the rejection of H_0 is defined as α, where we claim discovery if p-value $\leq \alpha$, and $\alpha \in [0, 1]$. Also, the probability to *wrongly* rule out H_0 (known as a "Type-I error") is equal to α, namely[5].

$$P(\text{Type-I error}) = P(p\text{−value} \leq \alpha | H_0) = \alpha. \tag{8.5}$$

In general, a hypothesis test must be constructed using the following steps [145]:

- Define a test statistic, t, which describes the difference between data and H_0. In this thesis we shall use definitions of t for which a bigger difference between data and H_0 corresponds to a larger value of t.
- Generate pseudo-experiments of H_0 and find the distribution of the test statistic.
- Calculate a p-value of the test as the fraction of PE resulting in a test statistic greater than, or equal to, the value observed in data.

Thus, the result of the test is a p-value. For a given α and a p-value $= \gamma$, if $\gamma < \alpha$ then we would reject H_0, and if $\gamma > \alpha$ then we would keep H_0. For the first case ($\gamma < \alpha$), the discovery algorithm with the smallest Type-I error probability that would still declare

[3]The Binomial probability distribution function describes the probability of obtaining n successes, out of N trials, given a probability of success p: $\binom{N}{n} p^n (1-p)^{N-n}$, where $\binom{N}{n} = \frac{N!}{n!(N-n)!}$.

[4]This is found by solving $\frac{\partial \mathrm{P}(p\text{−value}|S)}{\partial (p\text{−value})} = 0$.

[5]It is shown in 8.1.5 that this is true no matter what hypothesis test the p-value is coming from, under one condition: that there exist a solution ζ for which $\int_\zeta^\infty \rho_t(x)\,\mathrm{d}x = \alpha$, where ρ_t is the PDF followed by the test statistic (t) under H_0.

discovery, would still have a probability of α to be wrong, i.e. α is the smallest false-discovery probability we can have, if we declare H_0 to be false.

In this thesis two complementary approaches are used in order to quantify the agreement between data and MC simulation.

First of all, a simple $t = -\ln L$ test statistic is used to calculate a p-value, where L is the likelihood of the background prediction being correct, given the observed data[6]. p-values are calculated for each mass bin in χ, such that p-values of lower mass bins can be used as a quantitative indication of background validation. p-values are then calculated for the search regions of the χ and $F_\chi(m_{jj})$ analyses.

Secondly, for $F_\chi(m_{jj})$, the BumpHunter [145] approach is used in order to identify the most discrepant region of the observed spectrum, whilst also producing a $p-$value that includes a trials factor: thus accounting for the fact that we are looking for new physics with more than one test statistic (we must define a new test statistic for each mass window).

8.1.3 $t_\chi = -\ln L_\chi$ test statistic and systematics with χ distributions

In the case of the normalised χ distributions, a test statistic $t_\chi = -\ln L_\chi$ is constructed, where we wish to assess the likelihood of observing d_i events in χ-bin i, given that we are expecting b_i. The likelihood distribution is therefore constructed using a Poisson[7] probability distribution:

$$t_\chi = -\ln L_\chi \equiv -\ln \prod_i L_{\chi,i}(d_i|b_i) = -\sum_i \ln\left[\frac{b_i^{d_i} e^{b_i}}{d_i!}\right]. \tag{8.6}$$

A value of t_χ is calculated for data and also for each of the PE. For each PE, a value of d_i is produced by sampling a Poisson probability distribution with mean b_i. Systematic uncertainties are included as *nuisance parameters*, λ_ν, reflecting the potential variation of the JES and scale uncertainties and their effect on the expected number of events b_i:

$$t_\chi = -\ln L_\chi = -\ln \prod_i \int\int L_i(d_i|b_i,\lambda_\nu) \prod_{\nu=1}^{2} \mathrm{d}\lambda_\nu \tag{8.7}$$

$$= -\sum_i \ln \int\int \left[\frac{b_i(\lambda_\nu)^{d_i} e^{b_i(\lambda_\nu)}}{d_i!}\right] \prod_{\nu=1}^{2} \mathrm{d}\lambda_\nu. \tag{8.8}$$

[6]The exact prescription for calculating a likelihood depends on the type of process under consideration, with two examples being given in this thesis: a Binomial process for $F\chi(m_{jj})$ (see Section 8.1.4) and a Poisson process for χ (see Section 8.1.3).

[7]A Poisson distribution is obtained from a Binomial distribution in the limit of a large sample size N. The probability of obtaining exactly n successes is given by $\nu^n e^{-\nu}/n!$, where ν is the expected number of successes. In terms of the Binomial parameters: $\nu = Np$.

As discussed in Section 7.4.2, the PDF, JER and JAR uncertainties will not be considered, since they are small compared to the JES and scale uncertainties.

The nuisance parameters are varied, in turn, such that their variation is captured into the overall likelihood. Practically, this is done by generating PE for each of the nuisance parameters where each parameter is varied. For the case of the JES, each jet is varied according to a Gaussian of mean 0 and a variance corresponding to a the JES uncertainty for that jet (as described in Section 5.4). This is done for each of 1000 PE[8]. For the case of the systematic uncertainty due to the renormalisation and factorisation scales, each of the 9 variations described in Section 7.4.1 is included on each of the JES pseudo-experiments. This results in $9 \times 1,000 = 9,000$ PE.

A p-value is calculated, for each of the broad bins in dijet mass, as the number of PE resulting in a value of t_χ greater than or equal to the value observed in data. The χ distributions in the lowest 4 mass bins can are used as further background validation (as discussed in Section 7.9), and for the highest mass bin: the p-value is used as an indication of the presence of the NP. The resulting p-values for each dijet mass bin are given in Table 8.1. The p-values for each of

m_{jj} bin [GeV]	p-value
800-1200	0.23
1200-1600	0.31
1600 -2000	0.56
2000-2600	0.83

TABLE 8.1: Comparing χ distributions to QCD predictions. p-values are calculated for each of the broad dijet mass bins using the likelihood defined in Equation 8.8.

the mass bins indicate reasonable agreement with the null hypothesis of QCD background: i.e. non of the p-values are even close to $\alpha = 0.05$.

8.1.4 $t_{F_\chi} = -\ln L_{F_\chi}$ test statistic and systematics with $F_\chi(m_{jj})$

A test statistic $t_{F_\chi} = -\ln L_{F_\chi}$ is constructed from the Binomial probabilities $L_{F_\chi,i}$, for each dijet mass bin i, of observing: d_i data events with $y^* < 0.6$, given that there are D_i data events in total with $y^* < 1.7$, and assuming an expected fraction $F_{\chi,i}$ of events with $y^* < 0.6$ due to background:

$$t_{F_\chi} = -\ln L_{F_\chi} \equiv -\ln \prod_i L_{F_\chi,i}(d_i|D_i, f_i) = -\sum_i \ln \left[\binom{D_i}{d_i} (F_{\chi,i})^{d_i} [1 - F_{\chi,i}]^{D_i - d_i} \right]. \quad (8.9)$$

[8]After performing calculations with varying numbers of PE, it was found that results were unchanged when using > 1000 PE. Values of up to 10000 PE were tried.

For each PE, a value of d_i is produced by sampling a binomial probability distribution with parameters $F_{\chi,i}$ and D_i, where D_i corresponds to the number of events observed in data for mass bin i. Systematic uncertainties are included as *nuisance parameters*, λ_ν, reflecting the potential variation of the JES and scale uncertainties and their effect on the expected fraction $F_{\chi,i}(\lambda_\nu)$:

$$L_{F_\chi,i}(d_i|D_i, F_{\chi,i}(\lambda_\nu)) = \binom{D_i}{d_i}(F_{\chi,i}(\lambda_\nu))^{d_i}[1 - F_{\chi,i}(\lambda_\nu)]^{D_i - d_i}. \tag{8.10}$$

Denoting the JES and scale nuisance parameters as λ_1 and λ_2, respectively, these nuisance parameters are integrated-over in order to convolve systematic uncertainties with the final likelihood:

$$-\ln L_{F_\chi} = -\ln \prod_i \int\int L_{F_\chi,i}(d_i|D_i, F_{\chi,i}(\lambda_1, \lambda_2)) \prod_{\nu=1}^{2} \mathrm{d}\lambda_\nu \tag{8.11}$$

$$= -\sum_i \ln \int\int \binom{D_i}{d_i}(F_{\chi,i}(\lambda_\nu))^{d_i}[1 - F_{\chi,i}(\lambda_\nu)]^{D_i - d_i} \prod_{\nu=1}^{2} \mathrm{d}\lambda_\nu. \tag{8.12}$$

A p-value is calculated for the search region: $m_{jj} > 1798$ GeV. Using the definition in Equation 8.12, values are generated for each of 9,000 PE. The distribution of likelihood values from the 900,000 PE is shown in Figure 8.1, along with the value in data. By looking at the number of PE with a likelihood as extreme, or worse, than the value from data, a $p-$value is determined to be 0.380. This value indicates a reasonable agreement between data and the QCD background prediction, taking all systematic uncertainties into account.

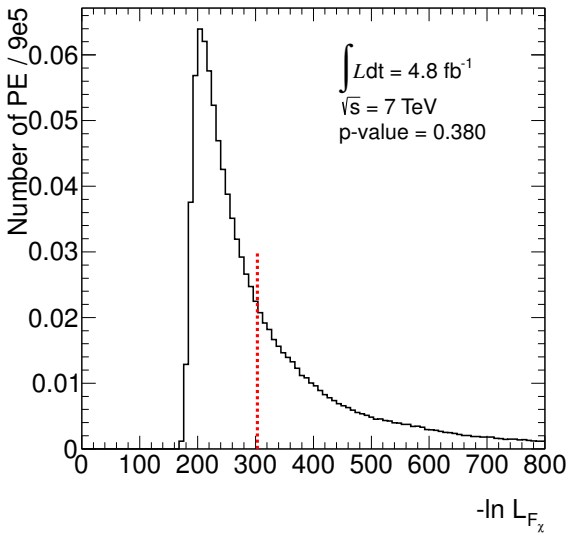

FIGURE 8.1: $-\ln L$ distribution for $F_\chi(m_{jj})$ PE compared to value from data. The corresponding p-value is found to be 0.380.

8.1.5 Statistical interpretation with BumpHunter

The BumpHunter [145] procedure scans localised windows of various width in the $F_\chi(m_{jj})$ spectrum and returns a $p-$value that corresponds to the most discrepant region, i.e. the region where there is the most significant deviation from the predicted QCD background. The size of the window can vary from two to half of the number of dijet mass bins.

Using the results in data, a $p-$value is calculated for each mass window using Equation 8.10. The resulting $p-$value for each mass window combination, is shown in Figure 8.2(a). The figure shows that the mass range $1798-2882$ GeV corresponds to the smallest p-value with a value of $\mathcal{O}(10^{-18})$. However, this p-value does not take into account systematic uncertainties, or the fact that we have performed multiple statistical tests over a much larger mass-range: these effects must be included in a final p-value.

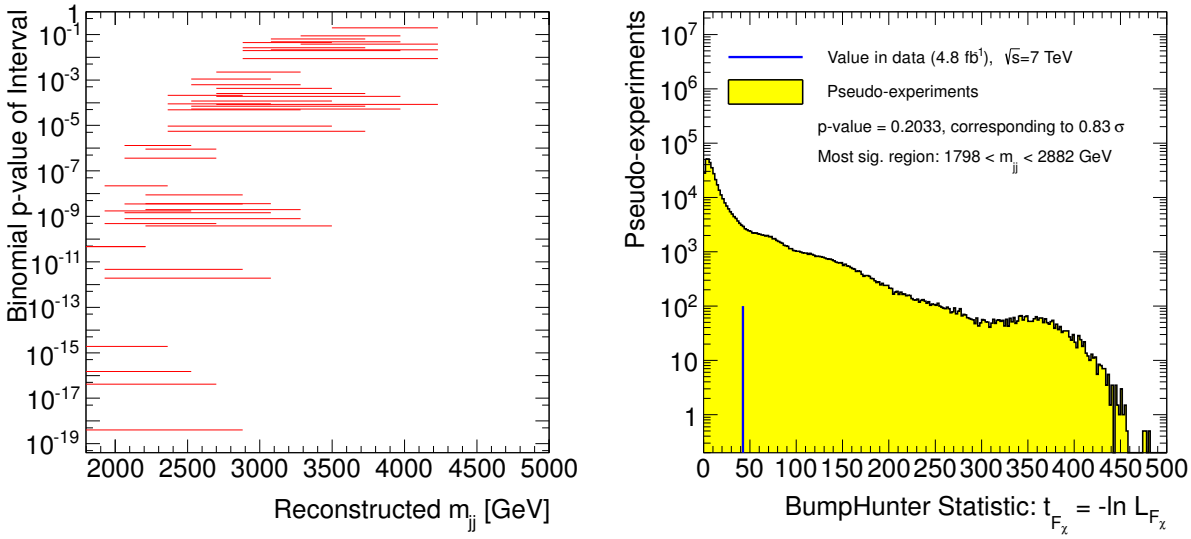

(a) (b)

FIGURE 8.2: (a) Possible resonance-like intervals with the corresponding probabilities in data. Each possible mass window is shown as a red horizontal line. Systematic uncertainties are not included. The interval with the smallest probability is found to be the region 1798 - 2882 GeV. Note that the p-values on the y-axis do not include a look-elsewhere effect. (b) Likelihood distribution determined from pseudo-experiments used to convolve the systematic uncertainties, and include a look-elsewhere effect, are employed to determine the $p-$value that quantifies the agreement between the QCD prediction at data. The resulting $p-$value $= 0.2031$, which corresponds to 0.83 σ.

A corresponding set of p-values calculations is carried out for the 900,000 PE described above: taking statistical and systematic uncertainties into account. The smallest $p-$value for each PE is identified and its $t_{F_\chi} = -\ln L_{F_\chi}$ is entered into the distribution shown in Figure 8.2(b). Taking the smallest $p-$value, regardless of the mass window to which it corresponds, leads

to the inclusion of a trials factor: allowing for the fact that there is no prior belief for a discrepancy to appear at any particular mass range.

Comparing the value of t_{F_χ} in data to the distribution in Figure 8.2(b), we calculate a p-value of 0.2031, which corresponds to a 0.83 σ deviation from the null hypothesis. This result provides no evidence for a significant deviation from our null hypothesis, and therefore no evidence for NP.

8.1.5.1 TailHunter configuration

An alternative configuration of the BumpHunter, known as the TailHunter, is used to search for slow onset effects at the high-mass end of the distribution. The upper edge of each mass window is fixed to the highest dijet mass bin in the spectrum and the search window is then expanded downward, to include lower bins. The method then proceeds in the same vein as the BumpHunter and the results are shown in Figures 8.3(a) and 8.3(b). The most discrepant region in data corresponds to the region $m_{jj} > 1798$ GeV (i.e. the

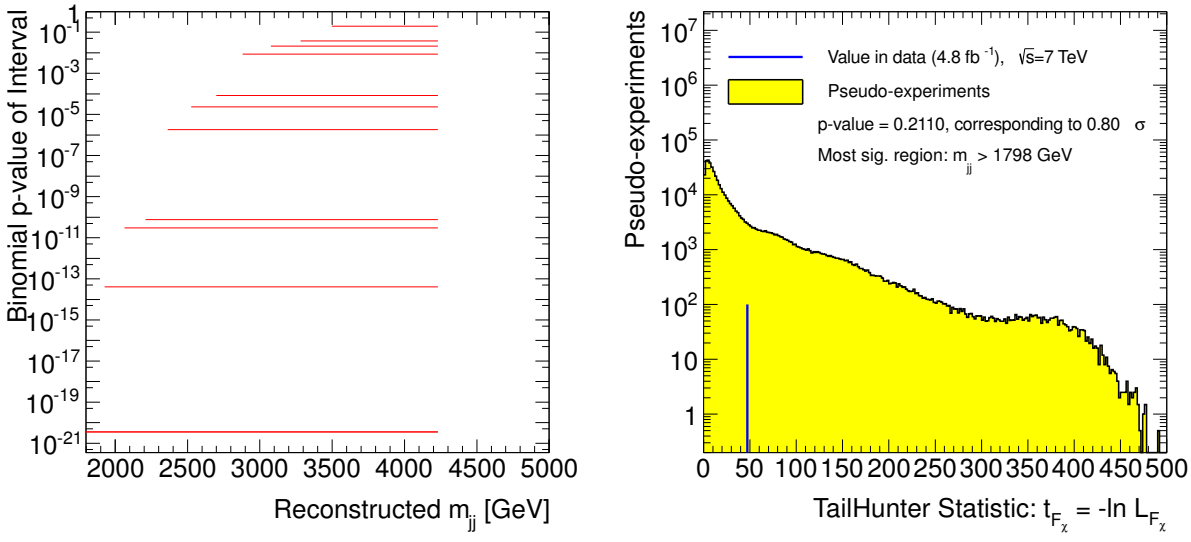

(a) (b)

FIGURE 8.3: (a) Possible threshold-like intervals with the corresponding probabilities in data. Each possible mass window is shown as a red horizontal line. Systematic uncertainties are not included. The interval with the smallest probability is found to be the region $m_{jj} > 1798$ GeV. Note that the p-values on the y-axis do not include a look-elsewhere effect. (b) Likelihood distribution determined from pseudo-experiments used to convolve the systematic uncertainties are employed to determine the $p-$value that quantifies the agreement between the QCD prediction at data. The resulting $p-$value = 0.2111, which corresponds to 0.80 σ.

whole mass range), with a p-value = 0.2111, corresponding to a 0.80 σ deviation from the null hypothesis. Again, this result indicates no evidence for NP.

8.2 Limit-setting phase: constraints on new physics

In order to draw quantitative conclusions from a search for new physics, a null hypothesis and at least one alternative hypothesis is defined. In this thesis, alternative hypotheses consist of particular new physics models, for which a model parameter is allowed to vary. In this case, an upper or lower limit can be placed on the values of this free parameter, at some credibility level. For example, in a BSM scenario with extra dimensions it is useful to establish which values of the fundamental Planck mass have been excluded by the data. Since data are subject to statistical fluctuations, one must define a convention from which a conclusion can be drawn that is *beyond reasonable doubt*. In this thesis, limits are set at the $(1 - \alpha) = 95\%$ credibility level.

8.2.1 Acceptance for signal samples

In Figure 8.4, the acceptance $\times$ efficiency for each signal considered in this thesis. These values are calculated by comparing the initial number of events in each MC sample, to the the number of events passing the complete event selection specified in Section 7.1. Values are shown as a function of the signal model parameters: i.e. M_D for the QBH samples, M_{q^*} for the excited quarks and Λ for the contract interactions.

It can be seen that the acceptance and efficiency are roughly constant across the respective parameter ranges. In the remainder of this thesis, the combined acceptance $\times$ efficiency is denoted by $\mathcal{A}$.

8.2.2 Limit setting with $F_\chi(m_{jj})$

As discussed in previous chapters, the $F_\chi(m_{jj})$ spectrum is sensitive to both resonant NP and also processes with a slow-onset in mass. Example distributions of the signal samples considered in this thesis are shown in Figure 6.9.

Two different limit setting approaches are employed depending on whether the signal model under consideration interferes with the QCD background. For models such as excited quarks and quantum black holes, which do not interfere with QCD, there is the possibility to calculate a limit on the cross-section times acceptance for the model across the whole mass spectrum. An alternative method must be used in the case of quark contact interactions. The distinction between the two cases is made clear in the following two subsections.

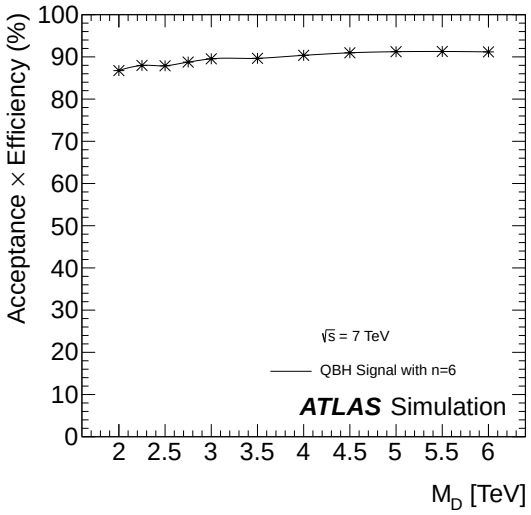

(a) QBH Signal Sample with $n = 6$.

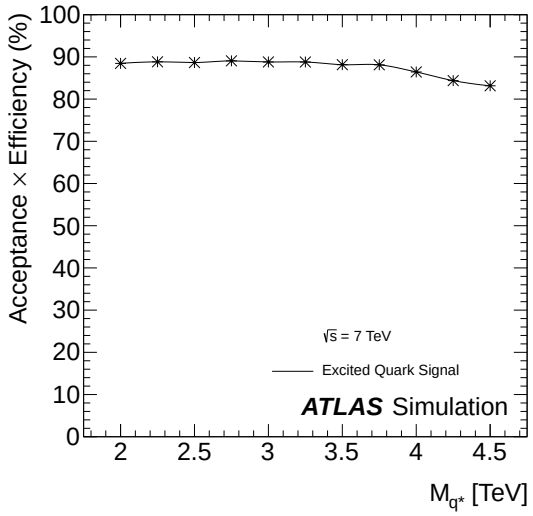

(b) Excited Quark Signal Samples

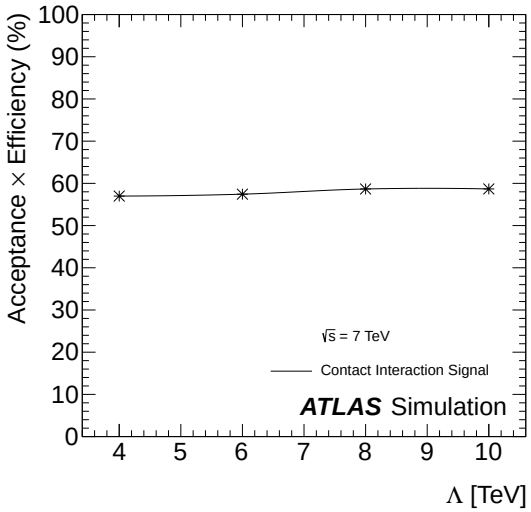

(c) Contact Interaction Signal Samples

FIGURE 8.4: Acceptance times efficiency for each of the signals considered in this thesis. Values are shown as a function of the main signal parameters.

8.2.2.1 Limits on models that do not interfere with QCD

For a NP scenario that does not interfere with the dominant QCD background, it is possible to set a limit on $\alpha \times (\sigma \times \mathcal{A})$, where σ is the cross-section for a given signal, $\mathcal{A}$ is the acceptance[9] and α is a positive scaling factor. Starting with the likelihood defined in Equation 8.12, a likelihood is calculated after an amount $\alpha_\theta (\geq 0)$ of signal sample θ has been added to the

[9]In this thesis, the acceptance $\mathcal{A}$ is defined to include both the detector acceptance and efficiency.

NLO QCD background[10]:

$$L_{F_\chi,i}(d_i|D_i, F_{\chi,i}(\lambda_\nu)) \rightarrow L_{F_\chi,i}(d_i|D_i, F_{\chi,i}(\alpha_\theta, \lambda_\nu)),$$

where $F_{\chi,i}$ is now a function of α_θ, as well as a function of each λ_ν. In a given mass bin, the number of QCD background events with $|y^*| < 0.6$ and $|y^*| < 1.7$ are denoted by b_{inner} and b_{total}, respectively. The corresponding number of events from the signal prediction are αs_{inner} and αs_{total}. The expected value of $F_{\chi,i}(\alpha)$ is therefore given by $(b_{inner} + \alpha s_{inner})/(b_{total} + \alpha s_{total})$. Since the signal prediction is also subject to nuisance parameters:

$$F_{\chi,i}(\alpha, \lambda_\nu) = \frac{b_{inner}(\lambda_\nu) + \alpha s_{inner}(\lambda_\nu)}{b_{total}(\lambda_\nu) + \alpha s_{total}(\lambda_\nu)}. \tag{8.13}$$

Using Bayes Theorem (See Equation 8.4), a limit can then calculated at the 95% CL:

$$\begin{aligned} 0.95 &= \int_0^{\alpha_\theta^{\text{limit}}} L_{F_\chi}(F_\chi(\alpha_\theta)|d_i, D_i)\ \mathrm{d}\alpha_\theta & (8.14)\\ &= \int_0^{\alpha_\theta^{\text{limi}}} L_{F_\chi}(d_i|F_\chi(\alpha_\theta), D_i) \times \frac{\pi(F_\chi(\alpha_\theta, D_i))}{\mathcal{N}}\ \mathrm{d}\alpha_\theta & (8.15)\\ &= \frac{1}{\mathcal{N}} \int_0^{\alpha_\theta^{\text{limit}}} \sum_i \ln \int\int \left[\binom{D_i}{d_i} F_{\chi,i}(\alpha_\theta, \lambda_\nu)^{d_i} [1 - F_{\chi,i}(\alpha_\theta, \lambda_\nu)]^{D_i - d_i} \right] \prod_{\nu=1}^{2} \mathrm{d}\lambda_\nu \mathrm{d}\alpha_\theta, \end{aligned}$$

where a constant prior, $\pi(F_\chi, D_i)$ has been assumed[11].

In practice, values of $\hat{\alpha}_\theta$ are chosen according to[12]:

$$\hat{\alpha}_\theta(n) = 10^{(-5+10n/1000)}, \tag{8.16}$$

where $n = 1, \ldots, 1000$. These choices of $\hat{\alpha}_\theta$ ensure a full coverage over the full range of 10^{-5} to 10^5. Increasing the number of steps was found to have an insignificant effect on the final result, and a range of 10^{-5} to 10^5 in $\hat{\alpha}_\theta$ was found to be sufficient to contain the limit of each signal.

For each value of $\hat{\alpha}_\theta$, the likelihood is calculated, as described in the previous section. A sum is formed of the likelihoods of increasing values of $\hat{\alpha}_\theta$ (normalised to the total sum of all likelihoods) to a value of 0.95. The value of $\hat{\alpha}_\theta$ corresponding to last likelihood in the sum,

[10] As described in Chapter 7, the NLO QCD background is produced by multiplying LO QCD spectra for $F_\chi(m_{jj})$ and χ with bin-wise NLO k-factors.

[11] This is a reasonable assumption, since there is no reason to prefer one version of new physics to another.

[12] Note that the final limit figures (e.g. Figure 8.5) are plotted with a log-scale on the y-axis. The distribution of $\hat{\alpha}_\theta$ is chosen to reflect the distribution of the resulting likelihoods and ensure a good coverage over the full range of $\hat{\alpha}_\theta$.

is $\hat{\alpha}_\theta^{\text{limit}}$:

$$0.95 = \frac{\sum_{\hat{\alpha}_\theta=10^{-5}}^{\hat{\alpha}_\theta=\hat{\alpha}_\theta^{\text{limit}}} L_{F_\chi}(d_i|F_\chi(\hat{\alpha}_\theta), D_i)}{\sum_{\hat{\alpha}_\theta=10^{-5}}^{\hat{\alpha}_\theta=10^{5}} L_{F_\chi}(d_i|F_\chi(\hat{\alpha}_\theta), D_i)}. \tag{8.17}$$

For each signal sample, θ, a value of $\hat{\alpha}_\theta^{\text{limit}}$ is calculated in data and for each PE. Looking at Figure 8.5, as an example of a limit setting procedure for an excited quark, the black points represent the values of $\hat{\alpha}_\theta^{\text{limit}} \times \sigma_\theta \times \mathcal{A}$, from data, for each of the signal samples (which are parameterised by different excited quark masses). The black dashed line surrounded by green and yellow bands represent the mean, 1-σ and 2-σ values in the distribution of $\hat{\alpha}_\theta^{\text{limit}}$ values coming from the 900,000 PEs.

The red dotted line in the figure, is formed from the values of $\sigma_\theta \times \mathcal{A}$ for each signal sample. The points where the black dashed curve and the black solid curve cross the red dotted curve determine the expected and observed upper limits on the model parameter[13], respectively.

Limits are set on both the excited quark model (q^*) and the quantum black hole model (QBH). The resulting limits for the excited quark (with the corrected FSR as explained in Section 4.3) are shown in Figure 8.5. The analysis results in a lower limit on the mass of the q^*, with an expected limit of 2.85 TeV and an observed limit of 2.75 TeV. Acceptance values for the q^* mass points range between 86-89%.

For the Pythia 6 excited quark model with the mis-calculated FSR, the observed (expected) limit is 2.86 TeV (2.95 TeV). This result in included in order to aid comparison to previous ATLAS limits, as well as limits set by other experiments.

In the case of the QBH model, the limit setting is performed using signal samples with $n = 6$ extra dimensions. Truth level distributions for QBH samples with a range of values of n are shown in Figure 8.6. Figure 8.6(a) shows the normalised χ distributions for values of n ranging from 3 to 7 - note that these distributions do not include QCD. Since these distributions are normalised (and given they do not contain any SM QCD background) it is clear that the angular distribution is independent of n. Figure 8.6(b) shows the cumulative distributions of the normalised cross-section for values of n ranging from 3 to 7 - again, note that these distributions do not include QCD. The fact that the cumulative dijet mass profile for QBH is largely independent of n above the dijet mass thresholds that we are considering, also suggests an acceptance independent of n in this mass region.

It is clear that the mass profile for the QBH samples is also largely independent of n. It is therefore concluded that the acceptance of a given QBH signal mass point, is independent of

[13] In the case of Figure 8.5, the model parameter, on which limits are set, is the mass of the excited quark: m_{q^*}.

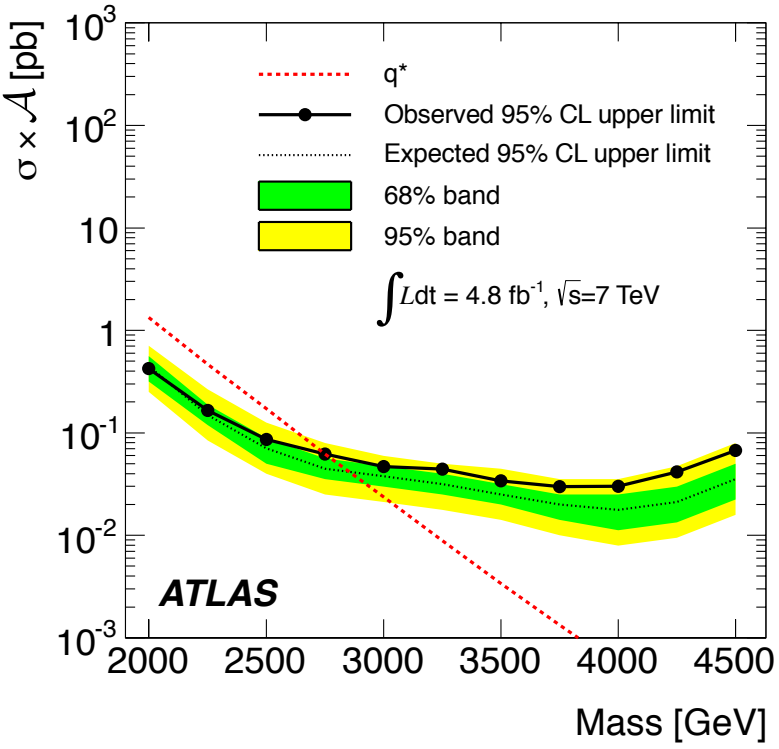

FIGURE 8.5: The 95% CL upper limits of $\sigma \times \mathcal{A}$ as a function of the q^* mass using $F_\chi(m_{jj})$ (black filled circles). The black dashed curve shows the 95% CL upper limit expected from Monte Carlo and the light and dark yellow shaded bands represent the 68% and 95% contours of the expected limit, respectively. Theoretical predictions of $\sigma \times \mathcal{A}$ for the excited quark model as shown as dotted lines. The observed (expected) limit occurs at the crossing of the theory curve with the observed (expected) 95% CL upper limit curve.

n extra dimensions	Expected limit (TeV)	Observed limit (TeV)
2	3.85	3.71
3	3.99	3.84
4	4.07	3.92
5	4.12	3.99
6	4.16	4.03
7	4.19	4.07

TABLE 8.2: Lower limits at the 95% CL on M_D of the QBH model with $n = 2 - 7$ extra dimensions.

the number of extra spatial dimensions. The acceptance of the fully-simulated $n = 6$ QBH sample, which is close to 90 % for all values of M_D, is then used as the acceptance for other values of n and the resulting theory lines can be included in Figure 8.7. The resulting limits on the reduced Planck Scale M_D for the QBH model are shown in Table 8.2.

This approach to limit setting is dependent upon the ability to add an arbitrary amount of signal to the QCD background, which can only easily be done for models where interference

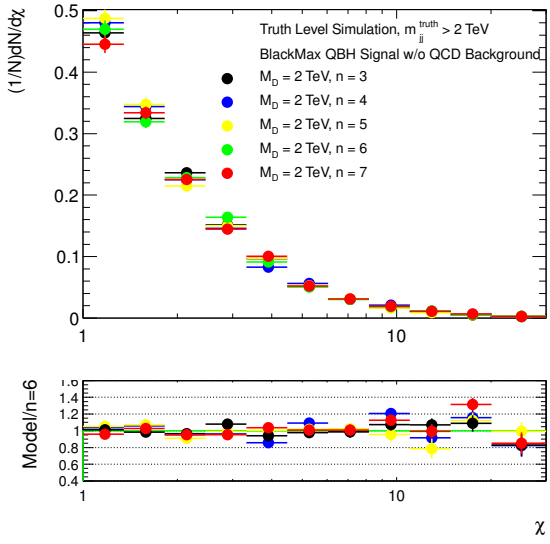

(a) Normalised χ distributions

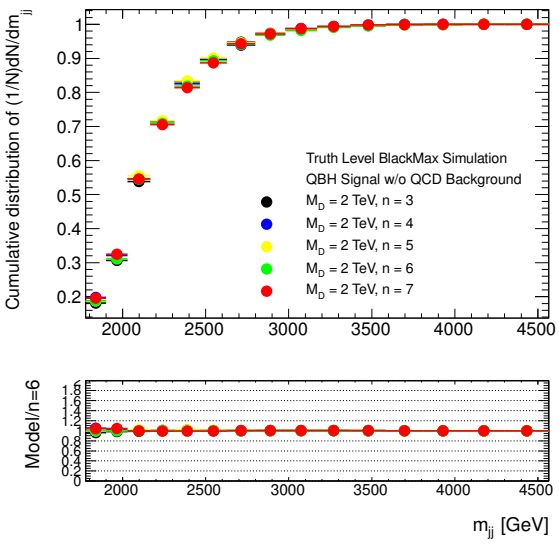

(b) Cumulative normalised dijet mass profile

FIGURE 8.6: Distributions for QBH signal samples with $n = 3, 4, 5, 6$ and 7. QCD background is not included. Distributions suggest that angular distribution and mass profile is independent of n.

with the QCD background is not a consideration.

8.2.2.2 Limits on quark contact interactions

MC samples of LO QCD production modified by quark **C**ontact **I**nteractions (CI) (as described in Section 4.3.2) are created for values of Λ ranging from 4.0 to 10.0 TeV. For the CI distributions, QCD k-factors must be applied to the QCD-only components of the inner and outer dijet mass spectra that form the numerator and denominator of $F_\chi(m_{jj})$ respectively. This is done by subtracting the LO QCD cross section from each sample, and then re-adding the QCD cross section after the NLO correction has been included.

Individual $F_\chi(m_{jj})$ distributions are smoothed by a fit in m_{jj}. For the pure QCD samples (corresponding to $\Lambda = \infty$) a second order polynomial is used, while for the MC distributions with finite Λ, a Fermi function is added to the polynomial. The final fit function has the form

$$f(x) = p_4 \times (1/\exp(p_1 \times (p_2 - \log(x))) + 1) + p_3, \quad x = 1/\Lambda^2 \tag{8.18}$$

where p_1, p_2, p_3 and p_4 are parameters of the fit. Next, all m_{jj} bins of the MC $F_\chi(m_{jj})$ distributions are interpolated in Λ creating a smooth predicted $F_\chi(m_{jj})$ surface as a function of m_{jj} and Λ. This surface enables integration in m_{jj} vs Λ for continuous values of Λ and is shown in Figure 8.8.

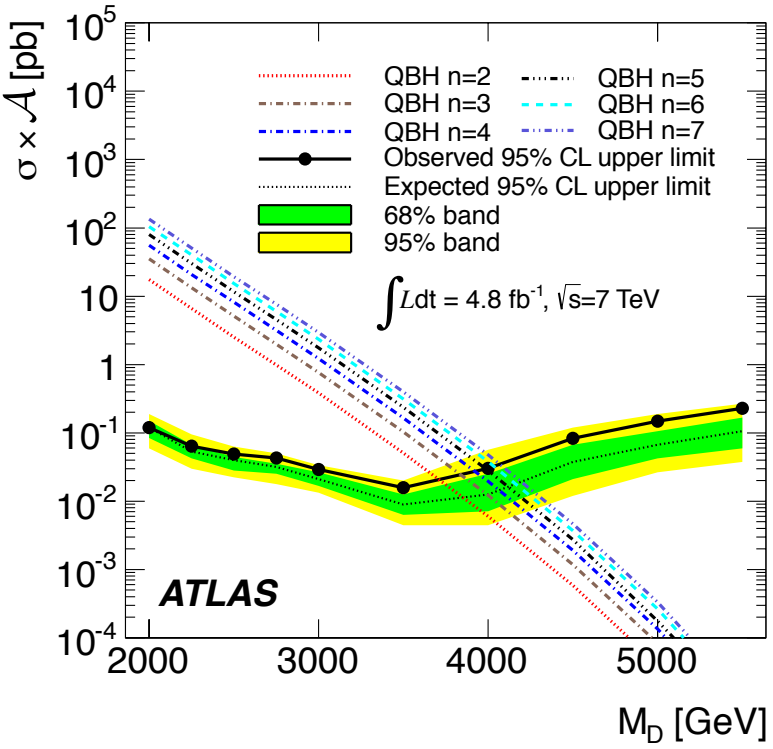

FIGURE 8.7: The 95% CL upper limits of $\sigma \times \mathcal{A}$ as a function of the reduced Planck Mass M_D of the QBH model using $F_\chi(m_{jj})$ (black filled circles). The black dashed curve shows the 95% CL upper limit expected from Monte Carlo and the light and dark yellow shaded bands represent the 68% and 95% contours of the expected limit, respectively. Theoretical predictions of $\sigma \times \mathcal{A}$ are shown for various numbers of extra dimensions. The observed (expected) limit occurs at the crossing of the theory curve with the observed (expected) 95% CL upper limit curve.

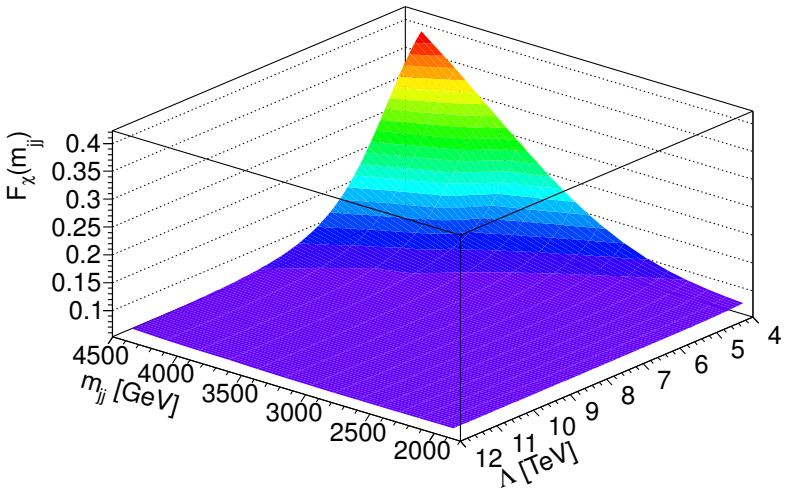

FIGURE 8.8: 2-dimensional surface of F_χ for quark contact interactions as a function of Λ and m_{jj}.

Pseudo-experiments and a Bayesian limit method is then employed to construct a posterior probability, assuming a prior that is flat in $1/\Lambda^4$. For the case of destructive interference (defined in Section 4.3.2), this analysis sets a 95% CL observed (expected) lower limit on $\Lambda > 7.6$ TeV ($\Lambda > 7.7$ TeV). The observed posterior probability distribution function is shown in Figure 8.9.

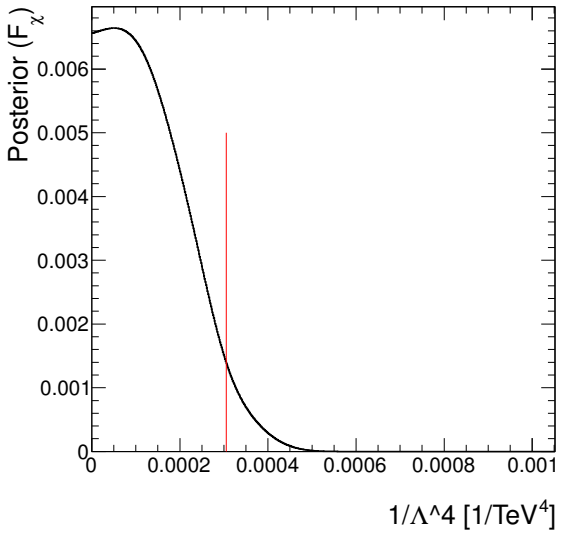

FIGURE 8.9: Limit setting for contact interactions using the $F_\chi(m_{jj})$ distribution: observed posterior probability distribution function including systematic uncertainties due to JES and scale uncertainty.

8.2.3 Limit setting with benchmark χ distributions

The highest mass bin in Figure 7.15 is used to set 95% CL limits on two NP hypotheses, CI and QBH. In the contact interaction analysis, four MC samples of QCD production modified by a contact interaction are created for values of Λ ranging from 4.0 TeV to 10.0 TeV. For the CI distributions, QCD k-factors are applied to the QCD-only component of the cross section, as follows: before normalising the χ-distributions, the LO QCD part of the cross section, determined from a QCD-only simulation sample, is replaced by the QCD cross-section corrected for NLO effects.

Using the QCD distribution and finite set of MC CI distributions, each χ-bin is fit as a function of Λ against a four-parameter interpolation function[14], allowing for smooth integration of the posterior probability density functions over Λ. From the signal fits, a posterior probability density is constructed as a function of Λ. The systematic uncertainties described in the previous chapter are convolved with the posterior distribution through PE, in the

[14]This function has the same form as Equation 8.18.

same way as the $F_\chi(m_{jj})$ analysis. For the expected limit, PE are performed on the QCD background and used as pseudo-data: as with the $F_\chi(m_{jj})$ analysis. This analysis sets a 95% CL lower limit on Λ at 7.6 TeV with an expected limit of 7.7 TeV.

An analogous method is used to set limits on QBH, using eleven signal samples with M_D ranging from 2.0 TeV to 6.0 TeV. A constant prior in $1/M_D^4$ is used, since this is proportional to the cross-section. This analysis results in an expected and observed 95% CL lower limit on M_D of 4.20 TeV and 4.11 TeV, respectively.

Chapter 9

Summary and conclusions

9.1 Summary of results

In this chapter, the results of this thesis will be summarised, and compared to results form independent analysis methods and experiments. Possible future analyses and developments are also discussed, before concluding.

9.1.1 Results from search phase

Angular distributions of jet pairs (dijets) produced in proton-proton collisions at a centre-of-mass energy $\sqrt{s} = 7$ TeV have been studied with the ATLAS detector at the Large Hadron Collider using the full 2011 data set with an integrated luminosity of 4.8 fb^{-1}, and reaching dijet masses up to 4.5 TeV.

Searches are made by comparing data to an NLO QCD MC simulation, which presents the dominant background for a search of this kind. The associated systematic uncertainties have been considered, with the dominant contributions being due to the Jet Energy Scale uncertainty and the uncertainty on the renormalisation and factorisation scale, μ_R and μ_F.

Searches have been performed by slicing the dijet angular-mass phase space in two ways: normalised χ distributions are more sensitive to angular information, with a course bins of dijet mass; whilst $F_\chi(m_{jj})$ sacrifices some angular information in order to take advantage of a finer granularity in mass.

Once the background hypothesis was found to provide a good description of the data in specified *control regions*, a quantitative search for significant deviations from the predicted background was performed in pre-specified *search regions* of the phase space.

For the analysis with χ distributions, a p-value for the the search region ($m_{jj} > 2$ TeV) was calculated, including systematic uncertainties, and found to be 0.83. This value indicates reasonable agreement with the null hypothesis of QCD background.

For the $F_\chi(m_{jj})$ analysis, a p-value for the search region ($m_{jj} > 1798$ GeV) was calculated, including systematic uncertainties, and was found to be 0.380. This value indicates a reasonable agreement with the null hypothesis of QCD background.

The BumpHunter search algorithm was also applied to the $F_\chi(m_{jj})$ distribution, including systematic uncertainties, which identified the mass range $1798 < m_{jj} < 2882$ GeV as the region with the most significant discrepancy between the data and the QCD null hypothesis. The p-value for this discrepancy, including look elsewhere effect, is 0.2031. This p-value does not suggest the presence of any new physics effect.

9.1.2 Results from limiting setting stage

Dijet angular distributions have been studied by the ATLAS experiment over a large angular range and spanning dijet mass up to approximately 4.0 TeV. Since, all angular distributions are consistent with QCD predictions, this analysis places limits on hypotheses of physics phenomena beyond the Standard Model, including quark substructure and strong gravity. The resulting limits described in this thesis are presented in Table 9.1.

Model and Analysis Strategy	95% C.L Limits [TeV]	
	Expected	Observed
Excited quark, mass of q^*		
Resonance in $F_\chi(m_{jj})$	2.85	2.75
Contact interaction, Λ, destructive interference		
$F_\chi(m_{jj})$	7.7	7.6
χ, $m_{jj} > 2.6$ TeV	7.7	7.6
Quantum black hole for $n = 6$, M_D		
$F_\chi(m_{jj})$	4.16	4.13
χ, $m_{jj} > 2.6$ TeV	4.20	4.11

TABLE 9.1: The 95% CL lower limits on the masses and energy scales of the models exampled in this thesis. All limit analyses are Bayesian, with statistical and systematic uncertainties included.

For $\sqrt{s} = 7$ TeV pp collisions at the LHC, the integrated luminosity used in the current studies represents a substantial increase over that available in previously published ATLAS dijet searches. A comparison of previous dijet angular analysis results from ATLAS is presented in Table 9.2.

	36 pb^{-1} [15]	4.8 fb^{-1} [31]
	Excited quark, mass of q^*	
$F_\chi(m_{jj})$	2.12 TeV	2.85 TeV
	Quantum black hole for $n = 6$, M_D	
$F_\chi(m_{jj})$	3.49 TeV	4.16 TeV
χ	3.36 TeV ($m_{jj} > 2$ TeV)	4.20 TeV ($m_{jj} > 2.6$ TeV)
	Contact interaction, Λ, destructive interference	
$F_\chi(m_{jj})$	5.2 TeV	7.7 TeV
χ	5.4 TeV ($m_{jj} > 2$ TeV)	7.7 TeV ($m_{jj} > 2.6$ TeV)

TABLE 9.2: ATLAS previous and current expected 95% CL upper limits on new phenomena. The current expected limits for q^* cannot be compared directly to the previous limits since they have employed PYTHIA 6 samples with an error in the simulation of final state radiation. Had such samples been used in the current analysis, the expected q^* limit would be 0.10 TeV higher. For the 36 pb^{-1} [15] results, the more conservative Bayesian $F_\chi(m_{jj})$ limit on Λ is quoted.

No other experiments have set limits on the QBH model described in this thesis, nor have limits successfully been set using alternative final state signatures. The CMS collaboration has, however, published results on a similar QBH model, which allow for a difference between M_D and the minimum possible black hole mass [146]. With a branching ratio of 96.35 % to dijet final states (see Table 4.2), the QBH signal will be much weaker in other final states. However, there are plans within ATLAS to set limits on this model in the analysis that searches for new particles decaying into top - anti-top quark pairs. Although the limits on M_D from this analysis more stringent that those given in Section 4.1.2, they are, unfortunately, not directly comparable due differences in the underlying extra dimensional models and phenomenology.

The excited quark model has been investigated in other experiments, and other final states. The best non-LHC exclusion limits, to-date, on the mass of the q^* were set by CDF Run 2 at the Tevatron ($\sqrt{s} = 1.96$ TeV) and excluded the mass region $260 < m_{q^*} < 870$ GeV [102]. From the CMS experiment (also with $\sqrt{s} = 7$ TeV), a limit has been calculated in the dijet channel of $m_{jj} > 3.32$ TeV [146], and also a limit in the $q^* \to qW$ and $q^* \to qZ$ of $m_{jj} > 2.38$ TeV and $m_{jj} > 2.15$ TeV, respectively [147]. Within ATLAS, limits on m_{q^*} have been calculated for γ-jet final states ($m_{q^*} > 2.46$ TeV) [148].

The quark contact interaction model has also been investigated for alternative final states, and by other experiments. Previous restrictions on the scale Λ of such contact interactions have been placed using data from the Tevatron ($\sqrt{s} = 1.96$ TeV) excluding $\Lambda_{qq} > 2.7$ TeV at the 95% confidence level [106]. Within ATLAS, limits have been placed on Λ by analysing finals states with two leptons [149] ranging from 9.0 to 13.9 TeV, depending upon the lepton flavour and the exact model configuration. The CMS experiment has also published results: setting limits using the inclusive jet p_T spectrum of $\Lambda > 9.9 - 14.3$ TeV, depending upon the exact model configuration [150]; and also setting limits in the dimuon channel of $\Lambda > 9.5$ TeV [151].

Note that a direct comparison cannot be easily made between the above results from competing experiments and analyses. This is due to the fact that different statistical methods (e.g. Bayesian vs Frequentist) and also different new physics model parameters have been used.

9.2 Comparison of dijet analysis techniques

As discussed in Section 6.4, when comparing limits from the χ and $F_\chi(m_{jj})$ analyses, the χ distributions give up some resolution in m_{jj} in order to achieve a high precision measurement of the changing shape of the angular distribution as m_{jj} rises. Each limit setting method will therefore make more use of information about either the angular or the mass differences between the SM background and NP signal.

From Table 9.1, we see that the limits calculated using χ and $F_\chi(m_{jj})$ are the same for the contact interaction model. However, for the QBH model the expected limit on M_D calculated from the χ distribution is larger than the expected limit calculated from the $F_\chi(m_{jj})$ distribution. Given the expected limit of $M_D = 4.20$ TeV from the χ analysis, Figures 6.8 and 6.9 suggest why this is the case. Figure 6.9 shows that the $M_D = 4$ TeV begins to depart from the QCD background at around 2.5 TeV. This is very close to the lower boundary for the search region in χ. Therefore, one explanation of a high limit using χ, could be due to the *coincidence* of choosing a search region in χ (whose definition is independent of any particular NP model), which happens to contain close to the optimal value for the signal to background ratio, whilst also retaining the higher resolution angular information.

9.2.1 The independent dijet resonance search

Within [31], and alongside other previous ATLAS dijet angular distribution publications [15], searches for NP have been performed using the dijet mass spectrum. Whilst the event selection for this analysis is close to that of the angular analyses in many ways, there are also some big differences. Most importantly, the resonance analysis does not make use of a MC simulation to model the SM QCD background. Instead, a fit is performed of the dijet mass spectrum in data, and then deviations from this fit are quantified. The fit function is of the form $f(x) = p_1(1-x)^{p_2}x^{p_3+p_4\ln x}$, where $x = m_{jj}/\sqrt{s}$ and p_1, p_2, p_3 and p_4 are parameters of the fit. In the event that there is no feature in the spectrum with a significant deviation from the fit, limits setting calculations are performed, where the fit is used as the null hypothesis.

Using a fit, as opposed to a NLO QCD prediction, makes for a streamlined analysis process, allowing the production of fast and reliable results. Whilst the use of a fit also eliminates systematic uncertainties due to the scale and PDF uncertainties associated with the QCD MC, the analysis is subject to an uncertainty associated with the fit itself, and also an uncertainty due to the luminosity of the data that is being fitted. The use of a fit can also reduce sensitivity to the effects of some NP signals. For example, it is possible to fit a NP scenario which predicts a smooth departure from the SM as a function of m_{jj}, or even a very broad resonance that extends to high dijet invariant masses.

The BumpHunter procedure is performed on the m_{jj} spectrum, where for each window under consideration, a new null hypothesis is calculated: as the fit of the dijet mass spectrum excluding the window under consideration. Using the full 2011 dataset, corresponding to 4.8 fb^{-1}, the most discrepant region is found to be 2.21 TeV to 2.88 TeV. The probability of observing such an excess or larger somewhere in the mass spectrum for a background-only hypothesis is 0.69. This test shows no evidence for a resonance signal in the m_{jj} spectrum.

For the independent dijet resonance analysis, expected and observed limits are calculated for the mass of the q^* with values of 2.94 TeV and 2.83 TeV, respectively. The expected limit from the m_{jj} search is better than that from the $F_\chi(m_{jj})$ analysis by 0.9 TeV. This can be explained by considering the above differences between the background predictions for the analyses.

9.3 Future work and conclusions

For 2012 running, the collision of the LHC have been raised from 7 TeV to 8 TeV. The higher energy, and the associated rise in parton luminosity, will increase search sensitivities and the possibility of NP discoveries. The analysis presented in this thesis will, most likely, present the last analysis of its kind for proton-proton collisions at $\sqrt{s} = 7$ TeV and will therefore provide a reference for the study of energy-dependent effects in $\sqrt{s} = 8$ TeV proton-proton collisions, and future experiments. In terms of analysis methodology and techniques, there is still room for improvement and advancement in a few areas.

As the tools for QCD calculation and simulation improve, it may be possible to reduce the effect of systematic uncertainties due to factorisation and renormalisation scales, whilst also potentially allowing the possibility of higher order QCD simulation (NNLO and beyond). It is also hoped that the uncertainty due to JES can be reduced in future analyses: new techniques aiming calibrate the energy of the highest energy jets are under development within the ATLAS collaboration and will hopefully be deployed soon.

Whilst it may be possible to focus a search for resonant new physics decaying into heavier quark flavours, such as the bottom and top quark, the arguments for disentangling angular behaviour as described in this thesis will probably not apply. This is due to the fact that SM production of heavier quark flavours, at the high dijet masses in question, will have a larger contribution from s-channel processes.

In any event, as the LHC probes yet higher energies, it is hoped that the analysis techniques and discussion in this thesis will be utilised and developed further - and with any luck will contribute to the discovery of physics beyond the standard model - which ever form this may take.

Chapter 10

Metadata aided run selection

Management of the large volume of data collected by any large scale scientific experiment requires the collection of coherent metadata quantities, which can be used by reconstruction or analysis programs and/or user interfaces, to pinpoint collections of data needed for specific purposes.

In this chapter, a new web based interface called "runBrowser"[1], which makes these Conditions Metadata available as a Run based selection service, is introduced.

This chapter is based on results [20], which I presented at the CHEP 2010 conference in Taipei, Taiwan.

10.1 Introduction & motivation

The LHC is currently the world's largest and highest energy particle accelerator. After over 10 years of waiting, thousands of physicists scattered throughout the world are eager to get their hands on this long awaited data. With beam crossings at a rate of $10^9\ \mathrm{s}^{-1}$ during regular LHC operation, the ATLAS detector will produce petabytes of data which must be managed and processed in a computing grid which extends world-wide.

As we deal with these new levels of data acquisition rates, size and complexity, it is increasingly important to ensure that data, and metadata (i.e. data about data) are stored in an efficient and easily accessible manner which is able to take advantage of the latest database, software and internet technologies available. This is achieved through the use of various

[1] *runBrowser* has recently been renamed *COMA Browser*

database systems coupled with a variety of purpose built interfaces: each with a different role and purpose.

10.2 ATLAS Conditions Database

Over the course of a physics Run[2], there are many variables relating to the operation of the beam and detector which can vary considerably. These 'conditions' are not recorded on an event-by-event basis but are instead organised into an **IOV** (**I**nterval **O**f **V**alidity). This can be an interval in time or a period specified by a range of Run Numbers or Luminosity Blocks[3]. 'Conditions data' are stored in the ATLAS Conditions Database which is accessed using the **COOL** (**C**onditions database **O**f **O**bjects for **L**HC) **API** (**A**pplication **P**rogramming **I**nterface).

Examples of conditions stored in the ATLAS Conditions Database are: LHC beam conditions, online configuration and operation, calibration & alignment, data quality, luminosity normalisation, object reconstruction efficiency and book-keeping data for various cross checks of data completeness/integrity.

The runQuery [152] utility is the web interface to Run-related information in the Conditions Database. Users are able to find Runs and their associated information using a command line interface. This interface does not however allow the user to see what they are selecting from. Output from runQuery is in the form of a human-readable table and an XML output[4] containing all Luminosity Blocks from the selected Runs.

10.2.1 Metadata

Management of the large volume of data collected by any large scale scientific experiment requires the collection of coherent Metadata quantities, which can be used by reconstruction or analysis programs and/or user interfaces, to pinpoint collections of data needed for specific purposes. The production of these metadata has many advantages [153] making it possible to

[2] A Run is a consecutive interval of time of data recording, usually a few hours in duration, during which many aspects of the detector configuration are constant.

[3] A Luminosity Block is a period in time, usually lasting a few minutes, for which the instantaneous luminosity is approximately constant.

[4] This format is that of a 'Good Run List' [135] which can be used within the ATLAS Athena framework allowing users to run their analysis on only those luminosity blocks which have satisfied their selection criteria. This analysis can be run on the Grid where it will automatically locate and run over only the files necessary to include all the specified runs.

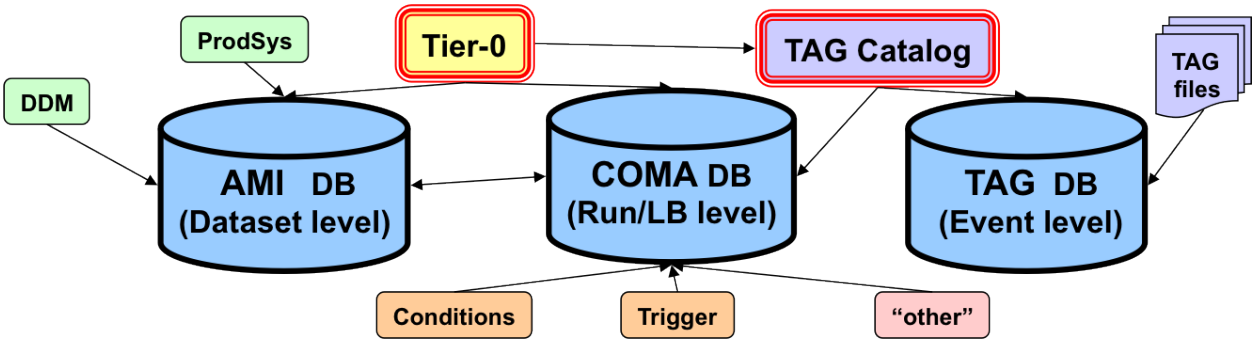

FIGURE 10.1: The three dedicated metadata repositories in the ATLAS Experiment [154]. The **AMI** (**A**TLAS **M**etadata **I**nterface) database stores metadata about datasets, with inputs from Distributed Data Management (DDM), Production Systems (ProdSys) and the Tier-0 of the Grid. The COMA database stores Run/LB level metadata and the TAG database stores event-level metadata, and both systems are discussed further in the text.

- know which data does not have sufficient quality to be included in a final analysis,
- improve and/or understand the resolution of various measurements and their efficiencies,
- follow the data through various stages of processing (and know when processing failure occurs) and
- make the connection between the data in the final physics analysis to the conditions existing when those events were recorded online.

In the ATLAS experiment at the LHC, metadata from systems storing non-event-wise data (Conditions) has been collected into a relational database. The **COMA** (**CO**nditions **M**et**a**data)[5] database tables not only contain conditions known at the time of event recording, but also allow for the addition of conditions data collected as a result of later analysis of the data (such as improved measurements of beam conditions or assessments of data quality).

The COMA Database is one of the three dedicated metadata repositories in the ATLAS Experiment (see Figure 10.1).

10.3 Event selection using ATLAS TAGS

Building on the experience of previous experiments, ATLAS is attempting to go one step further and build an event-level selection capability allowing the user to select only those

[5]This acronym has recently been redefined to stand for ***CO**nditions/**CO**nfiguration **M**etadata for **A** TLAS*.

events which are of particular interest. The RAW data collected by the ATLAS detector is passed through various stages of processing in order to produce slimmed and compact data sets which contain only those variables essential to the end user. The final smallest files produced, TAGs, are produced for each event and contain all of the variables needed to make an event selection. When a user runs their analysis code using TAGs on the Grid, the software will find the original larger data set in order to access all of the required data.

ELSSI (**E**vent **L**evel **S**election **S**ervice **I**nterface) [155] allows users to make an event level selection based on TAGs. Selection can be made using criteria, stored at the event level, such as physics stream, run number, triggers and physics objects in the event.

But many run-level selections, such as conditions of data taking and processing, are outside the scope of event level selections because that data is not stored event-by-event. So, a run-level selection system is needed.

10.4 runBrowser - Dynamic metadata aided Run selection

The ATLAS metadata infrastructure has been designed to facilitate logical and efficient access to all flavors of analysis. The runBrowser interface [155], shown in Figure 10.2, allows users to select Runs based on all available conditions data and conditions metadata. A flow diagram of their dependencies is shown in Figure 10.3. The target audience of the interface ranges from those who are not aware of exactly what data is available (and therefore a dynamic selection interface gives transparency) to the expert user who wants full flexibility to select a precise combination of Luminosity Blocks based on all available information.

The bulk of the browser is coded using PHP, interfaced with HTML and CSS. Faced with the challenge of allowing selection from such a large pool of information, we employ JavaScript and jQuery to develop the 'ergonomics' of the interface. Although a first version has now been put into production, there are still many plans for further development - this is discussed in section 10.5.

The main page consists of multiple expandable sections: one for each selection criteria. Using jQuery, the user may collapse and expand each section to reveal the values which are available for selection. In most cases these values are in the form of a table. Values are retrieved from the database using SQL queries which are built using PHP. For some criteria, a text box alternative is included allowing the use of ranges and wild-cards - for example, a

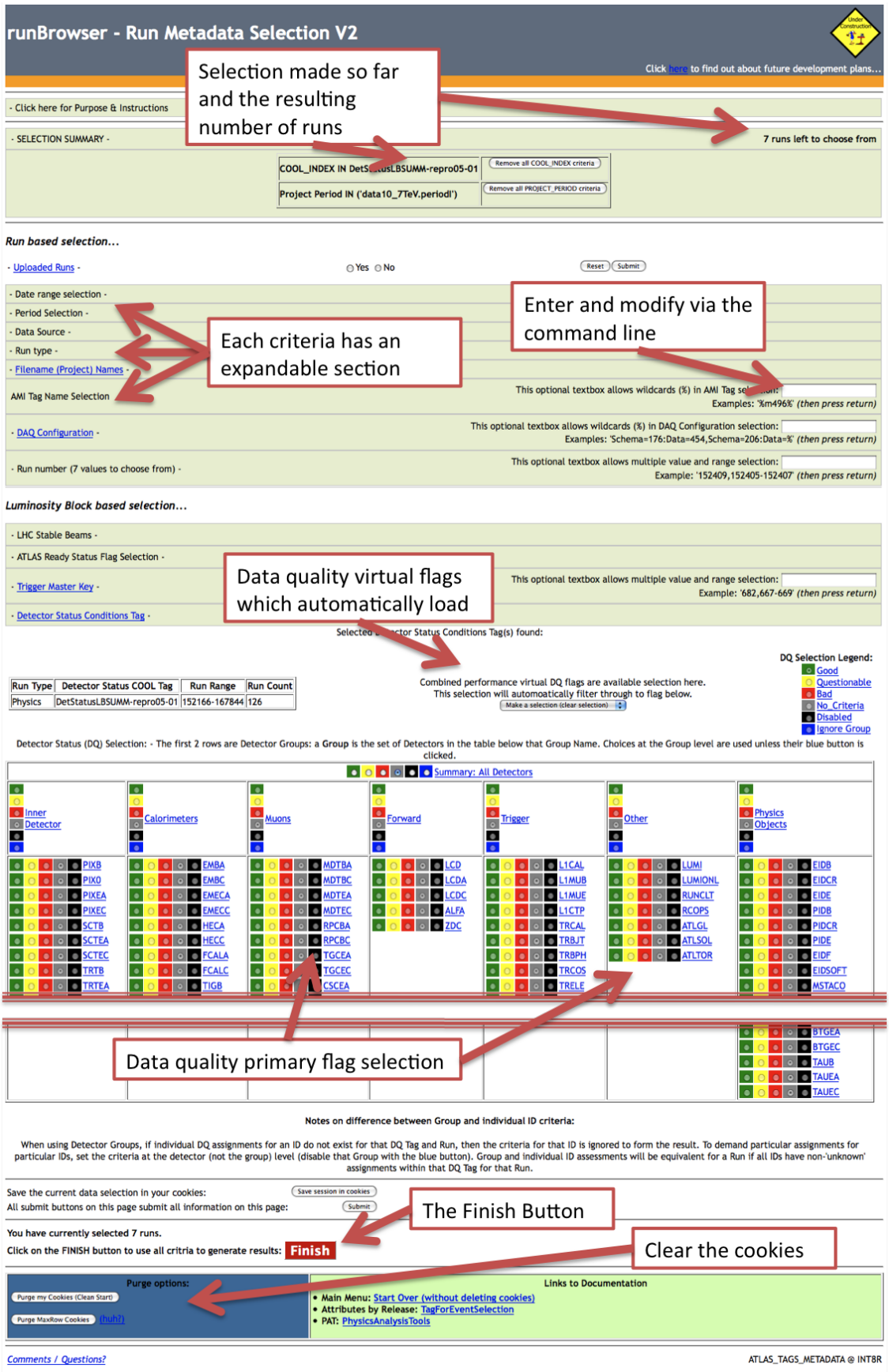

FIGURE 10.2: Detailed screen shot from runBrowser

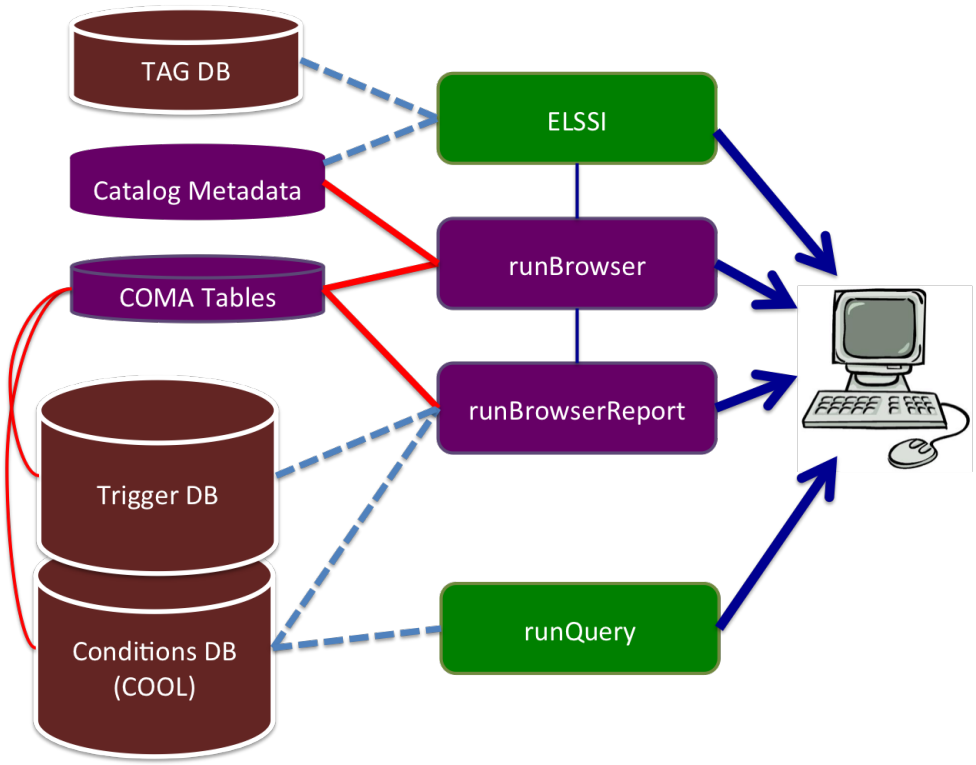

FIGURE 10.3: Flow diagram of the relational dependencies of the Data Bases (DB), COMA tables and the various interfaces. Solid (red) lines signify transfer of metadata and dashed (blue) lines signify transfer of data.

run selection may consist of 152409-152415,15250%[6]. There is also one expandable section which contains all those criteria which have been selected so far. If a user has made a selection using a text box, they may also edit/update the contents of the text box without 'going back' to a previous page.

Selection criteria can be split into two types: those which allow the user to select whole runs; and those which allow the user to make a Luminosity Block level selection. The selection criteria which are currently included in the the interface are:

- **Data Source** - i.e. Is the data simulation or 'real' data?
- **Run Type** - Allows more specific selection for simulation data: e.g. runs based on different Monte Carlo releases and the ATLAS Full Dress Rehearsal (FDR) simulated Runs.
- **Date Range** - Allows users to select the dates between which a selections of Run have taken place. It also includes a dynamic pop-up calendar.

[6]In the SQL environment, the percentage sign (%) is the symbol for a wild-card.

- **Period Selection** - Periods are periods in time for which LHC configuration was approximately stable. The periods are human defined and allow a convenient division of the data into smaller, more manageable chunks.
- **Filename (Project) Names** - A further tag given to data. Examples include 'data09_900GeV' and 'data10_7TeV'.
- **Trigger Master Key**[7] - Each set of unique logical conditions imposed by the online (or simulated) trigger system is assigned a unique integer 'Trigger Super Master Key'. runBrowser allows selection of one or more of these keys.
- **DAQ Configuration** - This is an online configuration tag used by the Tier 0 - may be useful to experts in a detector and TDAQ (Trigger & Data AcQuisition) commissioning.
- **Detector Status Conditions Tag**[8] - Detector Status (Data Quality) is assessed on a Run/Luminosity Block level by experts. When a set of DQ assessments becomes official, that set is assigned a unique tag in the ATLAS Conditions Database called a 'Conditions Tag'.
- **Run Number** - This table shows the runs which fit all of the selection criteria so far. With each Run are associated links to run specific information on AMI[9] [156], runQuery (see section 10.2) and a separate interface to the trigger database [157]. The table also includes a link to the runBrowser Run Report for each run. This report contains a concise compilation of the information contained within the COMA tables. This information currently includes general Run conditions, load status, debug information, DQ assessments, prescale evolution and trigger information.
- Current status of **TAG availability** - This Yes/No selection allows the user to select Runs which are available, via the ELSSI browser, to the TAG DB: Current policy is to keep only the 2 latest processing of Runs available in the TAG database- this directs the user to the latest/best data and conserves database resources to optimize that access.

Help and documentation is available throughout the interface in the form of pop-up windows, an expandable section containing 'Purpose and Instructions' and short strings of text which appear when the cursor hovers over certain objects.

[7]Selection of a Trigger Master Key then allows further selection of the Level 1 and High Level Trigger (HLT) prescales.

[8]Selection of a Detector Status Condition Tag then allows further selection of individual detector flags (shown in Figure 10.2). It is also possible to choose from a list of pre-prescribed 'Virtual Flags' [135] which, using JavaScript, automatically set each of the individual detector flags to the correct position.

[9]AMI is a cataloging system using the Tier 0 database and production database in order to display information about all of the registered ATLAS datasets.

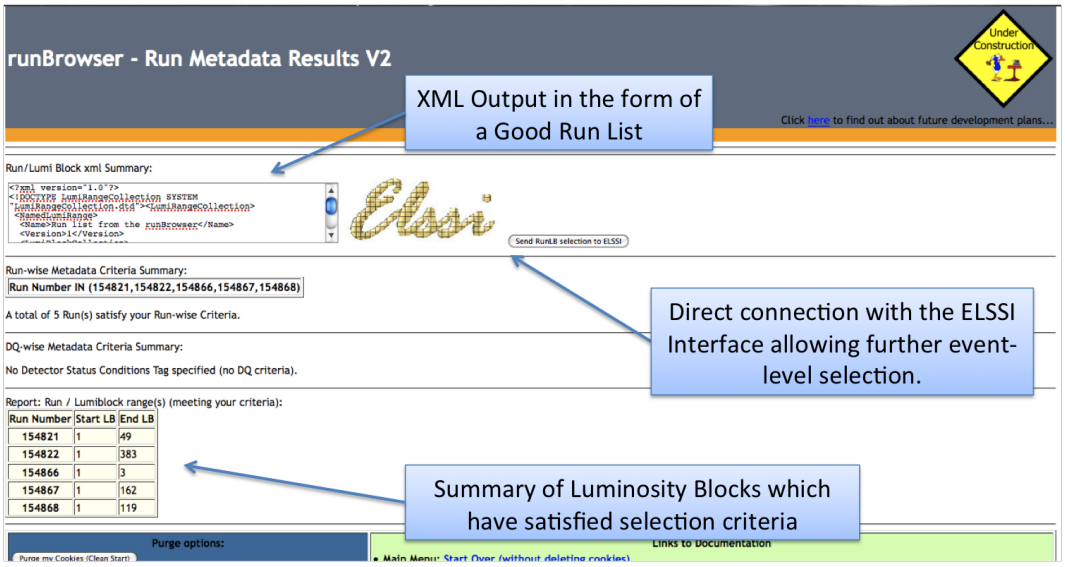

FIGURE 10.4: Screen shot from runBrowser results page

10.4.1 runBrowser Results

When a set of COMA selections are complete, runBrowser produces a results page (shown in Figure 10.4) containing a human readable report as well as an XML file in a standardized ATLAS format (see footnote 4). This XML can be saved for later use or refinement in a future runBrowser session, shared with physics/detector groups, or used as input to ELSSI or other ATLAS run or event processing services.

10.5 Conclusions and future work

At present the runBrowser interface facilitates logical, dynamic and efficient access to COMA information, allowing users to choose a selection of runs (or Luminosity Blocks) for further analysis. The interface, as well as the COMA tables themselves, are still in development and there are plans to add:

- **Stable Beams** - A boolean selection allowing the user to include only those Luminosity Blocks, within a run, for which the collisions in the detector are in a stable state which is good for data taking.
- **ATLAS Ready** - A boolean selection allowing the user to include only those Luminosity Blocks, within a run, for which the ATLAS detector has declared itself 'ready'. This flag will only be true during a period of stable beams.

- Specific **Magnet Information** - the status of the ATLAS toroid and solenoid.
- Also other information concerning Luminosity, triggers and data streams.

Appendix A

Determination of binning in χ and m_{jj}

A.1 Determination of binning in χ

The fine χ binning is determined by considering the *purity* and *stability* of bin migrations in χ. These quantities are designed to quantify the bin migrations when going from truth level information to fully-reconstructed simulation level. These quantities are defined as

$$Purity_{ij} = \frac{N_{rec(i)\&gen(j)}}{N_{rec(i)}} \quad \text{and} \quad Stability_{ij} = \frac{N_{rec(i)\&gen(j)}}{N_{gen(j)}} \tag{A.1}$$

where $N_{rec(i)\&gen(j)}$ is, for a given Monte Carlo sample, the number of jets or events which are placed in bin j using particle level truth information and are placed in bin i using reconstruction-level data. N_{rec} is the total number of reconstructed entries in bin i and $N_{gen(j)}$ is the total number of entries using truth information in bin j. It is noted that $\sum_j Purity_{ij} = 1$ for all i and $\sum_i Stability_{ij} = 1$ for all j. Using this prescription, the optimal binning is achieved through a high bin $Purity_{i=j}$ and $Stability_{i=j}$ over the whole range of χ.

Two further aspects to be considered are the ability to resolve the detailed shape of χ-spectra at low χ (where new physics models predict an excess), and the typical cell granularity of the ATLAS hadronic calorimetry (which is 0.1 in η for the Tile Calorimeter). In a previous ATLAS study [138] it was found that small migrations of the jet axes due to the granularity can be observed, which lead to a modulation of jet η-spectra with a periodicity of 0.1. As migrations and the same periodicity result for η-differences, it is advisable to place the borders of χ-bins at points of minimal migration to minimise the influence on χ spectra. It

was found in [138] that borders b_i of bins satisfy the last two considerations:

$$b_i = \exp(0.1 \times a \times i), \quad a \in \aleph, \tag{A.2}$$

Combined with a value a of 3, continuously high values of purity and stability are obtained, as seen in Fig. A.1. The resulting values (with the exception that the final bin is extended to $\chi_{max} = 30$) are shown in Table A.1.

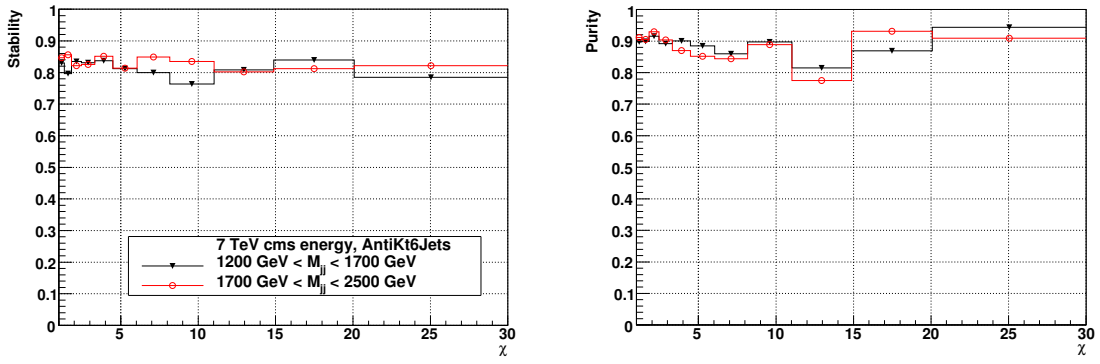

(a) (b)

FIGURE A.1: Stability and purity, considering migrations in χ and M_{jj}, for two mass bins [138].

1	1.350	1.822	2.460	3.320	4.482	6.050	8.166	11.023	14.880	20.086	30

TABLE A.1: Table containing χ bin boundaries. Taken from [138].

A.2 Determination of fine binning in m_{jj}

The $F_\chi(m_{jj})$ analysis uses a m_{jj} binning that is motivated by the absolute mass resolution of the reconstructed signal. A detailed explanation of the this method is given in Chapter 4 of [100]. The width of a reconstructed signal in m_{jj} is a convolution of the intrinsic mass width and the energy resolution of the two reconstructed jets (see Figure A.2).

The dijet mass resolution, $\sigma_{m_{jj}}/m_{jj}$, is calculated for fully-reconstructed excited quark samples, for a range of m_{q^*}. The distribution is then fit with a function of the form

$$\frac{\sigma_{m_{jj}}}{m_{jj}} = \frac{b}{\sqrt{m_{jj}}} \oplus c, \tag{A.3}$$

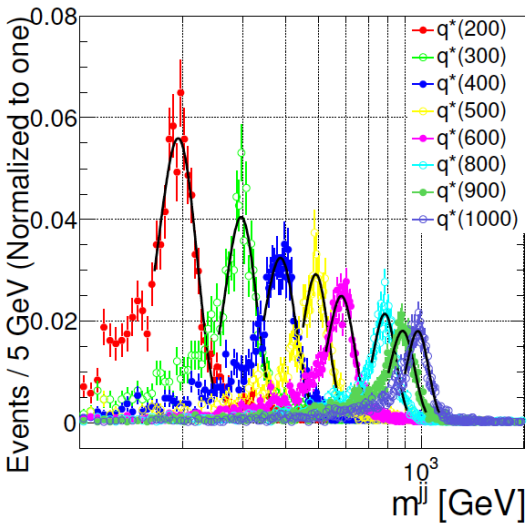

FIGURE A.2: The reconstructed m_{jj} distributions, in constant bins of 5 GeV due to hypothetical excited quarks with masses of 200, 300, 400, 500, 600, 800, 900 and 1000 GeV are shown after applying the selection criteria [100].

as motivated in Section 5.5.2 of this thesis. Parameters of $b = 1.7 \pm 0.1$ and $c = 0.054 \pm 0.004$ are found with a p-value of 0.1324. Using the above fit, bins of size $\sigma_{m_{jj}}$ are chosen with a minimum mass of 500 GeV.

The study results in dijet mass bin boundaries of: 500, 548, 601, 657, 717, 780, 847, 919, 995, 1076, 1162, 1253, 1350, 1452, 1561, 1676, 1798, 1927, 2064, 2209, 2363, 2526, 2699, 2882, 3076, 3281, 3498, 3728, 3972, 4230, 4503, 4792, 5098, 5422, 5765, 6128, 6513, 7000 GeV.

Appendix B

Comparing ATLFAST II to GEANT full simulation

The full 2011 dataset, with an integrated luminosity of 4.8 fb^{-1}represents a substantial increase over 2010, and has greatly decreased the statistical uncertainties in data distributions. This necessitates a corresponding increase in the size of MC samples, to prevent MC statistical fluctuations from becoming a dominant source of uncertainty in dijet mass and angular analyses. Full simulation of events using GEANT4 is time intensive, and the available Grid capacity does not allow for the processing of larger fully-simulated MC samples on the timescales required for publication of results.

The ATLFAST II [65] program, which employs FastCaloSim [66] for calorimeter simulation, typically runs one order of magnitude faster than GEANT, and is in the process of becoming the new default for MC full simulation. To validate this new procedure, MC truth samples have been passed through ATLFAST II detector simulation and compared to GEANT full simulation of the same samples.

PYTHIA 6 dijet event samples are typically generated in broad bins of partonic p_T. The GEANT samples have J0-J8, with 2.8 million events for J3 through J6, and 1.4 million each in J7 and J8. In order to increase the statistics for the angular distributions, the ATLFAST II samples have the partonic range of J7 split into two halves; J7a from 1120 to 1680 GeV and J7b from 1680 to 2240 GeV. The ATLFAST II samples have 1.4 million events for J0-J3 and for J7, J7a and J7b, and 2.8 million events for J4-J6 and J8. Note that in order to avoid double counting the J7 cross section, all weights of the J7(a/b) samples get a factor 0.5. Each simulation comes with its own set of calibration constants.

Figures B.1 through B.3 compare GEANT and ATLFAST II simulation samples. These plots are the 11-bin χ distributions in each of the five m_{jj} bins. Within statistical uncertainties, GEANT and ATLFAST II are in close agreement in all χ and m_{jj} bins.

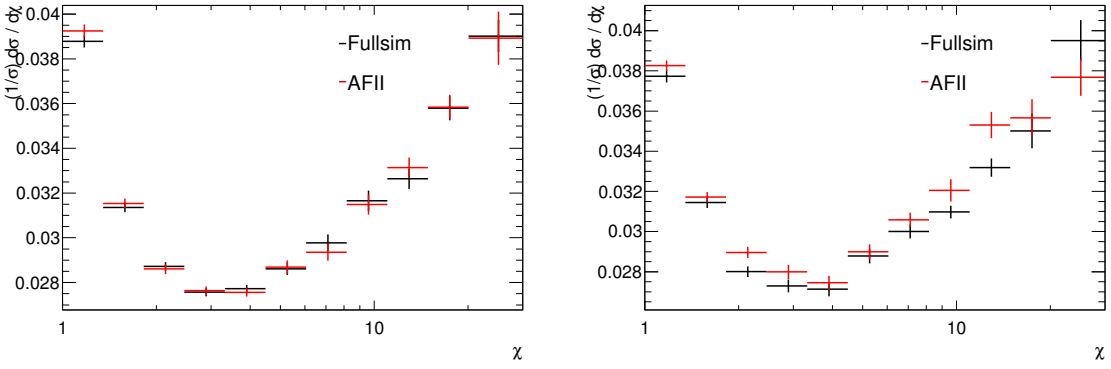

(a) $800 < m_{jj} < 1200$ GeV (b) $1200 < m_{jj} < 1600$ GeV

FIGURE B.1: χ distributions, comparing ATLFAST II to GEANT simulation in the lowest m_{jj} bins

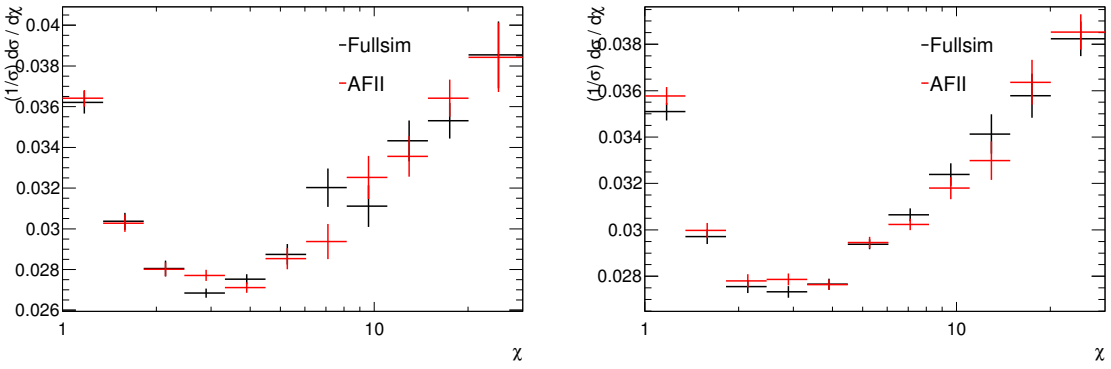

(a) $1600 < m_{jj} < 2000$ GeV (b) $2000 < m_{jj} < 2600$ GeV

FIGURE B.2: χ distributions, comparing ATLFAST II to GEANT simulation in intermediate m_{jj} bins

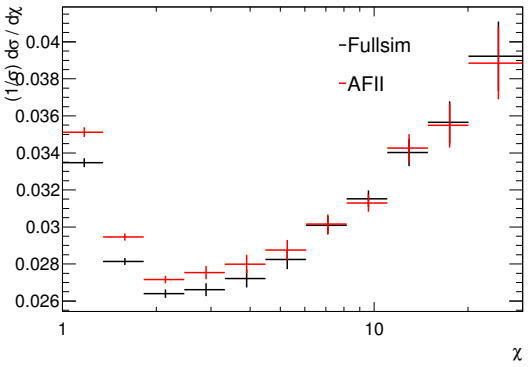

FIGURE B.3: χ distributions, comparing ATLFAST II to GEANT simulation for highest mass bin, $2600 < m_{jj} < 7000$ GeV

Appendix C

Determination of trigger efficiencies

As described in Section 3.3, the ATLAS trigger system is composed of 3 levels. After an initial period of data-taking with only the Level 1 (L1) trigger in operation, the Level 2 (L2) and Event Filter (EF) were used from August 2010. Each of the single jet trigger chains is formed from a L1, L2 and EF component. Each of the trigger levels must be considered when calculating the efficiency of the overall trigger chain.

In this analysis, we use the bootstrap method [158] in order to calculate the trigger efficiency. This method proceeds by taking the the ratio between all events where at least one of the jets fired the trigger, and all events considered, where the latter events are counted using a trigger chain with a lower threshold. The dijet invariant mass, m_{jj}, of the leading jet pair is calculated for each of the events and then the efficiency is plotted as a function of m_{jj}. The trigger efficiency is dependent upon the η of the jet from which it is triggered, since this will determine which part of the detector hardware was responsible for measurement. It is therefore important to calculate the trigger efficiency for the subset of events which satisfy the restrictions placed upon y^* and y_B. Figures C.1(a) and C.1(b) therefore display the trigger efficiency, split between two ranges in y^*, where events with lower values of y^* contain jets that have a larger transverse component in the detector. It can be seen that the trigger efficiency is generally better for events containing centrally produced jets.

Within [159], trigger efficiencies are also calculated as a function of jet transverse momentum, p_T, and jet rapidity, y. It is demonstrated that the efficiency as a function of jet p_T is dependent upon the rapidity of the jet (with reduced efficiencies at larger rapidity), however when considering jets with $1.2 < |y| < 2.1$, all tiggers are found to be efficient above 300 GeV.

In order to include as many events as possible in the efficiency determination of a given trigger, a trigger decision is reconstructed offline for all events that pass the lower-energy

reference trigger. A trigger decision can be determined by looking at the energy recorded at level 1, level 2 and the event filter, and requiring that the energy at each trigger level is above the required threshold.

Although the above method is constrained to the number of events passing the reference trigger (after prescale), the statistics are sufficient to construct the efficiency curves in Figure C.1 as a function of m_{jj}.

By zooming into these plots, one is able to determine that value of m_{jj} above which the efficiency is $> 99\%$, which is an ATLAS convention for trigger efficiency requirements.

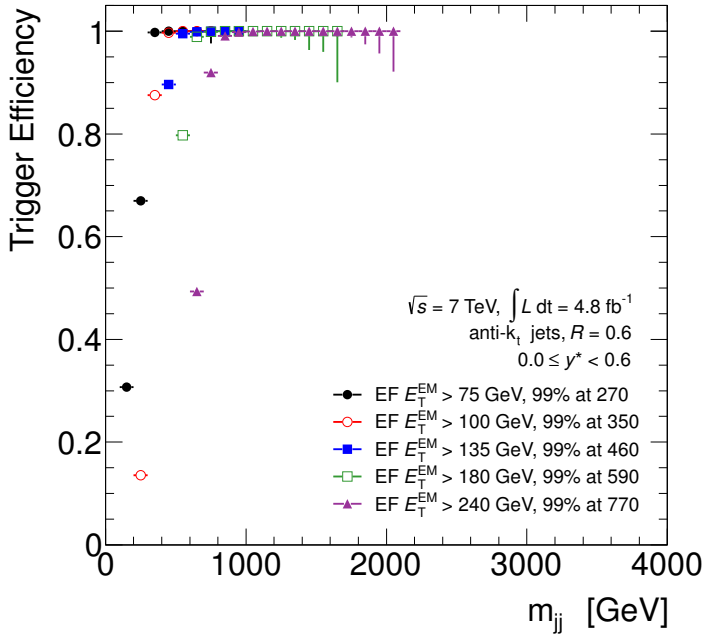

(a) EF Inner

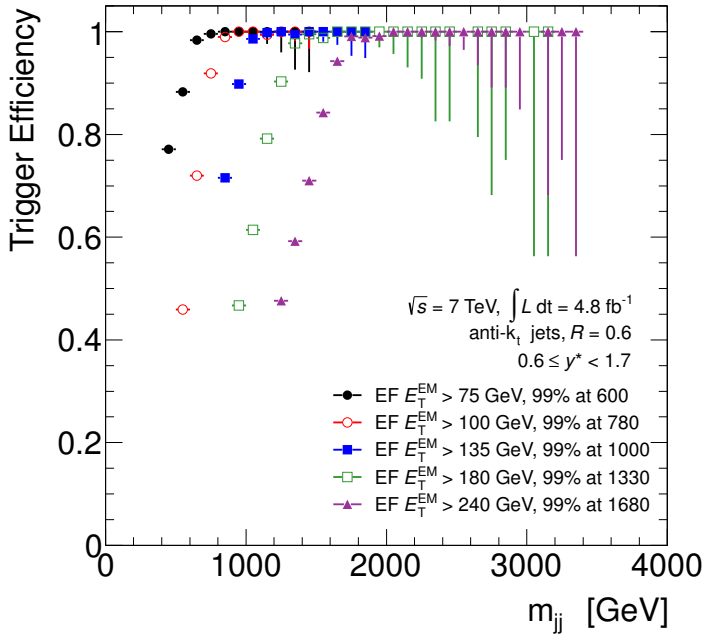

(b) EF Outer

FIGURE C.1: Trigger efficiencies as a function of m_{jj}. Efficiencies are provided to dijet events with (a) $0.0 < y^* < 0.6$ and (b) $0.6 < y^* < 1.7$ [130].

Appendix D

Debug stream investigation in early data

An analysis with early 2010 data was performed in order to assess whether potentially interesting jet events are systematically causing triggers within the detector to fail and/or time-out. If the trigger system is biased towards rejecting events of a certain type, this could bias many physics analyses. It is therefore critical that the characteristics of events that are in the debug stream are understood so that, where possible, improvement can be made to the trigger.

An early study found that events containing punch-through jets, resulting in a large number of muon hits behind the jet, were causing a time-outs in muon trigger chains. This resulted in a bias for events containing high-momentum jets or high jet multiplicity to be placed into the debug stream: and so excluded from an analysis. One of the distributions from this study is shown in Figure D.1: the transverse momentum, p_T, of jets from events is shown for both the physics stream, and for the debug stream, know as *debugrec_hltacc*. The rate of events entering the debug stream is seen to approach 0.3 % for a jet with transverse momentum ~ 350 GeV.

In reaction to this study, the muon trigger was re-configured for faster performance, and the bias was removed [28].

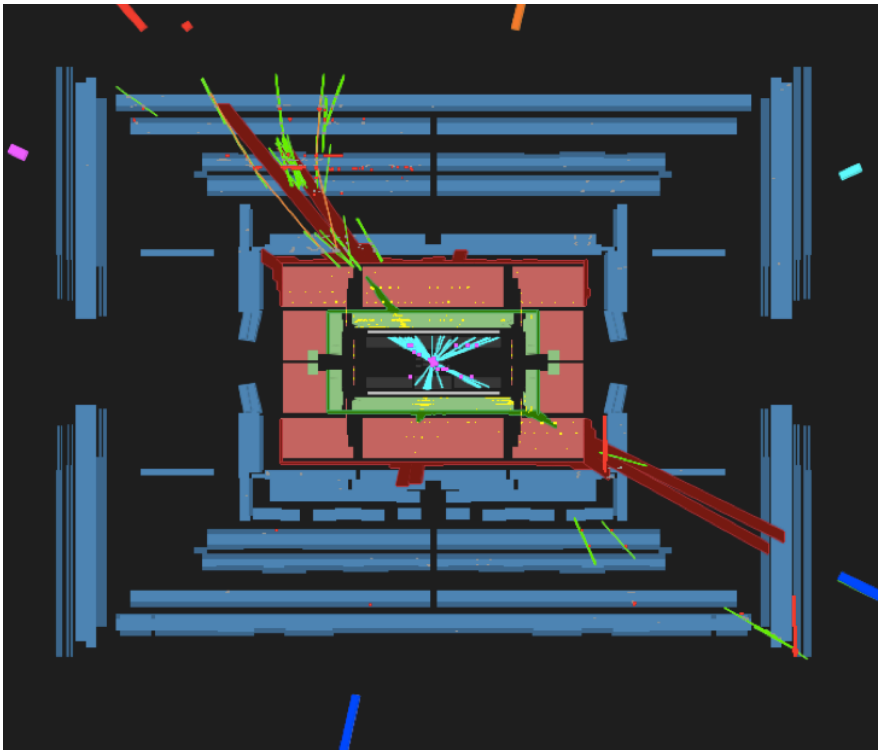

(a)

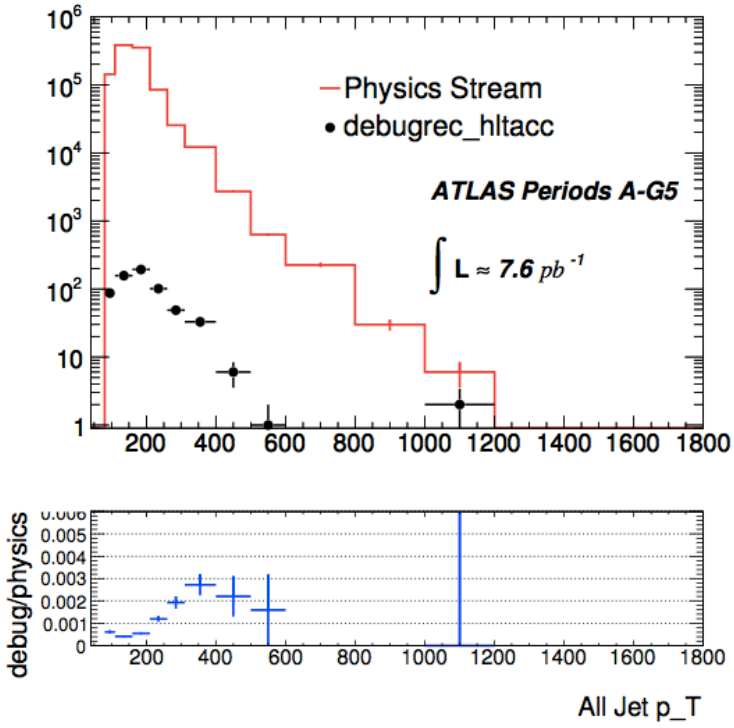

(b)

FIGURE D.1: (a) Event display for a debug stream event. The event contains two high p_T jets, with the upper jet pointing to numerous red hits in the muon detectors. These muon hits are indicative of jet punch through. (b) Distribution of jet momentum for events which enter the physics stream vs. the debug stream. A clear bias can be seen for events with high p_T jets to be passed to the debug stream.

Appendix E

BlackMax paramter.txt

Below is the contents of the parameter.txt file used to generate the Quantum Black Hole model used in this thesis.

```
Number_of_simulations
5600
incoming_particle(1:pp_2:ppbar_3:ee+)
1
Center_of_mass_energy_of_incoming_particle
7000
M_pl(GeV)
1000.
definition_of_M_pl:(1:M_D_2:M_p_3:M_DL_4:put_in_by_hand)
1
if_definition==4
1.
Choose_a_case:(1:tensionless_nonrotating_2:tension_nonrotating_
3:rotating_nonsplit_4:Lisa_two_particles_final_states)
4
number_of_extra_dimensions
6
number_of_splitting_dimensions
0
size_of_brane(1/Mpl)
0.0
extradimension_size(1/Mpl)
10.
tension(parameter_of_deficit_angle:1_to_0)
1.0
choose_a_pdf_file(200_to_240_cteq6)Or_>10000_for_LHAPDF
10800
Chose_events_by_center_of_mass_energy_or_by_initial_black_hole_mass
(1:center_of_mass_2:black_hole_mass)
2
Minimum_mass(GeV)
1000.
Maxmum_mass(GeV)
7000.
```

```
Include_string_ball:(1:no_2:yes)
1
String_scale(M_s)(GeV)
0
string_coupling(g_s)
0
The_minimum_mass_of_a_string_ball_or_black_hole(in_unit_Mpl)
1.
fix_time_step(1:fix_2:no)
2
time_step(1/GeV)
1.e-5
other_definition_of_cross_section(0:no_1:yoshino_2:pi*r^2_3:4pi*r^2)
2
calculate_the_cross_section_according_to(0:the_radius_of_initial_black_hole
_1:centre_of_mass_energy)
1
calculate_angular_eigen_value(0:calculate_1:fitting_result)
0
Mass_loss_factor(0~1.0)
0.
momentum_loss_factor(0~1.0)
0.
Angular_momentum_loss_factor(0~1.0)
0.
turn_on_graviton(0:off_1:on)
0
Seed
1
Write_LHA_Output_Record?_0=NO__1=Yes_2=More_Detailed_output
2
L_suppression(1:none_2:delta_area_3:anular_momentum_4:delta_angular_momentum)
1
angular_momentum_suppression_factor
1
charge_suppression(1:none_2:do)
1
charge_suppression_factor
1
color_suppression_factor
20
split_fermion_width(1/Mpl)_and_location(from-15to15)(up_to_9extradimensions)
u_quark_Right(Note:do_not_insert_blank_spaces)
1.0
10.0,0.0,0.0,0.0,0.0,0.0,0.0,0.0,0.0,0.0
u_quark_Left(Note:do_not_insert_blank_spaces)
1.0
10.0,0.0,0.0,0.0,0.0,0.0,0.0,0.0,0.0,0.0
u_bar_quark_Right(Note:do_not_insert_blank_spaces)
1.0
10.0,0.0,0.0,0.0,0.0,0.0,0.0,0.0,0.0,0.0
u_bar_quark_Left(Note:do_not_insert_blank_spaces)
1.0
10.0,0.0,0.0,0.0,0.0,0.0,0.0,0.0,0.0,0.0
d_quark_Right(Note:do_not_insert_blank_spaces)
1.0
10.0,0.0,0.0,0.0,0.0,0.0,0.0,0.0,0.0,0.0
d_quark_Left(Note:do_not_insert_blank_spaces)
```

```
1.0
10.0,0.0,0.0,0.0,0.0,0.0,0.0,0.0,0.0,0.0
d_bar_quark_Right(Note:do_not_insert_blank_spaces)
1.0
10.0,0.0,0.0,0.0,0.0,0.0,0.0,0.0,0.0,0.0
d_bar_quark_Left(Note:do_not_insert_blank_spaces)
1.0
10.0,0.0,0.0,0.0,0.0,0.0,0.0,0.0,0.0,0.0
s_quark_Right(Note:do_not_insert_blank_spaces)
1.0
10.0,0.0,0.0,0.0,0.0,0.0,0.0,0.0,0.0,0.0
s_quark_Left(Note:do_not_insert_blank_spaces)
1.0
10.0,0.0,0.0,0.0,0.0,0.0,0.0,0.0,0.0,0.0
s_bar_quark_Right(Note:do_not_insert_blank_spaces)
1.0
10.0,0.0,0.0,0.0,0.0,0.0,0.0,0.0,0.0,0.0
s_bar_quark_Left(Note:do_not_insert_blank_spaces)
1.0
10.0,0.0,0.0,0.0,0.0,0.0,0.0,0.0,0.0,0.0
c_quark_Right(Note:do_not_insert_blank_spaces)
1.0
10.0,0.0,0.0,0.0,0.0,0.0,0.0,0.0,0.0,0.0
c_quark_Left(Note:do_not_insert_blank_spaces)
1.0
10.0,0.0,0.0,0.0,0.0,0.0,0.0,0.0,0.0,0.0
c_bar_quark_Right(Note:do_not_insert_blank_spaces)
1.0
10.0,0.0,0.0,0.0,0.0,0.0,0.0,0.0,0.0,0.0
c_bar_quark_Left(Note:do_not_insert_blank_spaces)
1.0
10.0,0.0,0.0,0.0,0.0,0.0,0.0,0.0,0.0,0.0
b_quark_Right(Note:do_not_insert_blank_spaces)
1.0
10.0,0.0,0.0,0.0,0.0,0.0,0.0,0.0,0.0,0.0
b_quark_Left(Note:do_not_insert_blank_spaces)
1.0
10.0,0.0,0.0,0.0,0.0,0.0,0.0,0.0,0.0,0.0
b_bar_quark_Right(Note:do_not_insert_blank_spaces)
1.0
10.0,0.0,0.0,0.0,0.0,0.0,0.0,0.0,0.0,0.0
b_bar_quark_Left(Note:do_not_insert_blank_spaces)
1.0
10.0,0.0,0.0,0.0,0.0,0.0,0.0,0.0,0.0,0.0
t_quark_Right(Note:do_not_insert_blank_spaces)
1.0
10.0,0.0,0.0,0.0,0.0,0.0,0.0,0.0,0.0,0.0
t_quark_Left(Note:do_not_insert_blank_spaces)
1.0
10.0,0.0,0.0,0.0,0.0,0.0,0.0,0.0,0.0,0.0
t_bar_quark_Right(Note:do_not_insert_blank_spaces)
1.0
10.0,0.0,0.0,0.0,0.0,0.0,0.0,0.0,0.0,0.0
t_bar_quark_Left(Note:do_not_insert_blank_spaces)
1.0
10.0,0.0,0.0,0.0,0.0,0.0,0.0,0.0,0.0,0.0
e_-_Left(Note:do_not_insert_blank_spaces)
1.0
```

```
-10.0,0.0,0.0,0.0,0.0,0.0,0.0,0.0,0.0
e_-_Right(Note:do_not_insert_blank_spaces)
1.0
-10.0,0.0,0.0,0.0,0.0,0.0,0.0,0.0,0.0
e_+_Left(Note:do_not_insert_blank_spaces)
1.0
-10.0,0.0,0.0,0.0,0.0,0.0,0.0,0.0,0.0
e_+_Right(Note:do_not_insert_blank_spaces)
1.0
-10.0,0.0,0.0,0.0,0.0,0.0,0.0,0.0,0.0
mu_-_Left(Note:do_not_insert_blank_spaces)
1.0
-10.0,0.0,0.0,0.0,0.0,0.0,0.0,0.0,0.0
mu_-_Right(Note:do_not_insert_blank_spaces)
1.0
-10.0,0.0,0.0,0.0,0.0,0.0,0.0,0.0,0.0
mu_+_Left(Note:do_not_insert_blank_spaces)
1.0
-10.0,0.0,0.0,0.0,0.0,0.0,0.0,0.0,0.0
mu_+_Right(Note:do_not_insert_blank_spaces)
1.0
-10.0,0.0,0.0,0.0,0.0,0.0,0.0,0.0,0.0
tau_-_Left(Note:do_not_insert_blank_spaces)
1.0
-10.0,0.0,0.0,0.0,0.0,0.0,0.0,0.0,0.0
tau_-_Right(Note:do_not_insert_blank_spaces)
1.0
-10.0,0.0,0.0,0.0,0.0,0.0,0.0,0.0,0.0
tau_+_Left(Note:do_not_insert_blank_spaces)
1.0
-10.0,0.0,0.0,0.0,0.0,0.0,0.0,0.0,0.0
tau_+_Right(Note:do_not_insert_blank_spaces)
1.0
-10.0,0.0,0.0,0.0,0.0,0.0,0.0,0.0,0.0
nutrino_e-(Note:do_not_insert_blank_spaces)
1.0
-10.0,0.0,0.0,0.0,0.0,0.0,0.0,0.0,0.0
nutrino_e+(Note:do_not_insert_blank_spaces)
1.0
-10.0,0.0,0.0,0.0,0.0,0.0,0.0,0.0,0.0
nutrino_mu-(Note:do_not_insert_blank_spaces)
1.0
-10.0,0.0,0.0,0.0,0.0,0.0,0.0,0.0,0.0
nutrino_mu+(Note:do_not_insert_blank_spaces)
1.0
-10.0,0.0,0.0,0.0,0.0,0.0,0.0,0.0,0.0
nutrino_tau-(Note:do_not_insert_blank_spaces)
1.0
-10.0,0.0,0.0,0.0,0.0,0.0,0.0,0.0,0.0
nutrino_tau+(Note:do_not_insert_blank_spaces)
1.0
-10.0,0.0,0.0,0.0,0.0,0.0,0.0,0.0,0.0
number_of_conservation
1
d,s,b,u,c,t,e,mu,tau,nu_e,nu_mu,nu_tau
1,1,1,1,1,1,0,0,0,0,0,0
1,1,1,1,1,1,-3,-3,-3,-3,-3,-3
0,0,0,0,0,0,1,1,1,1,1,1
```

```
0,0,0,0,0,0,0,0,0,0,0,0
0,0,0,0,0,0,0,0,0,0,0,0
0,0,0,0,0,0,0,0,0,0,0,0
0,0,0,0,0,0,0,0,0,0,0,0
0,0,0,0,0,0,0,0,0,0,0,0
```

Appendix F

Pileup reweighting

When the MC samples were produced, there was no knowledge about the pileup conditions in data. Pileup reweighting is a procedure to reweight the μ distribution in MC to the one observed in data, by assigning a weight to every event in the MC sample.

During analysis, pileup reweighting is done following event selection since it depends on dijet mass. In this section the accuracy of this procedure is being studied with a closure test.

The inputs for the pileup reweighting procedure are (1) the μ distribution of the MC sample, (2) the μ distribution of the data, and (3) the μ of the given MC event.

In this test, the pileup reweighting factors are obtained before any event selection, and the closure of the reweighting is being checked after event selection. The plots in this section show, for each χ distribution, the μ distribution in data compared to the μ distributions in MC, before and after MC pileup reweighting.

It is clear from Figs. F.1(a) through F.1(e) that pileup reweighting successfully reshapes the μ distribution from MC to match the distribution seen in collision data.

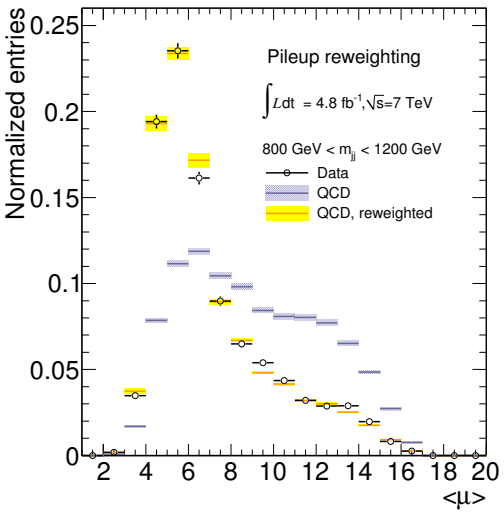

(a) 800 GeV $< m_{jj} <$ 1200 GeV.

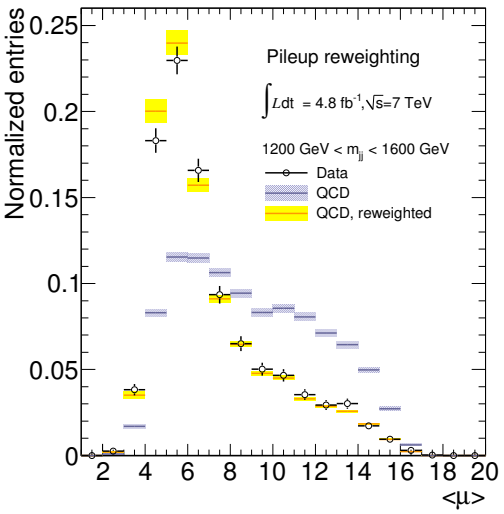

(b) 1200 GeV $< m_{jj} <$ 1600 GeV.

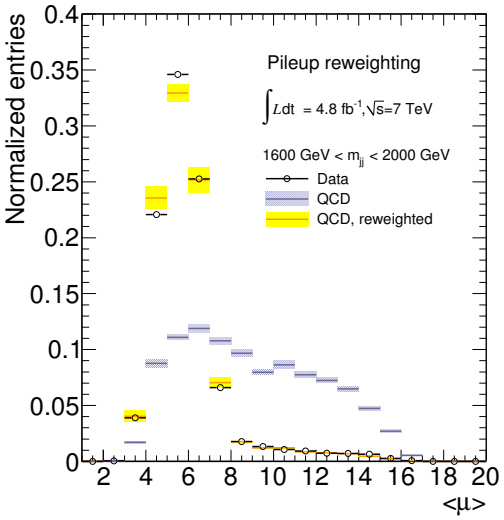

(c) 1600 GeV $< m_{jj} <$ 2000 GeV.

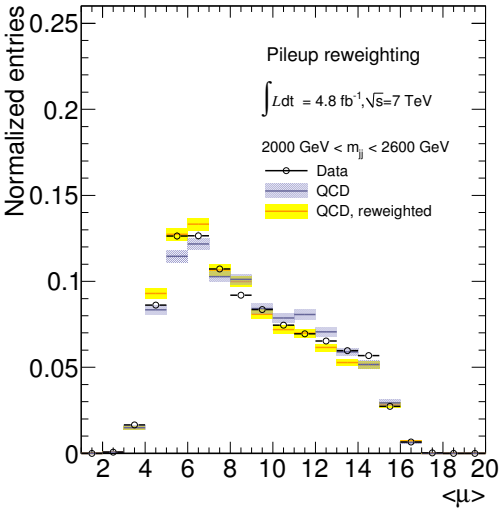

(d) 2000 GeV $< m_{jj} <$ 2600 GeV.

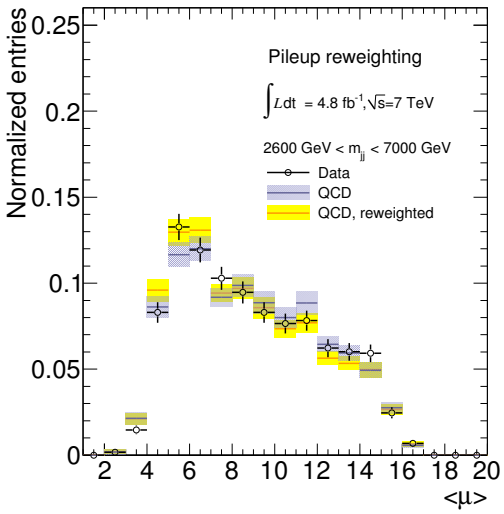

(e) 2600 GeV $< m_{jj} <$ 7000 GeV.

FIGURE F.1: Effects of pile-up reweighing for all χ distributions.

Appendix G

Cut flows for signal samples

Below, are the cut flows and cut efficiencies for one mass point of each signal used. See Section 7.1 for a discussion of these cuts, and for the relevant numbers in data. The overall cut efficiencies for each signal sample, as a function of the model parameter, are shown in Figures X.

TABLE G.1: Cut flow and efficiency for excited quark sample with $m_{q^*} = 3$ TeV.

Selection criteria	N_{ev}	Efficiency wrt previous cut (%)
A (before cuts)	10000	
F (njet check)	9998	100.0
G (ugly jets + LAr hole)	9735	97.4
I (bad jet cleaning)	9732	100.0
J (jet pT cuts)	9620	98.8
K (y^* cut)	9127	94.9
L (y_B cut)	9023	98.9
M (m_{jj} cut)	8880	98.4
Overall Efficiency		88.8

TABLE G.2: Cut flow and efficiency for QBH with $m_{q^*} = 3$ TeV.

Selection criteria	N_{ev}	Efficiency wrt previous cut (%)
A (before cuts)	10000	
F (njet check)	9996	100.0
G (ugly jets + LAr hole)	9772	97.8
I (bad jet cleaning)	9770	100.0
J (jet pT cuts)	9621	98.5
K (y^* cut)	9078	94.4
L (y_B cut)	9040	99.6
M (m_{jj} cut)	8954	99.0
Overall Efficiency		89.5

TABLE G.3: Cut flow and efficiency for contact interaction sample with $\Lambda = 10$ TeV.

Selection criteria	N_{ev}	Efficiency wrt previous cut (%)
A (before cuts)	3298997	
F (njet check)	3298996	100.0
G (ugly jets + LAr hole)	3214069	97.4
I (bad jet cleaning)	3213455	100.0
J (jet pT cuts)	3005853	93.5
K (y^* cut)	2976993	99.0
L (y_B cut)	2687414	90.3
M (m_{jj} cut)	1935761	72.0
Overall Efficiency		58.7

Bibliography

[1] Lydon Evans and Philip Bryant (editors). Lhc machine. *JINST*, 3(S08001), 2008.

[2] Derek Greenwood W. Cottingham. *An Introduction to the Standard Model of Particle Physics*. 1998.

[3] S.L. Glashow. Partial Symmetries of Weak Interactions. *Nucl.Phys.*, 22:579–588, 1961. doi: 10.1016/0029-5582(61)90469-2.

[4] Steven Weinberg. A model of leptons. *Phys. Rev. Lett.*, 19:1264–1266, Nov 1967. doi: 10.1103/PhysRevLett.19.1264. URL `http://link.aps.org/doi/10.1103/PhysRevLett.19.1264`.

[5] A. salam in elementary particle theory, n. svartholm, ed., almquist and wiksells, stockholm (1969), p. 367.

[6] S. L. Glashow, J. Iliopoulos, and L. Maiani. Weak interactions with lepton-hadron symmetry. *Phys. Rev. D*, 2:1285–1292, Oct 1970. doi: 10.1103/PhysRevD.2.1285. URL `http://link.aps.org/doi/10.1103/PhysRevD.2.1285`.

[7] Barton Zwiebach. *A First Course in String Theory*. CUP, 2009.

[8] K. Nakamura et al. The review of particle physics. *J. Phys.*, G 37(075021), 2010.

[9] M. Gonzalez-Garcia, Michele Maltoni, and Jordi Salvado. Updated global fit to three neutrino mixing: status of the hints of $\theta_{13} > 0$. *Journal of High Energy Physics*, 2010: 1–20, 2010. ISSN 1029-8479. URL `http://dx.doi.org/10.1007/JHEP04(2010)056`. 10.1007/JHEP04(2010)056.

[10] Ian Brock and Thomas Schorner-Sadenius. *Physics at the Terascale*. Whiley, 2010.

[11] Stephen P. Martin. *A Supersymmetry Primer*. 1997.

[12] Christopher T. Hill and Elizabeth H. Simmons. Strong dynamics and electroweak symmetry breaking. *Physics Reports*, 381(46):235 – 402, 2003. ISSN 0370-1573. doi:

10.1016/S0370-1573(03)00140-6. URL http://www.sciencedirect.com/science/article/pii/S0370157303001406.

[13] The ATLAS Collaboration. Observation of a new particle in the search for the standard model higgs boson with the atlas detector at the lhc. *Physics Letters B*, 716(1): 1 – 29, 2012. ISSN 0370-2693. doi: 10.1016/j.physletb.2012.08.020. URL http://www.sciencedirect.com/science/article/pii/S037026931200857X.

[14] The CMS Collaboration. Observation of a new boson at a mass of 125 gev with the cms experiment at the lhc. (arXiv:1207.7235 [hep-ex]), .

[15] ATLAS Collaboration. A search for new physics in dijet mass and angular distributions in pp collisions at $\sqrt{s} = 7$ tev with the atlas detector. *New Journal of Physics*, 13(5): 053044, 2011. URL http://stacks.iop.org/1367-2630/13/i=5/a=053044.

[16] R Buckingham, A Cooper-Sarkar, J Ferrando, C Issever, K Lohwasser, and S Whitehead. Using the charge asymmetry in w+jet production as a new probe of parton distribution functions in different kinematic regions at the lhc. Technical Report ATL-COM-PHYS-2010-893, CERN, Geneva, Nov 2010. We recently asked permission to publish this study outside of the collaboration, but had used official EVGEN samples to make our plots. Given that, we were recommended to submit as an INT note.

[17] RM Buckingham, EJ Gallas, JC-L Tseng, F Viegas, and E Vinek. Metadata aided run selection at atlas. Technical Report ATL-SOFT-PROC-2011-023, CERN, Geneva, Jan 2011.

[18] RM Buckingham, EJ Gallas, JC-L Tseng, F Viegas, and E Vinek. Metadata aided run selection at atlas. *ATLAS-COM-SOFT-2010-025*, Oct 2010.

[19] W Ehrenfeld, R Buckingham, J Cranshaw, T Cuhadar Donszelmann, T Doherty, E Gallas, J Hrivnac, D Malon, M Nowak, M Slater, F Viegas, E Vinek, and Q Zhang. Using tags to speed up the atlas analysis process. Technical Report ATL-SOFT-PROC-2011-003, CERN, Geneva, Jan 2011.

[20] R M Buckingham, E J Gallas, J C-L Tseng, F Viegas, and E Vinek for the ATLAS Collaboration. Metadata aided run selection at atlas. *Journal of Physics: Conference Series*, 331(4):042030.

[21] S Bahinipati, R Buckingham, A Casteneda, C Dallapiccola, T Dietzsch, S French, J Frost, D Gingrich, M Henke, H Ji, M Kaneda, M Kim, V Lendermann, K Loureiro, V Moeller, F Mueller, M Parker, H Peng, T Sarangi, V Scharf, J Tanaka, M Vlasak,

and SL Wu. Search for new physics in multi-body final states at high invariant masses with atlas. Technical Report ATL-COM-PHYS-2010-358, CERN, Geneva, Jun 2010.

[22] S Baker, M Begel, N Boelaert, J Butterworth, R Buckingham, M Campanelli, T Carli, V Cavasinni, G Choudalakis, B Demirkoz, P O DeViveiros, C Doglioni, S Eckweiler, E Feng, P Francavilla, M Henke, E Hughes, M Kaneda, H Li, M Martinez-Perez, E Meoni, F Mueller, J Monk, K Perez, J Pilcher, S Poddar, J Poveda, J Robinson, C Roda, G Romeo, F Ruehr, B Salvachua, V Scharf, M Spousta, R Stamen, P Starovoitov, K Terashi, E Torregrosa, F Vives Vaque, S L Wu, and Z Zinonos. Measurement of jet production in 7 tev proton-proton collision with the atlas detector. Technical Report ATL-COM-PHYS-2010-407, CERN, Geneva, Jun 2010.

[23] N Boelaert, R Buckingham, SL Cheung, G Choudalakis, T Davidek, P-O Deviveiros, E Feng, S Ferrag, J Frost, M Kaneda, H Li, H Peng, L Pribyl, F Ruehr, M Shupe, K Terashi, and SL Wu. High-pt dijet angular distributions in pp interactions at 7 tev measured with the atlas detector at the lhc. Technical Report ATL-COM-PHYS-2010-384, CERN, Geneva, Jun 2010. An internal backup note will take shape as ATL-COM-PHYS-2010-359.

[24] G Choudalakis, SL Cheung, N Boelaert, R Buckingham, T Davidek, PO DeViveiros, E Feng, S Ferrag, J Frost, H Ji, M Kaneda, H Li, H Peng, L Pribyl, F Ruehr, K Terashi, A Warburton, and SL Wu. Search for new particles decaying into dijets in proton-proton collisions at sqrts = 7 tev with the atlas detector. Technical Report ATL-COM-PHYS-2010-419, CERN, Geneva, Jun 2010. Derived from ATL-COM-PHYS-2010-357.

[25] ATLAS Collaboration. Search for new particles in two-jet final states in 7 tev proton-proton collisions with the atlas detector at the lhc. *Phys. Rev. Lett.*, 105:161801, 2010. URL `http://arxiv.org/abs/1008.2461`.

[26] ATLAS Collaboration. Search for quark contact interactions in dijet angular distributions in pp collisions at sqrt(s) = 7 tev measured with the atlas detector. 09 2010. URL `http://arxiv.org/abs/1009.5069`.

[27] ATLAS Collaboration. Measurement of inclusive jet and dijet cross sections in proton-proton collisions at 7 tev centre-of-mass energy with the atlas detector. 09 2010. URL `http://arxiv.org/abs/1009.5908`.

[28] JL Almond, M Owen, A OH, N Van Eldik, E Pueschel, and M Woudstra. Timeout studies for trigmuonef. Technical Report ATL-COM-DAQ-2012-021, CERN, Geneva, Apr 2012.

[29] Patrick Meade and Lisa Randall. Black holes and quantum gravity at the lhc. *JHEP*, 0805:003, 2008. URL http://arxiv.org/abs/0708.3017.

[30] New Journal of Physics. Highlights of 2011. 2011. URL http://iopscience.iop.org/1367-2630/page/Highlights%20of%202011.

[31] The ATLAS Collaboration. ATLAS search for new phenomena in dijet mass and angular distributions using pp collisions at sqrt(s)=7 TeV. 2012. URL http://arxiv.org/abs/1210.1718.

[32] J. D. Bjorken. Asymptotic sum rules at infinite momentum. *Phys. Rev.*, 179:1547–1553, Mar 1969. doi: 10.1103/PhysRev.179.1547. URL http://link.aps.org/doi/10.1103/PhysRev.179.1547.

[33] Richard P. Feynman. Very high-energy collisions of hadrons. *Phys. Rev. Lett.*, 23:1415–1417, Dec 1969. doi: 10.1103/PhysRevLett.23.1415. URL http://link.aps.org/doi/10.1103/PhysRevLett.23.1415.

[34] L. W. MO and Y. S. TSAI. Radiative corrections to elastic and inelastic ep and up scattering. *Rev. Mod. Phys.*, 41:205–235, Jan 1969. doi: 10.1103/RevModPhys.41.205. URL http://link.aps.org/doi/10.1103/RevModPhys.41.205.

[35] Richard E. Taylor. Deep inelastic scattering: The early years. *Rev. Mod. Phys.*, 63:573–595, Jul 1991. doi: 10.1103/RevModPhys.63.573. URL http://link.aps.org/doi/10.1103/RevModPhys.63.573.

[36] Henry W. Kendall. Deep inelastic scattering: Experiments on the proton and the observation of scaling. *Rev. Mod. Phys.*, 63:597–614, Jul 1991. doi: 10.1103/RevModPhys.63.597. URL http://link.aps.org/doi/10.1103/RevModPhys.63.597.

[37] Jerome I. Friedman. Deep inelastic scattering: Comparisons with the quark model. *Rev. Mod. Phys.*, 63:615–627, Jul 1991. doi: 10.1103/RevModPhys.63.615. URL http://link.aps.org/doi/10.1103/RevModPhys.63.615.

[38] E. D. Bloom, D. H. Coward, H. DeStaebler, J. Drees, G. Miller, L. W. Mo, R. E. Taylor, M. Breidenbach, J. I. Friedman, G. C. Hartmann, and H. W. Kendall. High-energy inelastic $e - p$ scattering at 6 degrees and 10degrees. *Phys. Rev. Lett.*, 23:930–934, Oct 1969. doi: 10.1103/PhysRevLett.23.930. URL http://link.aps.org/doi/10.1103/PhysRevLett.23.930.

[39] Michael E. Peskin and Daniel V. Schroeder. *An Introduction to Quantum Field Theory*. ABP, 1995.

[40] Siegfried and Bethke. alpha$_s$ at zinnowitz 2004. *Nuclear Physics B - Proceedings Supplements*, 135(0):345–352, 2004. URL http://www.sciencedirect.com/science/article/pii/S0920563204003809.

[41] W.J. Stirling. Private communication. URL www.hep.phy.cam.ac.uk/~wjs/plots/plots.html.

[42] A.D. Martin, W.J. Stirling, R.S. Thorne, and G. Watt. Parton distributions for the lhc. *Eur.Phys.J.C*, 63:189–285, 2009. URL http://arxiv.org/abs/0901.0002.

[43] Daniel Stump, Joey Huston, Jon Pumplin, Wu-Ki Tung, H. L. Lai, Steve Kuhlmann, and J. F. Owens. Inclusive jet production, parton distributions, and the search for new physics. *JHEP*, 0310:046, 2003. URL http://arxiv.org/abs/hep-ph/0303013.

[44] A M Cooper-Sarkar. Including heavy quark production in zeus-pdf fits. 08 2008. URL http://arxiv.org/abs/0808.1856.

[45] J. C. Collins and D. E. Soper. The theorems of perturbative qcd. *Annual Review of Nuclear and Particle Science*, 37(1):383409, 1987.

[46] A. Gehrmann-De Ridder, T. Gehrmann, E. W. N. Glover, and J. Pires. Second-order qcd corrections to jet production at hadron colliders: The all-gluon contribution. *Phys. Rev. Lett.*, 110:162003, Apr 2013. doi: 10.1103/PhysRevLett.110.162003. URL http://link.aps.org/doi/10.1103/PhysRevLett.110.162003.

[47] Paolo Nason. A New method for combining NLO QCD with shower Monte Carlo algorithms. *JHEP*, 0411:040, 2004. doi: 10.1088/1126-6708/2004/11/040.

[48] Stefano Frixione, Paolo Nason, and Carlo Oleari. Matching NLO QCD computations with Parton Shower simulations: the POWHEG method. *JHEP*, 0711:070, 2007. doi: 10.1088/1126-6708/2007/11/070.

[49] Simone Alioli, Paolo Nason, Carlo Oleari, and Emanuele Re. A general framework for implementing NLO calculations in shower Monte Carlo programs: the POWHEG BOX. *JHEP*, 1006:043, 2010. doi: 10.1007/JHEP06(2010)043.

[50] Torbjorn Sjostrand, Stephen Mrenna, and Peter Skands. Pythia 6.4 physics and manual. *Journal of High Energy Physics*, 2006(05):026, 2006. URL http://stacks.iop.org/1126-6708/2006/i=05/a=026.

[51] J W Huston JM Campbell and W J Stirling. Hard interactions of quarks and gluons: a primer for lhc physics. *Reports on Progress in Physics*, 70(1):89, 2007. URL http://stacks.iop.org/0034-4885/70/i=1/a=R02.

[52] Bo Andersson, G. Gustafson, G. Ingelman, and T. Sjostrand. Parton fragmentation and string dynamics. *Phys. Rept.*, 97:31–145, 1983. doi: 10.1016/0370-1573(83)90080-7.

[53] Giuseppe Marchesini Stefano Moretti Kosuke Odagiri Peter Richardson Michael H. Seymour Gennaro Corcella, Ian G. Knowles and Bryan R. Webber. Herwig 6: an event generator for hadron emission reactions with interfering gluons (including supersymmetric processes). *Journal of High Energy Physics*, 2001(01):010, 2001. URL `http://stacks.iop.org/1126-6708/2001/i=01/a=010`.

[54] Gennaro Corcella, Ian G. Knowles, Giuseppe Marchesini, Stefano Moretti, Kosuke Odagiri, Peter Richardson, Michael H. Seymour, and Bryan R. Webber. Herwig 6: an event generator for hadron emission reactions with interfering gluons (including supersymmetric processes). *Journal of High Energy Physics*, 2001(01):010, 2001. URL `http://stacks.iop.org/1126-6708/2001/i=01/a=010`.

[55] ATLAS Collaboration. Atlas tunes of pythia 6 and pythia 8 for mc11. Technical Report ATL-PHYS-PUB-2011-009, CERN, Geneva, Jul 2011.

[56] A. Sherstnev and R.S. Thorne. Parton distributions for lo generators. *The European Physical Journal C - Particles and Fields*, 55:553–575, 2008. ISSN 1434-6044. URL `http://dx.doi.org/10.1140/epjc/s10052-008-0610-x`. 10.1140/epjc/s10052-008-0610-x.

[57] Zoltán Nagy. Next-to-leading order calculation of three-jet observables in hadron-hadron collisions. *Phys. Rev. D*, 68:094002, Nov 2003. doi: 10.1103/PhysRevD.68.094002. URL `http://link.aps.org/doi/10.1103/PhysRevD.68.094002`.

[58] Atlas experiment cern. URL `http://www.atlas.ch/photos/index.html`.

[59] Luminosity determination in pp collisions at sqrt(s) = 7 tev using the atlas detector in 2011. Technical Report ATLAS-CONF-2011-116, CERN, Geneva, Aug 2011.

[60] The ATLAS Collaboration. The atlas experiment at the cern large hadron collider. .

[61] ATLAS Collaboration. Expected performance of the atlas experiment detector, trigger, physics. Technical Report CERN-OPEN-2008-020, CERN, Geneva, .

[62] ATLAS Collaboration. Performance of the atlas trigger system in 2010. Technical Report arXiv:1110.1530. CERN-PH-EP-2011-078, CERN, Geneva, Oct 2011. Comments: 50 pages, 64 figures.

[63] S. Agostinelli et al. GEANT4: A simulation toolkit. *Nucl. Instrum. Meth.*, A 506: 250–303, 2003.

[64] ATLAS Collaboration. The atlas simulation infrastructure. *Eur. Phys. J.*, C 70:823–874, 2010.

[65] Elzbieta Richter-Was, D Froidevaux, and Luc Poggioli. Atlfast 2.0 a fast simulation package for atlas. Technical Report ATL-PHYS-98-131, CERN, Geneva, Nov 1998.

[66] T Yamanaka. The atlas calorimeter simulation fastcalosim. Technical Report ATL-SOFT-PROC-2011-021, CERN, Geneva, Jan 2011.

[67] Public plots from the atlas experiment on luminosity. URL `https://twiki.cern.ch/twiki/bin/view/AtlasPublic/LuminosityPublicResults`.

[68] T. Kaluza. On the problem of unity in physics. *Sitzungsber. Preuss. Akad. Wiss. Berlin (Math. Phys.)*, 966-972(966), 1921.

[69] O. Klein. *Quantum Theory and Five-Dimensional Relativity Theory (translated from the German)*, pages 67–+. 1991.

[70] Nima ArkaniHamed, Savas Dimopoulos, and Gia Dvali. The hierarchy problem and new dimensions at a millimeter. *Physics Letters B*, 429(34):263 – 272, 1998. ISSN 0370-2693. doi: 10.1016/S0370-2693(98)00466-3. URL `http://www.sciencedirect.com/science/article/pii/S0370269398004663`.

[71] Lisa Randall and Raman Sundrum. Large mass hierarchy from a small extra dimension. *Phys. Rev. Lett.*, 83:3370–3373, Oct 1999. doi: 10.1103/PhysRevLett.83.3370. URL `http://link.aps.org/doi/10.1103/PhysRevLett.83.3370`.

[72] Gian F. Giudice, Riccardo Rattazzi, and James D. Wells. Quantum gravity and extra dimensions at high-energy colliders. *Nuclear Physics B*, 544(12):3 – 38, 1999. ISSN 0550-3213. doi: 10.1016/S0550-3213(99)00044-9. URL `http://www.sciencedirect.com/science/article/pii/S0550321399000449`.

[73] D. M. Gingrich. Experimental limits on the fundamental planck scale in large extra dimensions. 2008.

[74] Steen Hannestad and Georg G. Raffelt. Supernova and neutron-star limits on large extra dimensions reexamined. *Phys. Rev. D*, 67:125008, Jun 2003. doi: 10.1103/PhysRevD.67.125008. URL `http://link.aps.org/doi/10.1103/PhysRevD.67.125008`.

[75] Michel Cassé, Jacques Paul, Gianfranco Bertone, and Günter Sigl. Gamma rays from the galactic bulge and large extra dimensions. *Phys. Rev. Lett.*, 92:111102, Mar 2004. doi: 10.1103/PhysRevLett.92.111102. URL `http://link.aps.org/doi/10.1103/PhysRevLett.92.111102`.

[76] Luis A. Anchordoqui, Jonathan L. Feng, Haim Goldberg, and Alfred D. Shapere. Updated limits on tev-scale gravity from the absence of neutrino cosmic ray showers mediated by black holes. *Phys. Rev. D*, 68:104025, Nov 2003. doi: 10.1103/PhysRevD.68.104025. URL `http://link.aps.org/doi/10.1103/PhysRevD.68.104025`.

[77] E.G. Adelberger, B.R. Heckel, and A.E. Nelson. Tests of the gravitational inverse-square law. *Annual Review of Nuclear and Particle Science*, 53(1):77–121, 2003. doi: 10.1146/annurev.nucl.53.041002.110503. URL `http://www.annualreviews.org/doi/abs/10.1146/annurev.nucl.53.041002.110503`.

[78] Albert Einstein. Zur elektrodynamik bewegter krper. *Annalen der Physik*, 322:891921, 1905.

[79] Douglas M. Gingrich. Quantum black holes with charge, colour, and spin at the lhc. 12 2009. URL `http://arxiv.org/abs/0912.0826v1`.

[80] S. Hawking. Particle creation by black holes. *Communications in Mathematical Physics*, 43(3):199–220, 1975.

[81] S. W. Hawking. Black hole explosions? *Nature*, 248:30–31, March 1974. doi: 10.1038/248030a0.

[82] K. S. Thorne. *Nonspherical Gravitational Collapse–A Short Review*, pages 231–+. 1972.

[83] Ashok Goyal. Neutrinos as the source of ultrahigh energy cosmic rays in extra dimensions. *Phys. Rev. D; Physical Review D*, 63(4), 2001. doi: 10.1103/PhysRevD.63.043003.

[84] Jonathan Feng. Black hole production by cosmic rays. *Phys. Rev. Lett.; Physical Review Letters*, 88(2), 2001. doi: 10.1103/PhysRevLett.88.021303.

[85] Luis Anchordoqui. Experimental signature for black hole production in neutrino air showers. *Phys. Rev. D; Physical Review D*, 65(4), 2002. doi: 10.1103/PhysRevD.65.047502.

[86] Roberto Emparan. Cosmic rays as probes of large extra dimensions and tev gravity. *Phys. Rev. D; Physical Review D*, 65(6), 2002. doi: 10.1103/PhysRevD.65.064023.

[87] Steven Giddings. High energy colliders as black hole factories: The end of short distance physics. *Phys. Rev. D; Physical Review D*, 65(5), 2002. doi: 10.1103/PhysRevD.65.056010.

[88] Savas Dimopoulos and Greg Landsberg. Black holes at the large hadron collider. *Phys. Rev. Lett.*, 87:161602, Sep 2001. doi: 10.1103/PhysRevLett.87.161602. URL http://link.aps.org/doi/10.1103/PhysRevLett.87.161602.

[89] Douglas M. Gingrich and Kevin Martell. Study of highly excited string states at the large hadron collider. *Phys. Rev. D*, 78:115009, Dec 2008. doi: 10.1103/PhysRevD.78.115009. URL http://link.aps.org/doi/10.1103/PhysRevD.78.115009.

[90] Xavier Calmet, Wei Gong, and Stephen D.H. Hsu. Colorful quantum black holes at the lhc. *Physics Letters B*, 668(1):20 – 23, 2008. ISSN 0370-2693. doi: 10.1016/j.physletb.2008.08.011. URL http://www.sciencedirect.com/science/article/pii/S0370269308009878.

[91] Patrick Meade and Lisa Randall. Black holes and quantum gravity at the lhc. *Journal of High Energy Physics*, 2008(05):003, 2008. URL http://stacks.iop.org/1126-6708/2008/i=05/a=003.

[92] De-Chang Dai, Glenn Starkman, Dejan Stojkovic, Cigdem Issever, Eram Rizvi, and Jeff Tseng. Blackmax: A black-hole event generator with rotation, recoil, split branes and brane tension. *Phys.Rev.D*, 77:076007, 2008. URL http://arxiv.org/abs/0711.3012.

[93] De-Chang Dai, Cigdem Issever, Eram Rizvi, Glenn Starkman, Dejan Stojkovic, and Jeff Tseng. Manual of blackmax, a black-hole event generator with rotation, recoil, split branes, and brane tension. 02 2009. URL http://arxiv.org/abs/0902.3577.

[94] Estia J. Eichten, Kenneth D. Lane, and Michael E. Peskin. New tests for quark and lepton substructure. *Phys. Rev. Lett.*, 50:811–814, Mar 1983. doi: 10.1103/PhysRevLett.50.811. URL http://link.aps.org/doi/10.1103/PhysRevLett.50.811.

[95] G. Jikia. Excited quark production at ep and p colliders. *Nuclear Physics B*, 333 (2):317 – 334, 1990. ISSN 0550-3213. doi: 10.1016/0550-3213(90)90040-K. URL http://www.sciencedirect.com/science/article/pii/055032139090040K.

[96] U. Baur, M. Spira, and P. M. Zerwas. Excited-quark and -lepton production at hadron colliders. *Phys. Rev. D*, 42:815–824, Aug 1990. doi: 10.1103/PhysRevD.42.815. URL http://link.aps.org/doi/10.1103/PhysRevD.42.815.

[97] Search for excited quarks. *Physics Letters B*, 140(34):253 – 258.

[98] Excited quarks and leptons. *Physics Letters B*, 147(13):189 – 196, 1984.

[99] Atlas monte carlo tunes for mc09. Technical Report ATL-PHYS-PUB-2010-002, CERN, Geneva, Mar 2010.

[100] Sing Leung Cheung and P Savard. *Search for Dijet Resonances in $\sqrt{s}$ = 7 TeV Proton-Proton Collisions with the ATLAS Detector at the LHC. oai:cds.cern.ch:1399633*. PhD thesis, Toronto U., Toronto, 2011. Presented 03 Aug 2011.

[101] Torbjrn Sjstrand, Stephen Mrenna, and Peter Skands. A brief introduction to pythia 8.1. *Computer Physics Communications*, 178(11):852 – 867, 2008. ISSN 0010-4655. doi: 10.1016/j.cpc.2008.01.036. URL `http://www.sciencedirect.com/science/article/pii/S0010465508000441`.

[102] CDF Collaboration. Search for new particles decaying into dijets in proton-antiproton collisions at $\sqrt{s}$ = 1.96 TeV. *Phys. Rev. D*, 79:112002, Jun 2009. doi: 10.1103/PhysRevD.79.112002. URL `http://link.aps.org/doi/10.1103/PhysRevD.79.112002`.

[103] Jogesh C. Pati and Abdus Salam. Lepton number as the fourth "color". *Phys. Rev. D*, 10:275–289, Jul 1974. doi: 10.1103/PhysRevD.10.275. URL `http://link.aps.org/doi/10.1103/PhysRevD.10.275`.

[104] Harari H. A schematic model of quarks and leptons. *Phys. Lett. B*, 86, April 1979.

[105] Sundance O. Bilson-Thompson. A topological model of composite preons. 2005.

[106] D0 Collaboration. Dijet mass spectrum and a search for quark compositeness in proton-anti-proton collisions at sqrts = 1.7 tev. *Phys. Rev. Lett.*, 82:2457–2462, Mar 1999. doi: 10.1103/PhysRevLett.82.2457. URL `http://link.aps.org/doi/10.1103/PhysRevLett.82.2457`.

[107] C. Buttar et al. Standard model handles and candles working group: Tools and jets summary report. (arXiv:0803.0678 [hep-ph]), 2007.

[108] S.D. Ellis, J. Huston, K. Hatakeyama, P. Loch, and M. Toennesmann. Jets in hadron-hadron collisions. 12 2007. URL `http://arxiv.org/abs/0712.2447v1`.

[109] Matteo Cacciari and Gavin P. Salam. Dispelling the myth for the jet-finder. *Physics Letters B*, 641(1):57 – 61, 2006. ISSN 0370-2693. doi: 10.1016/j.physletb.2006.08.037. URL `http://www.sciencedirect.com/science/article/pii/S0370269306010094`.

[110] G. P. Salam M. Cacciari and G. Soyez. URL `http://fastjet.fr`.

[111] L. Asquith et al. (Technical Report ATL-COM-PHYS-2009-630), Dec 2009.

[112] W. Lampl et al. Calorimeter clustering algorithms: description and performance. (ATL-LARG-PUB-2008-002), April 2008.

[113] Caterina Doglioni. *Measurement of the inclusive jet cross section with the ATLAS detector at the Large Hadron Collider*. PhD thesis, University of Oxford, Oxford, UK, 2011. Presented November 24, 2011.

[114] The ATLAS Collaboration. Energy linearity and resolution of the atlas electromagnetic barrel calorimeter in an electron test-beam. *Nuclear Instruments and Methods in Physics Research Section A: Accelerators, Spectrometers, Detectors and Associated Equipment*, 568(2):601 – 623, 2006. ISSN 0168-9002. doi: 10.1016/j.nima.2006.07.053. URL `http://www.sciencedirect.com/science/article/pii/S0168900206013222`.

[115] The ATLAS Collaboration. Response uniformity of the atlas liquid argon electromagnetic calorimeter. *Nuclear Instruments and Methods in Physics Research Section A: Accelerators, Spectrometers, Detectors and Associated Equipment*, 582(2): 429 – 455, 2007. ISSN 0168-9002. doi: 10.1016/j.nima.2007.08.157. URL `http://www.sciencedirect.com/science/article/pii/S0168900207018591`.

[116] The ATLAS Collaboration. Measurement of the response of the atlas liquid argon barrel calorimeter to electrons at the 2004 combined test-beam. *Nuclear Instruments and Methods in Physics Research Section A: Accelerators, Spectrometers, Detectors and Associated Equipment*, 614(3):400 – 432, 2010. ISSN 0168-9002. doi: 10.1016/j.nima.2009.12.055. URL `http://www.sciencedirect.com/science/article/pii/S0168900209023924`.

[117] The ATLAS Collaboration. Combined performance studies for electrons at the 2004 atlas combined test-beam. *Journal of Instrumentation*, 5(11):P11006, 2010. URL `http://stacks.iop.org/1748-0221/5/i=11/a=P11006`.

[118] The ATLAS Collaboration. Performance of the atlas liquid argon endcap calorimeter in the pseudorapidity region in beam tests. *Nuclear Instruments and Methods in Physics Research Section A: Accelerators, Spectrometers, Detectors and Associated Equipment*, 593(3):324 – 342, 2008. ISSN 0168-9002. doi: 10.1016/j.nima.2008.05.033. URL `http://www.sciencedirect.com/science/article/pii/S0168900208007456`.

[119] The ATLAS Collaboration. Electromagnetic energy scale in-situ calibration and performance: Supporting document for the egamma performance paper. Technical Report ATL-COM-PHYS-2011-263, CERN, Geneva, Mar 2011.

[120] ATLAS Collaboration. Jet energy measurement with the atlas detector in proton-proton collisions at $\sqrt{s} = 7$ tev. (arXiv:1112.6426 [hep-ex]), .

[121] S Adomeit, T Carli, C Doglioni, D Gillberg, G Halladjan, B Malaescu, L Mijovic, and A Picazio. Jet energy scale and its systematic uncertainty in proton-proton collisions at sqrt(s)=7 tev with atlas 2011 data. Technical Report ATL-COM-PHYS-2012-975, CERN, Geneva, Jul 2012. This is the backup documentation for the CONF note draft ATLAS-COM-CONF-2012-171.

[122] In-situ jet energy scale and jet shape corrections for multiple interactions in the first atlas data at the lhc. Technical Report ATLAS-CONF-2011-030, CERN, Geneva, Mar 2011.

[123] In situ jet pseudorapidity intercalibration of atlas detector using dijet events in $\sqrt{s} = 7$ tev proton-proton 2011 data. Technical Report ATLAS-COM-CONF-2012-079, CERN, May 2012. URL `https://cdsweb.cern.ch/record/1450047?` Reference not yet public.

[124] ATLAS Collaboration. Data-quality requirements and event cleaning for jets and missing transverse energy reconstruction with the atlas detector in proton-proton collisions at a center-of-mass energy $\sqrt{s} = 7$ tev. Technical Report ATLAS-CONF-2010-038, CERN, 2010. URL `http://cdsweb.cern.ch/record/1277678`.

[125] A. Bhatti, F. Canelli, B. Heinemann, J. Adelman, D. Ambrose, J.-F. Arguin, A. Barbaro-Galtieri, H. Budd, Y.S. Chung, K. Chung, B. Cooper, C. Currat, M. D?Onofrio, T. Dorigo, R. Erbacher, R. Field, G. Flanagan, A. Gibson, K. Hatakeyama, F. Happacher, D. Hoffman, G. Introzzi, S. Kuhlmann, S. Kwang, S. Jun, G. Latino, A. Malkus, M. Mattson, A. Mehta, P.A. Movilla-Fernandez, L. Nodulman, M. Paulini, J. Proudfoot, F. Ptohos, S. Sabik, W. Sakumoto, P. Savard, M. Shochet, P. Sinervo, V. Tiwari, A. Wicklund, and G. Yun. Determination of the jet energy scale at the collider detector at fermilab. *Nuclear Instruments and Methods in Physics Research Section A: Accelerators, Spectrometers, Detectors and Associated Equipment*, 566(2):375 – 412, 2006. ISSN 0168-9002. doi: 10.1016/j.nima.2006.05.269. URL `http://www.sciencedirect.com/science/article/pii/S0168900206011053`.

[126] Jeroen Hegeman. Jet energy scale calibration in the d0 experiment. *Journal of Physics: Conference Series*, 160(1):012024, 2009. URL `http://stacks.iop.org/1742-6596/160/i=1/a=012024`.

[127] The ATLAS Collaboration. Jet energy resolution and selection efficiency relative to track jets from in-situ techniques with the atlas detector using proton-proton collisions at a center of mass energy *sqrts* = 7 tev. Technical Report ATLAS-CONF-2010-054, CERN, Geneva, Jul 2010.

[128] S Sacerdoti and G Romeo. Jet energy resolution twiki. URL `https://twiki.cern.ch/twiki/bin/view/Main/JetEnergyResolutionProvider`. ATLAS Twiki.

[129] C Doglioni and D Gillberg. Jet energy resolution for top analyses. URL `https://twiki.cern.ch/twiki/bin/view/AtlasProtected/JERProviderTop`. ATLAS Twiki.

[130] H S Bawa, N Boelaert, R Buckingham, G Choudalakis, T Dietzsch, C Doglioni, E Ertel, F Guescini, C Issever, H Li, M Kaneda, C J Meyer, F Ruehr, P Savard, M Shupe, T Sumida, K Terashi, and S L Wu. Search for new phenomena in dijet mass and angular distributions using 4.8 fb-1 of pp collisions at $\sqrt{s}$ = 7 tev collected by the atlas detector. Technical Report ATL-COM-PHYS-2012-801, CERN, Geneva, Jun 2012.

[131] Robin Devinish and Amanda Cooper-Sarkar. *Deep Inelastic Scattering*. OUP, 2004.

[132] R. K. Ellis, W. J. Stirling, and B. R. Webber. *QCD and Collider Physics*. Cambridge monographs on particle physics, nuclear physics and cosmology, 1996.

[133] D0 Collaboration Alex Melnitchouk, for the CDF. High mass dijet and ttbar resonance searches. Oct 2008. URL `http://arxiv.org/abs/0810.3338v1`.

[134] The ATLAS Collaboration. Technical report, CERN, Geneva, .

[135] M Baak, C Guyot, M Hauschild, R Hawkings, B Heinemann, A Höcker, M Martínez-Pérez, D Malon, P Onyisi, and E Torrence. Data quality status flags and good run lists for physics analysis in atlas. *ATL-COM-GEN-2009-015, CERN*, (ATL-COM-GEN-2009-015), March .

[136] N Makovec. Selection of jets produced in proton-proton collisions with the atlas detector using 2011 data. (ATL-COM-PHYS-2012-067), Jan 2012.

[137] S.-L. Cheung and P. Savard. Dijet resonance searches in atlas. Technical Report ATL-COM-PHYS-2009-027, CERN, Geneva, 2009.

[138] N Boelaert, G Choudalakis, PO Deviveiros, E Feng, H Li, J Poveda, L Pribyl, F Ruehr, and SL Wu. Atlas sensitivity to contact interactions and gravity mediated effects in large extra dimensions using dijet events at $\sqrt{s} = 7$ tev. Technical Report ATL-COM-PHYS-2010-136, CERN, Geneva, Mar 2010.

[139] Nele Boelaert and Torsten Akesson. *Dijet angular distributions in proton-proton collisions at $\sqrt{s} = 7$ TeV and $\sqrt{s} = 14$ TeV. oai:cds.cern.ch:1300762.* PhD thesis, Lund U., Lund, 2010. Presented on 21 Sep 2010.

[140] Hung-Liang Lai, Marco Guzzi, Joey Huston, Zhao Li, Pavel M. Nadolsky, et al. New parton distributions for collider physics. *Phys.Rev.*, D82:074024, 2010. doi: 10.1103/PhysRevD.82.074024.

[141] Pavel M. Nadolsky, Hung-Liang Lai, Qing-Hong Cao, Joey Huston, Jon Pumplin, Daniel Stump, Wu-Ki Tung, and C.-P. Yuan. Implications of cteq global analysis for collider observables. *Phys. Rev. D*, 78:013004, Jul 2008. doi: 10.1103/PhysRevD.78.013004. URL `http://link.aps.org/doi/10.1103/PhysRevD.78.013004`.

[142] Tancredi Carli, Dan Clements, Amanda Cooper-Sarkar, Claire Gwenlan, Gavin P. Salam, Frank Siegert, Pavel Starovoitov, and Mark Sutton. A posteriori inclusion of parton density functions in nlo qcd final-state calculations at hadron colliders: the applgrid project. *Eur Phys J*, C 66(503), 2010. doi: 10.1140/epjc/s10052-010-1255-0.

[143] ATLAS Collaboration. Updated Luminosity Determination in pp Collisions at $\sqrt{s} = 7$ TeV using the ATLAS Detector. Technical Report ATLAS-CONF-2011-011, CERN, 2011. URL `https://cdsweb.cern.ch/record/1334563`.

[144] ATLAS Collaboration. Luminosity determination in *pp* collisions at $\sqrt{s} = 7$ TeV using the ATLAS detector at the LHC. *Eur. Phys. J.*, C71:1630, 2011. doi: 10.1140/epjc/s10052-011-1630-5.

[145] Georgios Choudaliakis. On hypothesis testing, trials factor, hypertests and the BUMPHUNTER. Jan 2011. doi: arXiv:1101.0390v2.

[146] The CMS Collaboration. Search for narrow resonances and quantum black holes in inclusive and b-tagged dijet mass spectra from pp collisions at 7 tev. *Journal of High Energy Physics*, 2013(1):1–40, 2013. doi: 10.1007/JHEP01(2013)013.

[147] The CMS Collaboration. Search for heavy resonances in the w/z-tagged dijet mass spectrum in pp colliions at 7 tev. 2012. URL `http://arxiv.org/abs/1212.1910`.

[148] The ATLAS Collaboration. Search for production of resonant states in the photon-jet mass distribution using *pp* collisions at $\sqrt{s} = 7$ TeV collected by the atlas detector. *Phys. Rev. Lett.*, 108:211802, May 2012. doi: 10.1103/PhysRevLett.108.211802. URL `http://link.aps.org/doi/10.1103/PhysRevLett.108.211802`.

[149] ATLAS Collaboration. Search for contact interactions and large extra dimensions in dilepton events from *pp* collisions at $\sqrt{s}$=7 TeV with the atlas detector. *Phys. Rev. D*, 87:015010, Jan 2013. doi: 10.1103/PhysRevD.87.015010. URL `http://link.aps.org/doi/10.1103/PhysRevD.87.015010`.

[150] Search for contact interactions using the inclusive jet p_t spectrum in pp collisions at $\sqrt{s} = 7$ tev, author = CMS Collaboration, journal = Phys. Rev. D, volume = 87, issue = 5, pages = 052017, numpages = 19, year = 2013, month = Mar, doi = 10.1103/PhysRevD.87.052017, url = http://link.aps.org/doi/10.1103/PhysRevD.87.052017, publisher = American Physical Society. .

[151] Search for contact interactions in $\mu^+ \mu^-$ events in pp collisions at $\sqrt{s} = 7$ tev, author = CMS Collaboration, journal = Phys. Rev. D, volume = 87, issue = 3, pages = 032001, numpages = 19, year = 2013, month = Feb, doi = 10.1103/PhysRevD.87.032001, url = http://link.aps.org/doi/10.1103/PhysRevD.87.032001, publisher = American Physical Society. .

[152] The runquery interface, May . URL `http://atlas-runquery.cern.ch/`.

[153] E J Gallas, D Malon, R J Hawkings, S Albrand, and E Torrence. An integrated overview of metadata in atlas. *Journal of Physics: Conference Series*, 219(4):042009, 2010. URL `http://stacks.iop.org/1742-6596/219/i=4/a=042009`.

[154] E J Gallas, S Albrand, J Fulachier, F Lambert, K E Pachal, J C L Tseng, and Q Zhang. Conditions and configuration metadata for the atlas experiment. Technical Report ATL-SOFT-PROC-2012-040, CERN, Geneva, May 2012.

[155] The runbrowser and elssi interfaces, November . URL `https://atlddm10.cern.ch/tagservices/index.htm`.

[156] The ami interface. URL `http://ami.in2p3.fr/opencms/opencms/AMI/www/index.html`.

[157] Interface to trigger database. URL `http://atlas-trigconf.cern.ch`.

[158] B. Demirkoz, M. Martinez, and E. Meoni. Measurement of level1 jet trigger efficiencies in atlas using *pp* minimum bias data at $\sqrt{s} = 7$ tev. Technical Report ATL-COM-DAQ-2010-114, CERN, 2010. URL `https://cdsweb.cern.ch/record/1279622/`.

[159] The ATLAS Collaboration. Measurement of inclusive jet and dijet production in pp collisions at $\sqrt{s}$=7 TeV using the atlas detector. *Phys. Rev. D*, 86:014022, Jul 2012. doi: 10.1103/PhysRevD.86.014022. URL `http://link.aps.org/doi/10.1103/PhysRevD.86.014022`.